



Torsten Müller

**Low Energy Ion Beam Synthesis  
of Si Nanocrystals for Nonvolatile  
Memories – Modeling and Process  
Simulations**



Wissenschaftlich-Technische Berichte  
**FZR-439**  
November 2005

Torsten Müller

**Low Energy Ion Beam Synthesis  
of Si Nanocrystals for Nonvolatile Memories –  
Modeling and Process Simulations**

Bibliothek FZ Rossendorf



01291544



Forschungszentrum  
Rossendorf

---

**Low Energy Ion Beam Synthesis of Si  
Nanocrystals for Nonvolatile Memories –  
Modeling and Process Simulations**

Torsten Müller

---

Dresden, October 24, 2005





FORSCHUNGSZENTRUM ROSSENDORF  
Institut für Ionenstrahlphysik und Materialforschung

**Low Energy Ion Beam Synthesis of Si  
Nanocrystals for Nonvolatile Memories –  
Modeling and Process Simulations**

**Dissertation**

zur Erlangung des akademischen Grades

Doctor Rerum Naturalium

eingereicht an der

Fakultät Mathematik und Naturwissenschaften

der Technischen Universität Dresden

vorgelegt von

Dipl. Phys. TORSTEN MÜLLER

geboren am 1. März 1976 in Dresden

Tag der Verteidigung:

19.10.2005

Gutachter:

PROF. DR. WOLFHARD MÖLLER  
PROF. DR. HARRY BERNAS  
PROF. DR. DIMITRIS TSOUKALAS

Technische Universität Dresden  
CNRS-CSNSM Orsay, Frankreich  
IMEL Demokritos Athen, Greece

# Contents

<b>1. Si Nanocrystal Based Nonvolatile Semiconductor Memories – An Introduction</b>	<b>1</b>
1.1. The floating gate memory . . . . .	1
1.2. Competing nonvolatile memory concepts . . . . .	2
1.3. Si nanocrystal based multi-dot floating gate memory . . . . .	4
1.4. Synthesis of Si nanocrystals for nonvolatile memories – A challenge to materials research . . . . .	8
1.5. Outline of the thesis . . . . .	10
<b>2. Ion Beam Synthesis of Nanostructures</b>	<b>17</b>
2.1. High-fluence ion implantation . . . . .	18
2.1.1. Ion stopping . . . . .	19
2.1.2. Implantation profiles . . . . .	20
2.1.3. Target modification by high-fluence ion implantation . . . . .	21
2.2. Nanostructure formation by phase separation – relaxing far-from-equilibrium states . . . . .	23
2.2.1. Binary Phase Diagram . . . . .	23
2.2.2. Decomposition mechanisms . . . . .	24
2.2.3. Growth, coarsening and percolation . . . . .	30
<b>3. Modeling of Si Excess Depth Profiles by Dynamic Binary Collision Calculations</b>	<b>39</b>
3.1. Dynamic BCA simulations using TRIDYN . . . . .	39
3.1.1. TRIDYN parameters for SiO <sub>2</sub> . . . . .	40
3.1.2. Validation of low-energy sputtering yields . . . . .	42
3.2. Si excess in low energy Si <sup>+</sup> implanted SiO <sub>2</sub> films . . . . .	43
3.2.1. Si excess - Over-stoichiometric Si in SiO <sub>2</sub> . . . . .	44
3.2.2. Si excess depth profiles predicted by TRIDYN calculations . . . . .	45
3.2.3. Profile approximations . . . . .	46
3.2.4. Si excess in as-implanted SiO <sub>2</sub> layers – Comparison with ToF-SIMS results . . . . .	47
3.3. Tailoring the Si excess depth profile . . . . .	48
3.3.1. Influence of the ion energy . . . . .	49
3.3.2. Influence of the SiO <sub>2</sub> thickness . . . . .	50
3.4. Summary . . . . .	51

<b>4. Modeling of Phase Separation by Kinetic Monte Carlo Simulations</b>	<b>53</b>
4.1. Si Mass Transport in SiO <sub>2</sub>	54
4.1.1. Si self-diffusion in SiO <sub>2</sub> – Experimental Data	54
4.1.2. Mass transport of Si excess in SiO <sub>2</sub> – What is the mobile defect?	56
4.2. The kinetic lattice Monte Carlo method	57
4.2.1. Gauging simulation parameters	62
4.2.2. Analysis of kinetic Monte Carlo results	64
4.2.3. Simulation conditions for low energy IBS in thin gate oxides	66
<b>5. Results and Discussion: Predictions on Tailored Si NC Formation</b>	<b>71</b>
5.1. Si NC formation in the vicinity of an absorbing interface	73
5.2. Morphology and morphology control of Si multi-dot floating gates	76
5.2.1. Regimes of phase separation	76
5.2.2. Mapping Si and SiO <sub>2</sub> plasmons by Electron Energy Loss Spectroscopy – Comparison to KMC predictions	79
5.2.3. Processing routes for self-aligned NC layer formation – Choosing the right precipitate morphology	85
5.3. Prediction of the optimum NC size and density	86
5.3.1. Regimes of phase separation	87
5.3.2. Impact of the oxide thicknesses	88
5.3.3. Annealing temperature and time scale	90
5.3.4. Characterization of the NC size distribution	92
5.3.5. Process options for an optimum NC size and density	94
5.4. Process modeling of a self-aligned NCs formation	95
5.4.1. Prediction of a self-adjusted electron tunneling barrier	95
5.4.2. Comparison to XTEM results	97
5.4.3. Evolution of the tunneling distance in different regimes of phase separation	98
5.4.4. Control of the NC layer location by the implantation energy	99
5.4.5. Optimization of the initial oxide thickness	104
5.4.6. Spatial fluctuations of tunneling distances	106
5.5. Impact of the ambient on the NC formation	107
5.5.1. Humidity penetration into ion beam damaged oxide layers	108
5.5.2. Parasitic oxidation of NCs by penetrated humidity	108
<b>6. Results and Discussion: Electron Tunneling Percolation and Lateral Charge Isolation</b>	<b>117</b>
6.1. Nearest Neighbor Distances and Their Distribution	118
6.2. Lateral Electron Tunneling – A Percolation Problem	119
6.2.1. Groups of percolated NCs	120
6.2.2. Predicted tunneling percolation threshold	122
6.2.3. Percolation thresholds in simple analytical models	123
6.2.4. A relation to variable range hopping conduction	125

<b>7. Resume: Prospects of Ion Beam Synthesized Si NCs for Future Non-volatile Memories</b>	<b>129</b>
7.1. Process simulations of low energy IBS – A summary . . . . .	129
7.2. IBS of Si NCs for nanocrystal memories – Advantages and feasibility . . .	130
7.3. Can NC memories compete with other NVSM concepts? . . . . .	131
<b>A. Bit Encoding of the Kinetic Monte Carlo Lattice</b>	<b>135</b>

This work is based on the following publications and presentations. It has been supported by the European Commission through the Growth project G5RD/2000/00320 – NEON (Nanoparticles for Electronics) and is documented in NEON projects reports.

## Articles

T. Müller, C. Bonafos, M. Tencé, K.-H. Heinig, H. Coffin, N. Cherkashin, G. Ben Assayag, S. Schamm, G. Zanchi, C. Colliex, W. Möller, and A. Claverie. Multi-dot floating-gates for nonvolatile semiconductor memories - Their ion beam synthesis and morphology. *Applied Physics Letters*, **85**:2373-2375, 2004.

T. Müller, C. Bonafos, M. Tencé, K.-H. Heinig, H. Coffin, N. Cherkashin, G. Ben Assayag, S. Schamm, G. Zanchi, C. Colliex, W. Möller, and A. Claverie. Multi-dot floating-gates in MOSFETs for nonvolatile memories - Their ion beam synthesis and morphology. *Materials Research Society Proceedings*, **792**, 2004.

T. Müller, K.-H. Heinig, and W. Möller. Size and location control of Si nanocrystals at ion beam synthesis in thin SiO<sub>2</sub> films. *Applied Physics Letters*, **81**:3049-3051, 2002.

T. Müller, K.-H. Heinig, and W. Möller. Nanocrystal formation in Si implanted thin SiO<sub>2</sub> layers under the influence of an absorbing interface. *Materials Science and Engineering B*, **101**(1-3):49-54, 2003.

C. Bonafos, M. Carrada, N. Cherkashin, H. Coffin, D. Chassaing, G. B. Assayag, A. Claverie, T. Müller, K. H. Heinig, M. Perego, M. Fanciulli, P. Normand, and D. Tsoukalas. Manipulation of two-dimensional arrays of si nanocrystals embedded in thin SiO<sub>2</sub> layers by low energy ion implantation. *Journal of Applied Physics*, **95**(10):5696-5702, 2004.

K.-H. Heinig, T. Müller, B. Schmidt, M. Strobel, and W. Möller. Interfaces under ion irradiation: Growth and taming of nanostructures. *Applied Physics A*, **77**:17-25, 2003) .

## Conference Contributions (selected)

T. Müller, K.-H. Heinig, B. Schmidt and K.-H. Stegemann. Si Nanocrystal Formation for Nonvolatile Memories by Ion Beam Synthesis (*invited talk*), to be held at the *International Workshop on Si Nanocrystals*, 2005, Budapest, Hungary.

T. Müller, K.-H. Heinig, C. Bonafos, H. Coffin, G. Ben Assayag, S. Schamm, G. Zanchi, A. Claverie, M. Tencé and C. Colliex. Comparison of Kinetic MC Simulations and EF-STEM Observations of Phase Separation in Si<sup>+</sup> Implanted Thin SiO<sub>2</sub> Films (*talk*), *Annual meeting of the German Physical Society*, 2004, Regensburg, Germany.

T. Müller, K.-H. Heinig, C. Bonafos, H. Coffin, G. Ben Assayag, S. Schamm, G. Zanchi, A. Claverie, M. Tencé and C. Colliex. Comparison of Kinetic MC Simulations and EF-STEM

Observations of Phase Separation in Si<sup>+</sup> Implanted Thin SiO<sub>2</sub> Films (*talk*), *Fall meeting of the Material Research Society (MRS)*, 2003, Boston, USA.

T. Müller and K.-H. Heinig. Optimizing Nanocrystal Synthesis for Multi-dot Floating Gates of Nonvolatile Memories (*talk*), *Spring meeting of the European Materials Research Society E-MRS*, 2003, Strasbourg, France.

T. Müller, K.-H. Heinig, W. Möller. Size and Location Control of Si Nanocrystals at Ion Beam Synthesis in Thin Gate Oxides (*talk*). *International Workshop on Nanostructures for Electronics and Optics (NEOP)*, 2002, Dresden, Germany.

T. Müller, K.-H. Heinig, W. Möller. Nanocrystal Formation by Phase Separation in Ultra-Thin Si<sup>+</sup> Implanted Gate Oxides (*talk*). *Spring meeting of the European Materials Research Society E-MRS*, 2002, Strasbourg, France. Received Graduate Student Award.

## **NEON project reports**

Nanoparticles for electronics. *Final technical report*, EU Growth Project NEON GRD1-2000-25619, Toulouse, France, March 2004. <http://www.cemes.fr/neon.html>.

Influence of ion implantation conditions on nanocrystal positioning within thin oxides. *Deliverable D1*, EU Growth Project NEON GRD1-2000-25619, January 2002. <http://www.cemes.fr/neon.html>.

Report on model evaluation for process understanding of WP1 to WP3. *Deliverable D11*, EU Growth Project NEON GRD1-2000-25619, June 2002. <http://www.cemes.fr/neon.html>.

Predictive computer simulations and data base improvement. *Deliverable D13*, EU Growth Project NEON GRD1-2000-25619, August 2003. <http://www.cemes.fr/neon.html>.

## List of Acronyms

Often repeated expressions or lengthy technical descriptions will be abbreviated. For greater clearness, however, the use of acronyms is reduced wherever this is possible.

AFM	atomic force microscopy
BCA	binary collision approximation
CMOS	complementary metal-oxide-semiconductor
CNT	classical nucleation theory
CHC	Cahn-Hilliard-Cook theory of spinodal decomposition
CVD	chemical vapor deposition
dpa	displacements per atom
DOS	density of states
DRAM	dynamic random access memory
EELS	electron energy loss spectroscopy
EEPROM	electrically erasable and programmable read only memory
EFSTEM	energy filtered scanning transmission electron microscopy
fcc	face-centered cubic
FET	field-effect-transistor
FN	Fowler-Nordheim (tunneling)
FWHM	full-width half-maximum
GT	Gibbs-Thomson (equation)
HREM	high resolution electron microscopy
IBS	ion beam synthesis
LPCVD	low pressure chemical vapor deposition
LSW	Lifschitz-Slyozov-Wagner theory of precipitate coarsening
KMC	Kinetic Monte Carlo (simulation)
MC	Monte Carlo
MCS	Monte Carlo steps
MOS	metal-oxide-semiconductor
MOSFET	metal-oxide-semiconductor field effect transistor
NC	nanocrystal or nanocluster
NRA	nuclear reaction analysis



NVSM	nonvolatile semiconductor memory
PECVD	plasma enhanced chemical vapor deposition
PEELS	parallel (detection) electron energy loss spectroscopy
RAM	random access memory
SBE	surface binding energy
SONOS	silicon-oxide-nitride-oxide-silicon (stack or memory)
STEM	scanning transmission electron microscopy
TEM	transmission electron microscopy
ToF-SIMS	time-of-flight secondary ion mass spectroscopy
ULE	ultra low energy (ion implantation)
VASE	variable angle spectroscopic ellipsometry
XTEM	cross sectional transmission electron microscopy



# Chapter 1.

## Si Nanocrystal Based Nonvolatile Semiconductor Memories – An Introduction

Since the mid-1960s, nonvolatile semiconductor memories (NVSM) have been intensively studied in order to alleviate the main drawback of the metal-oxide-semiconductor (MOS) memory concept, that is, its intrinsic volatility. From the early development stage, a dominant design emerged, the *floating gate* concept.

### 1.1. The floating gate memory

Charge is stored on an electrically fully isolated poly-Si layer, the floating gate, that is embedded in the gate oxide of a MOS transistor. Charge brought to the floating gate screens the control gate potential and induces a threshold voltage shift whose magnitude is a measure of the charge on the floating gate. The isolation by the gate dielectric then guarantees true nonvolatile operation, i.e. a charge and therefore information retention for periods up to ten years (the industry standard). Altering the information requires charging/discharging of the floating gate layer and can be achieved by means of different physical mechanisms. The most common ones are channel hot electron injection and Fowler-Nordheim tunneling. Details on the floating gate technology, memory array circuitry as well as on retention and reliability can be found in the reviews of Brown and Brewer (1998) and Cappelletti et al.

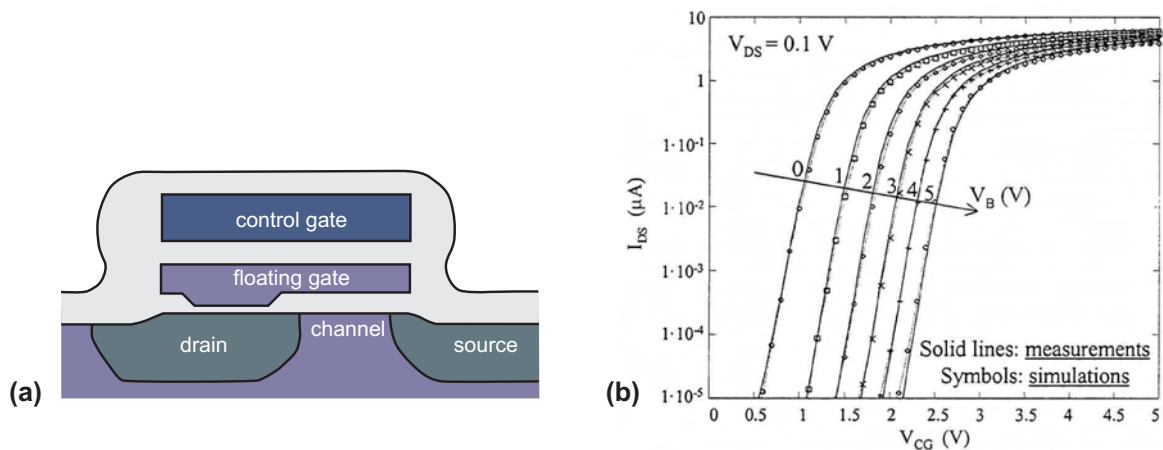


**Figure 1.1.:** (a) Schematic cross section of a conventional floating gate memory cell. (b) Subthreshold transfer characteristic (drain current  $I_{DS}$  vs. gate voltage  $V_{CG}$ ) of an EEPROM cell of 300 nm width and 700 nm length. The back bias  $V_B$  was varied in addition. From Larcher et al. (2001).

(1999).

Despite of the huge commercial success, conventional floating gate devices have their limitations. The most prominent today, is the limited scalability of the principle device structure, which mostly stems from the extreme requirements on the floating gate isolation, in particular from the crystalline Si substrate, by the tunnel oxide. On the other hand, the tunnel oxide should allow for quick and efficient charge transfer to the floating gate layer – preferably under low electric fields. The trade-off that is to be made between fast, low-voltage and low-power write and erase operations and sufficient data integrity is additionally worsened by defects within the tunnel oxide (Hsia and Tyree, 1998). Repeated stressing of the oxide during alternate write/erase operations lead to bulk or interface trap generation and stress induced leakage currents. Nonetheless, thin tunnel oxides are more prone to trap generation in general, the stress induced leakage proves to be the main limitation on both the retention and the endurance of floating gate devices.

As a result of the conflicting demands, manufacturers have settled on a compromise of 8 – 11 nm tunnel oxide thickness, that has hardly been reduced during past technology generations (Taub et al., 2005). As a consequence, operation speeds and voltages have only marginally been improved by scaling the floating gate devices.

## 1.2. Competing nonvolatile memory concepts

These limitations of the floating gate concept has prompted intensive research exploring alternative storage structures. However, the ultimate solution – a genuine nonvolatile memory that retains data without external power, can be read from and programmed like a static or dynamic random access memory (RAM), and still achieve high-speed, high-density, and low-power consumption remains unfeasible today.

Yet tremendous progress has been made and several memory concepts were proposed. The underlying storage mechanisms of contemporary devices being either under research or entering the production stage utilize

- **electrical charge** stored isolated in the gate oxide of a MOS field effect transistor (MOSFET) providing hysteresis in the transistor transfer characteristic:
  - charge on a *floating gate* as used in electrically erasable and programable read only memory (EEPROM) and *flash* memories (conventional approach)
  - distributed charge storage in trapping defects, e.g. in a nitride layer of a NROM devices (Eitan et al., 2000) or the oxinitride of a SONOS cell (Libsch and White, 1998)
  - charge stored on isolated semiconductor *nanocrystals* (NC) (*NC memory* or Nano-floating-gate memory) (Tiwari et al., 1995)
  - polarization charges in ferroelectric gate oxides (ferroelectric field effect transistors) (Kohlstedt and Ishiwara, 2003)
- electrical resistance of a **magneto-electrical tunneling junction** (magneto-resistive RAM)

## 1.2. Competing nonvolatile memory concepts

Storage Mechanism	Present Day Baseline Technologies		Phase Change Memory*	Floating Body DRAM	Nano-floating Gate Memory**	Single/Few Electron Memories**	Insulator Resistance Change Memory**	Molecular Memories**
Device Types	DRAM	NOR Flash	OOM	1TDRAM	Engineered tunnel barrier or nanocrystal	SET	MIM	Bi-stable switch
Availability	2004	2004	~2006	~2006	>2006	>2007	~2010	>2010
Cell Elements	1T1C	1T	1T1R	1T	1T	1T	1T1R	1T1R
Initial F	90 nm	90 nm	100 nm	70 nm	80 nm	65 nm	65 nm	45 nm
Cell Size	8F <sup>2</sup> 0.065 μm <sup>2</sup>	12.5F <sup>2</sup> 0.101 μm <sup>2</sup>	~6F <sup>2</sup> 0.06 μm <sup>2</sup>	~4F <sup>2</sup> [A] 0.0049 μm <sup>2</sup>	~6F <sup>2</sup> 0.038 μm <sup>2</sup>	~6F <sup>2</sup> 0.025 μm <sup>2</sup>	~6F <sup>2</sup> 0.025 μm <sup>2</sup>	Not known
Access Time	<15 ns	~80 ns	<100 ns	<10 ns <sup>[A,B]</sup>	<10 ns	<10 ns	Slow	~10 ns
Store Time	<15 ns	~1 ms	<100 ns	<10 ns <sup>[A,B]</sup>	<10 ns	<100 ns	<100 ns	~10 ns
Retention Time	64 ms	10–20 yrs	>10 yrs	<10 ms <sup>[A]</sup>	>10 yrs	~100 sec	~1 year	~1 month
E/W Cycles	Infinite	1E5	>1E13	>1E15 <sup>[A]</sup>	>1E6	>1E9	>1E3	>1E15
General Advantages	<ul style="list-style-type: none"> <li>Density</li> <li>Economy</li> </ul>	<ul style="list-style-type: none"> <li>Non-volatile</li> <li>Multi-bit cells</li> </ul>	<ul style="list-style-type: none"> <li>Non-volatile</li> <li>Low power</li> <li>Rad hard</li> <li>Multi-bit cells</li> </ul>	<ul style="list-style-type: none"> <li>Density</li> <li>Economy</li> </ul>	<ul style="list-style-type: none"> <li>Non-volatile</li> <li>Fast read and write</li> <li>Multi-bit cells</li> </ul>	<ul style="list-style-type: none"> <li>Density</li> <li>Low power</li> </ul>	<ul style="list-style-type: none"> <li>Low voltage</li> <li>Multi-bit cells</li> </ul>	<ul style="list-style-type: none"> <li>Density</li> <li>Low power</li> <li>3D potential</li> <li>Defect tolerant</li> </ul>
Challenges	<ul style="list-style-type: none"> <li>Scaling</li> </ul>	<ul style="list-style-type: none"> <li>Scaling</li> </ul>	<ul style="list-style-type: none"> <li>Large E/W current</li> <li>New materials and integration</li> </ul>	<ul style="list-style-type: none"> <li>Need SOI</li> <li>Retention versus scaling</li> <li>Dopant fluctuation</li> <li>Endurance</li> </ul>	<ul style="list-style-type: none"> <li>Material quality</li> </ul>	<ul style="list-style-type: none"> <li>Dimension control for RT operation</li> <li>Background charge disturb</li> </ul>	<ul style="list-style-type: none"> <li>New materials and integration</li> <li>Slow access</li> <li>Speed versus R trade-off</li> </ul>	<ul style="list-style-type: none"> <li>Volatile</li> <li>Thermal stability</li> </ul>
Maturity	Production	Production	Development	Demonstrated	Research	Research	Research	Research
Research Activity****			3***	3	61	40	3	43

**Figure 1.2.:** Emerging research devices and projected parameters according to the International Technology Roadmap for Semiconductors (2003).

- reversible **phase change** from amorphous to crystalline that induces a change in the electrical resistivity (Chalcogenite or Ovonic-memory)

On applicability, time scale of introduction, and risk involved in the development of these emerging NVSM devices, detailed information can be found in the 2003 edition of the International Technology Roadmap for Semiconductors (2003). Figure 1.2 redrawn from it shows the one anticipated technology sequence of emerging memory concepts and their projected key parameters. Additional information on these devices is contained in the *Technology Roadmap for Nanoelectronics* produced by European Commission's IST program (Future and Emerging Technologies) (Compano, 2000) and in recent reviews of Waser (2003) and Goronkin and Yang (2004).

When evaluating emerging memory concepts, it is also important to acknowledge the

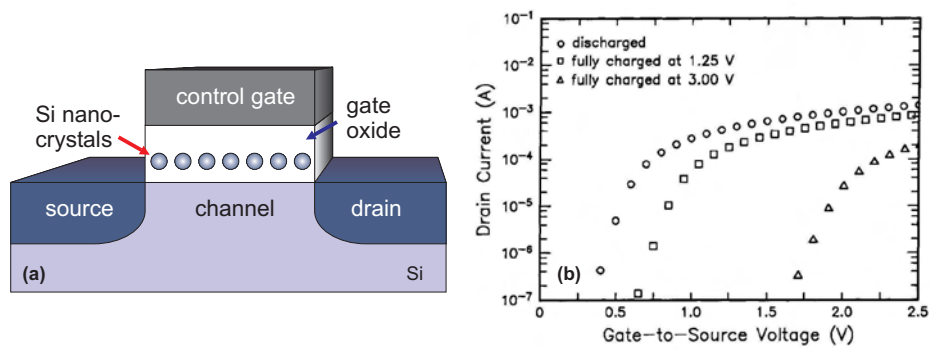


**Figure 1.3.:** (a) Schematic cross section of a CMOS transistor with Si NCs embedded in the gate oxide. (b) Bistability of the NC memory as a result of the charge injection into the NCs. Taken from Tiwari et al. (2000).

nonprocessing related value components embedded in conventional nonvolatile memory devices. Indeed, the floating gate devices are proven, mature and trusted concepts containing also considerable intellectual property in the array architectures and in the operating algorithms used in commercial Flash memories. New concepts that are capable to preserve at least parts of these intangibles will find it much easier to enter the NVSM market. Good examples are e.g. charge trapping memories that relies on the time-proven concept of discrete charge storage in a nitride layer (Brown and Brewer, 1998, chapter 5). It further attracted additional interest due to the possibility of *2 bit* cell concept proposed by Eitan (1998) that relaxes devices scaling issues due to the doubled bit density at the same die size. Programming with channel hot electron injection is used in this approach to inject hot electrons locally into the nitride layer either on the source or drain side that can be sensed in forward or reverse read operations (Eitan et al., 1999, 2000).

### 1.3. Si nanocrystal based multi-dot floating gate memory

Nanocrystal (NC) memories are fully CMOS-compatible floating gate memory structures where the conventional poly-Si floating gate layer is replaced by a layer of distributed 0D objects (e.g. Si NCs) that store finite and small number of electrons because of the reduction of the dimensions. This type of memory with the schematic cross section shown in Figure 1.3(a) has been first proposed by Tiwari et al. (1995) with Si NCs as charge storage nodes. The injection of electrons into the NCs alters the coupling of the gate potential to the transistor channel and therefore induces a shift of the threshold voltage<sup>1</sup> plotted in Figure 1.3(b) similar to the conventional floating gate transistor.

Its main advantage is however the isolation of the Si NCs from each other that allows to reduce reliability constraints arising from charge leakage and hence improving reliability. Possible conduction paths originating from oxide defects, either process or operation related, have only a very local effect and cannot lead to a complete discharging of the dis-

<sup>1</sup>Which is the gate voltage at which significant conduction in the transistor channel is possible.

tributed NC floating gate layer. As a result, the injection oxide thickness between the NCs and the channel can be made thinner. At these distances, electrons can tunnel by *quantum mechanical direct electron tunneling* at low gate voltages into the Si NCs. Thicker injection oxides would require a defect generating charging either by *Fowler-Nordheim* tunneling at higher gate voltages or by *channel hot electron injection* in order to be efficient. Both processes therefore limit the memory endurance, which is the ability to conduct repeated write and erase cycles without device degradation.

The reduced density of states in the NC layer restricts the states available for electrons and holes to tunnel to, and the Coulomb blockade effect that arises from a larger electrostatic energy associated with placing a charged particle onto a smaller capacitance brings forward that less charged carriers are used in the operation of the device and results in low-power operation without sacrificing speed. Low voltage operation in addition improves the cell scalability as constraints on electrical contact isolation can be relaxed. Utilizing Si NCs, large nonvolatile memory arrays have been demonstrated (Compagnoni et al., 2004; Steimle et al., 2004) and a wealth of literature is now available (De Blauwe, 2002; Silva et al., 2003; Tiwari et al., 2000, and further).

In addition, NC memory devices exhibit convergence/saturation in electron storage due to single electron and confinement effects (Tiwari et al., 2000; Wahl et al., 1999). Pronounced single electron charging/discharging effects occurring at room temperature were reported for ultra-small devices, e.g. by Molas et al. (2003) for a Yano-type architecture with an active area of  $20 \times 20 \text{ nm}^2$ .

### NC charging – Quantum Mechanical Modelling

The charging/discharging of a *single* NC – a quantum dot – is ideally modeled quantum mechanically, which has been carried out by Rana et al. (1998) using a density matrix approach in second quantization. The interaction by direct tunneling of the 2D electron gas in the transistor channel and the quantum dot is governed by the interaction Hamiltonian  $\mathcal{H} = \mathcal{H}_{deg} + \mathcal{H}_{dot} + \mathcal{H}_T$  with

$$\mathcal{H}_{deg} = \sum_n (\epsilon_n + eV) a_n^\dagger a_n, \quad \mathcal{H}_{dot} = \sum_m \epsilon_m b_m^\dagger b_m + E_s(\mathbf{v}), \quad (1.1)$$

and

$$\mathcal{H}_T = \sum_{n,m} T_{nm} a_n^\dagger b_m + c.c., \quad (1.2)$$

where  $\mathcal{H}_{deg}$  and  $\mathcal{H}_{dot}$  are the Hamiltonians for the two dimensional channel electron gas and the quantum dot, respectively.  $\mathcal{H}_T$  describes the coupling by electron tunneling between quantum dots and channel states labeled by the  $m$ 's and  $n$ 's.  $E_s(\mathbf{v})$  is the electrostatic energy and the state of the system is described by  $|n_n, n_m\rangle$ .

The time evolution of the density matrix in Heisenberg representation can be rewritten and yields a master equation  $\partial \mathbf{P}(t) / \partial t = \mathbf{W} \mathbf{P}(t)$ . The eigenstates in the channel can then be calculated self-consistently for a given number of electrons stored in the quantum dot for all gate voltages. The calculation has to be repeated for the different number of electrons allowed from which the transition rates are determined and therefore the time-dependence from the rate equation. The probability of quantum dot occupation numbers  $\{n_m\}$  can be

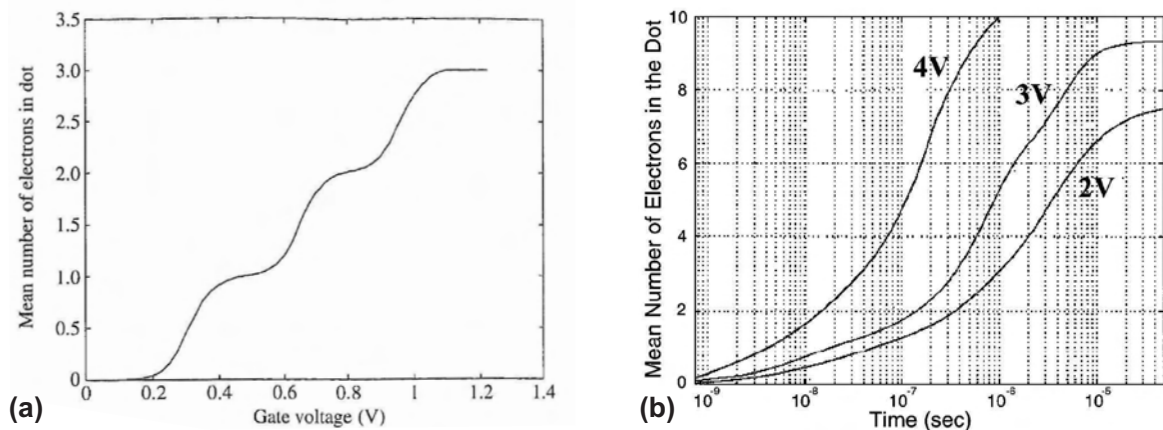


**Figure 1.4.:** (a) Mean number of electrons in a quantum dot upon charging and (b) charging transient for different gate biases. From Rana et al. (1998).

calculated by the trace of the density matrix in interaction representation  $\hat{\mathbf{P}}_{\mathcal{J}}(t)$  over all channel states from which then the probability of having  $\nu$  electrons in the quantum dot can be derived.

For the example of a quantum dot of  $10 \times 10 \times 6 \text{ nm}^3$ , Rana et al. (1998) calculated an injection time of 20 ns to charge the quantum dot at 3 V gate bias in average with one electron. The thickness of the tunnel and control oxide was assumed to be 1.5 nm and 5 nm thick, respectively. The mean electron population in the quantum dot and the charging transient are shown in Figure 1.4. The apparent saturation in number of electrons for longer pulse durations clearly shows the effect of reduced dimensions. Discharging, however, requires higher voltages and write times are much smaller than erase times. At conditions without external bias, the discharge process has considerably slowed down. The life time in the dot has become very large (Tiwari et al., 2000).

### Si NCs in large area transistors

Despite of the successive quantum mechanical modeling of a single quantum dot coupled by directed electron tunneling to the transistor channel, a comparison with realistic, large area NC memory transistor characteristics is difficult. More than a single time constant of charging/discharging has been identified and was related to interface states involved in the carrier dynamics (Silva et al., 2003; Tiwari et al., 2000).

More severe, fabricated Si NCs have a finite *size distribution* that washes out the single electron effects at room temperature measurements. Wang et al. (2001) have shown in a semi-classical calculation that a standard deviation of 0.6 nm at a mean NC size of 5 nm blurs effectively the Coulomb blockade effects at room temperature. The staircase behavior observed in Figure 1.4 can no longer be observed experimentally. Measurements of Tiwari et al. (1996a) on NC memories support these calculations, a staircase behavior due to Coulomb blockade is only found up to liquid N<sub>2</sub> temperatures but not at room temperature measurements<sup>2</sup>.

<sup>2</sup>By reducing the active area of the memory transistor and therefore the number of relevant NCs, room temperature single electron effects can be observed (Molas et al., 2003), although a large threshold voltage distribution has to be expected for these devices due to the fluctuations in NC size and number among



Despite quantum effects are certainly present at the charging/discharging processes of individual NCs, the NC memory transistor itself is **not** a quantum device, i.e. does not exploit single electron effects for the normal device operation. Semi-classical approaches have been proposed that rely on current continuity and use direct tunneling current characteristics only, which neglect Coulomb blockade and quantum confinement (De Salvo et al., 2000, 2001). Studies of Perniola et al. (2003a,b) using a similar semi-classical model further relate the distribution of the threshold voltage shifts of different devices to the size distribution of the Si NCs.

### Endurance, data retention, and advanced device concepts

NC memories have been shown to yield excellent endurance, i.e. the threshold voltage window shows only a limited closure up to  $10^7$  write/erase cycles and no erase degradation is observed (Dimitrakis et al., 2004; Hanafi et al., 1996; King et al., 2001; NEON, 2003, 2004a; Schmidt et al., 2004). However, questions have been raised by De Blauwe (2002) whether this has been performed in a fair comparison to conventional Flash memories. Many NC memory devices obey rather small threshold voltage shifts of some 100 mV that requires little charge to be transferred per cycle, which then can only cause a limited wear-out of the memory during repeated cycling. Moreover, NC memories are fabricated typically with thin injection oxides that are less prone to charge trap generation and charge trapping, a result that is known from floating gate memories (Brown and Brewer, 1998).

Thin tunnel oxides, on the other hand, guarantee only retention times that are too short for true nonvolatile operation as listed in Table 1.1. Nonetheless, retention has been found to increase if the transistor channel is kept in depletion (Ohba et al., 2000), 2 – 3 nm tunnel oxide thickness might not be sufficiently thick for true nonvolatile long term data storage (Compagnoni et al., 2003; Iannaccone, 2002). On the contrary, thicker tunnel oxides allow better retention but worsens the write/erase speeds such that a trade-off between demands on speed and retention has to be made.

It should also be noted that the retention characteristics of NC memories certainly deserves additional investigations including on the statistical information on long term data retention. Such studies might also trigger an optimization of the devices as already started in the recent

different devices.

tunnel oxide thickness	write condition	threshold voltage shift	refresh time
1.6 nm	200 ns, 3 V	$\sim 0.65$ V	$> 1$ week (RT) and $\sim 1$ h (85 °C)
2.1 nm	400 ns, 3 V	$\sim 0.48$ V	$> 1$ week (RT) and $\sim 5$ h (85 °C)
3.0 nm	1 $\mu$ s, 3 V	$\sim 0.55$ V	large (RT) and $\gg 1$ h (85 °C)
3.6 nm	5 $\mu$ s, 4 V	$\sim 0.50$ V	large (RT) and large (85 °C)

**Table 1.1.:** Experimental write and refresh characteristics of NC memory devices with LPCVD synthesized Si NCs. From Tiwari et al. (2000).

past. Layers of different tunnel dielectrics (crested barriers) have been proposed by Likharev (1998) and further detailed by Casperson et al. (2002) to allow for higher write/erase speeds at maintained data retention, e.g. the use of  $\text{Si}_3\text{N}_4$  (Park et al., 2003) or  $\text{ZrO}_2/\text{Al}_2\text{O}_3$  (Wan et al., 2003).

Other advances are coming from the opposite side, the DRAM development. A direct-tunneling DRAM has been suggested by Kuo et al. (2003) with a nanoscale poly-Si floating gate coupled by an ultra thin gate oxide to the transistor channel. This approach does not provide nonvolatile operation but could enlarge refresh times of conventional DRAMs by orders of magnitude while the cell size can be reduced due to the one-transistor concept. Si NCs appear then as natural next step, which was discussed already by King et al. (1999) and further improved by Steimle et al. (2003) who proposed a DRAM concept that is a hybrid between a Si NC memory and a SONOS cell. In a synergetic manner this approach combines better charge retention due to the incorporated nitride layer as well as improved programming speeds. This approach utilizes extremely thin tunnel oxides and therefore puts extreme constraints on the fabrication of the Si NCs that sharpens the already high demands on location and size control of the NCs during synthesis, which remain one of the critical issues of the NC memory.

## 1.4. Synthesis of Si nanocrystals for nonvolatile memories – A challenge to materials research

Si NCs have been fabricated in numerous ways. Common to all of them is the usage of *bottom-up* principles. On the contrary to classical *top-down* approaches, which are currently not able to define sub-10 nm Si dots by direct structuring techniques as, e.g. by e-beam lithography, *bottom-up* techniques rely on self-assembly or self-organization techniques that assemble the desired nanoscale structures from the bottom, i.e. from single atoms.

All fabrication techniques published so far either use nucleation, growth and more generally phase separation processes occurring in the solid or gas phase, or rely on the fragmentation of larger poly-Si structures that involve some self-organization during their decay. E.g. thin poly-Si layers on  $\text{SiO}_2$  were shown to fragment into Si dots upon thermal treatment as they are not stable enough at that thickness (Kim et al., 2001; Tsybeskov et al., 2000).

The most common processes however are: Si excess precipitation in the solid phase, nucleation in the gas phase and subsequent deposition, and direct growth on the tunnel oxide from the gas phase.

### A. Direct growth techniques

In direct growth approaches, usually low pressure chemical vapor deposition (LPCVD) is applied to deposit small amounts of Si from a low pressure silane atmosphere. Si islands form at nucleation sites on top of the tunnel oxide and grow in size during the deposition. The deposition is stopped before a continuous poly-Si film has formed. Special care has to be taken to slow down the deposition process, e.g. by low silane partial pressure and the reduction of the deposition temperature. This technique has been shown to give very planar NCs films with hemispherical precipitates and a well-determined tunnel oxide thickness

between the NCs and the SiO<sub>2</sub>/Si interface. However, dot densities and sizes are more difficult to control. Areal densities above 10<sup>12</sup> cm<sup>-2</sup> require a special treatment of the tunnel oxide surface prior to the LPCVD growth in order to maximize the number of nucleation sites (Madhukar et al., 2001). NC sizes below 5 nm are difficult to obtain in a controlled manner. Nevertheless, studies of Ammendola et al. (2004); De Salvo et al. (2003); Lombardo et al. (2004); Steimle et al. (2004); Tiwari et al. (1996b) report successive deposition of Si NCs for nonvolatile NC memories. This method of Si NC synthesis has also been recently investigated within the European IST project ADAMANT.

### **B. Deposition from the gas phase (Aerosols)**

The aerosol deposition has been proposed by De Blauwe et al. (2000). In a first step, Si NCs are nucleated in the gas phase by pyrolysis of diluted silane. Sufficient isolation can be achieved in an additional oxidation step covering the Si particles with an oxide shell. Charged nanoparticles can then be mass separated with an applied electric field and finally deposited onto a pre-grown tunnel oxide (Ostraat et al., 2001a). This method effectively divides the particle growth from the deposition process, which then can be controlled independently. Despite of the obvious advantages of the aerosol method (Ostraat et al., 2001b), little is known about contamination issues and size and density uniformity on a large scale.

### **C. Precipitation of excess Si**

In this approach, Si NCs are not grown directly on or deposited onto the tunnel oxide. Rather, an overstoichiometric silicon dioxide is created in a first step, which can be achieved, e.g. by ion implantation or by direct deposition using plasma enhanced CVD. Then during a thermal anneal step, excess Si atoms precipitate and form distinct Si NCs in the SiO<sub>2</sub> host matrix. The main advantage of this technique is its simplicity and compatibility to a CMOS process flow. Small Si NCs (< 3 nm) can be grown at large areal densities (> 10<sup>12</sup> cm<sup>-2</sup>). Further NC properties depend on the method at which the Si excess is created.

**Layer deposition:** As one method, the overstoichiometric SiO<sub>x</sub> can be deposited directly by plasma enhanced CVD (Iacona et al., 2004), co-sputtering of Si and SiO<sub>2</sub> (Gourbilleau et al., 2001; Schmidt and Schmidt, 2003), or by evaporation of silicon monoxide that decomposes during thermal treatment (Zacharias et al., 2002). Common to all of these deposition techniques is the box-like Si excess depth profile that is obtained. It gives a good control over the tunnel oxide thickness and the mean NC size. However, the size distribution of the NCs remains less controllable due to nucleation and coarsening by Ostwald ripening. Additionally, uniformity of the Si excess in the SiO<sub>x</sub> layer and the layer thickness itself are critical issues as well as contamination control.

**Ion Beam Synthesis:** Far more clean is Si<sup>+</sup> ion implantation into the SiO<sub>2</sub> due to the possibility of mass separation of the accelerated ions (Hanafi et al., 1996; von Borany et al., 2002). The subsequent annealing step then leads to the growth of Si NCs on the expense of the introduced Si excess. This process consisting of ion implantation and NCs formation during annealing is often referred to as *ion beam synthesis* (IBS) and has been explored

on several ion-target combinations beyond Si in SiO<sub>2</sub>. However, ion beam synthesis has inherently to cope with a broad size and spatial distribution of the formed Si NCs. The main reason comes from the depth distribution of the incorporated Si excess, that in many cases obeys a Gaussian shape and the further broadening of the size distribution by OSTWALD ripening. Additionally, the control of the tunnel oxide thickness renders difficult in first place.

For this reason, Si<sup>+</sup> ion implantation has been carried out by Normand et al. (1998) at ultra low ion energies. The very shallow and narrow implantation profile thereby promises two main advantages. (i) The profile narrowing reduces the depth distribution of the Si NCs formed during by annealing. An almost two-dimensional layer of Si precipitates can be expected. (ii) Thinner gate oxides can be used without compromising the SiO<sub>2</sub>/Si interface by ion implantation due to the limited ion range.

Alternatively, ion implantation might even be carried out through the already deposited poly-Si control gate, which minimizes the possibility that contamination can be incorporated (Heinig et al., 2003; Schmidt and Heinig, 1999; Schmidt et al., 2004). Then, ion beam mixing of the Si/SiO<sub>2</sub> interface displaces Si into the gate oxide, giving rise to a high Si supersaturation close to the interface where during annealing Si NCs will form.

These findings have been the starting point of the European Commission's GROWTH project – **Nanoparticles for Electronics (NEON)**, whose main technical and scientific objectives were materials science investigations on different processes that could lead to the formation of well-defined two-dimensional patterns of small (3-5 nm) Si or Ge NCs within the gate oxide of a MOS transistor. Apart from an unconventional MBE approach (Kanjilal et al., 2003) to synthesize Ge NCs by an oxidation/reduction procedure proposed by King et al. (2001), the project followed two major routes. These were low energy Si<sup>+</sup> ion implantation into thin gate oxides prior to the poly-Si deposition defining the control gate and secondly the unconventional approach of ion irradiation through the poly-Si/SiO<sub>2</sub>/Si stack (Heinig et al., 2003).

## **1.5. Outline of the thesis**

The work that will be presented in this thesis focuses on low energy ion beam synthesis of Si NCs for NC memories. Extensive process simulations will be used to develop an understanding of the interplay of high fluence ion implantation and subsequent nanostructure formation by phase separation. In addition, process simulations provide here an excellent tool to study the impact of different factors of influence without the need of extensive and time consuming experiments. In particular, the analysis of the simulation results is notably more flexible and powerful than corresponding experimental results could allow for due to the small dimensions involved. In that sense, process simulation provide eminent help to identify best process conditions for the synthesis of optimum Si NC ensembles for NC memories.

Following this introduction, the underlying method of IBS will be shortly reviewed in Chapter 2 and general aspects of ion-solid interactions and phase separation of supersaturated solid solutions will be presented. In Chapter 3 and 4, the methodology of the applied process simulations is discussed. In order to describe the two quite different stages of IBS

– ion implantation and phase separation – the modeling was dived accordingly. Chapter 3 considers the build-up of the Si excess in the implantation stage and utilizes *dynamic binary collision calculations*. The obtained depth profiles are prerequisite for the modeling of the Si phase separation in the following Chapter 4. The status of kinetic data on Si phase separation from SiO<sub>2</sub> is reviewed and the ISING model based kinetic Monte Carlo code introduced.

Predictions of performed kinetic Monte Carlo simulations on low energy IBS are reported in Chapter 5. The discussion of these obtained results specifically focuses on the identification of optimum condition for the Si NC formation for memories. The simulation results will – wherever possible – be compared to experimental data that were gathered by NEON project partners in close cooperation. The obtained predictions of the process simulation as well as the the experimental results were part of an active and fruitful feedback loop (NEON, 2004b).

Furthermore, a percolation model on lateral charge isolation in NC layers is developed in Chapter 6 in conjunction with the obtained process simulation results. The percolation model allows thereby to maximize the NC area density without compromising the lateral charge isolation among the Si NCs – a fact that is of great importance for a data retention in NC memories.

## References

- ADAMANT. Advanced memories based on discrete traps. European IST Project 2001 34234, 2001. URL <http://www-leti.cea.fr/commun/europe/adamant/adamant.htm>.
- G. Ammendola, V. Ancarani, V. Triolo, M. Bileci, D. Corso, I. Crupi, L. Perniola, C. Gerardi, S. Lombardo, and B. DeSalvo. Nanocrystal memories for FLASH device applications. *Solid-State Electronics*, 48:1483–1488, 2004.
- W. D. Brown and J. E. Brewer, editors. *Nonvolatile Semiconductor Technology - A comprehensive Guide to Understanding and Using NVSM Devices*. IEEE Press Series on Microelectronic Systems. IEEE Press, New York, 1998.
- P. Cappelletti, C. Golla, P. Olivo, and E. Zanoni. *FLASH Memories*. Kluwer Academic Publishers, Boston, 1999.
- J. D. Casperson, L. D. Bell, and H. A. Atwater. Materials issues for layered tunnel barrier structures. *Journal of Applied Physics*, 92(1):261–266, 2002.
- C. M. Compagnoni, D. Ielmini, A. S. Spinelli, A. L. Lacaita, C. Previtali, and C. Gerardi. Study of data retention for nanocrystal flash memories. In *Proceedings of the 41st Annual International Reliability Physics Symposium*, pages 506–512, Dallas, Texas, 2003. IEEE 03CH37400.
- C. M. Compagnoni, D. Ielmini, A. S. Spinelli, A. L. Lacaita, and C. Gerardi. Study of nanocrystal memory reliability by cast structures. *Solid-State Electronics*, 48:1497–1502, 2004.
- R. Compano, editor. *Technology Roadmap for Nanoelectronics*. European Commission, 2 edition, 2000.
- J. De Blauwe. Nanocrystal nonvolatile memory devices. *IEEE Transactions on Nanotechnology*, 1(1):72–77, Mar. 2002.
- J. De Blauwe, M. Ostraat, M. Green, G. Weber, T. Sorsch, A. Kerber, F. Klemens, R. Cirelli, E. Ferry, J. L. Grazul, F. Baumann, Y. Kim, W. Mansfield, J. Bude, J. T. C. Lee, S. J. Hillenius, R. C. Flagan,

- and H. A. Atwater. A novel, aerosol-nanocrystal floating gate device for nonvolatile memory applications. *IEEE International Electron Devices Meeting Technical Digest*, pages 683–686, 2000.
- B. De Salvo, G. Ghibaudo, G. Pananakakis, B. Guillaumot, and T. Baron. Investigation of charging/discharging phenomena in nano-crystal memories. *Superlattices and Microstructures*, 28(5/6): 339–344, 2000.
- B. De Salvo, G. Ghibaudo, P. Luthereau, T. Baron, B. Guillaumot, and G. Reimbold. Transport mechanisms and charge trapping in thin dielectric/Si nano-crystals structures. *Solid-State Electronics*, 45:1513–1519, 2001.
- B. De Salvo, C. Gerardi, S. Lombardo, T. Baron, L. Perniola, D. Mariolle, P. Mur, A. Toffoli, M. Gely, M. N. Semeria, S. Deleonibus, G. Ammendola, V. Ancarani, M. Melanotte, R. Bez, L. Baldi, D. Corso, I. Crupi, R. A. Puglisi, G. Nicotra, E. Rimini, F. Mazen, G. Ghibaudo, G. Pananakakis, C. M. Compagnoni, D. Ielmini, A. S. Spinelli, A. L. Lacaita, Y. M. Wan, and K. van der Jeugd. How far will Silicon nanocrystals push the scaling limits of NVMs technologies? *IEEE International Electron Devices Meeting Technical Digest*, pages 597–600, 2003.
- P. Dimitrakis, E. Kapetanakis, D. Tsoukalas, D. Skarlatos, C. Bonafos, G. B. Assayag, A. Claverie, M. Perego, M. Fanciulli, V. Soncini, R. Sotgiu, A. Agarwal, M. Ameen, C. Sohl, and P. Normand. Silicon nanocrystal memory devices obtained by ultra-low-energy ion-beam synthesis. *Solid-State Electronics*, 48:1511–1517, 2004.
- B. Eitan. Non-volatile semiconductor memory cell utilizing asymmetrical charge trapping. US Patent No. 5,768,192, June 1998.
- B. Eitan, P. Pavan, I. Bloom, E. Aloni, A. Frommer, and D. Finzi. Can NROM, a 2-bit, trapping storage NVM cell, give a real challenge to floating gate cells? Saifun Semiconductors Ltd., presented at the International Conference on Solid State Devices and Materials, Tokyo, 1999.
- B. Eitan, P. Pavan, I. Bloom, E. Aloni, A. Frommer, and D. Finzi. NROM: a novel localized trapping, 2-bit nonvolatile memory cell. *IEEE Electron Device Letters*, 21:543–545, 2000.
- H. Goronkin and Y. Yang. High performance emerging solid-state memory technologies. *MRS Bulletin*, 29(11):805–808, Nov. 2004.
- F. Gourbilleau, X. Portier, C. Ternon, P. Voivenel, R. Madelon, and R. Rizk. Si-rich SiO<sub>2</sub> nanostructured multilayers by reactive magnetron sputterin. *Applied Physics Letters*, 78(20):3058–3060, 2001.
- H. I. Hanafi, S. Tiwari, and I. Khan. Fast and long retention-time nano-crystal memory. *IEEE Transactions on Electron Devices*, 43:1553–1558, 1996.
- K. Heinig, T. Müller, B. Schmidt, M. Strobel, and W. Möller. Interfaces under ion irradiation: growth and taming of nanostructures. *Applied Physics A: Materials Science & Processing*, 77(1):17–25, June 2003.
- Y. Hsia and V. C. Tyree. Reliability and NVSM reliability. In W. D. Brown and J. E. Brewer, editors, *Nonvolatile Semiconductor Technology - A comprehensive Guide to Understanding and Using NVSM Devices*, IEEE Press Series on Microelectronic Systems, chapter 6, pages 358–436. IEEE Press, New York, 1998.
- F. Iacona, C. Bongiorno, C. Spinella, S. Boninelli, and F. Priolo. Formation and evolution of luminescent Si nanoclusters produced by thermal annealing of SiO<sub>x</sub> films. *Journal of Applied Physics*, 95(7):3723–3732, 2004.

- G. Iannaccone. Evaluation of program, erase and retention times of flash memories with very thin gate dielectric. In *IEEE-NANO - Nanoelectronics: devices components and transport*, pages 247–250, Aug. 2002.
- International Technology Roadmap for Semiconductors. Emerging research devices, 2003. URL <http://public.itrs.net/Files/2003ITRS/Home2003.htm>.
- A. Kanjilal, J. Hansen, P. Gaiduk, A. N. Larsen, N. Cherkashin, A. Claverie, P. Normand, E. Kapelanakos, D. Skarlatos, and D. Tsoukalas. Structural and electrical properties of silicon dioxide layers with embedded germanium nanocrystals grown by molecular beam epitaxy. *Applied Physics Letters*, 82:1212–1214, 2003.
- Y. Kim, K. H. Park, T. H. Chung, H. J. Bark, J.-Y. Y. and W. C. Choi, E. K. Kim, J. W. Lee, and J. Y. Lee. Ultralarge capacitance-voltage hysteresis and charge retention characteristics in metal oxide semiconductor structure containing nanocrystals deposited by ion-beam-assisted electron beam deposition. *Applied Physics Letters*, 78(7):934–936, 2001.
- Y.-C. King, T.-J. King, and C. Hu. A long-refresh dynamic/quasi-nonvolatile memory device with 2-nm. *IEEE Electron Device Letters*, 20(8):409–411, 1999.
- Y.-C. King, T.-J. King, and C. Hu. Charge-tap memory device fabricated by oxidation of  $\text{Si}_{1-x}\text{Ge}_x$ . *IEEE Transactions on Electron Devices*, 48:696–700, Apr. 2001.
- H. Kohlstedt and H. Ishiwara. Ferroelectric field effect transistors. In R. Waser, editor, *Nanoelectronics and Information Technology*, chapter 14, pages 387–405. Wiley-VCH, 2003.
- C. Kuo, T.-J. King, and C. Hu. Direct tunneling RAM (DT-RAM) for high-density memory applications. *IEEE Electron Device Letters*, 24(7):475–477, July 2003.
- L. Larcher, P. Pavan, F. Gattell, L. Albani, and A. Marmiroli. A new compact model of floating gate non-volatile memory cells. *Modeling and Simulation of Microsystems*, pages 56–59, 2001. URL <http://www.cr.org>.
- F. R. Libsch and M. H. White. SONOS nonvolatile memory devices. In W. D. Brown and J. E. Brewer, editors, *Nonvolatile Semiconductor Technology - A comprehensive Guide to Understanding and Using NVSM Devices*, IEEE Press Series on Microelectronic Systems, chapter 5, pages 309–357. IEEE Press, New York, 1998.
- K. K. Likharev. Layered tunnel barriers for nonvolatile memory devices. *Applied Physics Letters*, 73(15):2137–2139, 1998.
- S. Lombardo, R. Puglisi, I. Crupi, D. Corso, G. Nicotra, L. Perniola, B. DeSalvo, and C. Gerardi. Distribution of the threshold voltage window in nanocrystal memories with Si dots formed by chemical vapor deposition: Effect of partial self-ordering. In *IEEE Nonvolatile Semiconductor Workshop*, pages 69–70, Aug. 2004.
- S. Madhukar, K. Smith, R. Muralidhar, D. O’Meara, M. Sadd, B.-Y. Nguyen, B. White, and B. Jones. CVD growth of Si nanocrystals on dielectric surfaces for nanocrystal floating gate memory application. *Proceeding of Materials Research Society*, 638:F5.2.1–5, 2001.
- G. Molas, B. De Salvo, D. Mariolle, G. Ghibaud, A. Toffoli, N. Buffet, and S. Deleonibus. Single electron charging and discharging phenomena at room temperature in a silicon nanocrystal memory. *Solid-State Electronics*, 47:1645–1649, 2003.
- NEON. Report on write/erase, endurance and retention time characteristics of exploratory transistors. Deliverable D16, EU Growth Project NEON GRD1-2000-25619, Athens, Greece, Feb. 2003. URL <http://www.cemes.fr/neon.html>.

- NEON. Report on memory performance and integration issues when using conventional ion implantation through polysilicon. Deliverable D19, EU Growth Project NEON GRD1-2000-25619, Dresden, Germany - Athens, Greece, Jan. 2004a. URL <http://www.cemes.fr/neon.html>.
- NEON. Nanoparticles for electronics. Final technical report, EU Growth Project NEON GRD1-2000-25619, Toulouse, France, Mar. 2004b. URL <http://www.cemes.fr/neon.html>.
- P. Normand, D. Tsoukalas, E. Kapetanakis, J. A. V. D. Berg, D. G. Armour, J. Stoemenos, and C. Vieud. Formation of 2-D arrays of silicon nanocrystals in thin SiO<sub>2</sub> films by very-low energy Si<sup>+</sup> ion implantation. *Electrochemical and Solid-State Letters*, 1(2):88–90, 1998.
- R. Ohba, N. Sugiyama, J. Koga, K. Uchida, and A. Toriumi. Influence of channel depletion on the carrier charging characteristics in si nanocrystal floating gate memory. *Japanese Journal of Applied Physics*, 39(3A):989–993, Mar. 2000. Part 1.
- M. Ostraat, J. De Blauwe, M. Green, D. Bell, H. Atwater, and R. Flagan. Ultra-clean two-stage aerosol reactor for production of oxide-passivated silicon nanoparticles for novel memory devices. *Journal of the Electrochemical Society*, 148(5):265–270, 2001a.
- M. L. Ostraat, J. W. D. Blauwe, M. L. Green, L. D. Bell, M. L. Brongersma, J. Casperson, R. C. Flagan, , and H. A. Atwater. Synthesis and characterization of aerosol silicon nanocrystal nonvolatile floating-gate memory devices. *Applied Physics Letters*, 79(3):433–435, 2001b.
- N.-M. Park, S.-H. Jeon, H.-D. Yang, H. Hwang., and S.-J. Park. Size-dependent charge storage in amorphous silicon quantum dots embedded in silicon nitride. *Applied Physics Letters*, 83(5):1014–1016, Aug. 2003.
- L. Perniola, B. De Salvo, G. Ghibardo, A. Foglio Para, G. Pananakakis, T. Baron, and S. Lombardo. Influence of dots size and dots number fluctuations on the electrical characteristics of multi-nanocrystal memory devices. *Solid-State Electronics*, 47:1637–1640, 2003a.
- L. Perniola, B. De Salvo, G. Ghibardo, A. Foglio Para, G. Pananakakis, V. Vidal, T. Baron, and S. A. Lombardo. Modeling of the programming window distribution in multinanocrystals memories. *IEEE Transactions on Nanotechnology*, 2(4):277–284, Dec. 2003b.
- F. Rana, S. Tiwari, and J. J. Welser. Kinetic modelling of electron tunneling processes in quantum dots coupled to field-effect transistors. *Superlattices and Microstructures*, 23(3/4):757–770, 1998.
- B. Schmidt and K.-H. Heinig. Verfahren zur Herstellung von Monolagen aus Silizium-Nanoclustern in Siliziumdioxid. DE patent 19933632, July 1999.
- B. Schmidt, K.-H. Heinig, L. Röntzsch, T. Müller, K.-H. Stegemann, and E. Votintsev. Ion irradiation through SiO<sub>2</sub>/Si-interfaces: Non-conventional fabrication of Si nanocrystals for memory applications. *Nuclear Instruments and Methods in Physics Research B*, 2004. accepted for publication.
- J. U. Schmidt and B. Schmidt. Investigation of Si nanocluster formation in sputter deposited silicon sub-oxides for nanocluster memory structures. *Materials Science and Engineering B*, 101:28–33, 2003.
- H. Silva, M. K. Kim, A. Kumar, U. Avci, and S. Tiwari. Few electron memories: Finding the compromise between performance, variability and manufacturability at the nano-scale. *IEDM*, pages 271–274, 2003.
- R. F. Steimle, M. Sadd, R. Muralidhar, R. Rao, B. Hradsky, S. Straub, and B. E. White. Hybrid silicon nanocrystal silicon nitride dynamic random access memory. *IEEE Transactions on Nanotechnology*, 2(4):335–340, Dec. 2003.



- R. F. Steimle, R. Rao, C. Swift, K. Harber, S. Straub, R. Muralidhar, B. Hradsky, J. Yater, E. Prinz, W. Paulson, M. Sadd, C. Parikh, S. Anderson, T. Huynh, B. Acred, L. Grieve, M. Rossow, R. Mora, B. Darlington, K. Chang, and B. White Jr. Integration of silicon nanocrystals into a 6V 4Mb nonvolatile memory array. In *IEEE Nonvolatile Semiconductor Workshop*, pages 73–74, Aug. 2004.
- M. Taub, R. Bains, G. Barkley, H. Castro, G. Christensen, S. Eilert, R. Fackenthal, H. Giduturi, M. Goldman, C. Haid, R. Haque, K. Parat, S. Peterson, A. Proescholdt, K. Ramamurthi, P. Ruby, B. Sivakumar, A. Smidt, B. Srinivasan, M. Szwarc, K. Tedrow, and D. Young. A 90nm 512Mb 166MHz multilevel cell flash memory with 1.5MByte/s programming. In *Proceedings of the IEEE International Solid-State Circuits Conference*, pages 54–55. IEEE, 2005.
- S. Tiwari, F. Rana, K. Chan, H. Hanafi, C. Wei, and D. Buchanan. Volatile and nonvolatile memories in silicon with nano-crystal storage. *IEEE International Electron Devices Meeting Technical Digest*, pages 521–524, 1995.
- S. Tiwari, F. Rana, K. Chan, L. Shi, and H. Hanafi. Single charge and confinement effects in nanocrystal memories. *Applied Physics Letters*, 69(9):1232–1234, Aug. 1996a.
- S. Tiwari, F. Rana, H. Hanafi, A. Hartstein, E. F. Crabbe, and K. Chan. A silicon nanocrystals based memory. *Applied Physics Letters*, 68(10):1377–1379, Mar. 1996b.
- S. Tiwari, J. A. Wahl, H. Silva, F. Rana, and J. J. Welser. Small silicon memories: confinement, single-electron and interface state considerations. *Applied Physics A*, 2000.
- L. Tsybeskov, G. Grom, M. Jungo, L. Montes, P. Fauchet, J. McCaffrey, J.-M. Baribeau, G. Sproule, and D. Lockwood. Nanocrystalline silicon superlattices: building blocks for quantum devices. *Materials Science and Engineering B*, 69-70:303–308, 2000.
- J. von Borany, T. Gebel, K.-H. Stegemann, H.-J. Thees, and M. Wittmaack. Memory properties of  $\text{Si}^+$  implanted gate oxides: from MOS capacitors to nvSRAM. *Solid-State Electronics*, 46: 1729–1737, 2002.
- J. A. Wahl, H. Silva, A. Gokirmak, A. Kumar, J. J. Welser, and S. Tiwari. Write, erase and storage times in nanocrystal memories and the role of interface states. *IEEE International Electron Devices Meeting Technical Digest*, pages 375–378, 1999.
- Q. Wan, N. L. Zhang, W. L. Liu, C. L. Lin, and T. H. Wang. Memory and negative photoconductivity effects of ge nanocrystals embedded in  $\text{ZrO}_2/\text{Al}_2\text{O}_3$  gate dielectrics. *Applied Physics Letters*, 83 (1):138–140, July 2003.
- H. Wang, N. Takahashi, H. Majima, T. Inukai, M. Saitoh, and T. Hiramoto. Effects of dot size and its distribution on electron number control in metal-oxide-semiconductor-field-effect-transistor memories based on silicon nanocrystal floating gates. *Japanese Journal of Applied Physics*, 40(3B): 2038–2040, Mar. 2001. Part 1.
- R. Waser, editor. *Nanoelectronics and Information Technology*. Wiley-VCH, 2003.
- M. Zacharias, J. Heitmann, R. Scholz, U. Kahler, M. Schmidt, and J. Bläsing. Size-controlled highly luminescent silicon nanocrystals: A  $\text{SiO}/\text{SiO}_2$  superlattice approach. *Applied Physics Letters*, 80 (4):661–663, 2002.



## Chapter 2.

# Ion Beam Synthesis of Nanostructures

The formation of nanoscale structures by ion beam synthesis (IBS) has now been studied for many years (Arnold and Borders, 1977) but has not lost its initial appeal. It combines the creation of far-from-equilibrium states frozen in after ion beam treatment with a phase separation stage that leads towards thermodynamic equilibrium. Following this method, nanoscale inclusions of controlled composition can be formed in virtually any matrix with sizes that are much below the capabilities of present days direct structuring techniques, as e.g. extreme ultra-violet optical lithography or direct writing electron beam lithography. By now, literature contains a wealth of publications on different ion-matrix combinations that potentially might trigger applications of these novel nanoscale materials (Heinig et al., 2003; Meldrum et al., 2001; Skorupa et al., 2003). A specific application – the IBS of Si NCs in thin gate oxides ( $\text{SiO}_2$ ) for nonvolatile memories – has been outlined above in section 1.4.

Usually IBS in the classical sense consists of two consecutive experimental steps. High fluence ion implantation of atoms being immiscible in the target material is used to create a supersaturated solid solution. The achieved far-from-equilibrium state remains frozen in after the implantation and only thermal activation in a subsequent annealing step leads to phase separation and therefore the NC formation<sup>1</sup>. Phenomenologically, IBS can be divided into several stages:

**Accumulation and supersaturation:** After implanted ions have been slowed down by electronic and nuclear stopping to thermal energy, they are incorporated into the target material. Thermal activation at common implantation temperatures is usually too low to allow for impurity diffusion over larger length scales. The impurity distribution remains frozen in, especially at low impurity concentrations.

**Nucleation or early phase separation:** Upon annealing, thermal fluctuations could initiate phase separation through the (homogeneous) nucleation of precipitates. The necessary energy barrier can either be reduced by heterogeneities (defects) in the substrate, giving rise to inhomogeneous nucleation, or by considerably higher supersaturations. Then spinodal decomposition can lead to different secondary phase morphologies.

**Growth:** Secondary phase precipitates formed by nucleation grow on the expense of the reservoir of dissolved impurity atoms until the average monomer concentration has fallen below the equilibrium concentration given by the GIBBS-THOMSON relation.

---

<sup>1</sup>Phase separation might well take place during the implantation if the temperature is chosen high enough. The competition between ion and thermally activated process could then lead to a much different behavior (Heinig et al., 2003).

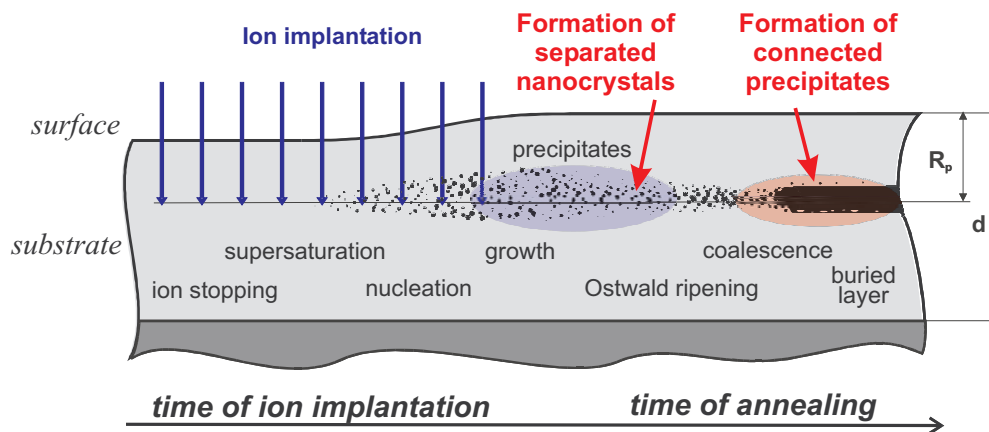


**Figure 2.1.:** Scheme of the major stages encountering in IBS.

For spinodal decomposition, the situation is rather different. Initial concentration fluctuations amplify spontaneously during early the phase separation without an activation barrier.

**Coarsening and Ostwald ripening:** Coarsening taking place after initial phase separation describes the increasing characteristic structure sizes of the precipitates (cluster or spinodal pattern) during further annealing. At low supersaturations, the competitive growth regime of NCs is often called OSTWALD ripening. Large NCs grow on the expense of smaller ones, which finally dissolve. Accordingly, the mean cluster size follows a power growth law. A similar scaling law is also observed for the characteristic structural wavelength of spinodal patterns.

**Coalescence and percolation:** To close NCs could coalesce during their growth and form larger ones. In the extreme, a completely interconnected structures can be formed at high supersaturations that span larger distances. Such percolation develops dynamically during phase separation and can decay due to interface minimization during long annealing times.

The classification of IBS in a set of consecutive stages is to some degree artificial. The border between the individual steps is rather ill-defined and depends on the specific implantation and annealing conditions.

## 2.1. High-fluence ion implantation

Ion implantation is commonly used for semiconductor doping at low or medium fluences but is extended for IBS to high ion fluences. Phenomena of high fluence ion implantation are shortly introduced in the following. More information on ion implantation technology and ion-solid interactions can be found in several reviews, e.g. in that of Ryssel and Ruge (1986), Ziegler (1992) and Nastasi et al. (1996). For IBS the knowledge of impurity distributions after implantation and the damage creation in the target material caused by the irradiation is of great importance. In addition, high-fluence ion implantation give rise to further effects as

surface erosion by sputtering, target swelling due to the incorporated atoms and ion beam mixing that might alter the target composition and its depth dependence. Those influence can be neglected only at lower implantation fluences.

### 2.1.1. Ion stopping

When an energetic ion penetrates a solid, it loses its kinetic energy in a complex cascade of collisions with the target atoms. It is common to distinguish between two different mechanisms of energy loss, these are *nuclear collisions*, in which kinetic energy is transferred elastically to target atoms, and *electronic collisions*, where the moving particle excites or ejects bound electrons. The energy-loss per unit length (stopping power) can be written as  $\frac{dE}{dx} = \frac{dE}{dx}|_n + \frac{dE}{dx}|_e$ , where the subscripts  $n$  and  $e$  denote nuclear and electronic collisions. More conveniently, the stopping cross-section  $S$  is considered, which is defined as  $S = N^{-1}(dE/dx)$  with  $N$  being the atomic density.

#### Nuclear stopping

Nuclear stopping considers the average energy loss caused by elastic collisions with target atoms. In a ballistic model, these collisions are considered to be a sequence of binary collisions (binary collision approximation, BCA), by which the kinetic energy is dissipated to substrate atoms. The nuclear stopping cross-section is then defined as

$$S_n(E) = \int_0^{T_{max}} T d\sigma, \quad (2.1)$$

where the differential scattering cross-section  $d\sigma(E, T)$  determines the probability of such a collision. The energy  $T$  transferred in the collision of the incident particle having the energy  $E$  (denoted in the following by the subscript 1) and the resting substrate atom is given by

$$T = \frac{4M_1M_2}{(M_1 + M_2)^2} E \sin^2(\theta/2). \quad (2.2)$$

The scattering angle in the center-of-mass frame is denoted by  $\theta$ . In a head-on collision with  $\theta = \pi$  the maximum kinetic energy can be transferred. The differential scattering cross-section is then determined by the interaction potential, which is usually described as screened Coulomb potential

$$V(R) = \frac{Z_1Z_2e^2}{4\pi\epsilon_0R} \varphi(R/a). \quad (2.3)$$

This reflects the efforts to reduce the interaction potential to an universal form being independent from specific electron configurations and is only dependent on atom separations and atomic masses. With an appropriate screening function  $\varphi$  and screening length  $a$ , Ziegler et al. (1985) derived a universal stopping power that is also applied in binary collision codes as, e.g., TRIDYN (Möller and Eckstein, 1984), while the SRIM BCA code (Ziegler, 1998) relies on the universal interaction potential (Ziegler et al., 1985).

## Electronic stopping

At high ion energies, electronic stopping becomes dominating and the electronic stopping cross-section  $S_e(E)$  exceeds  $S_n(E)$ . For ion velocities larger than  $v_0 Z_1^{2/3}$  with  $v_0$  being the Bohr velocity, the ion approaches a bare nucleus and its interaction with target electrons can be described by an unscreened Coulomb interaction potential. In that case, the stopping cross-section is well described by the Bethe formula (Nastasi et al., 1996, sec. 5.7.2). At lower energies, the Bethe theory of stopping breaks down and different approaches are needed. Fermi and Teller (1947) analyzed the stopping of energetic particles in a Fermi gas at velocities below  $v \ll v_F$ . The stopping cross-section is then roughly proportional to the ion velocity.

## Ion damage and the recoil cascade

Energy transfer by nuclear stopping of primary ions creates recoils which themselves could displace further substrate atoms, giving rise to a recoil cascade. This is achieved if more energy than a threshold value – the displacement threshold  $E_d$  – is transferred in a collision to a target atom. In this case a stable Frenkel pair being a pair of an interstitial atom and a vacancy is created, which is immobile at low temperatures. Then, damage can be accumulated during implantation and may eventually lead to the amorphization of the crystal structure. At higher temperatures however the ion damage may anneal out dynamically in the course of implantation and the number of Frenkel pairs does not exceed a temperature dependent steady state level.

### 2.1.2. Implantation profiles

With the knowledge of the stopping cross-sections, the total pathlength  $l$  of an ion can be calculated by integrating the energy loss, i.e.  $l = \int_E^0 NS(E)^{-1} dE$  – but is no meaningful quantity in general as the ion does not travel a straight path. Rather, it is convenient to define a *projected range*  $R_p$  that is the net penetration of the ion into the material and is measured along the incidence vector. The evaluation of this quantity then requires either transport-theoretical treatment or Monte Carlo calculations of individual ion trajectories from which  $R_p$  can be deduced. In addition, the traverse projected range can be quantified, which is the projected distance the ion departed from the vector of incidence in the traverse direction. Since ion stopping is in its nature a stochastic process, the trajectory and therefore the place where the ion comes to rest varies randomly from ion to ion. Accordingly, range parameters exhibit a probability distribution leading i.e. to a depth distribution of implanted impurity atoms that is often approximated by a Gaussian distribution. For low fluences, its width is determined by the range straggling. In case of small-angle scattering its size  $\Delta R_p$  is approximately given by  $R_p/2.5$ . For the most practical purposes however, Monte Carlo simulation tools, e.g. SRIM, are used to sample the 3D range distribution in order to determine the projected range parameters and the corresponding range straggling.

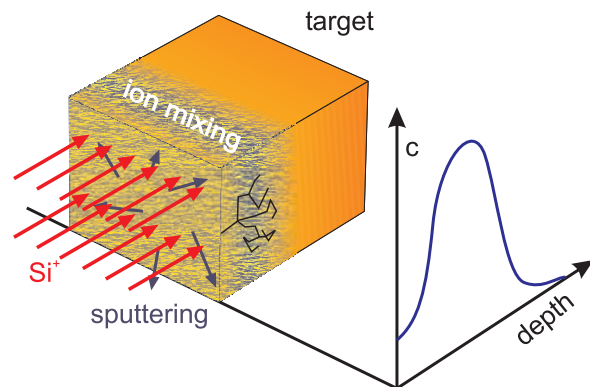


**Figure 2.2.:** High-fluence implantation simulations have to account for dynamic effects as sputtering, ion beam mixing and target swelling.

### 2.1.3. Target modification by high-fluence ion implantation

Most of the Monte Carlo calculations in BCA (e.g. SRIM) work within the single particle approximation simulating ion impacts into the virgin target material that is not changed by implantation. All cumulative effects as swelling, ion beam mixing and sputtering are neglected in this approach. Hence, these calculations describe the range and damage distribution in case low fluences reasonably well. At high fluence implantations, which are typically applied for IBS of nanostructures, the above effects become important.

#### Target swelling

Implanted material has to be accommodated within the host material and requires additional volume there. Consequently, high fluence implantation leads to swelling of the implanted target and a distortion of the impurity profile. The total target swelling is roughly given by the equivalent layer thickness of the implanted (deposited) material  $\Phi N^{-1}$  with  $\Phi$  being the ion fluence. This holds unless a compound formation takes place between implanted species and host material, e.g.  $\text{Co}^+$  implantation into Si results in  $\text{CoSi}_2$  formation with essentially no associated target swelling.

#### Ion sputtering

The opposite of a target swelling is achieved by ion sputtering, which is the erosion of the target surface by energetic ions. Part of the recoil cascade created by the ion impact could reach the target surface. Some of such backward recoils will approach the surface with enough energy to escape the surface. The threshold energy that has to be surmounted is often referred to as surface binding energy  $SBE$ . In this *linear cascade sputtering* regime the *sputtering yield*  $Y$  – the number of sputtered atoms per incident ion – is a strong function of the surface binding energy and the energy  $F_D(E_0)$  deposited per unit length into nuclear processes at the surface (Sigmund, 1981)

$$Y \propto SBE^{-1} F_D(E_0). \quad (2.4)$$

A semi-empirical formula for sputtering of single elemental targets has been derived by Yamamura et al. (1983) on the basis of Lindhard's theory of nuclear and electronic stopping, which will account for both heavy-ion and light-ion sputtering (Nastasi et al., 1996, chapter

9). Beyond this approximation, sputtering yields can also be calculated with the help of BCA calculations, e.g. with SRIM (Ziegler, 1998) or a sputter-dedicated version of it developed by Eckstein (1991).

During implantation, ion erosion removes target atoms as well as implanted species. Eventually, an equilibrium is reached where on average one implanted atom is sputtered for each introduced ion. The concentration distribution peaks under these conditions close to the target surface and falls off over a distance comparable to the projected ion range. For high fluences, where sputtering becomes dominating, the concentration profile becomes asymptotically an error function (instead of a Gaussian distribution for low fluences). This transition of the profile shape can be approximated in closed analytical form according to Krimmel and Pfeleiderer (1973). The steady state surface concentration of the implanted ion species in the target is then given by the inverse of the sputtering yield,  $Y^{-1}$ , which neglects preferential sputtering.

### Ion beam mixing

Beyond surface sputtering, ion irradiation can cause significant atomic rearrangements, i.e. an intermixing of a buried interface also known as *ion beam mixing*.

**recoil mixing:** The effect of recoil implantation is considered to be a relocation of atoms knocked off in single collisions with incident ions. For recoil mixing to be effective, the recoil should travel the maximum range possible, e.g. in a head-on collision between ion and the resting target atom. However, the probability of such collisions is very small, most collisions are *softer* due to a larger scattering angle. The recoils created in such soft collisions will have significantly less energy and therefore reduced ranges compared to head-on collision. Their trajectories will not necessarily be directed into the forward direction.

**cascade mixing:** The majority of collisions have rather large scattering angles with a low amount of transferred kinetic energy, giving rise to only short relocations. Their probability is however much larger and many substrate atoms are displaced more than once. Due to the statistically independent ion impacts events, the ion implantation of fluence  $\Phi$  can be considered to generate a random walk with a variable relocation range. Following the law of large numbers, the probability distribution of the total relocation of a target atom is then given by a Gaussian distribution in case the individual relocation lengths are small against the total standard variation of the random walk. Sigmund and Gras-Marti (1980) defined in their treatment of ion beam mixing a Gaussian propagator

$$G(x, x') = \frac{1}{\sqrt{2\pi\sigma^2}} \exp\left\{-\frac{x - x' - \alpha}{2\sigma^2}\right\}, \quad (2.5)$$

that transforms the initial distribution  $c(x)$  according to

$$c(x) = \int c(x')G(x, x') dx'. \quad (2.6)$$

The distribution parameters  $\sigma$  and  $\alpha$  are therein determined by the single relocation events. Due to the low-energy stochastic nature of these displacement events, the initial momentum



of the incident particle is soon lost, and the overall movement of the atoms in the collision cascade becomes isotropic, i.e.  $\alpha \cong 0$  and no mean profile shift due to ion beam mixing is observed. The remaining parameter  $\sigma$  controls the smearing out of the concentration profile and is determined by

$$\sigma^2 = \frac{\text{dpa}(x) \langle r^2 \rangle}{6} \cong \xi \frac{F_D \langle r^2 \rangle}{N E_d} \Phi \quad (2.7)$$

where  $\text{dpa}(x)$  is the number of cascade-induced displacements per target atom at depth  $x$ , and  $\langle r^2 \rangle$  is the mean squared range of the displaced target atoms. Substituting the displacement  $\text{dpa}(x)$  leads to the r.h.s. of (2.7) (Sigmund and Gras-Marti, 1981), where  $F_D(x)$  is the damage energy per unit length at distance  $x$ ,  $\Phi$  the ion fluence,  $E_d$  the displacement energy and  $\xi$  is a mass-sensitive kinematic factor. In close analogy to thermal diffusion, an effective diffusivity  $D_{cas}$  for cascade induced particle relocations can be defined as

$$D_{cas} = \xi \frac{F_D \langle r^2 \rangle}{N E_d}. \quad (2.8)$$

The ion fluence  $\Phi$  then takes the role of the time in thermally activated diffusion. An initially sharp concentration profile, e.g. a sharp interface, becomes broadened upon ion beam mixing. Its mean width is expected to increase proportional to the square root of the ion fluence  $\Phi^{1/2}$ .

### Further effects

Temperature dependent mixing effects are neglected in case of IBS at conventional energies and the implantation temperature commonly does not exceed 100 °C. Single ion impacts then possess not enough energy to induce a local melting of the target material. Ion beam mixing (and sputtering) is then a pure result of ballistic processes. Consequently, thermally activated processes including a later phase separation upon thermal annealing can be treated fully independently from ion implantation in further theoretical description.

## 2.2. Nanostructure formation by phase separation – relaxing far-from-equilibrium states

Phase separation comprises phenomena where a single-phase state unmixes or decomposes into two or more phases being stable and spatially separated. These processes can be well described within the framework of a first-order phase transition, where a wealth of literature exists on. Comprehensive reviews can be found in Gunton et al. (1983) and Wagner et al. (2001). The time evolution of the system undergoing phase separation can be understood with respect to the phase diagram.

### 2.2.1. Binary Phase Diagram

By definition, unmixing of the single-phase state only takes place under a gain of *Helmholtz free energy*  $\Delta F < 0$ . In a heterogenous binary alloy, equilibrium is reached when  $F$  is mini-



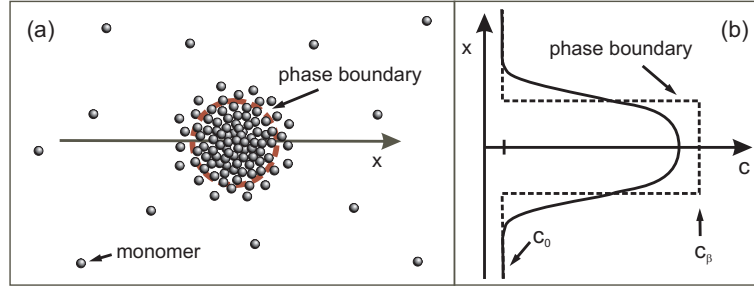


**Figure 2.4.:** a) Formation of a cluster of phase  $\beta$  from a homogeneous supersaturation of solute atoms ( $B$ ) with concentration  $c_0$ . b) Concentration profile (black curve) through the nuclei and its simplified, step-wise profile assumed in CNT. The dashed circle in (a) depicts the sharp phase boundary assumed in the CNT.

### Classical nucleation

Classical nucleation theory (CNT) considers the formation of large amplitude concentration fluctuations in a simple 'droplet' picture. This approach has been developed by Becker and Döring (1935); Volmer and Weber (1926); Zeldovich (1943) and recent comprehensive reviews can be found in Itkin and Kolesnichenko (1997); Kashchiev (2000); Langer (1992).

In the *metastable* region of the phase diagram (e.g. point 1 of Figure 2.3), i.e. if the initial solid solution is not quenched too deep into the miscibility gap, microclusters of solute atoms may form and decay spontaneously. The driving force for this process of nucleation is the supersaturation  $\Delta\mu$  that, for small values, might be approximated for an ideal solution by  $\Delta\mu = k_B T \ln\left(\frac{c_0}{c_\alpha}\right)$ , where  $c_\alpha \equiv c_\infty$  depicts the concentration at the coexistence curve<sup>2</sup>.

CNT assumes a spherical cluster shape with a sharp interface to the surrounding matrix ('droplet model') as depicted in Figure 2.4, but allows to calculate the change in free energy  $\Delta F$  associated with the formation of a nucleus of radius  $R$  containing  $i$  solute atoms

$$\Delta F(R) = \underbrace{-\frac{4\pi\Delta\mu}{3v_\beta} R^3}_{\text{volume}} + \underbrace{4\pi\sigma_{\alpha\beta} R^2}_{\text{interface}} = -\Delta\mu i + 4\pi \left(\frac{3V_\beta}{4\pi}\right)^{2/3} \sigma_{\alpha\beta} i^{2/3}, \quad (2.9)$$

with  $(4\pi/3)R^3 = iV_\beta$ , where  $V_\beta$  denotes the atomic volume of phase  $\beta$ . The two terms of (2.9) reflect volume and interface contributions to the free energy  $\Delta F$ . Binding energy is gained through the formation of the cluster but at the expense of the interfacial energy of the new cluster surface.

Both contributions on  $\Delta F$  are shown in Figure 2.5 depending on the droplet radius  $R$ . For a critical cluster radius  $R^*$  a maximum of  $\Delta F$  is obtained below which cluster are unstable and decay again. Clusters exceeding the critical size  $R^*$  become dynamically stable ( $\partial\Delta F/\partial R < 0$  and  $\Delta F > 0$ ), i.e. they can grow further while lowering their free energy. Finally, they become also energetically stable ( $\Delta F < 0$ ). The critical cluster size  $R^* = 2\sigma_{\alpha\beta}V_\beta\Delta\mu^{-1}$  depends on the ratio between the specific volume and interfacial energy. Therefore, thermal concentration fluctuations have to overcome an activation barrier

<sup>2</sup>For the more general case of non-ideal solid solutions the reader is referred to Kashchiev (2000, chapt. 2) and Wagner et al. (2001, chapt. 5.2.4).

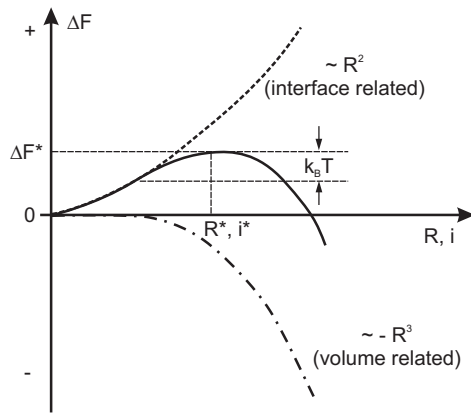


**Figure 2.5.:** Schematic Helmholtz free energy changes associated with the cluster nucleation as function of cluster radius  $R$  or number of atoms  $i$ .

$\Delta F^* \equiv \Delta F(R^*)$  for nucleation according to (2.9) that decreases at increasing supersaturation, i.e. with rising temperature or increasing concentration. With the knowledge of  $\Delta F$  for a single cluster, Volmer and Weber (1926) determined the nucleation rate  $J_{VW}$ , which is the product of the concentration of critical nuclei  $C^*$  and the rate  $\omega$  at which monomers impinge on the nuclei and therefore render clusters supercritical,

$$J_{VW} = \omega C^* = \omega N_0 \exp(-\Delta F^*/k_B T). \quad (2.10)$$

with  $N_0$  being the density of dissolved monomers. Becker and Döring (1935) extended this approach and included that stable clusters might become undercritical again by thermally activated detachment of monomers, which is accounted for by the Zeldovich factor (Zeldovich, 1943).

These approaches however refer to *steady-state nucleation* conditions implying that

- clusters larger than a certain threshold are artificially removed from the cluster size distribution,
- $\Delta\mu = \text{const}$ , and hence a continuous supply of monomers is needed to replace those who have been lost by nucleation,
- clusters are assumed to be non-interacting (depletion effects are ignored).

These assumption might only be meaningful in very few cases, e.g. if a homogeneous system exhibits a large nucleation barrier at a small supersaturation  $\Delta\mu$ . But more typical, nucleation is only the very first stage of a more complex phase separation process. Especially for high supersaturations (and a low nucleation barrier), nucleation occurs fast and nuclei are formed very close to each other. Nucleation around a previously formed cluster is then hindered (depletion of further nuclei) and a steady state (of nucleation) is never reached which is termed as *catastrophic nucleation* (Wagner et al., 2001).

### Classical spinodal decomposition

Contrary to classical nucleation theories for concentrations close to the coexistence line, spinodal theories consider deep quenches into the miscibility gap, where the quenched solid

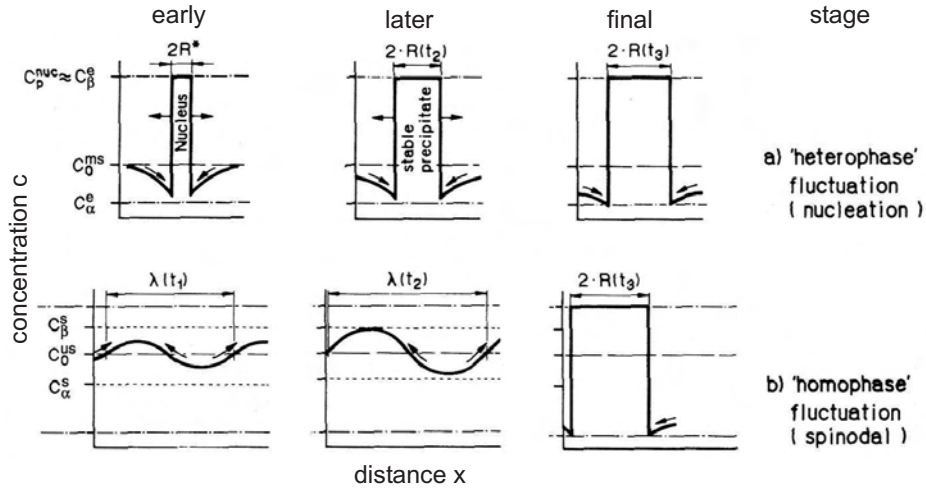


**Figure 2.6.:** Spatial variation of the composition  $c$  during (a) *nucleation and growth* for a metastable quench and (b) a continuous *spinodal* reaction. Modified from Wagner et al. (2001).

solution is unstable against small-amplitude concentration fluctuations, i.e. no activation energy is necessary for phase separation.

Cahn (1961); Cahn and Hilliard (1958) considered in their theory of spinodal decomposition a system described by a single, smoothly varying scalar order parameter, e.g. the average concentration  $c(\vec{r}, t)$  of one component in a binary solution. With the help of a coarse grained Ginzburg-Landau-type free energy functional ( $F(c) = \int f(c) + 1/2K(\nabla c)^2 dr$ ), the interdiffusion of atoms can be described by the continuity equation  $\partial c/\partial t = \nabla \vec{j}$  with  $\vec{j} = -M\nabla(\partial F/\partial c)$  being proportional to the gradient of the chemical potential and the mobility  $M$ . Substituting  $\vec{j}$ , Cahn and Hilliard (1959b) obtained a deterministic partial differential equation for the kinetics of the atoms interdiffusion upon phase separation – the CAHN-HILLIARD equation. Cook (1970) added later a random force term  $\eta_T(\vec{r}, t)$  to account for statistical fluctuations

$$\frac{\partial c(\vec{r}, t)}{\partial t} = -M\nabla^2 \left( \frac{\partial f}{\partial c} - K\nabla^2 c \right) + \eta_T(\vec{r}, t), \quad (2.11)$$

with  $\eta_T(\vec{r}, t)$  assumed to be delta-correlated Gaussian noise linked to the mobility  $M$  via a fluctuation-dissipation theorem

$$\langle \eta_T(\vec{r}, t) \eta_T(\vec{r}', t') \rangle = -2k_B T M \langle \eta_T^2 \rangle_T \nabla^2 \delta(\vec{r} - \vec{r}') \delta(t - t'). \quad (2.12)$$

In (2.11),  $K$  is the prefactor of the *gradient energy* term in the Ginzburg-Landau free energy functional and originates from the coarse graining procedure of the concentration field. It accounts for interface contributions, characterized by steep concentration gradients, to the free energy balance.

Cahn and Hilliard (1959b) further linearized (2.11) while neglecting the noise term

$$\frac{\partial u(\vec{r}, t)}{\partial t} = -M\nabla^2 \left[ \left( \frac{\partial^2 f}{\partial c^2} \right)_{c_0} - K\nabla^2 \right] u(\vec{r}, t) \xrightarrow{\mathcal{F}} \frac{\partial \hat{u}(k)}{\partial t} = -\omega(k) \hat{u}(k) \quad (2.13)$$

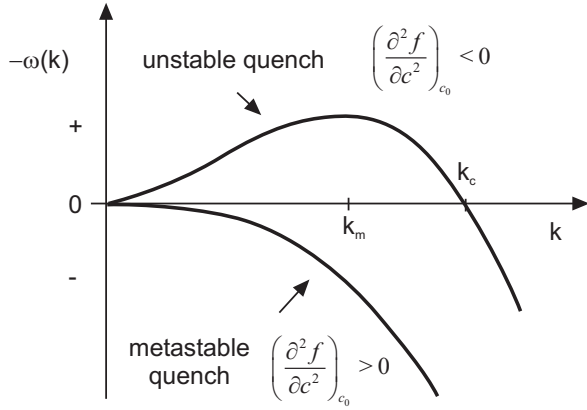


**Figure 2.7.:** Initial growth rate predicted by the linear Cahn-Hilliard theory for a metastable and unstable quench. The critical wavenumber and the wavenumber of the fastest growing mode are denoted by  $k_c$  and  $k_m = k_c/\sqrt{2}$ , respectively.

with  $u(\vec{r}, t) = c(\vec{r}, t) - c_0$  denoting the deviation from the average concentration  $c_0$ . The Fourier transform was performed with  $\hat{u}(k) = \mathfrak{F}\{u(\vec{r})\}$  and leads to

$$\omega(k) = MKk^2 \left[ k^2 + K^{-1} \left( \frac{\partial^2 f}{\partial c^2} \right)_{c_0} \right]. \quad (2.14)$$

As a results of the *linear stability analysis* of (2.13), the structure function  $\hat{S}(k, t) = \langle \|\hat{u}(k)\| \rangle$  is predicted to growth (or decay) exponentially in time

$$\hat{S}(k, t) = \hat{S}(k, 0)e^{-2\omega(k)t}. \quad (2.15)$$

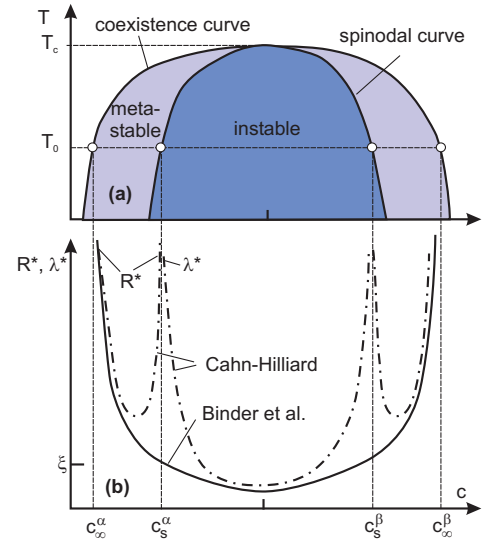
Inside the mean-field spinodal curve, where  $(\partial^2 f / \partial c^2)_{c_0} < 0$ , long-wavelength, small-amplitude concentration fluctuations will grow exponentially in time as  $\omega(k)$  becomes negative for  $k < k_c = K^{-1} |(\partial^2 f / \partial c^2)_{c_0}|$ . For  $k_m = k_c / \sqrt{2}$ ,  $-\omega(k)$  attains a maximum, giving rise to a fastest growing mode with the wavelength  $\lambda_m$  (mode selection) as shown in Figure 2.7. On approaching the mean-field spinodal where  $(\partial^2 f / \partial c^2)_{c_0}$  becomes zero the critical wavelength  $\lambda_c$  (and  $\lambda_m$ ) diverges. For the metastable region of the phase diagram, the linearized CH theory predict that all small-amplitude concentration fluctuations decay and do not lead to phase separation (Figure 2.7). (Phase separation by nucleation, on the other hand, requires the formation of localized, large-amplitude concentration fluctuation as depicted in Figure 2.6.)

The linear theory however fails at certain points. (i) Exponential growth of long-wavelength concentration fluctuations with a constant fastest growing mode  $k_m$  has not been observed experimentally (Binder and Fratzl, 2001; Marro and Bortz, 1975). Instead, non-linear terms of (2.11) are important from the beginning of the phase separation and lead to *domain coarsening*. (ii) Statistical fluctuations apart from the initial fluctuations must be included. (iii) *No singular behavior* is found experimentally and in computer simulation at the mean-field spinodal curve. In particular no distinct transition in the phase separation mechanism is observed.

### Beyond classical theories of early phase separation

Non-classical nucleation, i.e. nucleation at higher supersaturations, has been studied early by Cahn and Hilliard (1959a,b) in a phase-field, coarse grained approach. In contrast to

**Figure 2.8.:** (a) Schematic phase diagram of a binary alloy with symmetrical miscibility gap. b) Critical radius  $R^*$  and critical wavelength  $\lambda_c$  according to the non-classical Cahn-Hilliard nucleation theory and the linear spinodal theory. Approaching the mean-field spinodal curve from either the metastable or instable region causes  $R^*$  and  $\lambda_c$  to diverge in contrast to the generalized nucleation theories.



the CNT, homophase concentration fluctuations with large amplitude and *diffuse interfaces* were considered. The local composition is allowed to vary throughout the nuclei. For small supersaturations  $\Delta\mu$ , the CAHN-HILLIARD nucleation theory agrees well with the CNT and predicts a decreasing nucleation barrier  $\Delta F^*$  and critical radius  $R^*$  for an increasing supersaturation  $\Delta\mu$ . For concentrations however approaching the mean-field spinodal the size of critical nucleus  $R^*$  diverges as shown in Figure 2.8.

The existence of an unique spinodal curve within the framework of mean field theories associated with singularities in thermodynamic variables has lead to the assumption that the mechanism of phase separation itself is discontinuous. But this spinodal singularity is an artefact of an over-simplified theoretical picture: apart from the very special limit of infinitely weak long-ranged forces in which mean-field theory becomes correct (Binder, 1984), the transition from the nucleation mechanism to spinodal decomposition is completely *gradual* (Binder and Fratzl, 2001; Binder et al., 1978). The phase separation process can by no means be divided into two distinct regimes depending on the degree of supersaturation with a sharp transition line between both<sup>3</sup>.

Rather, the nucleation barrier  $\Delta F^*$  and the critical size  $R^*$  decrease with increasing supersaturation  $\Delta\mu$  and  $\Delta F^*$  becomes comparable to  $k_B T$ . Then concentration fluctuations can form spontaneously without having to pass a relevant nucleation barrier. *Generalized nucleation theories* predict in addition that  $R^*$  lowers to the order of the correlation length  $\xi$  of thermal concentration fluctuations (Binder et al., 1978), where a spinodal picture of spontaneous decomposition appears more appropriate but describes the same physical process of phase separation. On the other hand, the *linear spinodal theory* predicts a *diverging critical wavelength*  $\lambda_c$  for stable small-amplitude concentration fluctuations if the mean-field spinodal curve is approached. Fluctuations (with large amplitude) could form with low energy barrier, and are more probable than long-wavelength fluctuations. It has to be noted that apart from linear approximations, the non-linear CHC equation (2.11) can cover nucleation

<sup>3</sup>A phenomenological distinction can be made between the spatially isolated droplets formed by nucleation and the interconnected spinodal pattern observed for spinodal decomposition. It merely arises from the state of percolation which reached in most cases for spinodal decomposition but absent for nucleation.



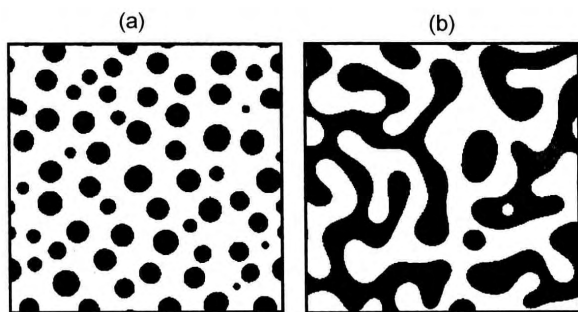


**Figure 2.9.:** Snapshot of a two-dimensional system with a volume fraction of (a)  $c = 0.21$  and (b)  $c = 0.5$ . These images were calculated by (Rogers and Desai, 1989) solving the non-linear Cahn-Hilliard-Cook equation (2.11) numerically.

as well as spinodal decomposition, depending on the degree of supersaturation. Figure 2.9 gives an example taken from Rogers and Desai (1989), who have solved (2.11) numerically.

### 2.2.3. Growth, coarsening and percolation

A common feature of phase separation is that, once separated domains have formed, their characteristic sizes (e.g. the droplet size) increase steadily during further annealing. The driving force of this process is *surface tension* that leads to interface minimization, in case other influences have negligible impact. The surface to volume ratio of the domains decrease, domains become larger and preferably spherical. In most cases, such *coarsening* effects have been (historically) discussed for low supersaturations (or volume fractions), i.e. for ensembles of spherical precipitates that have formed by nucleation. Coalescence of neighboring precipitates is neglected in these treatments. The obtained growth laws have been found to be of more general nature and hold also (at least qualitatively) in the case of spinodal decomposition even if accompanied by percolation.

#### Diffusion-controlled growth of isolated clusters

Once stable nuclei have formed during nucleation, they grow at the expense of the surrounding supersaturation  $\Delta\mu$  as sketched in Figure 2.10(a). The growing particle is surrounded by a monomer concentration gradient that provides the driving force for solute diffusion, and thus gives rise to particle growth (Glicksman, 2000). This process can either be controlled (esp. for small precipitates) by the rate atoms that react at the matrix/clusters interface or by flux of atoms delivered by the diffusion. The latter case becomes increasingly important, once the particles have attained a certain size and the matrix is depleted by solute atoms. For the resulting *diffusion controlled growth*, a parabolic growth law can be derived at small supersaturations for the cluster radius  $R$

$$\frac{dR}{dt} = \frac{DS}{R} \quad \text{with} \quad S = \frac{\bar{c}(t) - c_R}{c_\beta - c_R} \quad (2.16)$$

and the *dimensionless supersaturation*  $S$ , diffusion coefficient  $D$  and mean solute concentration  $\bar{c}(t)$  far away from the cluster.  $c_R$  describes here the equilibrium solute concentration at the curved interface of the a precipitate of size  $R$ . According to the GIBBS-THOMSON (GT) equation (also known as KELVIN equation),  $c_R$  depends on the cluster radius  $R$  (Glicksman,



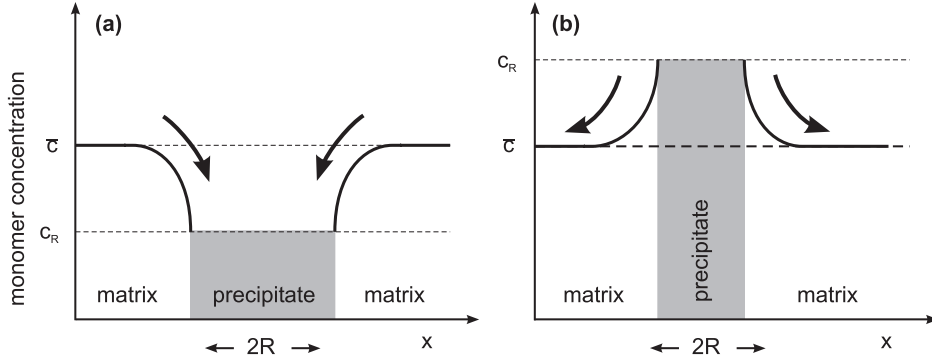


**Figure 2.10.:** Monomer concentration field around growing (a) or dissolving (b) precipitates. The concentration at the cluster interface is given by the GIBBS-THOMSON equation (2.17).

2000, chapt. 21.2)

$$c_R = c_\infty \exp\left(\frac{R_c}{R}\right) \quad \text{with} \quad R_c = \frac{2\sigma V_0}{k_B T} \quad \text{GIBBS-THOMSON,} \quad (2.17)$$

where  $R_c$  denotes the *capillary length* determined surface tension  $\sigma$ , atomic volume  $V_0$  and the temperature. More generally, the equilibrium concentration at an arbitrary curved interface depends on the local mean curvature  $\kappa$

$$c(\mathbf{x}) = c_\infty \exp(R_c \kappa) \quad \text{with} \quad \kappa = \frac{1}{2} \left( \frac{1}{R_1} + \frac{1}{R_2} \right), \quad (2.18)$$

and  $R_1, R_2$  being the principal radii of curvature.<sup>4</sup> For large precipitates ( $R \gg R_c$ ), the GIBBS-THOMSON equation can be linearized to

$$c_R \approx c_\infty (1 + R_c/R). \quad (2.19)$$

With this approximation, the time evolution of a monodisperse size distribution with an initial precipitate radius of  $R_0$  can be described by

$$R(t) \simeq \sqrt{R_0 + S D t} \quad (2.20)$$

assuming a constant supersaturation  $S$  throughout the cluster growth. However, nucleation leads to a more or less broad size distribution  $f(R)$  of nuclei that broadens even further during growth and competitive coarsening, e.g. by Ostwald ripening.

### Ostwald Ripening and Lifshitz-Slyozov-Wagner scaling

If supersaturation has decreased to values comparable to the GIBBS-THOMSON concentration  $c_R$  of (2.17), a competitive ripening among the precipitates sets in which is known as *Ostwald ripening*. Small precipitates with a  $c_R$  above the average concentration  $\bar{c}(t)$  lose monomers by diffusion and dissolve. Instead, large cluster having  $c_R < \hat{c}(t)$  grow on the expense of the smaller ones.

<sup>4</sup>For a sphere with  $\kappa = R^{-1}$ , equation (2.18) evaluates to the known GIBBS-THOMSON (2.17) equation.

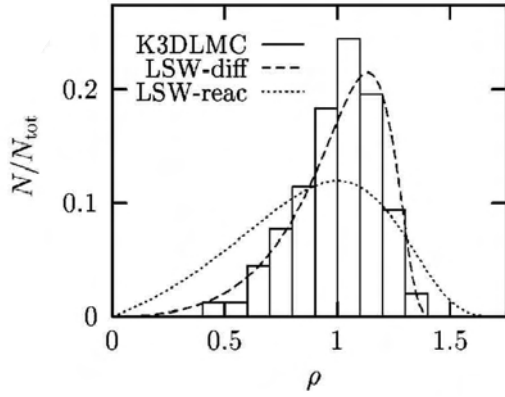


**Figure 2.11.:** Histogram of the particle size distribution obtained kinetic Monte Carlo simulation of second-phase precipitation with a volume fraction of  $\phi = 0.01$  on a  $f_{CC}$  lattice at  $T/T_c = 0.05$  (Strobel et al., 2001). Both stationary distributions of the LSW theory have been added.

In essence, this coarsening of randomly dispersed precipitates is a multi-particle diffusion problem, which is difficult to handle theoretically. Lifshitz and Slyozov (1961) and Wagner (1961) (LSW) used a mean field approach with simplifying assumptions.

- The precipitated volume fraction of the minority phase is close to zero. Hence, precipitates does not interact directly by diffusion but merely with an infinite matrix. This implicitly assumes a random spatial distribution with almost infinite separation.
- The linearized GIBBS-THOMSON eq. (2.19) can be applied, i.e. the NC radius is considerably larger than the capillary length  $R_c$ .
- The remaining supersaturation  $\Delta\mu$  is near zero, which automatically confines the LSW theory to late stages of phase separation.

This allows then to calculate the time evolution of the particle size distribution  $f(R,t)$ , that satisfies a continuity equation:

$$\frac{\partial f}{\partial t} + \frac{\partial}{\partial R} \left[ f \frac{dR}{dt} \right] = 0. \quad (2.21)$$

On the basis of this continuity equation and assuming diffusion control, the LSW theory yields in the asymptotic limit  $t \rightarrow \infty$  temporal power laws

$$\bar{R}(t) = \kappa_R^D t^{1/3}, \quad N(t) = \kappa_N^D t^{-1} \quad (\text{diffusion control}) \quad (2.22)$$

for the time evolution of the average particle radius  $\bar{R}(t)$  and the particle density  $N(t)$ . If the evolution is instead interface controlled, the growth laws reads as

$$\bar{R}(t) = \kappa_R^D t^{1/2} \quad N(t) = \kappa_N^D t^{-3/2} \quad (\text{reaction control}). \quad (2.23)$$

The corresponding rate constants can be found in (Lifshitz and Slyozov, 1961; Wagner, 1961) and have been reexamined for the more realistic case of non-zero solubilities and non-ideal solution by Schmitz and Haasen (1992) and Calderon et al. (1994). The LSW theory further predicts that the particle size distribution  $f(R,t)$  is time invariant (for  $t \rightarrow \infty$ ) under the scaling of the average particle size  $\bar{R}$ . A nice example is given by Strobel et al. (2001),

who have applied Kinetic Monte Carlo simulations to study NC formation. Figure 2.11 is redrawn from this work.

Surprisingly, LSW scaling as well as the existence of a stationary size distribution is a more general phenomenon than indicated by the stringent assumptions. The same scaling exponents also hold for *finite* precipitate volume fractions and the size distribution is only slightly modified (Wagner et al., 2001). Huse (1986) even argues for a general growth law of  $R(t) \sim t^{1/3}$  as long as diffusion through domains are the limiting process. This growth law has even been confirmed for arbitrary volume fractions including even coarsening after spinodal decomposition (Binder and Fratzl, 2001; Roland and Grant, 1989). However, the transient behavior at coarsening is long-lasting and truly stationary conditions are hardly reached (Alkemper et al., 1999). Interface diffusion might in addition hamper the domain scaling observed at intermediate times (Marko, 1993).

## Percolation

The discussion of phase separation commonly focusses on cluster properties and their time evolution in the case of nucleation or onto the description of the structure factor at spinodal decomposition. In real space however, patterns of quite different morphology are observed depending on the volume fraction of the minority phase, typical examples are shown in Figure 2.9. For small supersaturations, the minority phase is confined to independent clusters well separated from each other; for larger concentrations first coalescence of single cluster can be observed (Carrey and Maurice, 2001) and finally a *percolating* interconnected network is formed. The principle difference between both morphologies is often associated – erroneously – with a distinction between *nucleation and growth* versus *spinodal decomposition*. Rather, percolation is independent of the regime of phase separation (Heermann and Klein, 1983).

Percolation has been studied extensively under *static conditions*, e.g. for randomly placed particles (sites) or bonds on an  $\mathbb{f}_{CC}$  lattice (Isichenko, 1992; Stauffer, 1979; Stauffer and Aharony, 1992). A sharp change in the connectivity of large systems is found at a distinctive concentration - the percolation threshold  $p_c$ . Monte Carlo simulations delivered accurate estimates of  $p_c$  for various lattice types including the  $\mathbb{f}_{CC}$  lattice with  $p_c = 0.199$  (Frisch et al., 1961; Isichenko, 1992). Different values result depending on lattice dimensionality and coordination number, and several approaches have been taken to derive a general expression for a large classes of thresholds (Galam and Mauger, 1996; van der Mark, 1997).

For *dynamic* systems however precise data on percolation thresholds are rare. In addition, Hayward et al. (1987) and Heermann and Klein (1983) have shown that percolation at phase separation could be a time and temperature dependent phenomenon, i.e. percolation occurs for a given impurity concentration and temperature at an initial time  $t_1$  and persists up to  $t_2$  where then interface minimization leads to a fragmentation of the percolated structures. The knowledge of a single percolation threshold  $p_c$  at  $T = 0$  is not sufficient to assess system's connectivity at higher temperatures and later times of phase separation. Unfortunately, percolation has resisted up to now any analytical treatment in relevant cases. Only Monte Carlo simulations (and series approximation) allow to study *dynamic percolation* occurring at phase separation.

### Phase separation in confined geometries

Boundary conditions impose additional constraints and violate the system's homogeneity. Accordingly, studies on phase separation within the spinodal decomposition regime revealed an interesting interplay between surface and finite size effects (Ball and Essery, 1990; Binder and Fratzl, 2001; Marko, 1993). Usually, one component of the mixture will be enhanced at the surface in comparison with the bulk concentration as the interactions between the wall and the components differs. Such a preference leads to the formation of a wetting layer, which itself triggers surface-directed concentration waves with a wavevector normal to the surface at early stages of phase separation (Ball and Essery, 1990; Binder, 1983; Marko, 1993). In later stage of coarsening, an interesting competition is observed between domain growth in the bulk and a possible propagation of an ordered layer from the surface into the bulk (Puri and Frisch, 1997).

Interestingly, directing effects of a surface on phase separation can also be found upon nucleation at low supersaturations. Pronounced self-organization effects in the presence resulting from an absorbing (or depleting) surface are reported by (Borodin et al., 1997; Lacasta et al., 1999; Reiß and Heinig, 1994) and Brown et al. (1994). A layering of precipitates similar to surface-directed spinodal decomposition is found. In addition, a zone depleted of precipitates is predicted to form at the surface during coarsening by OSTWALD ripening (Burghaus, 1998).

### References

- J. Alkemper, V. A. Snyder, N. Akaiwa, and P. W. Voorhees. Dynamics of late-stage phase separation: A test of theory. *Physical Review Letters*, 82(13):2725–2728, 1999.
- G. W. Arnold and J. A. Borders. Aggregation and migration of ion-implanted silver in lithia-alumina-silica glass. *Journal of Applied Physics*, 48(4):1488–1496, Apr. 1977.
- R. C. Ball and R. L. H. Essery. Spinodal decomposition and pattern formation near surface. *Journal of Physics: Condensed Matter*, 2:10303–10320, 1990.
- R. Becker and W. Döring. Kinetische Behandlung der Keimbildung in übersättigten Dämpfen. *Annalen der Physik*, 24:719, 1935.
- K. Binder. Critical behaviour at surfaces. In C. Domb and J. L. Lebowitz, editors, *Phase Transitions and Critical Phenomena*, volume 8, chapter 1, pages 1–144. Academic Press, London, 1983.
- K. Binder. Nucleation barriers, spinodals, and the Ginzburg criterion. *Physical Review A*, 29(1):341–349, 1984.
- K. Binder and P. Fratzl. Spinodal decomposition. In G. Kostorz, editor, *Phase Transformations in Materials*, chapter 6, pages 409–480. Wiley-VCH, Weinheim, 2001.
- K. Binder, C. Billotet, and P. Mirol. On the theory of spinodal decomposition in solid and liquid binary mixtures. *Zeitschrift für Physik B*, 30:183–195, 1978.
- V. A. Borodin, K. H. Heinig, and S. Reiß. Self-organization kinetics in finite precipitate ensembles during coarsening. *Physical Review B*, 56(9):5332–5344, Sept. 1997.
- G. Brown, A. Chakrabarti, and J. F. Marko. Surface-induced nucleation. *Physical Review E*, 50(4):1674–1677, 1994.

- R. Burghaus. Ostwald ripening in a semi-infinite system. *Physical Review E*, 57(3):3234–3236, Mar. 1998.
- J. W. Cahn. On spinodal decomposition. *Acta Metallurgica*, 9:795–801, 1961.
- J. W. Cahn and J. E. Hilliard. Free energy of a nonuniform system. I. Interfacial free energy. *Journal of Chemical Physics*, 28:258, 1958.
- J. W. Cahn and J. E. Hilliard. Free energy of a nonuniform system. II. Thermodynamic basis. *Journal of Chemical Physics*, 30:1121–1124, 1959a.
- J. W. Cahn and J. E. Hilliard. Free energy of a nonuniform system. III. Nucleation in a two-component incompressible fluid. *Journal of Chemical Physics*, 31:688, 1959b.
- H. A. Calderon, P. W. Voorhees, J. L. Murray, and G. Kostorz. Ostwald ripening in concentrated alloys. *Acta Metallurgica*, 42(3):991–1000, 1994.
- J. Carrey and J.-L. Maurice. Transition from droplet growth to percolation: Monte carlo simulations and an analytical model. *Physical Review B*, 63:245408, 2001.
- E. Cook. Brownian motion in spinodal decomposition. *Acta Metallurgica*, 18:297–306, 1970.
- W. Eckstein. *Computer Simulation of Ion-Solid Interactions*. Springer-Verlag, Heidelberg, 1991.
- E. Fermi and E. Teller. The capture of negative mesotrons in matter. *Physical Review*, 72:399, 1947.
- H. L. Frisch, E. Sonnenblick, V. A. Vyssotsky, and J. M. Hammersley. Critical percolation probabilities (site problem). *Physical Review*, 124(4):1021–1022, Nov. 1961.
- S. Galam and A. Mauger. Universal formulas for percolation thresholds. *Physical Review E*, 53(3):2177–2181, Mar. 1996.
- J. W. Gibbs. *The Scientific Papers of J. Willard Gibbs*, volume 1. Longmans, Green and Co., New York, 1906. reprinted 1961 by Dover, New York.
- M. E. Glicksman. *Diffusion in solids: Field theory, solid-state principles and applications*. John Wiley & Sons, New York, 2000.
- J. D. Gunton, M. S. Miguel, and P. S. Sahni. The dynamics of first-order phase transitions. In C. Domb and J. L. Lebowitz, editors, *Phase Transitions and Critical Phenomena*, volume 8, chapter 3, pages 269–482. Academic Press, London, 1983.
- S. Hayward, D. W. Heermann, and K. Binder. Dynamic percolation transition induced by phase separation: A Monte Carlo analysis. *Journal of Statistical Physics*, 49(5/6):1053–1081, 1987.
- D. W. Heermann and W. Klein. Percolation and droplets in a medium-range three-dimensional Ising model. *Physical Review B*, 27:1732–1735, 1983.
- K. Heinig, T. Müller, B. Schmidt, M. Strobel, and W. Möller. Interfaces under ion irradiation: growth and taming of nanostructures. *Applied Physics A: Materials Science & Processing*, 77(1):17–25, June 2003.
- D. A. Huse. Corrections to late-stage behavior in spinodal decomposition: Lifshitz-Slyozov scaling and Monte Carlo simulation. *Physical Review B*, 34(11):7845–7850, 1986.
- M. B. Isichenko. Percolation, statistical topography, and transport in random media. 64(4):961–1043, Oct. 1992.
- A. L. Itkin and E. G. Kolesnichenko. *Microscopic Theory of Condensation in Gases and Plasma*, volume 44 of *Series on Advances in Mathematics for Applied Sciences*. World Scientific, 1997.

- D. Kashchiev. *Nucleation: Basic Theory with Applications*. Butterworth Heinemann, Oxford, 2000.
- E. F. Krimmel and H. Pfeleiderer. Implantation profiles modified by sputtering. *Radiation Effects*, 19: 23, 1973.
- A. M. Lacasta, F. Sagues, J. M. Sancho, and I. M. Sokolov. Evaporation and coarsening dynamics with open boundaries. *Physical Review E*, 59(1):189–193, 1999.
- J. S. Langer. An introduction to the kinetics of first-order phase transition. In C. Godreche, editor, *Solids Far From Equilibrium*, chapter 3, pages 297–364. Cambridge University Press, Cambridge, 1992.
- I. M. Lifshitz and V. V. Slyozov. The kinetics of precipitation from supersaturated solid solutions. *J. Phys. Chem. Solids*, 19:35, 1961.
- J. F. Marko. Influence of surface interactions on spinodal decomposition. *Physical Review E*, 48(4): 2861–2879, Oct. 1993.
- J. Marro and A. B. Bortz. Time evolution of a quenched binary alloy. II. Computer simulation of a three-dimensional model system. *Physical Review B*, 12(6):2000–2011, 1975.
- A. Meldrum, R. F. Haglund, L. A. Boatner, and C. W. White. Nanocomposite materials formed by ion implantation. *Advanced Materials*, 13(19):1431–1444, Oct. 2001.
- W. Möller and W. Eckstein. TRIDYN - A TRIM simulation code including dynamic composition changes. *Nuclear Instruments and Methods in Physics Research B*, 2:814–818, 1984.
- M. Nastasi, J. W. Mayer, and J. K. Hirvonen. *Ion-Solid Interactions: Fundamentals and Applications*. Cambridge University Press, Cambridge, 1996.
- S. Puri and H. L. Frisch. Surface-directed spinodal decomposition: modelling and numerical simulations. *Journal of Physics: Condensed Matter*, 9:2109–2133, 1997.
- S. Reiß and K.-H. Heinig. Ostwald ripening during ion beam synthesis - a computer simulation for inhomogeneous systems. *Nuclear Instruments and Methods in Physics Research B*, 84:229–233, 1994.
- T. M. Rogers and R. C. Desai. Numerical study of late-stage coarsening for off-critical quenches in the cahn-hilliard equation of phase separation. *Physical Review B*, 38(16):11956, 1989.
- C. Roland and M. Grant. Monte Carlo renormalization-group study of spinodal decomposition: Scaling and growth. *Physical Review B*, 39(39):11971–11981, 1989.
- H. Ryssel and I. Ruge. *Ion Implantation*. John Wiley and Sons Ltd, New York, 1986.
- G. Schmitz and P. Haasen. Decomposition of an Al-Li alloy – the early stages observed by HREM. *Acta Metallurgica*, 40(9):2209–2217, 1992.
- P. Sigmund. *Sputtering by Ion Bombardment: Theoretical Concepts*, volume 47 of *Topics in Applied Physics*, pages 9–71. Springer-Verlag, Berlin, 1981.
- P. Sigmund and A. Gras-Marti. Distortion of depth profiles during sputtering I. General description of collisional mixing. *Nuclear Instruments and Methods*, 168:389–394, 1980.
- P. Sigmund and A. Gras-Marti. Theoretical aspects of atomic mixing by ion beams. *Nuclear Instruments and Methods*, 182/183:25, 1981.
- W. Skorupa, L. Rebohle, and T. Gebel. Group-IV nanoduster formation by ion-beam synthesis. *Applied Physics A: Materials Science & Processing*, 76(7):1049–1059, 2003.

- D. Stauffer. Scaling theory of percolation structures. *Physics Reports*, 54(1):1–74, 1979.
- D. Stauffer and A. Aharony. *Introduction to Percolation Theory*. Taylor & Francis, London, 2 edition, 1992.
- M. Strobel, K.-H. Heinig, and W. Möller. Three-dimensional domain growth on the size scale of the capillary length: Effective growth exponent and comparative atomistic and mean-field simulations. *Physical Review B*, 64:245422, 2001.
- S. C. van der Mark. Percolation thresholds and universal formulas. *Physical Review E*, 55(2):1514–1517, Feb. 1997.
- M. Volmer and A. Weber. Keimbildung in übersättigten Gebilden. *Zeitschrift der Physikalischen Chemie (Leipzig)*, 119:277, 1926.
- C. Wagner. Theorie der Alterung von Niederschlägen durch Umlösen. *Z. Elektrochem.*, 65:581, 1961.
- R. Wagner, R. Kampmann, and P. W. Voorhees. Homogeneous second phase precipitation. In G. Kostorz, editor, *Phase Transformations in Materials*, chapter 5, pages 309–408. Wiley-VCH, Weinheim, 2001.
- Y. Yamamura, Y. Itakawa, and N. Itoh. Sputtering yield. In *IPPJ - AM -26, Nagoya*, chapter 4, pages 59–97. 1983.
- J. B. Zeldovich. On the theory of new phase formation; Cavitation. *Acta Physicochimica (URSS)*, 18(1):1, 1943.
- J. F. Ziegler. The stopping and range of ions in matter. <http://www.srim.org>, 1998. version 4.
- J. F. Ziegler, editor. *Handbook of Ion Implantation Technology*. North-Holland, New York, 1992.
- J. F. Ziegler, J. P. Biersack, and U. Littmark. *The Stopping and Range of Ions in Solids*. Pergamon Press, New York, 1985.





## Chapter 3.

# Modeling of Si Excess Depth Profiles by Dynamic Binary Collision Calculations

Low energy IBS of Si NCs consists of two consecutive steps (cp. Chapter 2, Figure 2.1), which will also be modeled separately. The Ion-solid interactions during the first step of synthesis– the ion implantation – can be considered at its own due to the different time (and temperature) scale on which the later phase separation occurs. In a first step, described in this Chapter, the creation of a *far-from-equilibrium state* by high fluence ion implantation of Si atoms being immiscible in the SiO<sub>2</sub> host matrix is discussed. *Dynamic binary collision calculations* are used to predict Si excess depth distribution that will serve as input for the second simulation step, the *kinetic Monte Carlo simulations* described in Chapter 4. These consider phase separation and, therefore, the time evolution of the supersaturated system relaxing towards the *thermodynamic equilibrium* during annealing.

### 3.1. Dynamic BCA simulations using TRIDYN

Depth profiles of implanted impurity atoms are usually calculated with the help of Monte Carlo codes using the binary collision approximation (BCA), among which TRIM/SRIM (Ziegler, 1998) is the most common one. In these *”single-ion” models*, which hold in the low-fluence limit, the target is considered as *”virgin”* for each simulated impact of a pseudo-particle for which the trajectories of the collision cascade is calculated. The set of all such trajectories is then used to predict range profiles and sputtering yields and allows to estimate the target damage.

However, ion implantation alters the target considerably at higher ion fluences. It cannot be approximated as virgin, undamaged target in *”single-ion”* BCA calculations. Here, conventional TRIM simulations fail. For this case, Möller and Eckstein (1984) developed a dynamic modification of TRIM – TRIDYN – that accounts for target changes during the course of the implantation. The application of this dynamic code covers a variety of problems that cannot be adequately treated with TRIM. The effects of (i) target swelling due to the implanted material, (ii) target erosion due to ion sputtering and (iii) ion beam induced intermixing of target atoms (Möller, 1986) are naturally included in TRIDYN (see Figure 3.1).

For the simulation, the surface layer affected by implantation is divided into thin slabs of equal thickness  $\Delta x$ . According to the TRIM-like calculation of the ion-cascade for a single pseudo-particle, atoms are relocated among different slabs and the material of the pseudo-particle<sup>1</sup> is added at the end of the primary ion track. Additionally, sputtering events remove

---

<sup>1</sup>A pseudo particle is defined as a fraction of the total ion fluence to be implanted,  $\Delta\Phi = \Phi/N$ , with a total number of  $N$  pseudo-particles.

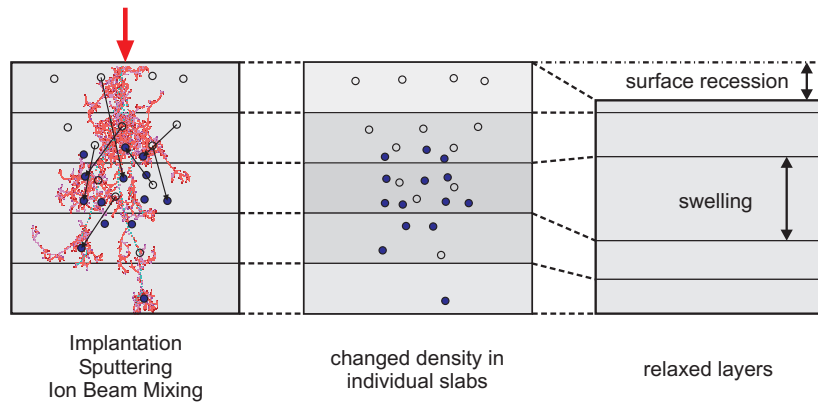


**Figure 3.1.:** Scheme of the dynamic target used in TRIDYN calculations.

material from the target surface and lead to a *surface recession*. All these processes, that created vacancies or have lead to the addition of material at certain depths, have changed the particle density of the target. In a subsequent relaxation step it is then assured that the target density  $n_i$  of the slab  $i$  is consistent with the target composition there, according to  $1/n_i = \sum c_{ij} V_j^a$ , when  $c_{ij}$  denotes the atomic concentration of the species  $j$  with the atomic volume  $V_j^a$  in the slab  $i$ . The atomic volumes are thereby chosen to give the correct compound densities, e.g. for  $\text{SiO}_2$ . Atomic densities and atomic volumes are listed in Table 3.1 for  $\text{SiO}_2$ . The free parameter of the atomic volume of oxygen was adjusted to yield the  $\text{SiO}_2$  density. In case the relaxed depth intervals get too small or too large, TRIDYN either joins adjacent intervals or splits large ones. All calculations shown here were performed with a minimum number of  $10^5$  pseudo-particles per simulation to limit the statistical scatter in depth profiles.

### 3.1.1. TRIDYN parameters for $\text{SiO}_2$

Among other input quantities necessary for TRIDYN calculations, energy parameters are the most important ones (Möller and Eckstein, 1984; Möller and Posselt, 2001). The values for  $\text{SiO}_2$  used in this work are listed in Table 3.2, they include:

Element	atomic volume $V^a$ ( $\text{\AA}^3$ )	atomic density $n$ ( $\text{nm}^{-3}$ )	comment
Si	20.1	49.8	<i>reference</i>
O	11.8	84.9	<i>adjusted from <math>\text{SiO}_2</math></i>
$\text{SiO}_2$		68.8	<i>reference</i>
SiO		62.7	<i>as calculated</i>

**Table 3.1.:** Atomic densities used for the target relaxation in TRIDYN simulation with a  $\text{SiO}_2$  target.

energy parameters	values (eV)	
	Si	O
cut-off energy $E_c$	4	4
bulk binding energy $E_b$	0	0
relocation threshold $E_D$	8	8
average SBE per atom in SiO <sub>2</sub>	6.4	6.4

**Table 3.2.:** TRIDYN energy parameters for a SiO<sub>2</sub> target.

**cut-off energy  $E_c$ :** This threshold determines the energy at which a pseudo-particle is considered to be stopped. Too low values increase the computational time without increasing the accuracy. However,  $E_c$  should always be less than other relevant energies, e.g. the surface binding energy which is important for sputtering.

**bulk binding energy  $E_b$ :** The binding energy that is subtracted from the kinetic energy before a recoil is generated. Here set to zero in conjunction with previous studies of Möller and Posselt (2001) and Möller (1985). The effect of the binding energy is included in the surface binding energy  $SBE$ .

**relocation threshold  $E_D$ :** This value defines the energy that is needed to create a stable *Frenkel* pair, which does not recombine immediately. For SiO<sub>2</sub> a value of  $E_D = 8$  eV is used for both species, Si and O. This value has proven to yield satisfactory agreement between earlier TRIDYN simulations of ion mixing and experiments (Möller, 1986) and is also consistent with the choice of Sigmund and Gras-Marti (1981) in their theoretical treatment of ion beam mixing<sup>2</sup>. It also accounts for the high degree of accumulated damage in strongly irradiated SiO<sub>2</sub> targets where otherwise larger values of 15...20 eV are used in TRIM calculations for virgin SiO<sub>2</sub>.

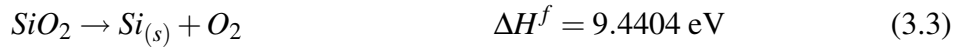
**surface binding energy  $SBE$ :** It defines the energy of the surface barrier that has to be overcome by a recoil in order to leave the target. It therefore critically determines the sputtering yield. The  $SBE$  varies with the surface composition during implantation and leads to a fluence dependent sputtering yield. TRIDYN applies here an advanced description and defines an effective  $SBE_i = \sum_j SBV_{ij}c_j$  for atoms of the species  $i$  depending on the surface concentrations  $c_j$ . The matrix elements  $SBV_{ij}$  allow to adopt for various situations. E.g., a  $SBE$  that does not depend on concentration leads to  $SBV_{ij} = SBE_i$ , but still accounts for preferential sputtering. In the full description with a concentration dependent SBE, thermodynamic data of the heat of formation  $\Delta H^f$  of SiO<sub>2</sub>, the heat atomization  $\Delta H_{Si}^a$  of Si and the heat of dissociation  $H_{O_2}^{diss}$  of O<sub>2</sub> are needed to estimate the matrix element  $SBV_{ij}$ , which were

<sup>2</sup>Simulations with  $E_d$  varied by factors of 0.5 and 2 do not show significant differences of the calculated Si depth profiles.

partial surface binding energies $SBV_{ij}$		values (eV)	
$SBV_{Si,Si}$	$SBV_{O,Si}$	4.67	13.28
$SBV_{Si,O}$	$SBV_{O,O}$	13.28	0

**Table 3.3.:** Partial surface binding energies  $SBV_{ij}$  for a SiO<sub>2</sub> target as used by TRIDYN for the advanced description of the surface composition dependent sputtering.

taken from Chase (1998).



From these data, the total heat of atomization of SiO<sub>2</sub> can be calculated, which is also the sum of the SBE's

$$\Delta H_{SiO_2}^a = \Delta H^f + \Delta H_{Si}^a + \Delta H_{O_2}^{diss} = SBE_{Si} + 2SBE_O = 19.269 \text{ eV}. \quad (3.4)$$

The matrix elements are then determined according to Kelly (1980) and Möller and Posselt (2001) as

$$SBV_{Si,Si} = \Delta H_{Si}^a \quad \text{and} \quad SBV_{O,O} = 0, \quad (3.5)$$

$$SBV_{Si,O} = SBV_{O,Si} = \frac{1}{2}\Delta H_{Si}^a + \frac{3}{4}\Delta H^f + \frac{3}{4}\Delta H_{O_2}^{diss}. \quad (3.6)$$

Oxygen is considered as volatile such that O-O interactions can be neglected ( $SBV_{O,O} = 0$ ). The values of the matrix elements  $SBV_{ij}$  are summarized in Table 3.3 for SiO<sub>2</sub>. For a pure SiO<sub>2</sub> target, the effective SBE's for Si and O are 10.4 eV and 4.4 eV, respectively. Oxygen will preferentially be sputtered and Si enriches at the target surface during ion irradiation. In total, an effective SBE of 6.4 eV governs the overall surface erosion of SiO<sub>2</sub>.

### 3.1.2. Validation of low-energy sputtering yields

High fluence Si<sup>+</sup> implantation into SiO<sub>2</sub> cause a considerable target swelling due to the incorporated material, which is partially compensated by sputtering. Accordingly, the total SiO<sub>2</sub> layer thickness achieved after implantation is critically determined by the competition between deposition and erosion.

For later comparisons to experiments of low energy Si<sup>+</sup> implantation it is necessary to predict sputter yields correctly by TRIDYN calculations. Experimentally, these sputter yields are difficult to access as other phenomena might affect the SiO<sub>2</sub> thickness. Among those are the cleaning procedure and the partial oxidation of the implanted Si. Even more, TRIDYN results will be used later on to discriminate these effects from pure ion induced thickness changes. If the ion related swelling and sputtering is precisely predicted, experimental observed differences could be attributed to such effects.

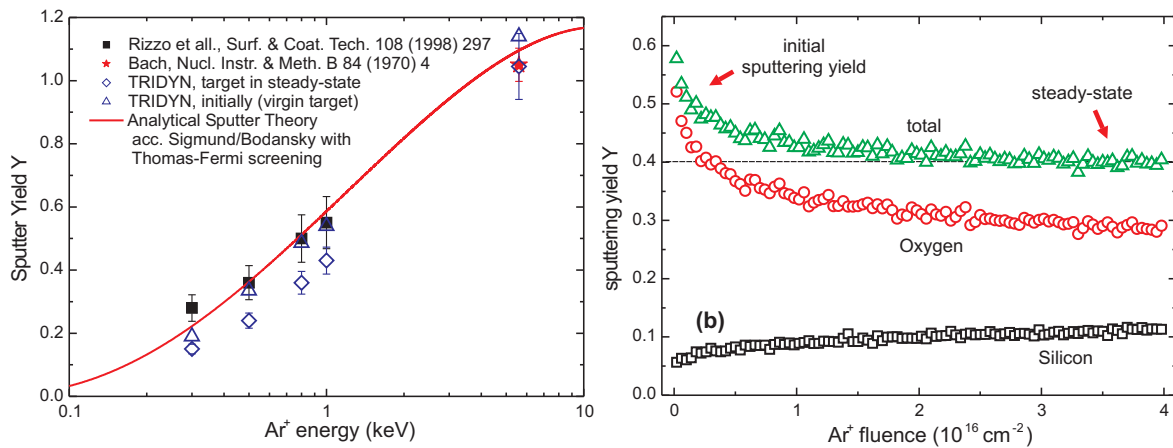


**Figure 3.2.:** (a) Comparison of measured sputter yields with predictions for Ar<sup>+</sup> irradiation of SiO<sub>2</sub> at a total fluence of  $1 \times 10^{16} \text{ cm}^{-2}$ . (b) Variation of the sputtering yield with Ar<sup>+</sup> fluence at 1 keV energy.

Literature data on low energy sputter yields for Si<sup>+</sup> implantation into SiO<sub>2</sub> is extremely rare. For comparison, work on low energy Ar<sup>+</sup> irradiation of SiO<sub>2</sub> is used instead. Bach (1970); Bach et al. (1974); Rizzo et al. (1998) have published experimental sputter yields for energies between 0.5 and 5 keV, which are compared here to TRIDYN results for Ar<sup>+</sup>. The required TRIDYN energy parameters for SiO<sub>2</sub> were chosen according to Table 3.2 and the calculated sputtering yields are displayed in Figure 3.2(a) for an Ar<sup>+</sup> fluence of  $1 \times 10^{16} \text{ cm}^{-2}$ . These results are in fair agreement with the measured values. However, TRIDYN calculations revealed that the sputter yield is fluence dependent, i.e. decreases during implantation due to preferential O sputtering. The Si content is locally enriched at the target surface and, hence, it is harder to be sputtered. This effect is shown in Figure 3.2(b) for a Ar<sup>+</sup> energy of 1 keV. TRIDYN sputtering yields for a virgin target (low fluence limit) are found to agree nicely with the experiment of Rizzo et al. (1998)<sup>3</sup>, which was not expected. Rather steady state conditions (and therefore steady state sputtering yields) are expected in the experiment, and were confirmed by Bach (1970). In addition, an approximation based on the analytical treatment of Sigmund (1969) using Thomas-Fermi screening is shown as solid line in Figure 3.2(a) calculated with an average SBE of 6.4 eV.

With the used energy parameters, TRIDYN sputtering yields are in reasonable agreement with experimental values. Even more, TRIDYN covers also composition (fluence) dependent sputtering that has not been adequately considered by the experiment of Rizzo et al. (1998).

### 3.2. Si excess in low energy Si<sup>+</sup> implanted SiO<sub>2</sub> films

High fluence Si<sup>+</sup> implantation introduces additional Si into the implanted SiO<sub>2</sub> that is later on available for NC formation. The amount of the Si excess and its depth distribution will be predicted by TRIDYN calculations. In addition, the total target swelling and the ion beam mixing of the SiO<sub>2</sub>/Si interface upon low energy ion implantation is considered.

<sup>3</sup>Note that the experimental error of the sputter yield measurements was estimated by Rizzo et al. (1998) to be approximately 15%.

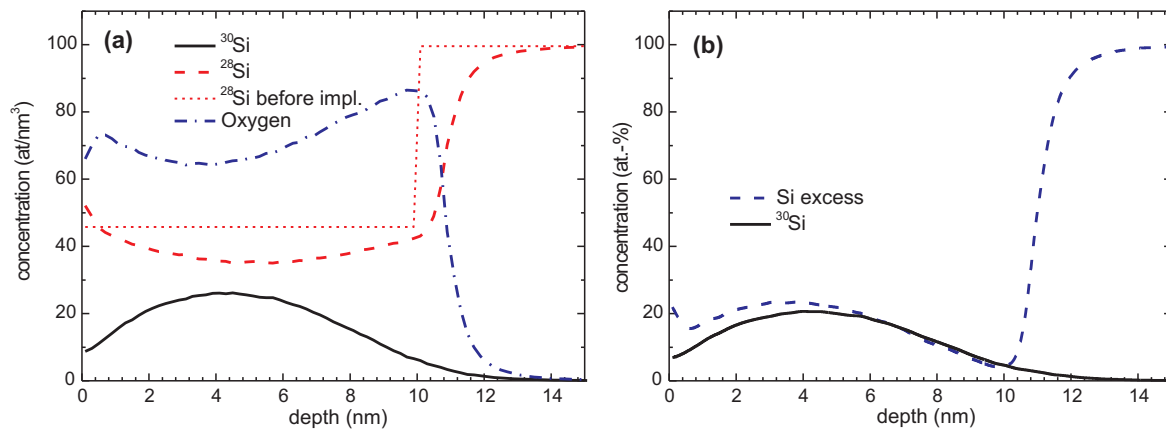


**Figure 3.3.:** Target composition after 2 keV  $^{30}\text{Si}^+$  implantation into 10 nm  $^{28}\text{SiO}_2$  on  $^{28}\text{Si}$  to a fluence of  $1 \times 10^{16} \text{ cm}^{-2}$ . In (a), the depth profiles of the  $^{28}\text{Si}$  and O of the  $\text{SiO}_2/\text{Si}$  target and the implanted  $^{30}\text{Si}$  are shown. The thin dotted line depicts the  $^{30}\text{Si}$  before implantation. The three profiles ( $^{28}\text{Si}$ ,  $^{30}\text{Si}$ , O) were reduced to a single quantity, the Si excess, shown in (b) together with the profile of implanted  $^{30}\text{Si}$ .

### 3.2.1. Si excess - Over-stoichiometric Si in $\text{SiO}_2$

Implanted Si is chemically indistinguishable from Si in the stoichiometric  $\text{SiO}_2$  substrate, a separation between both species is not necessary in studies of phase separation. Even more, ion implantation will damage the glassy  $\text{SiO}_2$  network considerably, i.e. many Si-O bonds are broken. This network can be assumed to reconfigure quickly locally during early annealing, such that only Si exceeding the stoichiometry of  $\text{SiO}_2$  is left over. Noting the indistinguishability of the Si atoms, implanted Si can be incorporated into the  $\text{SiO}_2$  bonding network while Si atoms remain unbonded (or weakly bonded) that previously resided in the host matrix. This local *Si excess* being available for phase separation is then defined as

$$c_{\text{Si},\text{excess}} \equiv (c_{\text{Si},\text{matrix}} + c_{\text{Si},\text{implanted}}) - \frac{1}{2}c_{\text{O}} = c_{\text{Si}} - \frac{1}{2}c_{\text{O}}, \quad (3.7)$$

where  $c_{\text{O}}$  and  $c_{\text{Si}}$  are the atomic concentrations, respectively. This definition uses the  $\text{SiO}_2$  matrix as reference system and allows to reduce the number of relevant parameters to one assuming that practically no Si diffusion occurs over larger length scales upon the reconfiguration of the  $\text{SiO}_2$  network. This crucial parameter, the local *Si excess*, is illustrated in Figure 3.3 exemplarily for 2 keV  $^{30}\text{Si}^+$  implantation into 10 nm thick  $\text{SiO}_2$ . The Si isotopes are distinguished here for a better understanding only<sup>4</sup>.

Figure 3.3(a) shows that the  $^{28}\text{Si}$  and O concentration in the  $\text{SiO}_2$  matrix is diminished due to implanted  $^{30}\text{Si}$ . Additionally, ion beam mixing leads to a smearing out of the original Si and O profiles at the  $\text{SiO}_2/\text{Si}$  interface, and preferential sputtering of O causes a slight  $^{28}\text{Si}$  enrichment at the oxide surface. With the definition of the Si excess (3.7), these three effects are combined into a single quantity, (Figure 3.3b) relying on the indistinguishability of implanted Si from Si of the oxide matrix. Nonetheless, the definition of the Si excess is based on  $\text{SiO}_2$  as reference system and the use of this quantity in the Si substrate is not straightforward. It nevertheless proves useful if oxygen mixed into the Si substrate is assumed to

<sup>4</sup>A corresponding isotopic experiment using  $^{30}\text{Si}^+$  implantation into  $^{28}\text{SiO}_2$  could of course be performed.

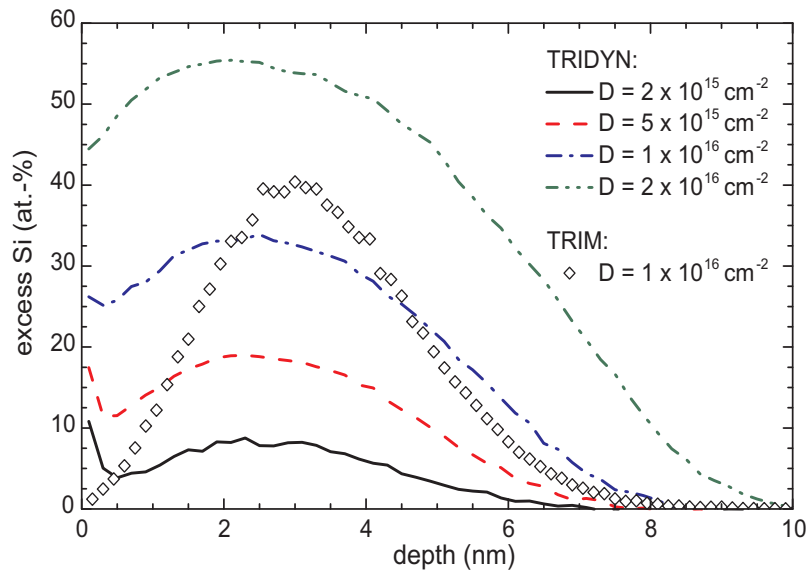


**Figure 3.4.:** TRIDYN depth profiles of Si excess for 1 keV Si<sup>+</sup> implantation into SiO<sub>2</sub>. One TRIM profile has been added for comparison.

form tiny SiO<sub>2</sub> precipitates there. In that case, the Si excess does not reach immediately the value of 100 at.-% in the Si substrate. Hence, a Si excess of 0 at.-% corresponds to pure SiO<sub>2</sub> while 100 at.-% reflects pure Si.

### 3.2.2. Si excess depth profiles predicted by TRIDYN calculations

Figure 3.4 shows Si excess depth profiles for 1 keV Si implantation into SiO<sub>2</sub>. The ion fluence was continuously raised from  $1 \times 10^{15} \text{ cm}^{-2}$  up to  $2 \times 10^{16} \text{ cm}^{-2}$ . The necessary input parameters for TRIDYN calculations were chosen according to Table 3.1, 3.2, and 3.3.

The Si excess, i.e. the peak concentration of the Si excess profile, increases for higher Si<sup>+</sup> ion fluences, while the profile broadens considerably due to ion beam mixing, sputtering and swelling. A slight Si enrichment at the target surface is observed as the result of preferential O sputtering. For comparison, a Si implantation profile calculated by TRIM (Ziegler, 1998) has been added to Figure 3.4, which is much sharper than the corresponding TRIDYN profile. Accordingly, the Si peak concentration is significantly overestimated by TRIM. The profile broadening observed by TRIDYN calculations cannot be described by TRIM. TRIDYN simulations are, therefore, required to predict a correct (broadened) profile for high fluence implants.

Mixing of the Si/SiO<sub>2</sub> interface becomes important if the Si<sup>+</sup> energy is increased up to 5 keV. Figures 3.5 shows the corresponding TRIDYN Si excess profiles for a constant initial SiO<sub>2</sub> thickness of 10 nm and a fluence of  $1 \times 10^{16} \text{ cm}^{-2}$ . At an ion energy of 0.6 keV, the Si excess is peaked with 42 at.-% in 1.9 nm depth. The Si/SiO<sub>2</sub> interface is hardly influenced since recoils come to rest before reaching the interface. At increasing energy, the Si excess peak broadens, shift towards greater depth and the peak concentration decreases. At 2 keV energy, ion beam mixing of the Si/SiO<sub>2</sub> interface sets in and the leads to a smearing out of the Si and O profiles. O atoms are displaced from the SiO<sub>2</sub> into the Si substrate while Si

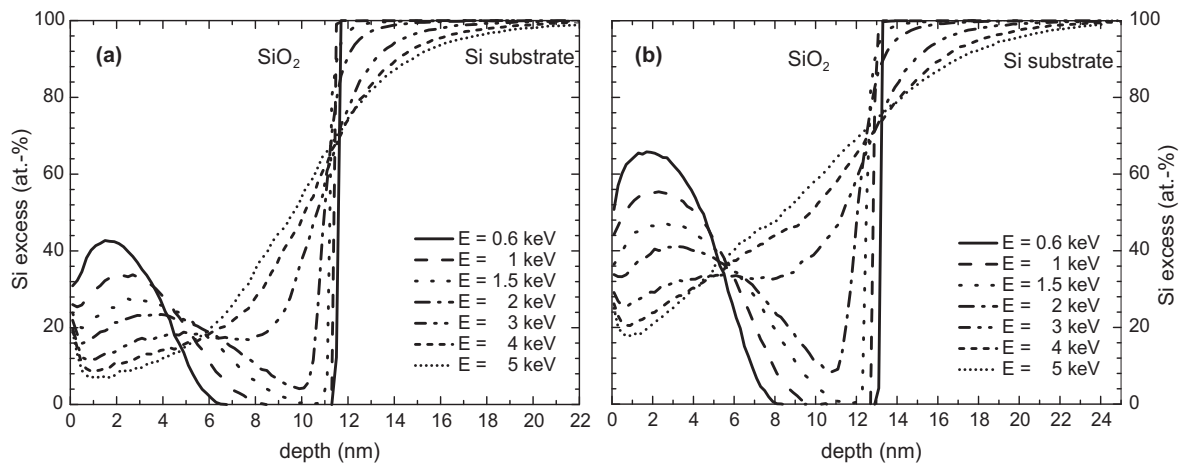


**Figure 3.5.:** Si excess depth profiles for low energy  $\text{Si}^+$  implantations between 0.6 and 5 keV energy into 10 nm thick  $\text{SiO}_2$  at a fluence of (a)  $1 \times 10^{16} \text{ cm}^{-2}$  and (b)  $2 \times 10^{16} \text{ cm}^{-2}$ .

atoms are mixed from the Si substrate into the  $\text{SiO}_2$ <sup>5</sup>. At even higher energies (e.g. 5 keV), ion beam mixing becomes the dominating effect and the Si excess rises continuously with increasing depth. A separated peak of Si excess located in the  $\text{SiO}_2$  cannot be distinguished in that case.

### 3.2.3. Profile approximations

These Si excess depth profiles can be described in good approximation by a superposition of a Gaussian peak representing the implanted Si and an error function that accounts for the broadened  $\text{SiO}_2/\text{Si}$  interface

$$c_{\text{Si excess}}(x) \cong c_{\text{max}} \exp\left(-\frac{(x-x_{c1})^2}{2\sigma^2}\right) + \frac{1}{2} \operatorname{erf}\left(\frac{x-x_{c2}}{w}\right) + \frac{1}{2}. \quad (3.8)$$

The Gaussian peak is located at the depth  $x_{c1}$  and obeys a full-width half-maximum (FWHM) that relates to the standard deviation  $\sigma$  by  $FWHM = 2\sigma\sqrt{\ln(4)}$ . In this peak, a maximum Si excess of  $c_{\text{max}}$  is obtained. The ion beam mixed interface is described by an error function centered at  $x_{c2}$ , which is approximately the position of the  $\text{SiO}_2/\text{Si}$  interface once it has reconfigured during the annealing<sup>6</sup>. The width of the irradiated interface is described by the parameter  $w$ . Since differentiation of the error function  $\operatorname{erf}$  gives a Gaussian profile, the width  $w$  can be naturally related to the peak width  $\sigma$  of the differentiated profile

$$\frac{\partial}{\partial x} \left[ \frac{1}{2} \operatorname{erf}\left(\frac{x-x_{c2}}{w}\right) + \frac{1}{2} \right] = \frac{1}{\sqrt{2\pi}\sigma_{IF}} \exp\left(-\frac{(x-x_{c2})^2}{2\sigma_{IF}^2}\right), \quad \text{with } w^2 = 2\sigma_{IF}^2. \quad (3.9)$$

The quality of this approximation is shown in Figure 3.6(a) for the case of 2 keV  $\text{Si}^+$  implantation into 10 nm thick  $\text{SiO}_2$  to a fluence of  $1 \times 10^{16} \text{ cm}^{-2}$ . The fitted profile agrees

<sup>5</sup>Si atoms are also displaced from the  $\text{SiO}_2$  into the Si substrate.

<sup>6</sup>This holds if the diffusion of O in Si and Si in  $\text{SiO}_2$  is equally fast.



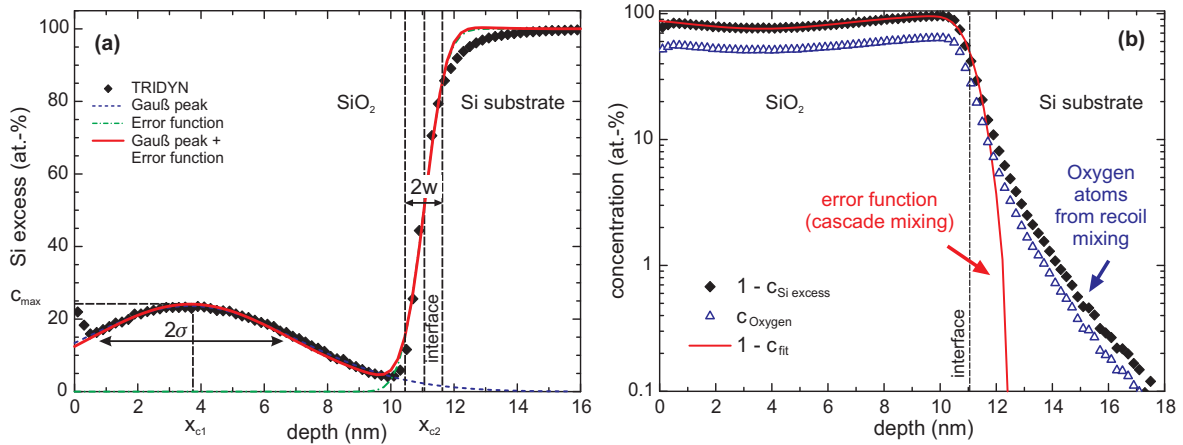


**Figure 3.6.:** (a) TRIDYN depth profiles of Si excess ( $2 \text{ keV}$ ,  $1 \times 10^{16} \text{ cm}^{-2}$ ) can be approximated by a superposition of a Gaussian peak and an error function (3.8). (b) However, the error function does not account for the tail of oxygen atoms in the Si substrate created by recoil mixing.

remarkably well with the TRIDYN data except for the deep tail of the broadened Si/SiO<sub>2</sub> interface. This discrepancy is shown more clearly in Figure 3.6(b) by the value of  $1 - c_{\text{Si excess}}$ . Deeply displaced O atoms form a far reaching tail into the Si substrate that can be attributed to recoil mixing. I.e. O atoms were displaced in energetic small-angle collisions much further than the average mixing length in cascade mixing, giving rise to the error function shape. The tail of the concentration profile merely reflects the probability distribution of such high energetic events.

### 3.2.4. Si excess in as-implanted SiO<sub>2</sub> layers – Comparison with ToF-SIMS results

The experimental proof of Si excess in as-implanted SiO<sub>2</sub> layers is usually difficult due to the high Si background in SiO<sub>2</sub>. Added traces of excess Si can hardly be quantified at nanometer depth resolution. One method that can accomplish this task is Time-of-Flight Secondary Ion Mass Spectroscopy (ToF-SIMS) analyzing the target composition by means of sputter profiling and secondary ion detection. Perego et al. (2003) have used a dual beam TOF-SIMS for depth profiling that achieves the required depth resolution by decoupling the sputtering gun from the analysis gun and can use sufficiently low energies for gently sputter erosion. A very high sensitivity is obtained using Cs as primary ion beam in negative mode detection. Perego et al. (2003) utilized in their work especially the detection various Si<sub>n</sub> microclusters. These clusters of three or more Si atoms are very unlikely to be sputtered from stoichiometric SiO<sub>2</sub> but are detected in implanted SiO<sub>2</sub> layers indicating the Si excess as shown in Figure 3.7.

To allow a direct comparison, TRIDYN calculations were performed for the same implantation conditions as used by Perego et al. (2003), i.e. for  $5 \text{ keV}$  Si<sup>+</sup> implantation into  $20 \text{ nm}$  thick SiO<sub>2</sub> to a fluence of  $1 \times 10^{16} \text{ cm}^{-2}$ . Following the experiment using Si<sub>n</sub> signals, profiles of powers of the Si excess concentration predicted by TRIDYN have been overlayed onto the ToF-SIMS curves in Figure 3.7 together with the usual Si excess profile. The n-th

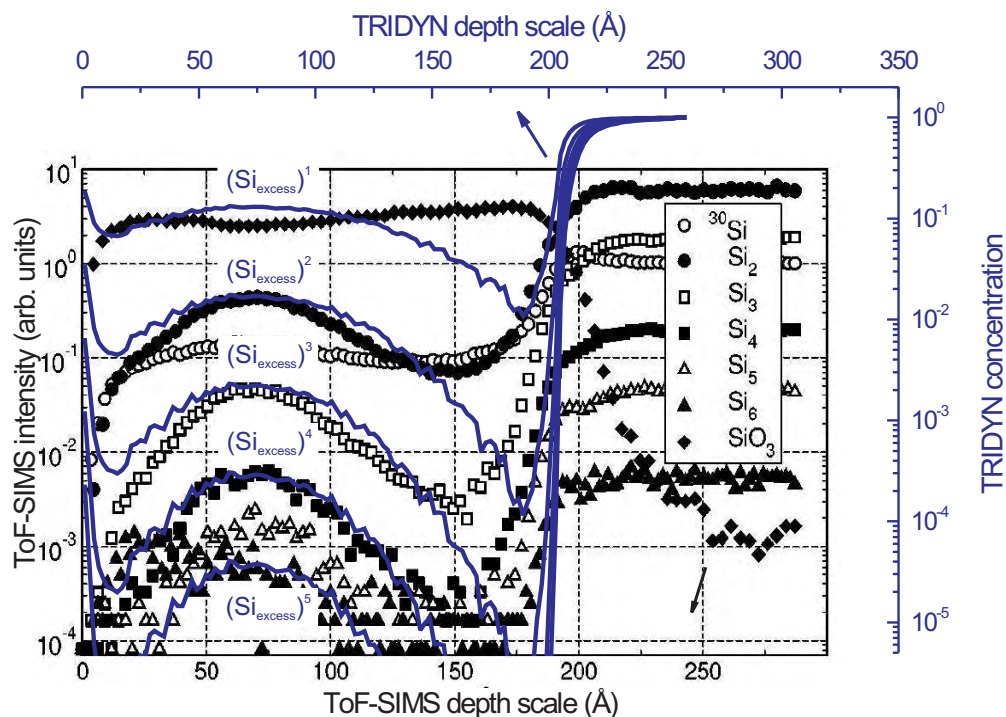


**Figure 3.7.:** Direct comparison between TRIDYN and ToF-SIMS depth profiles. TRIDYN results for 5 keV  $\text{Si}^+$  implantation into 20 nm  $\text{SiO}_2$  to a fluence of  $1 \times 10^{16} \text{ cm}^{-2}$  are overlaid onto the ToF-SIMS profiles of Perego et al. (2003). Additionally to the TRIDYN Si excess depth profile, powers of the predicted Si excess concentration  $(\text{Si}_{\text{excess}})^n$  with  $n = \{2, 3, 4, 5\}$  have been included.

power of the Si excess (monomer) concentration reflects here the likelihood of finding microclusters of 2 to 5 Si atoms (or larger) that have formed without disturbing the initial Si excess distribution<sup>7</sup>. Target swelling by the incorporated material has been accounted for by TRIDYN but was not considered for the ToF-SIMS curves of Perego et al. (2003), which were normalized to the initial oxide thickness of 20 nm. This explains the slightly different depth scales between TRIDYN prediction and ToF-SIMS measurements.

The TRIDYN profiles agree remarkably well with the ToF-SIMS measurements of Figure 3.7 for powers from 2 to 4 (or  $\text{Si}_4$  clusters). Strikingly, not only the profiles themselves fit well but also the ratio of the peak concentrations agrees exceptionally well with experimental values without the need of any additional adjusting sensitivity factors. This is remarkable since ToF-SIMS measurements are known to exhibit matrix effects, leading to non-linear ToF-SIMS intensities in many cases. Here, TRIDYN calculations have proven to be well-suited in order to predict Si excess profiles quantitatively.

### 3.3. Tailoring the Si excess depth profile

TRIDYN calculations provide efficient means to study the influence of the implantation parameters on the Si excess profile in the  $\text{SiO}_2$  layer without the need of excessive experiments.

<sup>7</sup>By taking powers of the Si excess concentrations to approximate the concentrations of  $\text{Si}_n$  clusters in the as-implanted  $\text{SiO}_2$ , implicitly an (equilibrium) reaction constant of  $K_c = 1$  has been assumed for the clustering reaction  $\text{Si}_n + \text{Si} \rightleftharpoons \text{Si}_{n+1}$ .

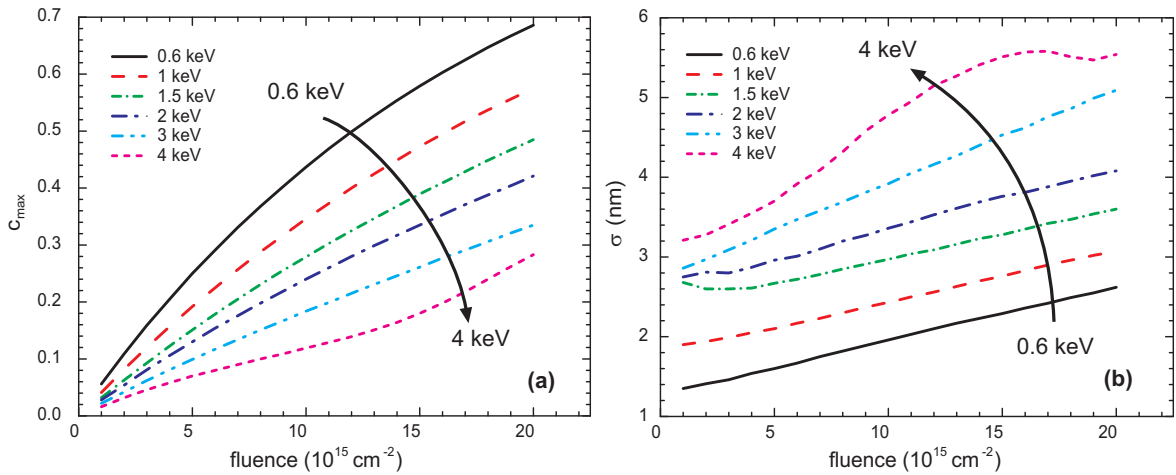


**Figure 3.8.:** (a) Height  $c_{max}$  and (b) width  $\sigma$  of the Gaussian peak fitted to TRIDYN Si excess depth profiles for  $\text{Si}^+$  energies between 0.6 and 5 keV.

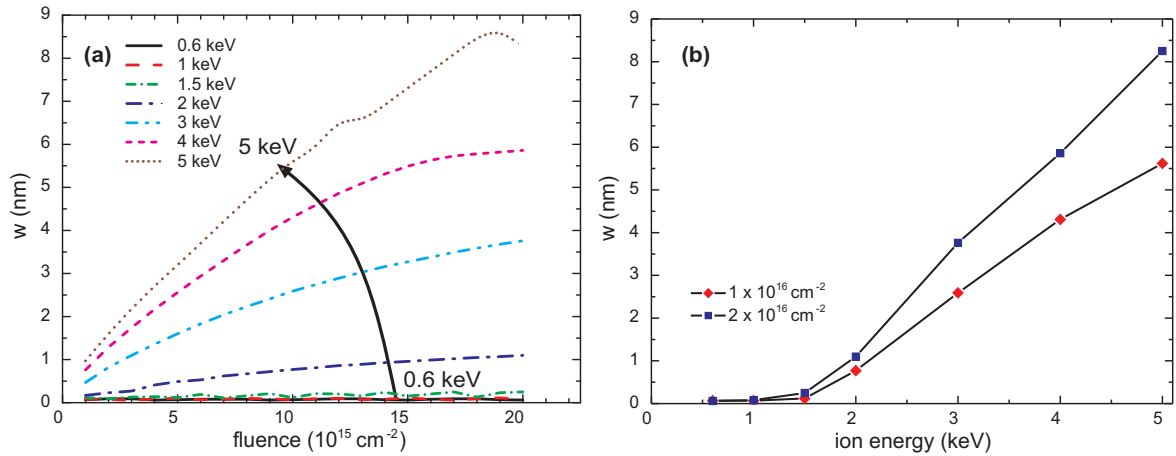


**Figure 3.9.:** Width of the ion beam mixed Si/SiO<sub>2</sub> interface depending on the ion fluence (a) and the ion energy (b).

With the profile approximation by equation (3.8) the impact of the ion energy, ion fluence and oxide thickness on the Si excess profile can be quantified by few parameters. In the following, the fitting of (3.8) to TRIDYN data is performed by a least square algorithm using a subspace trust region method described by Coleman and Li (1996).

### 3.3.1. Influence of the ion energy

TRIDYN calculations for  $\text{Si}^+$  implantations at ion energies ranging from 0.6 and 5 keV and fluences up to  $2 \times 10^{16} \text{ cm}^{-2}$  were fitted to (3.8). Figure 3.8 displays the evolution of the width  $\sigma$  and the maximum concentration  $c_{max}$  of the Gaussian Si excess peak at increasing ion fluences. As expected, both parameters rise with higher ion fluence due to the addition of Si to the SiO<sub>2</sub>. In contrast to low fluence implantations, the peak concentration  $c_{max}$  does *not* grow linearly with ion fluence, which is a result of the target swelling.

At higher energies, ions penetrate deeper into the target and the location of Gaussian peak

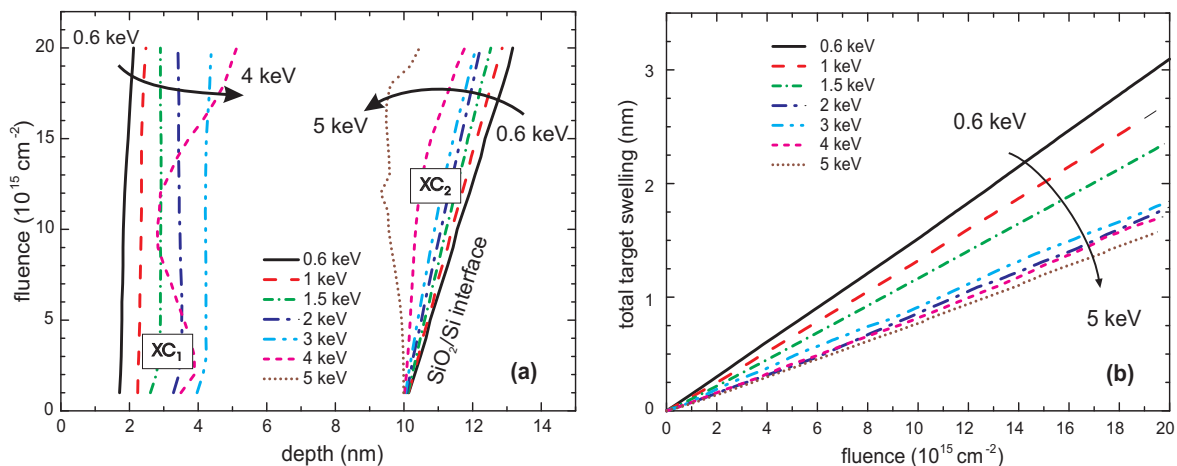


**Figure 3.10.:** (a) Location of the Gaussian peak  $x_{c1}$  and the locus  $x_{c2}$  of  $c_{Si\ excess} = 0.5$  of the broadened interface. (b) Total target swelling of the implanted sample.

$x_{c1}$  shifts independently from the ion fluence as shown in Figure 3.10(a). Simultaneously, range straggling increases leading to a broader Gaussian peak with lower peak concentration (Figure 3.8(b)). The Gaussian peak becomes ill-defined when ion beam mixing is dominating. At 5 keV, no separate Gaussian peak could be identified, hence, this energy is omitted in Figure 3.8. Moreover, ion beam mixing leads to smearing out of the initially sharp concentration profile at the SiO<sub>2</sub>/Si interface as shown above in Figure 3.5. The width  $w$  of this ion beam broadened interface is measured according to equation (3.9) and plotted in Figure 3.9. It increases with ion energy and fluence for ion energies above 2 keV. This threshold behavior becomes apparent in Figure 3.9(b). Ion beam mixing not only broadens the interface but also shifts its location defined by the locus  $x_{c2}$  of  $c_{Si\ excess} = 0.5$  and displayed in Figure 3.10(a).

A second factor influencing  $x_{c2}$  is the swelling of the SiO<sub>2</sub> layer due to incorporated Si ions. (i) The *swelling of the SiO<sub>2</sub> layer* indicated in Figure 3.10 by the location of  $x_{c2}$  is affected only by those Si<sup>+</sup> ions that come to rest within the SiO<sub>2</sub>. It is reduced by surface sputtering and additionally affected by ion beam mixing, which redistributes Si from the substrate into the oxide. In this context, also the definition of the (ion beam mixed) Si/SiO<sub>2</sub> interface becomes ambiguous. Here, the interface is defined as the locus of  $c_{Si\ excess} = 0.5$ . However, it reconfigures during the phase separation process and its location is determined by the redistribution kinetics of the Si and O atoms in SiO<sub>2</sub> and Si, respectively.

(ii) On the other hand, the *total target swelling* is defined much clearer as the net change in the substrate thickness that reflects the balance between *sputtering* and *swelling* due to the incorporated ions. It is not clear where the swelling occurs, i.e. if an implanted Si ion contributes to the SiO<sub>2</sub> or the Si substrate. For the current conditions, the total swelling is given in Figure 3.10.

### 3.3.2. Influence of the SiO<sub>2</sub> thickness

Changing the SiO<sub>2</sub> thickness (rather than increasing the ion energy) provides an other degree of freedom and allows to move the position the Si excess profile closer to the Si/SiO<sub>2</sub> interface. At 1 keV energy, ion beam mixing of the Si/SiO<sub>2</sub> interface is not effective even if the recoils cascade reach the interface. It can be expected that NCs, which form during

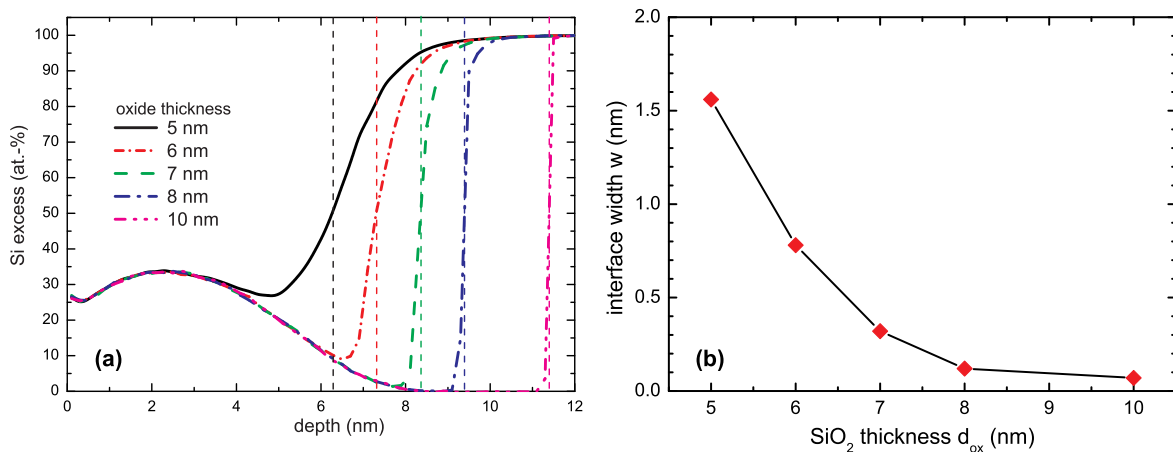


**Figure 3.11.:** (a) TRIDYN calculations of Si excess depth profiles for 1 keV Si<sup>+</sup> implantation at a fluence of  $1 \times 10^{16} \text{ cm}^{-2}$  into 5...10 nm thick oxides. (b) Interface width  $w$  according to (3.8) for different oxide thicknesses.

the subsequent phase separation stage, will be positioned closer to the interface and still remain sharply localized. Figure 3.11(a) shows TRIDYN calculations for a SiO<sub>2</sub> thickness of 5...10 nm. Obviously, the Gaussian Si excess peak is not affected by the SiO<sub>2</sub> thickness. The peak concentration  $c_{max}$  and position  $x_{c2}$  remain constant. Ion Beam mixing is weak (cp. Figure 3.11b). Only for oxides thinner than 6 nm the Si/SiO<sub>2</sub> interface is broadened considerably.

### 3.4. Summary

With low energy Si<sup>+</sup> implantation, several possibilities exist to tailor the Si excess profile created in thin SiO<sub>2</sub> layers. The implantation parameters provide the major element to control the formation of Si NCs in the later stage of Si phase separation from the SiO<sub>2</sub> upon annealing.

**ion fluence:** With a Si<sup>+</sup> fluence between  $1 \times 10^{15} \text{ cm}^{-2}$  and  $2 \times 10^{16} \text{ cm}^{-2}$  the amount of Si excess introduced into the gate oxide can be changed between a few atomic percent up to over 50 at.-%. This will certainly affect size, density and shape of the Si precipitates that are formed during the phase separation stage. As a side affect, the ion fluence has a direct impact on the gate oxide thickness due to swelling.

**ion energy:** Changing the ion energy at which Si<sup>+</sup> is implanted into the gate oxide gives some control over the location of Si excess peak maximum in the SiO<sub>2</sub>. However, at the same time the implantation profile broadens for higher energies. For a 10 nm thick SiO<sub>2</sub>, ion beam mixing of the Si/SiO<sub>2</sub> interface sets in for energies above 2 keV and changes the profile completely. Its impact of the NC formation is to be clarified.

**oxide thickness:** Reducing the SiO<sub>2</sub> thickness at constant ion energy, e.g. 1 keV, brings the Si excess peak closer to the S/SiO<sub>2</sub> interface. Ion beam mixing remains weak at this energy.

In summary, Si excess in the SiO<sub>2</sub> can be achieved (i) by *ion implantation* which directly introduces Si into the SiO<sub>2</sub> and (ii) by *ion irradiation* that exploits the interface mixing by recoils without introducing additional Si atoms in this depth region.

## References

- H. Bach. Determination of bond energy of silica glass by means of ion sputtering investigations. *Nuclear Instruments and Methods*, 84:4–12, 1970.
- H. Bach, I. Kitzmann, and H. Schröder. Sputtering yields and specific energy losses of Ar<sup>+</sup> ions with energies from 5 to 30 keV at SiO<sub>2</sub>. *Radiation Effects*, 21:31–36, 1974.
- M. W. Chase. *NIST-JANAF Thermochemical Tables*, volume 9. Journal of Physical and Chemical Reference Data, 4 edition, 1998.
- T. Coleman and Y. Li. An interior, trust region approach for nonlinear minimization subject to bounds. *SIAM Journal on Optimization*, 6:418–445, 1996.
- R. Kelly. On the problem of whether mass or chemical bonding is more important to bombardment-induced compositional changes in alloys and oxides. *Surf. Sci.*, 100:85–107, 1980.
- W. Möller. Ion mixing and recoil implantation simulations by means of TRIDYN. *Nuclear Instruments and Methods in Physics Research B*, 7/8:645–649, 1985.
- W. Möller. A computer study of the collisional mixing of Pt in Si. *Nuclear Instruments and Methods in Physics Research B*, 15:688–691, 1986.
- W. Möller and W. Eckstein. TRIDYN - A TRIM simulation code including dynamic composition changes. *Nuclear Instruments and Methods in Physics Research B*, 2:814–818, 1984.
- W. Möller and M. Posselt. TRIDYN.FZR user manual. Wissenschaftlich-Technische Berichte FZR-317, Forschungszentrum Rossendorf, Apr. 2001. URL <http://www.fz-rossendorf.de/FWI/FWIT/tridyn.htm>.
- M. Perego, S. Ferrari, S. Spiga, E. Bonera, M. Fanciulli, and V. Soncini. Time of flight secondary ion mass spectrometry study of silicon nanoclusters embedded in thin silicon oxide layers. *Applied Physics Letters*, 82(1):121–123, 2003.
- A. Rizzo, M. Alvisi, F. Sarto, S. Scaglione, and L. Vasanelli. The influence of ion mass and energy on the composition of IBAD oxide films. *Surface and Coatings Technology*, 108-109:297–302, 1998.
- P. Sigmund. Theory of sputtering. I. Sputtering yields of amorphous and polycrystalline targets. *Physical Review*, 184(2):383–416, 1969.
- P. Sigmund and A. Gras-Marti. Theoretical aspects of atomic mixing by ion beams. *Nuclear Instruments and Methods*, 182/183:25, 1981.
- J. F. Ziegler. The stopping and range of ions in matter. <http://www.srim.org>, 1998. version 4.

## Chapter 4.

# Modeling of Phase Separation by Kinetic Monte Carlo Simulations

Modeling phase separation requires a certain degree of approximation in order to treat systems at realistic sizes and to bridge the involved time scales. A sequence of different levels of abstraction can be constructed for simulation approaches starting with continuum methods at its highest level

**Reaction-diffusion equations** have been applied e.g. to predict OSTWALD ripening of NCs in nonhomogeneous situations (Reiß and Heinig, 1994; Strobel et al., 2001; Voorhees and Glicksman, 1984a,b). Especially the long term evolution can efficiently be modeled by continuum approaches. An adequate description of nucleation and coalescence is however beyond the capabilities of this framework. For studies on OSTWALD ripening, an *a priori distribution* of nuclei has to be assumed. Spinodal decomposition is beyond its scope.

**Phase field methods** describe the time evolution of an order parameter (field) by partial differential equations. Spinodal decomposition can be covered as well as nucleation (Cahn, 1961; Cahn and Hilliard, 1958, 1959a,b; Rogers and Desai, 1989), which requires the introduction of fluctuations by an additional noise term in the otherwise deterministic system (Binder and Fratzl, 2001; Cook, 1970).

**Kinetic Monte Carlo simulations** utilize statistical techniques to approximate physical observables that cannot be computed efficiently for large systems (Binder and Heermann, 1992; Metropolis et al., 1953; Newman and Barkema, 1999). By means of MC methods, the vast degrees of freedom, which do not lead to considerable changes in the system are reduced while at the same time the atomistic nature of the relevant processes is kept in the calculations. In that sense, KMC methods provides an atomistic extension of continuum reaction-diffusion models using an effective medium approach. Phase separation studies using KMC methods are able to cover nucleation, spinodal decomposition, coalescence and OSTWALD ripening (Müller et al., 2002a; Strobel et al., 2001).

**Classical Molecular Dynamics (MD) simulations** solve the Newtonian equations of motion for a set of interacting particles and a given interaction potential. Depending on the accuracy needed and the size of the model system, interaction potentials can range from empirical to ab-initio based potentials. Large systems of several thousand of interacting particles can be treated in great detail. Despite of these advantages, the availability of reliable interaction potentials is one of the main detractors to an



application of MD calculations in glassy materials as, e.g. SiO<sub>2</sub>. In addition, the time scale that can be spanned by MD is rather limited. MD studies are restricted to the early stages of phase separation, e.g. to study diffusion and nucleation.

**Time dependent *ab-initio* methods** apply first-principle quantum mechanical calculations to derive the time evolution of an usually small system of interacting particles. Electronic degrees of freedom are naturally taken into account well beyond the BORN-OPPENHEIMER approximation. *Ab-initio* methods are ideally suited to study defect configurations and to determine (semi-)classical interaction potentials for MD and KMC calculations. Migration energies and activation barriers can be extracted from *ab-initio* calculations but rely on a properly chosen reaction pathway. Phase separation in general remains out of scope of current *ab-initio* methods due to the excessive computation time (Ohno et al., 1999).

Calculations applying first-principle methods are still limited to a few thousand particles, and for all practical purposes, to systems of nanometer size at most. MD simulations allow then for much larger systems but with a limited simulation time scale in the order of few nanoseconds. To perform thermodynamic calculations, i.e. to study phase separation, one needs to treat large systems on a far-larger time scale. For such calculations, KMC simulations are more appropriate and will be applied throughout this work.

## 4.1. Si Mass Transport in SiO<sub>2</sub>

Diffusion is the predominant component of the phase separation process and needs to be described adequately. For that purpose, literature data on Si diffusion in SiO<sub>2</sub> are reviewed. It has to be noted that despite of the prominent role of SiO<sub>2</sub> in CMOS technology, Si (or in general defect) diffusion in SiO<sub>2</sub> in its microscopic dynamics is still hardly understood.

To develop a quantitative MC model of Si phase separation from SiO<sub>2</sub>, it is important (i) to identify the mobile Si-rich oxide defect that contributes to phase separation<sup>1</sup> and (ii) to determine its diffusional kinetics.

### 4.1.1. Si self-diffusion in SiO<sub>2</sub>– Experimental Data

Several experimental studies on Si self-diffusion in vitreous SiO<sub>2</sub> as well as in single crystalline quartz have been published. The extracted diffusivities follow an ARRHENIUS law  $D_{Si} = D_0 e^{-E_A/k_B T}$ , whose parameters  $D_0$  and the activation energy  $E_A$  are listed in Table 4.1. For a better comparison, Si self-diffusion coefficients calculated from the data of Table 4.1 for  $T = 1000$  °C are displayed in Figure 4.1. Differences of more than 15 orders of magnitude become apparent, which cannot be attributed to experimental errors. Rather a systematic origin is expected that might result from different microscopic dynamics.

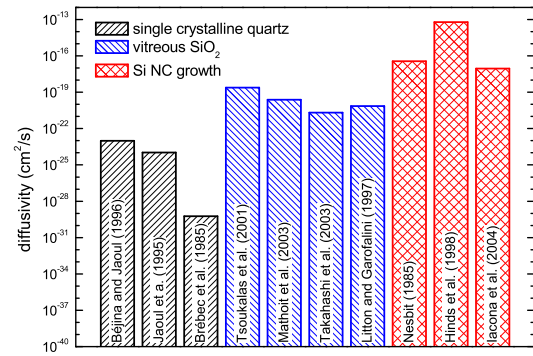
The References of Table 4.1 were divided into three different groups depending on the specific material system used to extract Si diffusivities. Early experiments of Brébec et al. (1980) and from others authors in the first group of Table 4.1 have used isotopically enriched

---

<sup>1</sup>Which is up to now assumed to be Si interstitials.



**Figure 4.1.:** Si self-diffusivity in SiO<sub>2</sub> estimated by different authors for T = 1000 °C. The values scatter over more than 15 orders of magnitude.



SiO<sub>2</sub> (or Si) on  $\beta$ -quartz. All other studies report self-diffusivity values for vitreous SiO<sub>2</sub>, which are considerably higher than for quartz.

The authors of the second group of Table 4.1 obtain activation energies around 5 eV for different experimental conditions. Activation energies determined by Mathiot et al. (2003) for equilibrium conditions, i.e. in undamaged SiO<sub>2</sub> without Si excess, deviate little from values obtained by Tsoukalas et al. (2001) using <sup>30</sup>Si<sup>+</sup> tracer atoms introduced by ion implantation. The activation energy is also confirmed in MD studies of Litton and Garofalini (1997) and Kob and Binder (1999). Still, the pre-exponential factor  $D_0$  varies over more than one order of magnitude. Additionally, the work of Fukatsu et al. (2003) revealed a dependence of the Si self-diffusivity on the specific location of the interface between grown SiO<sub>2</sub> and the Si substrate, which was not expected. The authors have shown that Si self-diffusion is enhanced if the SiO<sub>2</sub>/Si interface is located closer to the region of interest where the Si

reference	comment	diffusion coefficient	
		$D_0$ (cm <sup>2</sup> /s)	$E_A$ (eV)
Béjina and Jaoul (1996)	<sup>30</sup> Si on $\beta$ -quartz	$2.9 \times 10^7$	7.7
Jaoul et al. (1995)	<sup>30</sup> SiO <sub>2</sub> on $\beta$ -quartz	$10^{6.1}$	7.6
Brébec et al. (1980)	<sup>30</sup> SiO <sub>2</sub> on $\beta$ -quartz	$3.28 \times 10^{-6}$	6
Tsoukalas et al. (2001)	<sup>30</sup> Si <sup>+</sup> implantation in <sup>28</sup> SiO <sub>2</sub>	1.378	4.74
Mathiot et al. (2003)	<sup>nat</sup> SiO <sub>2</sub> on <sup>28</sup> SiO <sub>2</sub>	33.2	5.34
Takahashi et al. (2003)	<sup>nat</sup> SiO <sub>2</sub> on <sup>28</sup> SiO <sub>2</sub>	0.8	5.2
Litton and Garofalini (1997)	molecular dynamics	0.26	4.94
Kob and Binder (1999)	molecular dynamics		5.18
Nesbit (1985)	growth of Si NCs	$1.2 \times 10^{-9}$	1.9
Hinds et al. (1998)	SiO <sub>x</sub> decomposition	$5.5 \times 10^{-9}$	1.25
Iacona et al. (2004)	growth of Si NCs	$5 \times 10^{-13}$	1.2
	modified growth model		2.1

**Table 4.1.:** Si self-diffusion coefficients for SiO<sub>2</sub>

diffusion is measured. This is a strong indication that Si self-diffusion is influenced by an additional mechanisms, which was pointed out by Fukatsu et al. (2003).

In addition, it has to be noted that Si isotopes were used as tracer atoms in all studies listed in the first two groups of Table 4.1. There *isotopic exchange* between the tracer atoms, e.g.  $^{30}\text{Si}$ , and Si of the  $\text{SiO}_2$  matrix cannot be excluded. Since all Si isotopes are chemically identical there is no reason why, e.g. implanted  $^{30}\text{Si}$  atoms should diffuse over larger length scales without performing isotope exchange processes with Si atoms of the  $\text{SiO}_2$  matrix. In that sense it can be argued that studies using Si isotopes underestimate the diffusion of *Si excess in  $\text{SiO}_2$* , which is not linked to specific Si isotopes but to an overall Si mass transport. Si excess has specifically been created by  $^{30}\text{Si}^+$  implantation into  $\text{SiO}_2$  in the study of Tsoukalas et al. (2001). But their measurements delivers an activation energy that is not strongly reduced, as it would be expected for freely diffusing Si atoms. The activation energy of diffusion being the sum of formation and migration energy should reduce to the migration energy term only unless quick isotope exchange processes take place.

The authors in the last group of studies listed in Table 4.1 have taken a different approach. An effective diffusion coefficient for Si mass transport has been extracted from the experimental growth laws for Si NCs (Iacona et al., 2004; Nesbit, 1985) and the decomposition of  $\text{SiO}_x$  films (Hinds et al., 1998). All three studies report a much higher diffusion coefficient with activation energies between 1 and 2 eV. Still the data for the diffusivity scatter over 3 orders of magnitude (Figure 4.1), which partially can be attributed to different experimental conditions, problems in determining Si NCs sizes accurately over a large temperature range and different simplifications of the implied growth models.

#### 4.1.2. Mass transport of Si excess in $\text{SiO}_2$ – What is the mobile defect?

Experimental studies on Si self-diffusion in  $\text{SiO}_2$  revealed a strong scatter in the diffusivity data pointing towards additional mechanisms that influence the Si self-diffusion. Still, the microscopic origin of Si (excess) mass transport taking place during phase separation of Si from  $\text{SiO}_2$  remains unclear. Possible defects carrying Si excess are

**Si interstitials:** Theoretical calculations of Mousseau et al. (2000) have shown that the discussion of the formation and migration of isolated point defects (interstitials and vacancies in a classical sense) in vitreous  $\text{SiO}_2$  might be misleading. Rather, single-dangling-bond diffusion mechanisms are observed, which are jumps of dangling bonds from one atom to the other. It is unlikely that the diffusion of isolated Si interstitials trough the  $\text{SiO}_2$  network represents a major contribution to Si mass transport during NC growth.

**SiO molecules:** SiO molecules generated at the  $\text{SiO}_2/\text{Si}$  interface (Celler and Trimble, 1989) are believed to enhance the Si self-diffusivity in  $\text{SiO}_2$  by kick-out reactions with network Si. Uematsu et al. (2004) have used this hypothesis to successfully describe the experimental findings of Fukatsu et al. (2003), showing that a near  $\text{SiO}_2/\text{Si}$  interface enhances the Si self-diffusivity in  $\text{SiO}_2$ .

**Oxygen vacancies:** The most common one of the oxygen deficient defects, i.e. defects that carry Si excess in the SiO<sub>2</sub> (quartz or silica), is the *oxygen vacancy*. In this configuration, an oxygen atom has been removed from the silica networked leaving a Si-Si bond behind. *Ab-initio* calculations determined small energies of formation for O-vacancies at the SiO<sub>2</sub>/Si interface (Blöchl, 2000; Capron et al., 2002). Much higher energies are required for a formation in the bulk of the SiO<sub>2</sub>. Migration energies are still uncertain, but first studies revealed low values between 1.7 and 1.9 eV for charged configurations (Song et al., 2001). In that sense, migrating O-vacancies might as well induce Si diffusion due to long-ranged network distortions (Sulimov et al., 2002).

Thus, the use of currently available diffusivity data for the direct calibration of KMC simulations would introduce severe uncertainties. Therefore, an approach using relative time and temperature scales is chosen and will be discussed below.

## 4.2. The kinetic lattice Monte Carlo method

Here, KMC simulations of Si phase separation rely on a simplified picture of the atomistic process and their kinetics occurring during phase separation. The model reduces the description to the dominant components that are kinetically available during the Si phase separation from SiO<sub>2</sub>, i.e. Si impurity diffusion, clustering and coarsening is treated independently of the SiO<sub>2</sub> matrix which is chemically stable. This approach is justified since the ion damaged SiO<sub>2</sub> network is expected to reconfigure in the very early stage of annealing leaving only Si excess behind, which is then available for phase separation. Consequently, Si phase separation is studied in an effective medium (the SiO<sub>2</sub> host matrix) on an atomistic level using a 3D ISING model of effective nearest-neighbor interactions among Si impurities.

**Simulation lattice:** Phase separation is studied using a *lattice gas model*. Hence, the diffusion and clustering of Si atoms is restricted to sites of an underlying artificial lattice having fcc structure. This lattice represents the SiO<sub>2</sub> matrix, which does not take part actively in the KMC simulation, i.e. represents system's vacuum. It contains only the implanted Si excess whose initial depth profile has been calculated in Chapter 3 using TRIDYN. Accordingly, any influence of oxide defects on the phase separation and therefore on the Si NC formation is neglected. Internal stress in the oxide matrix is not considered for the simulation assuming a sufficient SiO<sub>2</sub> viscosity at typical annealing temperatures of 900 – 1100 °C. The slow Si NCs formation is not expected to be hindered by a rigid SiO<sub>2</sub> matrix.

**Hamiltonian:** The effective interaction of Si atoms exceeding the stoichiometry of SiO<sub>2</sub> is modeled using an ISING Hamiltonian in the *lattice gas* representation

$$H = -J \sum_{\{i<j\}_{nn}} s_i s_j \quad (4.1)$$

with occupation variables  $s_i$  and  $s_j$  taking either the values 1 if the site is occupied or 0 if its empty. The sum is taken over nearest neighbor pairs only. As  $s_i$  is a two state variable, it must

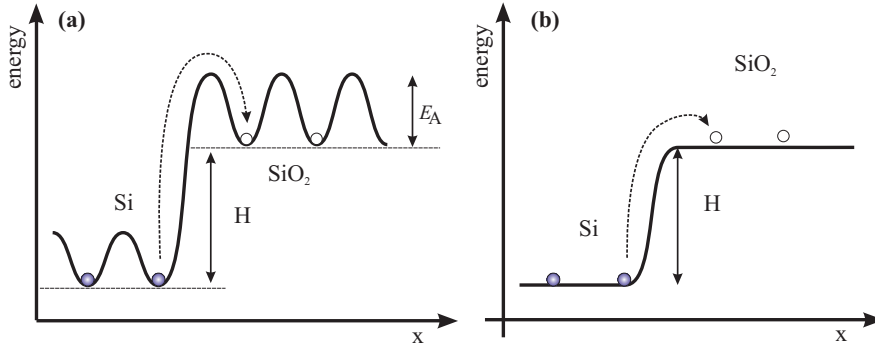


**Figure 4.2.:** KAWASAKI-type of energy barriers (a) for the Si impurity diffusion with activation energy  $E_A$  and binding energy  $\Delta H$  for the detachment of a monomer from the Si. (b) Renormalized energy to allow every diffusional jump attempt to succeed, which also leads to a renormalized time scale.

be possible to map it onto an ISING spin,  $\sigma_i = \pm 1$ . This is achieved by the transformation

$$s_i = \frac{1}{2}(\sigma_i + 1). \quad (4.2)$$

Substituting (4.2) into (4.1) one regains the usual nearest neighbor, spin-1/2 ISING Hamiltonian with the field  $h$  related to the lattice gas occupation

$$H = -\frac{J}{4} \sum_{\{i<j\}_{nm}} \sigma_i \sigma_j - h \sum_i \sigma_i. \quad (4.3)$$

In a bond counting picture, the lattice gas Hamiltonian (4.1) can be rewritten to

$$H = -\frac{J}{2} \sum_{i, s_i=1} n_i = -nJ/2, \quad (4.4)$$

where the summation is taken over occupied sites only and  $n_i$  is the number of bonds of the  $i$ -th atoms to neighboring ones. The total number of bonds is denoted by  $n$  and the factor  $1/2$  corrects for the double counting of each bond. The binding energy of a bulk atom is then  $E_b = -\xi J/2$ , where  $\xi = 12$  is the fcc coordination number.

**Dynamics:** Diffusing Si atoms not only have to overcome the binding energy, i.e. to break bonds, but also have to surpass a kinetic barrier  $E_A$  – the activation energy for diffusion – if no bond must be broken during a diffusional jump of a Si impurity atom. In this simplified model the diffusion of Si in the SiO<sub>2</sub> as well as the adatom diffusion on Si/SiO<sub>2</sub> interfaces is controlled by the same activation energy  $E_A$  (Figure 4.2(a)). This particular form of the energy barriers is sometimes also referred to as KAWASAKI-type energy barriers. This choice together with local spin (particle) exchange dynamics that conserves the order parameter leads to the Kawasaki MC algorithm (Kawasaki, 1966) that to a large extent is identical to the earlier developed METROPOLIS algorithm (Metropolis et al., 1953) except of the local dynamics.

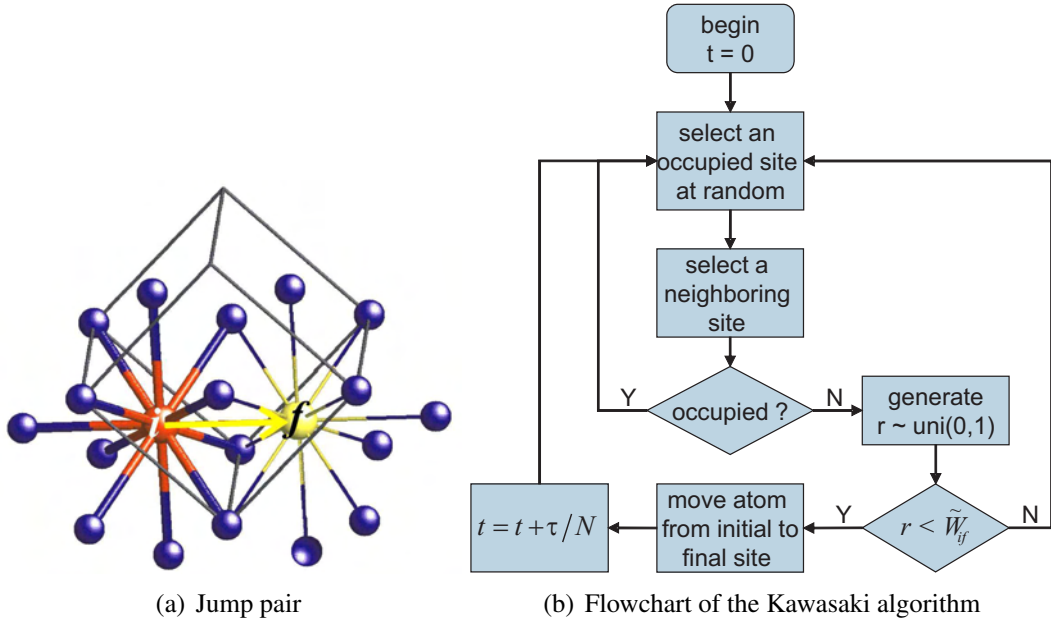


**Figure 4.3.:** (a) Nearest neighbor shell around a *jump pair* in the  $\text{fcc}$  lattice, i.e. the initial site  $i$  and final site  $f$  and all neighboring atoms to which bonds could exist. Adjusted from NEON (2002). (b) Flowchart of the Kawasaki algorithm.

The probability rate of a nearest neighbor jump of a Si atom from an occupied site to an empty site (Figure 4.3(a)) is given in the KAWASAKI algorithm by

$$W_{if} = \begin{cases} \tau_0^{-1} \exp\{-E_A \beta\}, & n_f \geq n_i, \\ \tau_0^{-1} \exp\{-[E_A + (n_i - n_f)J] \beta\}, & n_f < n_i, \end{cases} \quad (4.5)$$

with  $\tau_0^{-1}$  denoting the frequency of jump attempts.  $n_{(i,f)}$  denotes the number of nearest neighbor bonds at the initial  $i$  and the final site  $f$ , respectively.  $\beta = (k_B T)^{-1}$  has its usual meaning.

A common procedure to reduce the simulation time is to rescale the time such that every diffusion attempt is successful, i.e. set  $\tilde{W}_{if} = W_{if}/(\tau_0^{-1} \exp\{-E_A \beta\})$ . This corresponds to a renormalization of the energy as depicted in Figure 4.2(b). With the notation of

$$\varepsilon = J\beta, \quad (4.6)$$

it leads to the dimensionless transition probability

$$\tilde{W}_{if} = \begin{cases} 1, & n_f \geq n_i, \\ \exp\{-(n_i - n_f)\varepsilon\}, & n_f < n_i, \end{cases} \quad (4.7)$$

$$= \min(1, \exp\{-(n_i - n_f)\varepsilon\}), \quad (4.8)$$

where  $\tau = \tau_0 \exp\{E_A \beta\}$  defines the duration of a Monte Carlo step (MCS). Thus, energetically unfavored jumps are nevertheless allowed at a (low) probability following the BOLTZMANN statistics. Note that the METROPOLIS algorithm uses the same acceptance ratio as the

KAWASAKI algorithm, but applies single-spin flips, i.e. particle creation/annihilation, which violate the conservation of the order parameter (total number of particles) in the canonical ensemble.

Having defined the transition probabilities, the KAWASAKI algorithm itself consists of a simple loop depicted in Figure 4.3(b) that is repeated  $N$  times per MCS, where  $N$  is the number of atoms (occupied sites) in the simulation cell.

1. Choose an impurity (Si) at random<sup>2</sup>.
2. Chose a neighboring site at random. (E.g., one out of 12 for an fcc lattice.)
3. Start over if the chosen site is already occupied, the jump attempt is rejected.
4. Calculate the transition probability  $\tilde{W}_{if}$  according to (4.8).
5. Draw a random number uniformly distributed in  $(0, 1)$ .
6. Perform the nearest neighbor jump if the drawn number is smaller than  $\tilde{W}_{if}$ . Otherwise the jump attempt is rejected.

The generated sequence of states (*Markov chain*) starting from an initial far-from-equilibrium situation models the time evolution of the system towards the thermodynamical equilibrium. This specific choice of the Monte Carlo algorithm ensures that (Newman and Barkema, 1999)

- The ensemble of impurity atoms approaches the thermodynamical equilibrium for an infinite number of MCS. The *detailed balance* between monomer attachment and detachment is satisfied.
- The system is *ergodic*, i.e. every atom can (in principle) reach every lattice site<sup>3</sup>.
- The specific dynamics are chosen close to a physically meaningful model of diffusion. The dynamics is local and the order parameter is conserved throughout the simulation.

These constraints, however, are very loose. Many MC rules satisfy them and without further prejudice all are equally admissible. This arbitrariness of the dynamics is important. Some properties of the phase ordering process – e.g., the domain size growth law and the structure factor – have been proposed to be *independent* of the microscopic details of the dynamics, and to depend only on conservation laws, symmetries, dimensionalities, and geometries (Gunton et al., 1983).

Despite of their wide application range, the METROPOLIS as well as the KAWASAKI algorithm suffer from their high rejection ratio especially for stiff systems. At low temperatures, where the majority of events are generally confined to a minority of sites, many trials have to be attempted before a successful event is selected. For these conditions, more efficient algorithms are available (Newman and Barkema, 1999), but many of them use *nonlocal dynamics* that cannot be applied for physically meaningful KMC simulations.

---

<sup>2</sup>Substrate atoms might not actively take place in the simulation, but are used to calculate binding energies of neighboring impurity atoms.

<sup>3</sup>As long as the interaction Hamiltonian remains finite (Newman and Barkema, 1999, chapter 2.2.2).

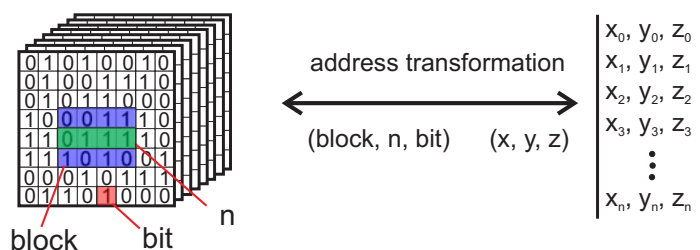


**Figure 4.4.:** Address transformation between the computer memory addresses and cartesian coordinates of the `fcc` lattice. Scheme adapted from NEON (2002).

The acceptance ratio can nevertheless be improved allowing for larger timescales of MC simulation runs. The class of *continuous time* Monte Carlo simulations introduced by Bortz et al. (1974) utilize local exchange dynamics as the KAWASAKI algorithm does but applies a time scale that is no longer constant but varies with sum of all possible transitions. In that manner it can be assured that every jump attempt is accepted. While this technique is in many respects a very elegant solution to the problem of simulating a system at low temperatures, i.e. to eliminate the large amount of unsuccessful jump attempts, it does suffer from one obvious drawback. The transition probabilities have to be calculated *a priori* for every possible transition and is to be updated after one has been performed. In that sense, continuous time MC algorithms are much more costly in computation time per MC move than the KAWASAKI algorithm. (Newman and Barkema, 1999, chapter 5.2.1) estimated that an average transition using a continuous time algorithm takes approximately as long as 40 KAWASAKI transitions. Thus, an advantage over the KAWASAKI algorithm can only be achieved if their average acceptance ratio is below 1/40.

Another route of optimization, which has been followed here, is the efficient implementation of the KAWASAKI algorithm using single bit algebra.

**Implementation:** Occupation variables of individual lattice sites can take only two distinct states (0 and 1). Thus, it is tempting to use single bits to store occupation states and to apply single bit algebra at system level for the manipulation of these states. The KAWASAKI algorithm has been shown to be very efficient if implemented on the basis of low-level bit manipulations (Heinig, 1994). It allows for the simulation of realistic systems with large simulation cells over long time scales (Antons, 1998; Michely et al., 2001; Strobel, 1999).

The KMC code used in this work has been derived from the bit-level cellular automaton KMC codes developed by Heinig (1994), which has been further extended by Strobel (1999). It uses a double bookkeeping strategy in bit and coordinate space to keep efficiently track of the positions of the Si atoms and their nearest neighbors such that excessive address-coordinate transformations can be avoided (Figure 4.4). Energy and therefore jump probability calculations are simplified by the use of a lookup table for all possible nearest neighbor configuration during the simulation run. The lookup table contains jump probabilities for all  $2^{18} = 262144$  configurations possible in the `fcc` lattice, which are calculated in advance to the simulation run. Using the full nearest neighbor configuration space gives the possibility to use a much more flexible cellular automaton model containing the standard ISING model as a special case. More complex interactions can also be treated in this

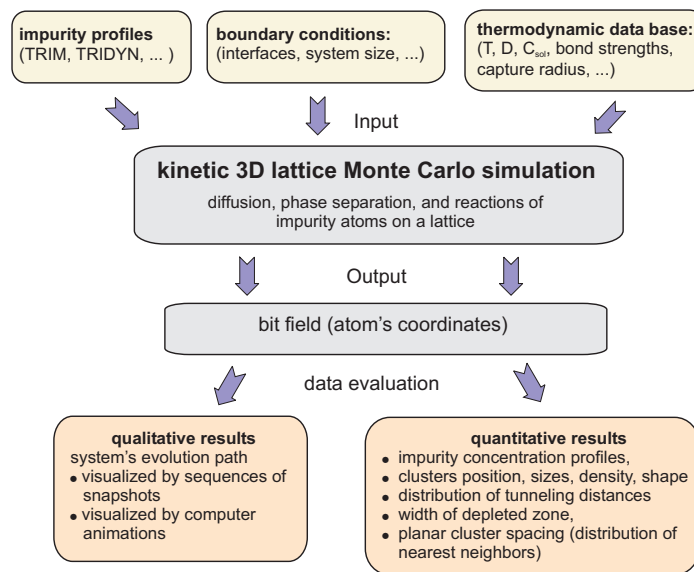


**Figure 4.5.:** Scheme of the kinetic Monte Carlo program package

framework at the same simulation speed. Antons (1998); Mantl et al. (1998) have used this approach to employ an embedded atom model for the study of  $\text{CoSi}_2$  evolution under local oxidation.

Further details on the specific KMC implementation can be found in Appendix A.

**Intrinsic properties and previous applications:** Strobel et al. (2001) have shown that this KMC model of phase separation reproduces extremely well fundamental relations as, e.g., the GIBBS-THOMSON equation, even for very small NCs. KMC simulations of coarsening in a diluted cluster system lead to a Lifshitz-Slyozov-Wagner size distribution, that is predicted from mean field calculations (Lifshitz and Slyozov, 1961; Wagner, 1961) for diffusion controlled OSTWALD ripening. Beyond the homogeneous case, late stage KMC simulations are one-to-one comparable to (local) mean-field calculations using reaction-diffusion equations which were solved numerically (Reiß and Heinig, 1994; Strobel et al., 2001).

Beyond fundamental studies, the model has been applied in broad application fields which include the formation of Au NCs in  $\text{SiO}_2$  at ion beam synthesis (Strobel et al., 1999b), the formation of core-shell NCs (Strobel et al., 1999a), inverse OSTWALD ripening of NCs at ion irradiation (Heinig et al., 2003; Strobel, 1999), pit coarsening upon ion erosion (Michely et al., 2001, 2002), nanowire formation at ion beam synthesis (Müller et al., 2001) and their Rayleigh instability (Müller et al., 2002b).

#### 4.2.1. Gauging simulation parameters

A necessary prerequisite for KMC simulations is the definition of the free parameters for the specific implantation conditions and the material system. In the present KMC model, these parameters include the lattice constant  $a_l$ , the activation energy for diffusion  $E_A$  and the bond



energy  $J$  between nearest neighbor impurity atoms, which determines the equilibrium solubility at a flat interface. Strobel (1999, chapter 3.5) described in detail the calibration of the length and time scale for given diffusivity and solubility data<sup>4</sup>, which is applied here for the specific system of Si impurities in a SiO<sub>2</sub> matrix. However, the unreliable thermodynamic database requires special measures.

### Length scale and lattice constant of the simulation cell

The basic length scale of the KMC simulation is the lattice constant of the used fcc lattice on which Si atoms diffuse and might precipitate. The SiO<sub>2</sub> is however an amorphous material with no regular structure. Thus, the choice of the lattice constant is to some extent arbitrary as far as the host matrix is concerned. This is not the case for the Si precipitates that will form in the SiO<sub>2</sub> matrix. Their regular lattice structure and more importantly their atomic density determines the lattice constant  $a_l$  of the fcc lattice. With

$$a_l = \sqrt[3]{4N_{Si}^{-1}} = 0.4338 \text{ nm} \quad (4.9)$$

the lattice constant is chosen such that the correct atomic density  $N_{Si} = 4.9 \times 10^{22} \text{ cm}^{-3}$  of bulk Si is obtained within the fcc simulation lattice. Note that  $a_l$  deviates from the Si lattice constant of 0.5431 nm due to the different number of atoms per unit cell which is 4 for the fcc and 2 for the diamond lattice.

The size of the simulation cell is counted in multiples of the lattice constant  $a_l$ , i.e.  $L_i = 2^i a_l$  with  $i = \{x, y, z\}$ . Choosing specifically powers of 2 gives advantages for the implementation of periodic boundary conditions as outlined in section 4.2 and appendix A.

### Time scale, diffusion coefficient and solubility

The diffusion coefficient of particles performing a random walk is given by the EINSTEIN relation

$$D_{latt} = \frac{1}{\xi} \Gamma a_l^2, \quad (4.10)$$

where  $\Gamma = \tau^{-1}$  denotes the jump frequency. Substituting the Arrhenius equation  $D = D_0 \exp\{-E_A \beta\}$  and solving for  $\tau$  gives the duration of a Monte Carlo step

$$\tau = \frac{a_l^2 / \xi}{D_0 \exp\{-E_A \beta\}}, \quad (4.11)$$

which can vary by orders of magnitude due to the temperature dependence of the diffusion coefficient.

The solid *solubility*  $c_\infty$  of impurity atoms at a flat interface is determined in the lattice gas model with Ising type interactions by the nearest-neighbor bond strength  $J$ . Strobel (1999) has shown that the following relation holds

$$c_\infty = c_0 \exp\{-B_{fcc} \varepsilon\} \quad (4.12)$$

<sup>4</sup>A shortened description can also be found in Strobel et al. (2001).

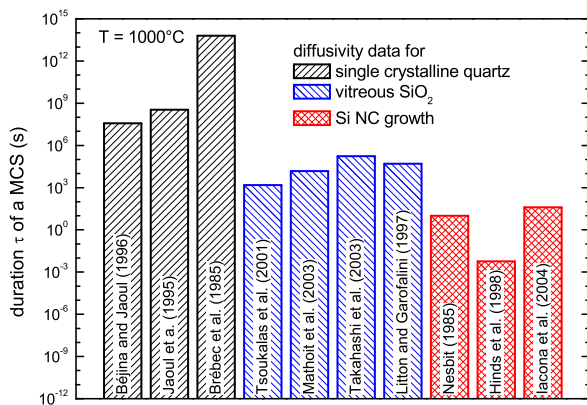


**Figure 4.6.:** Duration  $\tau$  of a MCS step according to (4.11) at  $T = 1000^\circ\text{C}$  for Si in SiO<sub>2</sub> using diffusivity data shown in Figure 4.1.

with the values  $B_{fcc} = 6$  and  $c_0 = 4/a_l^3$  for the  $f_{CC}$  lattice. The solubility and therefore the nearest-neighbor bond strength  $J$  merely calibrates the temperature of the simulation, i.e. the parameter  $\varepsilon = J\beta$  is used to determine jump probabilities according to (4.8).

### Relative time and temperature scale for Si in SiO<sub>2</sub>

The conflicting and uncertain thermodynamic data prevent currently a direct calibration of the time and temperature scale of the KMC model. Obviously, the diffusive Si mass transport by a mobile SiO<sub>2</sub> defect with local Si excess does not necessarily follow the same mechanism than as the <sup>28</sup>SiO<sub>2</sub>/<sup>30</sup>SiO<sub>2</sub> interface broadening, which was analyzed in self-diffusivity studies (Table 4.1). The origin of this discrepancy between diffusive Si mass transport and Si self-diffusivity was strived in the previous section but will not be detailed further as the theoretical predictions of phase separation aim at the reaction pathway of SiO<sub>x</sub> decomposition rather than at a quantitative prediction of annealing time and temperature. Thus, KMC simulations utilize a *relative time scale* – the Monte Carlo steps (MCS) – as well as a *relative temperature*  $\varepsilon$  according to equation (4.6) that allows a posterior recalibration as soon as reliable Si diffusivities and solubilities become available.

Following this philosophy, it also has to be noted that the KMC method in its present form cannot cover the complex microscopic defect dynamics during the phase separation process, which is also not the aim of these simulations. Rather a simple model system is used to study phase separation for realistic Si excess concentrations and geometrical conditions. The underlying  $f_{CC}$  lattice ensures here a nearly isotropic diffusion of Si impurities<sup>5</sup> in the host matrix and therefore comes close to an amorphous material.

### 4.2.2. Analysis of kinetic Monte Carlo results

In many cases KMC simulation results require further data evaluation, which can loosely be divided into two groups. According to Figure 4.5, system's reaction path towards the thermodynamical equilibrium can be evaluated in a qualitative manner, i.e. by visualizing the morphology of the phase separated Si embedded in the oxide matrix. Quantitative results

<sup>5</sup>Per definition, the Si interstitials are considered in the KMC simulation to be the only defect responsible for Si mass transport. Nonetheless, this allows a posterior recalibration as long as the responsible defect is associated with local Si excess.

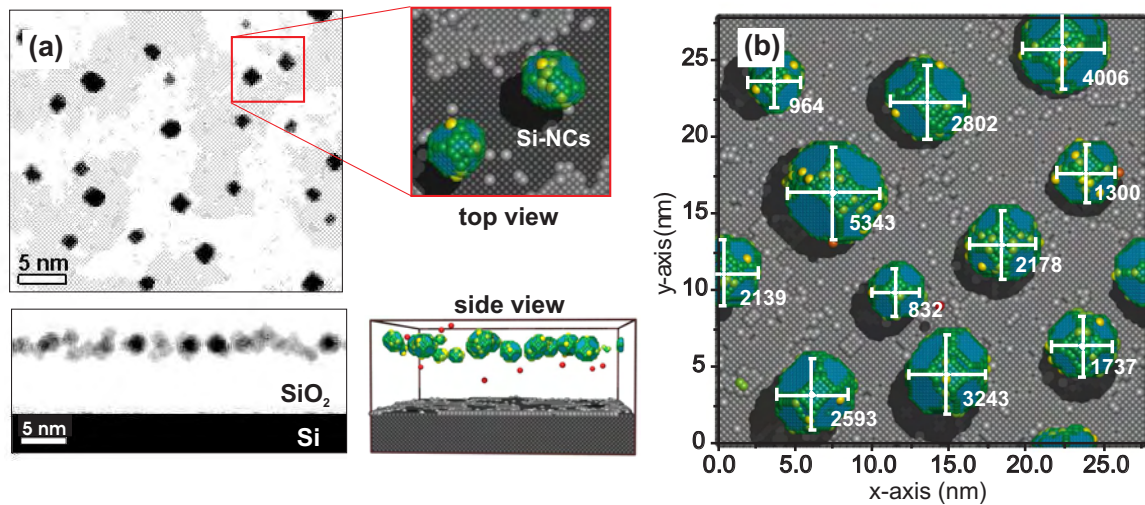


**Figure 4.7.:** (a) Visualization of KMC simulation results in top and side view. On the left hand side, TEM like projections are shown where Si is displayed in black. On the right, the same structure has been rendered by POVray. The color represents the coordination state of the Si atoms. (b) KMC simulation snapshot showing nice agreement between the size of the equilibrated octahedral Si NCs and the calculated cluster radius using equation (4.14). The number of Si atoms per cluster is annotated.

including NC properties as NC size and distribution require a further analysis of the KMC simulation data.

### Qualitative results - Visualizations

Further image processing could yield KMC simulation snapshots that can be directly compared to TEM images (either in cross-section or plane view). Since TEM micrographs represent projections through a thin specimen slab, similar projections are applied to visualize the KMC simulation results. For plane view images (projection perpendicular to the sample (SiO<sub>2</sub>) surface), the number of excess Si atoms in a vertical column below the image pixel at (x,y) is counted. This value determines the gray level of the pixel. The highest number of Si atoms occurring in such a column defines black, whereas white color corresponds to no Si excess in the SiO<sub>2</sub>. Si atoms in the underlying Si substrate are not considered for plane view images, but are displayed in cross section view. For these images a similar procedure is applied, i.e. the summation is taken over horizontal columns instead being parallel to the SiO<sub>2</sub> surface. An example of the used image processing is shown in Figure 4.7(a) with the plane view on top of the left hand side and the cross section view below.

Additionally, ray-tracing using the freely available POVray renderer (Povray, 2004) has been applied for further visualization, where each individual Si excess atom is modeled by a solid sphere. Its color is used to indicate the coordinate state of the atom. Red corresponds to the highest energy state, no bond to neighboring Si excess atoms exist. The opposite situation – the atom is fully coordinated – is indicated by a deep blue color. Si atoms belonging to the Si substrate are shown in gray only, where Si atoms that have condensed onto the Si substrate in the course of the simulation are displayed in lighter gray.

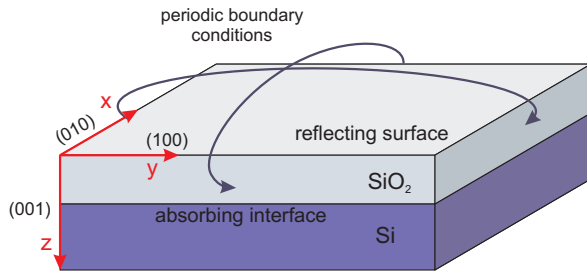


**Figure 4.8.:** Sketch of the simulation cell applied in low energy KMC simulations. Its dimension varies between  $28 \times 28 \times 14 \text{ nm}^3$  and  $56 \times 56 \times 28 \text{ nm}^3$ .

### Quantitative results - NC properties

To assess NC properties, the simulation lattice is scanned at intermediate times and clusters of interconnected atoms (NCs) are gathered in a recursive manner. As a result, Si excess is categorized in clusters starting from monomers, dimers over trimers to larger agglomerates. In the present work, only clusters with more than 6 atoms are taken into account and their properties are recorded. The position of a single cluster is defined by its center of mass, i.e. the average taken over the coordinates of all  $n$  atoms belonging to that cluster

$$\vec{r} = \sum_{i=1}^n \vec{r}_i. \quad (4.13)$$

Its size is approximated by the radius  $R$  of a sphere equal volume (Strobel, 1999, chapter 3.4)

$$\frac{4\pi}{3}R^3 = nV_a = n\frac{a_l^3}{4}, \quad n \gg 1, \quad (4.14)$$

where  $V_a$  denotes the atomic volume  $a_l^3/4$ . This approach is certainly oversimplified for very small clusters as well as for Si structures that deviate from a spherical shape. Rather the number of atoms belonging to a cluster should be used in these cases<sup>6</sup>. However, this method provides consistent results for Si NCs with nearly spherical shape. The sizes of the faceted (octahedral) clusters shown in Figure 4.7(b) agree nicely with the diameters calculated according to (4.14).

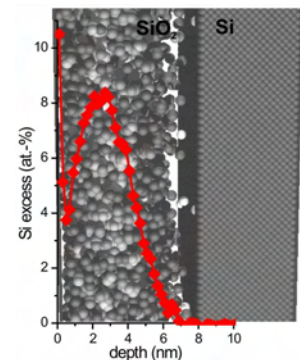
### 4.2.3. Simulation conditions for low energy IBS in thin gate oxides

The initial profile of Si excess, which is the starting condition of the KMC simulations, is taken from the TRIDYN predictions of the preceding Chapter. Si monomers are randomly placed on lattice sites of the simulation cell (the SiO<sub>2</sub> host) with a probability chosen according to the TRIDYN depth profile of Si excess. The lattice parameter of the simulation matrix was chosen according to section 4.1 to yield a density equal to bulk Si. This ensures that the volume fraction of the precipitates is correctly resembled, which is especially important for studies of cluster coalescence in the next Chapter.

The surface of the simulation cell, depicted schematically in Figure 4.8, spans in x-y direction. The z-axis points into the depth with the origin at surface. The simulation cell

<sup>6</sup>The shape parameter  $\delta$  will be used in section 5.2.1 to quantify the spheroidicity of the precipitates.

**Figure 4.9.:** The initial Si excess profile is set according to the TRIDYN predictions for the KMC simulations of phase separation. The TRIDYN profile (red) has here been overlaid onto a cross-section snapshot (shown in grayscale) of the initially set atom configuration for an ion fluence of  $2 \times 10^{15} \text{ cm}^{-2}$ .



sizes varies between  $28 \times 28 \times 14 \text{ nm}^3$  and  $56 \times 56 \times 28 \text{ nm}^3$  and therefore allows realistic simulations with a sufficiently large ensemble of NCs. Periodic boundary conditions are applied in the x-y plane emulating a semi-infinite layer. The  $\text{SiO}_2$  surface has been assumed to be perfectly reflecting, i.e. diffusing Si monomers cannot leave the simulation cell through the surface. The  $\text{SiO}_2/\text{Si}$  interface acts as an effective sink for Si atoms, i.e. Si atoms that have attached once are very unlikely to be detached according to (4.8). Bulk Si atoms do not take place actively in the simulation, but are used to calculate binding energies of adjacent Si atoms in the  $\text{SiO}_2$  according to (4.8) in order to determine jump probabilities. With this definition, thermally activated Si detachment from the Si interface is hindered in the first stage of the KMC simulation. The error made is small due to the rare rate at which detachment events occur, but this procedure allows a tremendous speed-up of the simulation. Additionally, Si atoms that have condensed previously onto the Si substrate cover the interface at later simulation times. Those atoms are allowed to detach according to their regular jump probability of equation (4.8).

## References

- A. Antons. Simulation eines neuen Strukturierungsverfahrens für Silizide basierend auf lokaler Oxidation. Master's thesis, RWTH Aachen, Mar. 1998.
- F. Béjina and O. Jaoul. Silicon self-diffusion in quartz and diopside measured by nuclear micro-analysis methods. *Physics of the Earth and Planetary Interiors*, 97:145–162, 1996.
- K. Binder and P. Fratzl. Spinodal decomposition. In G. Kostorz, editor, *Phase Transformations in Materials*, chapter 6, pages 409–480. Wiley-VCH, Weinheim, 2001.
- K. Binder and D. W. Heermann. *Monte Carlo Simulations in Statistical Physics*. Springer Series in Solid State Sciences. Springer-Verlag, Berlin, 1992.
- P. E. Blöchl. First-principles calculations of defects in oxygen-deficient silica exposed to hydrogen. *Physical Review B*, 62(10):6158–6179, 2000.
- A. B. Bortz, M. H. Kalos, J. L. Lebowitz, and M. A. Zendejas. Time evolution of a quenched binary alloy: Computer simulation of a two-dimensional model system. *Physical Review B*, 10(2):535–541, July 1974.
- G. Brébec, R. Seguin, C. Sella, J. Bevenot, and J. C. Martin. Diffusion du silicium dans la silice amorphe. *Acta Metallurgica*, 28:327–333, 1980.

- J. W. Cahn. On spinodal decomposition. *Acta Metallurgica*, 9:795–801, 1961.
- J. W. Cahn and J. E. Hilliard. Free energy of a nonuniform system. I. Interfacial free energy. *Journal of Chemical Physics*, 28:258, 1958.
- J. W. Cahn and J. E. Hilliard. Free energy of a nonuniform system. II. Thermodynamic basis. *Journal of Chemical Physics*, 30:1121–1124, 1959a.
- J. W. Cahn and J. E. Hilliard. Free energy of a nonuniform system. III. Nucleation in a two-component incompressible fluid. *Journal of Chemical Physics*, 31:688, 1959b.
- N. Capron, G. Boureau, A. Pasturei, and J. Hafner. Thermodynamic properties of the Si-SiO<sub>2</sub> system. *Journal of Chemical Physics*, 117(4):1843–1850, July 2002.
- G. K. Celler and L. E. Trimble. Catalytic effect of SiO on thermomigration of impurities in SiO<sub>2</sub>. *Applied Physics Letters*, 54(15):1427–1429, Apr. 1989.
- E. Cook. Brownian motion in spinodal decomposition. *Acta Metallurgica*, 18:297–306, 1970.
- S. Fukatsu, T. Takahashi, K. M. Itoh, M. Uematsu, A. Fujiwara, H. Kageshima, Y. Takahashi, K. Shiraiishi, and U. Gösele. Effect of the Si/SiO<sub>2</sub> interface on self-diffusion of Si in semiconductor-grade SiO<sub>2</sub>. *Applied Physics Letters*, 83:3897–3899, Nov. 2003.
- J. D. Gunton, M. S. Miguel, and P. S. Sahni. The dynamics of first-order phase transitions. In C. Domb and J. L. Lebowitz, editors, *Phase Transitions and Critical Phenomena*, volume 8, chapter 3, pages 269–482. Academic Press, London, 1983.
- K. Heinig, T. Müller, B. Schmidt, M. Strobel, and W. Möller. Interfaces under ion irradiation: growth and taming of nanostructures. *Applied Physics A: Materials Science & Processing*, 77(1):17–25, June 2003.
- K.-H. Heinig. Efficient cellular automaton algorithm based on low-level bit manipulations. (unpublished), 1994.
- B. J. Hinds, F. Wang, D. M. Wolfe, C. L. Hinkle, and G. Lucovsky. Investigation of postoxidation thermal treatments of Si/SiO<sub>2</sub> interface in relationship to the kinetics of amorphous Si suboxide decomposition. *Journal of Vacuum Science and Technology B*, 16(4):2171–2176, July 1998.
- F. Iacona, C. Bongiorno, C. Spinella, S. Boninelli, and F. Priolo. Formation and evolution of luminescent Si nanoclusters produced by thermal annealing of SiO<sub>x</sub> films. *Journal of Applied Physics*, 95(7):3723–3732, 2004.
- O. Jaoul, F. Bejina, F. Èlie, and F. Abel. Silicon self-diffusion in quartz. *Physical Review Letters*, 74(11):2038–2041, Mar. 1995.
- K. Kawasaki. Diffusion constants near the critical point for time-dependent ising models. I. *Physical Review*, 145(1):224–230, May 1966.
- W. Kob and K. Binder. How can computer simulations contribute to the understanding of the dynamics of glasses and glass melts? In H. Bach and D. Krause, editors, *Analysis of Composition and Structure of Glass and Glass Ceramics*, page 344. Springer, Berlin, 1999. arXiv:cond-mat/9712012.
- I. M. Lifshitz and V. V. Slyozov. The kinetics of precipitation from supersaturated solid solutions. *J. Phys. Chem. Solids*, 19:35, 1961.
- D. A. Litton and S. H. Garofalini. Vitreous silica bulk and surface self-diffusion analysis by molecular dynamics. *Journal of Non-Crystalline Solids*, 217:250–263, 1997.

- S. Mantl, L. Kappius, A. Antons, M. Löken, F. Klinkhammer, M. Dolle, Q. T. Zhao, S. Mesters, C. Buchal, H. L. Bay, H. Trinkaus, and K.-H. Heinig. Growth, patterning and microelectronic applications of epitaxial cobaltdisilicide. *Materials Research Society Symposium Proceedings*, 514:145, 1998.
- D. Mathiot, J. P. Schunck, M. Perego, M. Fanchiulli, P. Normand, C. Tsamis, and D. Tsoukalas. Silicon self-diffusivity measurement in thermal SiO<sub>2</sub> by <sup>30</sup>Si/<sup>28</sup>Si isotopic exchange. *Journal of Applied Physics*, 94(3):2136–2138, Aug. 2003.
- N. Metropolis, A. Rosenbluth, M. Rosenbluth, A. Teller, and E. Teller. Equation of state calculations by fast computing machines. *Journal of Chemical Physics*, 21:1087, 1953.
- T. Michely, M. Kalff, G. Comsa, M. Strobel, and K.-H. Heinig. Step edge diffusion and step atom detachment in surface evolution: Ion erosion of Pt(111). *Physical Review Letters*, 86:2589–2592, Mar. 2001.
- T. Michely, M. Kalff, G. Comsa, M. Strobel, and K.-H. Heinig. Coarsening mechanisms in surface morphological evolution. *JPC*, 14:4177–4185, 2002.
- N. Mousseau, G. T. Barkema, and S. W. D. Leeuw. Elementary mechanisms governing the dynamics of silica. *Journal of Chemical Physics*, 112(2):960–964, Jan. 2000.
- T. Müller, K.-H. Heinig, and B. Schmidt. Formation of ge nanowires in oxidized silicon v-grooves by ion beam synthesis. *Nuclear Instruments and Methods in Physics Research B*, 175-177:468–473, 2001.
- T. Müller, K.-H. Heinig, and W. Möller. Size and location control of Si nanocrystals at ion beam synthesis in thin SiO<sub>2</sub> films. *Applied Physics Letters*, 81:3049–3051, 2002a.
- T. Müller, B. Schmidt, and K.-H. Heinig. Template-directed self-assembly of buried nanowires and the pearling instability. *Materials Science and Engineering C*, 19(1-2):209–213, 2002b.
- NEON. Report on model evaluation for process understanding of WP1 to WP3. Deliverable D11, EU Growth Project NEON GRD1-2000-25619, June 2002. URL <http://www.cemes.fr/neon.html>.
- L. A. Nesbit. Annealing characteristics of Si-rich SiO<sub>2</sub> films. *Applied Physics Letters*, 46(1):1985–1987, Jan. 1985.
- M. E. J. Newman and G. T. Barkema. *Monte Carlo Methods in Statistical Physics*. Oxford University Press, Oxford New York, 1999.
- K. Ohno, K. Esfarjani, and Y. Kawazoe. *Computational Materials Science – From Ab Initio to Monte Carlo Methods*. Springer Series in Solid-State Sciences. Springer-Verlag, Berlin, 1999.
- Povray. Persistence of vision, 2004. URL <http://www.povray.org>.
- S. Reiß and K.-H. Heinig. Ostwald ripening during ion beam synthesis - a computer simulation for inhomogeneous systems. *Nuclear Instruments and Methods in Physics Research B*, 84:229–233, 1994.
- T. M. Rogers and R. C. Desai. Numerical study of late-stage coarsening for off-critical quenches in the cahn-hilliard equation of phase separation. *Physical Review B*, 38(16):11956, 1989.
- J. Song, L. R. Corrales, G. Kresse, and H. Jónsson. Migration of O vacancies in  $\alpha$ -quartz: the effect of excitons and electron holes. *Physical Review B*, 64:134102, 2001.



- M. Strobel. Modeling and computer simulation of ion beam synthesis of nanostructures. Wissenschaftlich-Technische Berichte FZR-277, Forschungszentrum Rossendorf, Dresden, Germany, Nov. 1999. PhD thesis.
- M. Strobel, K.-H. Heinig, and W. Moeller. Can core/shell nanocrystals be formed by sequential ion implantation? Predictions from kinetic lattice monte carlo simulations. *Nuclear Instruments and Methods in Physics Research B*, 148:104–109, 1999a.
- M. Strobel, K.-H. Heinig, W. Möller, A. Meldrum, D. S. Zhou, C. W. White, and R. A. Zuhr. Ion beam synthesis of gold nanoclusters in  $\text{SiO}_2$ : Computer simulations versus experiments. *Nuclear Instruments and Methods in Physics Research B*, 147:343–349, 1999b.
- M. Strobel, K.-H. Heinig, and W. Möller. Three-dimensional domain growth on the size scale of the capillary length: Effective growth exponent and comparative atomistic and mean-field simulations. *Physical Review B*, 64:245422, 2001.
- V. B. Sulimov, P. V. Sushkov, A. H. Edwards, A. L. Shlugger, and A. M. Stoneham. Asymetry and long-range character of lattice deformation by neutral oxygen vacancy in  $\alpha$ -quartz. *Physical Review B*, 66:024108, 2002.
- T. Takahashi, S. Fukatsu, K. M. Itoh, M. Uematsu, A. Fujiwara, H. Kageshima, Y. Takahashi, and K. Shiraishi. Self-diffusion of Si in thermally grown  $\text{SiO}_2$  under equilibrium conditions. *Journal of Applied Physics*, 93(6):3674–3676, Mar. 2003.
- D. Tsoukalas, C. Tsamis, and P. Normand. Diffusivity measurements of silicon in silicon dioxide layers using isotopically pure material. *Journal of Applied Physics*, 89(12):7809–7813, June 2001.
- M. Uematsu, H. Kageshima, Y. Takahashi, S. Fukatsu, K. M. Itoh, K. Shiraishi, and U. Gösele. Modeling of Si self-diffusion in  $\text{SiO}_2$  : Effect of the Si/ $\text{SiO}_2$  interface. *Applied Physics Letters*, 84:876–878, 2004.
- P. W. Voorhees and M. E. Glicksman. Solution to the multi-particle diffusion problem - I. theory. *Acta Metallurgica*, 32(11):2001–2011, 1984a.
- P. W. Voorhees and M. E. Glicksman. Solution to the multi-particle diffusion problem - II. computer simulations. *Acta Metallurgica*, 32(11):2013–2030, 1984b.
- C. Wagner. Theorie der Alterung von Niederschlägen durch Umlösen. *Z. Elektrochem.*, 65:581, 1961.



## Chapter 5.

# Results and Discussion: Predictions on Tailored Si NC Formation

Low energy IBS of Si NCs is modeled with the help of the simulation tools introduced in Chapter 3 and 4. The resulting predictions are presented in the following and will be compared to the experimental investigation. On that basis, conclusions about an tailored Si NC synthesis will be drawn and optimum conditions for an application in NC memories will be identified. Thereby, using low ion energies promises several advantages:

- *Shallow and narrow depth profiles* of Si excess are achieved. Phase separation is expected to results in a thin layer of Si NCs embedded in the SiO<sub>2</sub>, even a monolayer of Si NCs might be reached.
- The depth position of the NC layer should be adjustable by the *ion energy*. The total amount of Si contained in the precipitates is driven by the *ion fluence*, while the *annealing temperature* determines the mean NC size.
- *Small ion damage* at the SiO<sub>2</sub>/Si interface is expected since only a few recoil atom can reach the interface due to the low ion energy. Irradiation damage created within the SiO<sub>2</sub> is largely recovered during annealing.
- Like any implantation based technology, low energy IBS should allow for good contamination control due to the applied mass separation. A smooth integration into the standard CMOS process flow is anticipated.

However, recent work revealed a more complex picture of low energy IBS where predictive process simulations contributed considerably to an understanding of Si phase separation in the vicinity of absorbing interfaces. These simulations allowed to select preferred reaction pathways for optimized memory structures. In addition, clean computer experiments give the ability to identify additional factors of influence that are present in the experiment. These include the absorption of humidity in the ion damaged SiO<sub>2</sub> (Perego et al., 2004b; Schmidt et al., 2002), the parasitic oxidation of implanted Si (cp. section 5.5 and Müller et al. (2002); Normand et al. (2004); Schmidt et al. (2002)), oxide swelling (Bonafos et al., 2004; Carrada et al., 2003; NEON, 2003; Normand et al., 2004).

Since NC formation by low energy IBS involves a certain degree of self organization, it is important understand the phase separation process of implanted Si from the SiO<sub>2</sub> taking place in a rather confined geometry. The specific action of implantation, sample and annealing parameters has to be understood in order to gain control over the NC formation and to obtain an optimum NC configuration for NC memories. Low energy IBS has to fulfil several requirements there, which stand in the focus of the further work:

parameter	value
SiO <sub>2</sub> thickness	5...10 nm
Si <sup>+</sup> ion energy	0.6...5 keV
Si <sup>+</sup> ion fluence	1...20 × 10 <sup>15</sup> cm <sup>-2</sup>
peak concentration of Si excess	10...50 at.-%

**Table 5.1.:** Parameters for low energy IBS of Si NCs.

**Morphology:** IBS should lead to an ensemble of spherical NCs instead of elongated or even connected precipitates.

**Size and density:** NCs should be rather small and obey a high areal density in order to achieve high charge densities stored redundantly on isolated nodes in the SiO<sub>2</sub> layer.

**Location:** The ensemble of NCs should be arranged in a sharp layer close to the Si/SiO<sub>2</sub> interface. The variation of the distance between interface and the NCs needs to be controlled at the precision of one nanometer or less to allow for reliable direct electron tunneling.

**Isolation:** Charge brought to phase separated Si in the SiO<sub>2</sub> should be stored with sufficient isolation to guarantee the desired retention. This requires isolation of the NCs from the Si/SiO<sub>2</sub> interface, but also implies that direct percolation is avoided. NCs have to be spherical. Additionally, lateral direct electron tunneling among NCs has to be avoided and, thus, NCs have to be well separated in the SiO<sub>2</sub>.

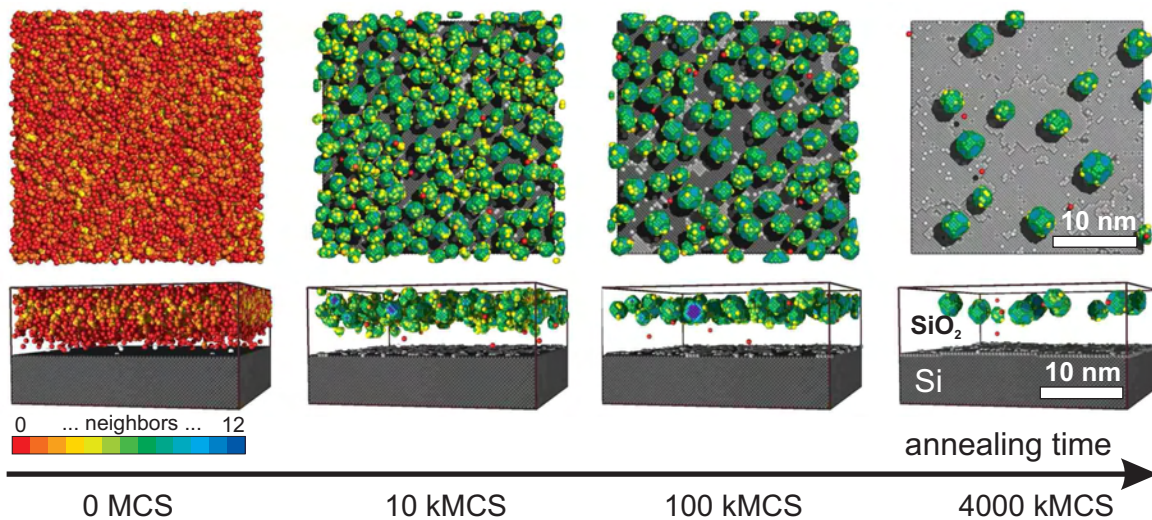


**Figure 5.1.:** Snapshots of a KMC simulation (top view and cross sections) for 1 keV Si<sup>+</sup> implantation into 8 nm thick SiO<sub>2</sub> on (100)Si taken. At a fluence of  $2 \times 10^{15} \text{ cm}^{-2}$ , NCs form in the course of annealing and dissolve finally due to Si loss to the absorbing SiO<sub>2</sub>/Si interface. The color scale of the Si atoms is described in the text. For clarity, a quarter of the KMC simulation cell is shown only.

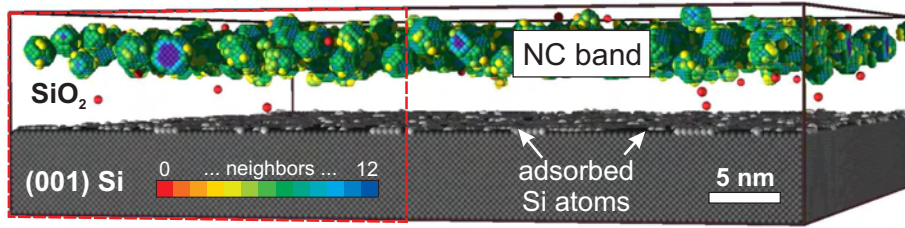


**Figure 5.2.:** Cross section view on a KMC simulation snapshot for 1 keV  $\text{Si}^+$  implantation into 8 nm thick  $\text{SiO}_2$  on (100)Si taken at 100 kMCS. The color scale of the Si atoms is described in the text. The band of Si NCs and the depleted zone underneath can be clearly seen. The dashed red line indicates the part of the cell shown in Figure 5.1, which gives a clearer overview in a series of snapshots.

The later question of electron tunneling percolation will be addressed in Chapter 6, while the other topics are discussed in the following. The implantation parameters used in this work are shown in Table 5.1 and were chosen in conjunction with the experimental conditions studied within the framework of the EU Growth Project NEON (2002a).

## 5.1. Si NC formation in the vicinity of an absorbing interface

Due to the thin gate oxide, Si NCs always form in the vicinity of the  $\text{SiO}_2/\text{Si}$  interface, which is a sink for diffusing Si monomers. Accordingly, the Si NCs formation at IBS is strongly affected by the resulting Si loss towards the interface. Process simulations clearly reveal this effect, e.g. for 1 keV  $\text{Si}^+$  implantation into 8 nm thick  $\text{SiO}_2$  films. Ion beam mixing of the  $\text{SiO}_2/\text{Si}$  interface is neglected in this case as the TRIDYN calculations of section 3.3 have shown that the interface is broadened by the ion beam to a width of less than 0.2 nm. Thus, the  $\text{SiO}_2/\text{Si}$  interface can be described in a very good approximation as a sharp one.

The initial Si excess distribution is generated in the simulation cell according to a Gaussian distribution, whose parameters were obtained by fitting the calculated TRIDYN profiles of Figure 3.4. They are listed in Table 5.2 for  $\text{Si}^+$  fluences up to  $1 \times 10^{16} \text{ cm}^{-2}$ . Starting from

ion fluence ( $10^{15} \text{ cm}^{-2}$ )	2	5	10
peak location (nm)	2.6	2.5	2.4
peak width $\sigma$ (nm)	1.8	2.3	3.0
peak concentration $c_{\text{max}}$ (at.-%)	9	19	34
$\text{SiO}_2$ swelling $d_{\text{swelling}}$ (nm)	0.2	0.6	1.3

**Table 5.2.:** Parameters of Gaussian distributions fitted to TRIDYN profiles of Figure 3.1 for 1 keV energy. Additionally, the swelling  $d_{\text{swelling}}$  of the  $\text{SiO}_2$  due to incorporated Si is given.

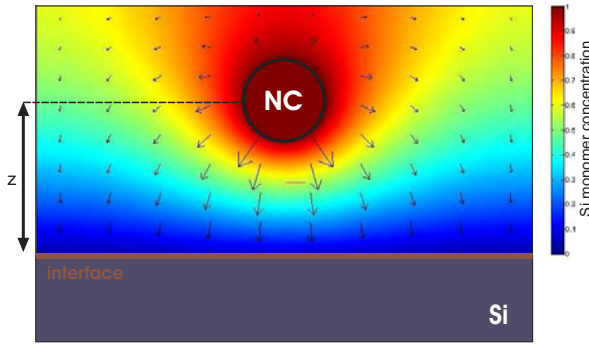


**Figure 5.3.:** Stationary concentration field of Si monomers around a Si NC close to the Si/SiO<sub>2</sub> interface in the adiabatic limit, equation (5.1). The GIBBS-THOMSON equation (2.17) determines the boundary conditions for the Si NC surface and the flat Si/SiO<sub>2</sub> interface, i.e. defines the Si monomer concentration there. The arrows indicate the diffusional flux of Si atoms towards the interface.

this Si excess profile, intermediate KMC simulation snapshots are displayed in Figure 5.1 for an ion fluence of  $2 \times 10^{15} \text{ cm}^{-2}$  and  $\varepsilon = E_B/k_B T$ .

The first snapshot on the left hand side of Figure 5.1 depicts the as-implanted SiO<sub>2</sub>. Si excess atoms are dispersed in the oxide with a distribution tail reaching almost up to the SiO<sub>2</sub>/Si interface. Bonds between neighboring Si atoms have not yet formed (indicated by the red color). In the first stage of annealing, small Si NCs form rapidly seen as tiny (green) dots in Figure 5.1(10 kMCS). The nucleation barrier is expected to be low for a Si supersaturation of ( $c_{max} = 9 \text{ at.-%}$ ), hence nucleation is likely to be *catastrophic*, i.e. the time dependent nucleation rate will not reach a steady state (Wagner et al., 2001). Accordingly, steady state descriptions based on classical nucleation theories outlined in section 2.2.2 are not applicable here. Nucleation of Si NCs in the sharp implantation profile can additionally not be considered as independent from coarsening of the NC ensemble. This becomes evident in Figure 5.1 (100 kMCS) since the NC density visibly decreases and the average size of the NCs increases, which will be subject of section 5.3 and is important for NC size and density control in NC memories.

### Late stage nanocluster dissolution

Long lasting annealing leads to a considerable amount of Si loss to the absorbing SiO<sub>2</sub>/Si interface. Si atoms attached there are colored in light gray (Figure 5.1) to enhance the visual contrast in simulation snapshots. From Figure 5.1, it is apparent that a complete Si monolayer has grown epitaxially onto the substrate in a time of 4000 kMCS.

Generally, the concentration field of Si monomers around Si NCs can be described in adiabatic approximation by the POISSON equation

$$\frac{\partial c(\vec{r})}{\partial t} = 0 = D\Delta c(\vec{r}) \quad (5.1)$$

with boundary conditions defined by the GIBBS-THOMSON equation (2.17), i.e.  $c(\vec{r}) = c_\infty$  at the Si/SiO<sub>2</sub> interface and  $c(\vec{r}) = c_R$  at the NC surface. At sufficiently low NC density, the NCs merely react with the SiO<sub>2</sub>/Si interface and lose Si monomers only to the interface but not neighboring NCs as they are too far away. In this case, the NC dissolution reduces to an effective one-particle problem whose time evolution can be calculated explicitly by solving (5.1). The concentration field around a single NC, determined by solving (5.1) numerically, has been plotted in Figure 5.3 for a single NC close to the SiO<sub>2</sub>/Si interface. The diffusional flux is indicated by arrows.

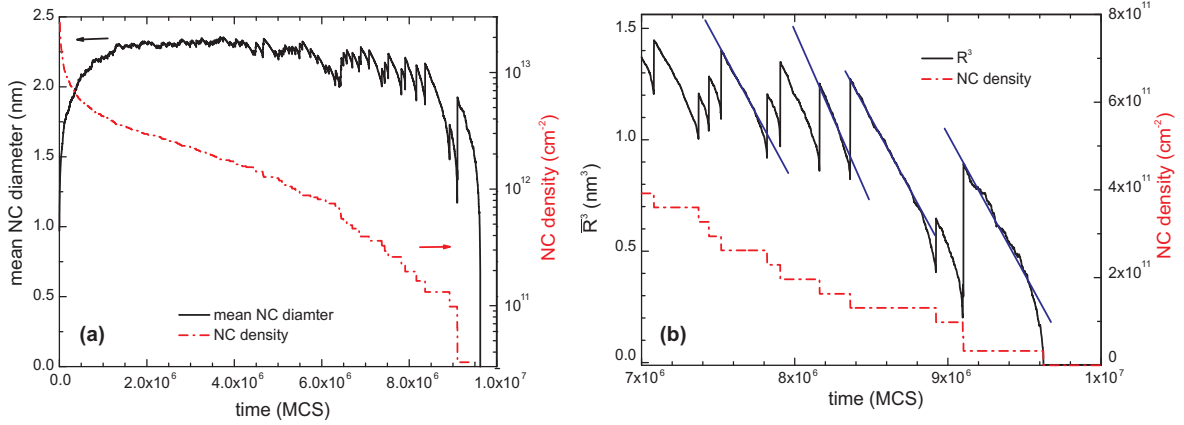


**Figure 5.4.:** (a) Time evolution of the mean NC diameter and density during annealing in the KMC simulation for the condition of Figure 5.1. (b) Dissolution of the NCs during the late stage of annealing. Plotted is the third power of the mean NC radius  $R$  and the NC density over time. Steps in the NC density indicate the dissolution of individual NCs in the simulation cell.

Using an expansion in spherical harmonics only up to monopoles together with the assumption of diffusion control, equation (5.1) can be simplified to (Voorhees and Glicksman, 1984a,b)

$$c(\vec{r}) \cong c_u + \frac{1}{4\pi D} \sum_{i=0}^N \frac{Q_i}{|\vec{r} - \vec{r}_i|} \quad (5.2)$$

with  $C_u$  being the mean monomer concentration. The number of source strengths is here limited to two, one at the center of the NC with a distance  $z$  from the interface. The other source is a mirror source inside the Si substrate at  $-z$ . Mass conservation requires further  $Q_1 + Q_2 = 0$ . The time evolution of the NC radius  $R$  is then given by

$$\frac{4\pi}{V_a} R_i^2(t) \frac{dR(t)}{dt} = -Q_1 \quad \text{with} \quad Q_1 = 4\pi D \left( \frac{c_R - c_\infty}{\frac{1}{R} - \frac{1}{2z}} \right). \quad (5.3)$$

and a mean monomer concentration of  $c_u = c_\infty$ . Using the linearized GIBBS-THOMSON equation (2.19) finally leads to

$$\frac{dR}{dt} = -DV_a \left( \frac{c_R - c_\infty}{R(1 - \frac{R}{2z})} \right) = -\frac{DV_a}{R^2} \left( \frac{c_R - c_\infty}{1 - \frac{R}{2z}} \right), \quad (5.4)$$

where integration with  $R(t=0) = R_0$  yields in the limit of  $R(t) \ll z$

$$R(t) = \left[ 3R_0^3 \left( \frac{1}{3} - \frac{R_0}{8z} \right) - 3DV_a R_c t \right]^{1/3}. \quad (5.5)$$

Consequently, the NC volume decreases linearly with time ( $R^3(t) \sim -t$ ) during the late stage of annealing. The time  $t_{diss}$  upon full NC dissolution is approximately determined by

$$t_{diss} = R_0^3 \left( \frac{1 - \frac{3R_0}{8z}}{3DV_a R_c} \right). \quad (5.6)$$

Despite the approximation relies on  $R(t) \ll z$ , it is evident that the cluster dissolves the faster the closer it is to the absorbing interface.

The described late stage dissolution behavior can be found in KMC simulations of phase separation. The mean NC size, being the average over a finite ensemble of NCs in the simulation cell, clearly shows the predicted behavior. Figure 5.4(b) reveals the predicted linear decrease of the NC volume during the late stage of annealing. In addition, the dissolution of individual NCs in the finite KMC simulation cell gives rise to a stepwise decrease of the NC density.

In addition, the evolution of a *NC ensemble* can show pronounced self-organization effects in the presence of a steep concentration gradient, e.g. originating from an absorbing interface nearby (Borodin et al., 1997; Reiß and Heinig, 1994). Under the present conditions, the oxide thickness (or the thickness of the NC layer) is in the order of the BRAILSFORD diffusive screening length (Brailsford et al., 1976), i.e. a layering of the precipitates is not observed in KMC simulations nor in the experiment. Rather, the dissolution of individual NCs is averaged out and the mean NC size becomes a smooth curve (Figure 5.4 a).

## 5.2. Morphology and morphology control of Si multi-dot floating gates

The morphology of the phase separated Si formed by low energy IBS in thin SiO<sub>2</sub> is predominantly controlled by the ion implantation conditions and annealing parameters. Process simulations allow to find a regime of synthesis that guarantees the formation of isolated, spherical NCs, which otherwise would require high experimental efforts. Within the European NEON project, predictions by these simulations (Müller et al., 2002) were thoroughly evaluated (NEON, 2004) and stimulated experimental research using advanced Electron Microscopy techniques to study the morphology of phase separated Si (Müller et al., 2004a,b).

### 5.2.1. Regimes of phase separation

KMC simulations were performed for the implantation conditions of Table 5.2, i.e. for 1 keV Si<sup>+</sup> implantation into a 8 nm thick SiO<sub>2</sub> layer on Si. Simulation snapshots at intermediate stages are shown in Figure 5.5 for ion fluences between  $2 \times 10^{15} \text{ cm}^{-2}$  and  $1 \times 10^{16} \text{ cm}^{-2}$ . These Si<sup>+</sup> fluences lead to a peak concentration of Si excess that varies between 9 at.-% and 34 at.-% according to TRIDYN depth profiles of Figure 3.4. Besides of the lower right corner in Figure 5.5, only a quarter of the simulation cell is shown in order to enlarge individual clusters. Figure 5.5 reveals a pronounced transition in precipitate morphology according to which roughly three regimes of phase separation can be distinguished.

#### Nucleation and growth

A *nucleation and growth* regime is observed for  $2 \times 10^{15} \text{ Si}^+ \text{ cm}^{-2}$ . Spherical Si NCs form by nucleation and grow further at the expense of Si supersaturation (Figure 5.5a, 100 kMCS). Later on, NCs grow by OSTWALD ripening in a competitive manner and finally dissolve by Si loss to the SiO<sub>2</sub>/Si interface.



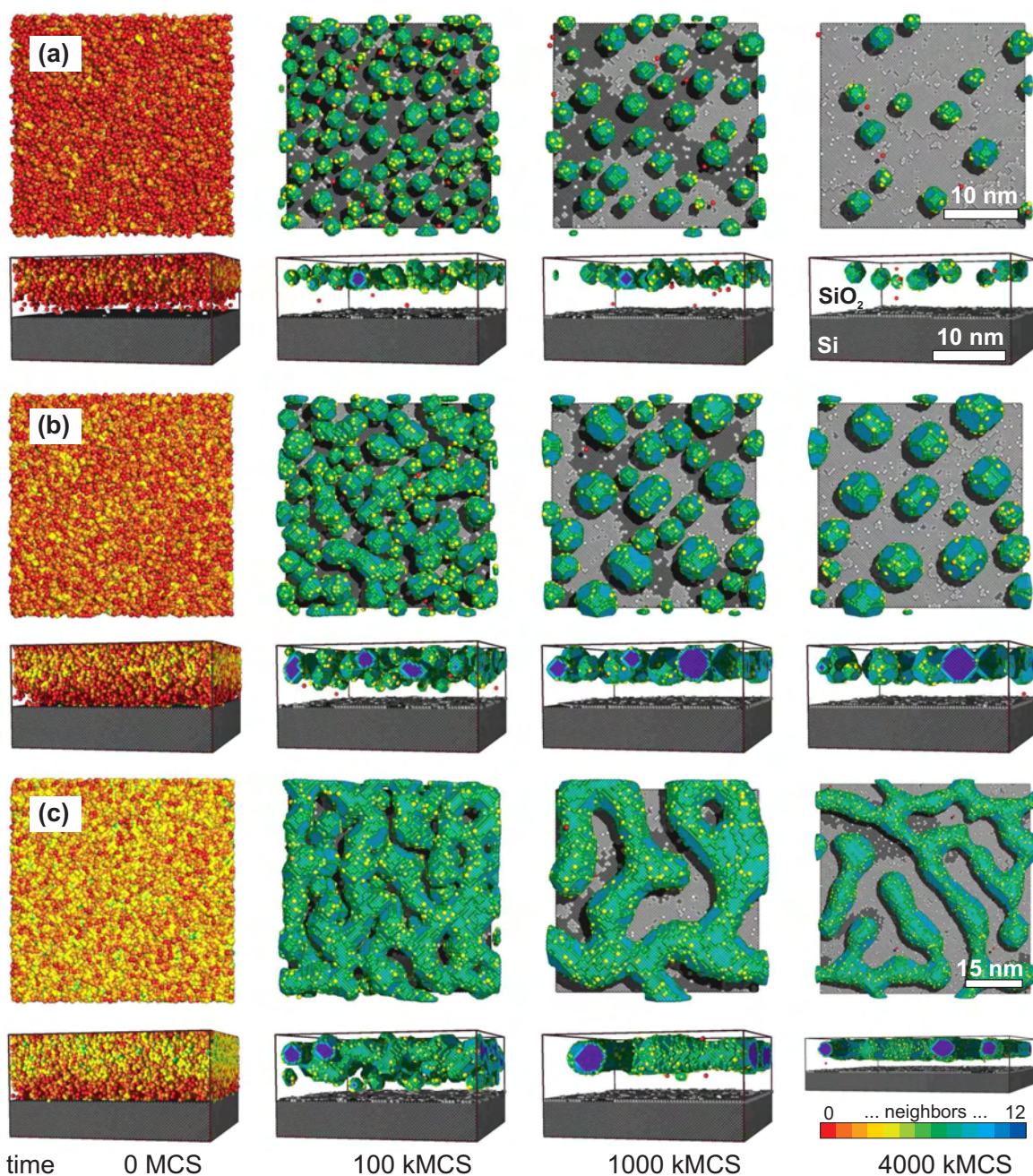


**Figure 5.5.:** Snapshots of KMC simulations (top view and cross section) of phase separation in 8 nm thick SiO<sub>2</sub> on (001) Si during annealing. The simulations start from 1 keV Si<sup>+</sup> TRIDYN profiles for fluences of (a)  $2 \times 10^{15} \text{ cm}^{-2}$ , (b)  $5 \times 10^{15} \text{ cm}^{-2}$ , and (c)  $1 \times 10^{16} \text{ cm}^{-2}$ , respectively. The regime of phase separation changes continuously from "nucleation and growth" (a) to "spinodal decomposition" (b), (c). Additionally, percolation is observed at the highest fluence (c). The 15 nm scale only applies for the lower right corner.

## Spinodal Decomposition

Above  $2 \times 10^{15} \text{ Si}^+ \text{ cm}^{-2}$  a *spinodal decomposition* regime is identified, where non-spherical, elongated Si structures are formed (Figure 5.5b, 100 kMCS). The reason for these irregular shape can be twofold, (i) the nucleation barrier is reduced by the high Si excess and phase separation triggers the formation of precipitates that from early stages on are non-spherical; (ii) non-spherical precipitates can form by the coalescence of spherical NCs. During long annealing, however, interface minimization leads in both cases to spherical NCs, which is seen in Figure 5.5b for 4000 kMCS.

## Structural percolation

At even higher Si concentrations ( $1 \times 10^{16} \text{ cm}^{-2}$ ), above the *percolation* threshold, the phase separated Si becomes laterally connected (Figure 5.5c, 100 kMCS) and extends over several tens on nanometer. Coarsening leads here only to a slow fragmentation of the connected structures (Figure 5.5c, 4000 kMCS), which certainly will not be reached within relevant annealing times.

It has to be noted that determining the exact percolation threshold was beyond the scope of the present work. Studies of Heermann and Klein (1983) and Hayward et al. (1987) have shown that dynamic percolation deviates principally from the well-understood site percolation (Stauffer and Aharony, 1992) of randomly placed particles on, e.g., an  $\text{fcc}$  lattice. Percolation in the dynamic Ising model, which has been applied here, is in general temperature and time dependent, i.e. percolation occurs for a given impurity concentration and temperature at an initial time  $t_1$  and persists up to  $t_2$  where then interface minimization has lead to a fragmentation of the percolated structures. A theory covering those dynamic percolation phenomena is not yet available, especially not for a sharp, inhomogeneous impurity profile. Nevertheless, several KMC simulation have shown that the dynamic percolation threshold for Si in  $\text{SiO}_2$  could be expected within a range of  $c_{\text{Siexcess}} = 0.2 \dots 0.3$ . Experimental studies for Si in  $\text{SiO}_2$  that could confirm this expectation are not yet available.

## Precipitate shape

This time evolution of the NCs shape can be assessed quantitatively by the *shape parameter*  $\delta$  (Strobel, 1999; Strobel et al., 2001). It measures the normalized mean squared distance from the center-of-mass of the NC in analogy to the moment of inertia  $I = \int r^2 dm$ <sup>1</sup>

$$\delta = \frac{1}{MR^2} \int r^2 dm \cong \frac{1}{NR^2} \sum_{i=1}^N (\vec{r}_i - \vec{r})^2, \quad (5.7)$$

with  $M$  being the mass of the NC.  $R$  denotes the radius of the NC according to (4.14),  $\vec{r}$  defines the center-of-mass of the NC, and the summation is taken over all  $N$  atoms connected to the cluster. For any non-spherical cluster geometry, the shape parameter  $\delta$  will exceed

<sup>1</sup>Note that the shape parameter  $\delta$  is *not* a discrete and normalized formulation of the moment of inertia  $I$ . The parameter  $\delta$  is calculated as mean squared distance of NC's atoms from the *NC center*, whereas the moment of inertia  $I$  uses the squared distance from the *rotation axis*.



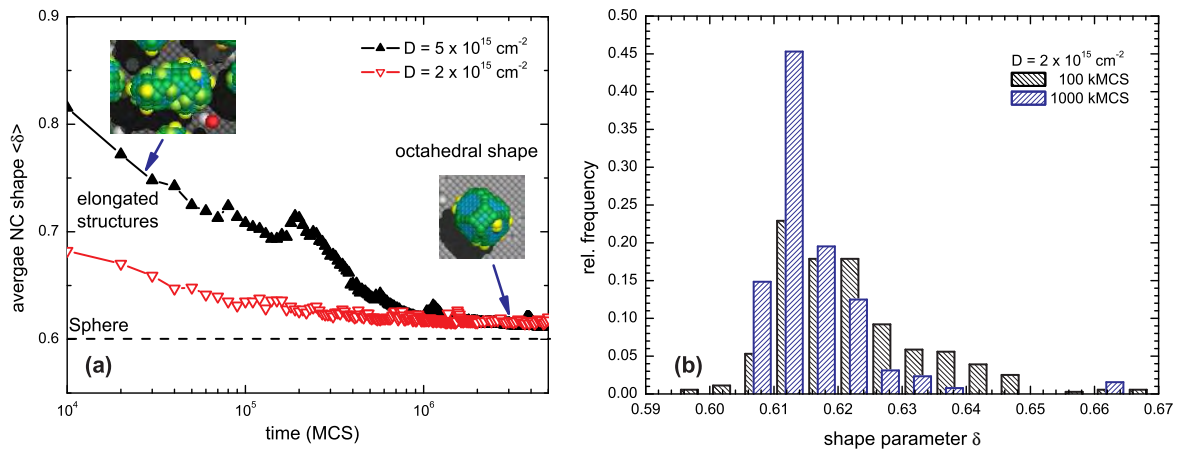


**Figure 5.6.:** (a) Time evolution of the average NC shape measured by  $\langle \delta \rangle$  according to (5.8). The highest fluence ( $1 \times 10^{16} \text{ cm}^{-2}$ ) has been omitted due to percolation of the phase separated Si. (b) Distribution of  $\delta$  for two different annealing times for a  $\text{Si}^+$  fluence of  $2 \times 10^{15} \text{ cm}^{-2}$ .

considerably the minimum value of  $\delta = 3/5$  of a homogeneous sphere. Taking the average of  $\delta$  over the full NC ensemble of  $N_{NC}$  clusters

$$\langle \delta \rangle = \frac{1}{N_{NC}} \sum_{i=1}^{N_{NC}} \delta_i \quad (5.8)$$

provides a means to check the deviation of the NC shape from the ideal sphere. It also allows to assess the amount of NC coagulation and gives a measure how far phase separation took place from the limit of *classical nucleation*, which leads to spherical precipitates only.

The time evolution of the mean NC shape  $\langle \delta \rangle$  according to (5.8) is shown in Figure 5.6a for implantation fluences of  $2 \times 10^{15} \text{ cm}^{-2}$  and  $5 \times 10^{15} \text{ cm}^{-2}$ . In the *nucleation* regime, the NC shape deviates slightly from the spherical form at the beginning of the annealing, while it quickly approaches a constant value of  $\delta = 0.61$  for an equilibrated octahedral NC shape. Contrarily, Si precipitates formed during the early stage of *spinodal decomposition* ( $5 \times 10^{15} \text{ cm}^{-2}$ ) are considerably non-spherical ( $\delta > 0.7$ ) which supports that spinodal decomposition itself causes irregular shaped NCs. A later coalescence then only adds up to the shape parameter  $\langle \delta \rangle$  as it can be seen by the peak at 200 kMCS in Figure 5.6a. Nevertheless below the percolation threshold, these precipitates evolve to spherical NC due to interface minimization, which then can hardly be distinguished from NCs that have formed by nucleation.

### 5.2.2. Mapping Si and $\text{SiO}_2$ plasmons by Electron Energy Loss Spectroscopy – Comparison to KMC predictions

The predictions of the last section have stimulated advanced experimental studies with the aim to identify the morphology of the Si nanostructures experimentally. These results then allows a direct comparison with KMC simulation snapshots (Müller et al., 2004a,b).

Using conventional TEM proves to be difficult to reveal Si nanostructures embedded in a  $\text{SiO}_2$  matrix. Both materials, Si and  $\text{SiO}_2$ , obey comparable electron densities and deliver

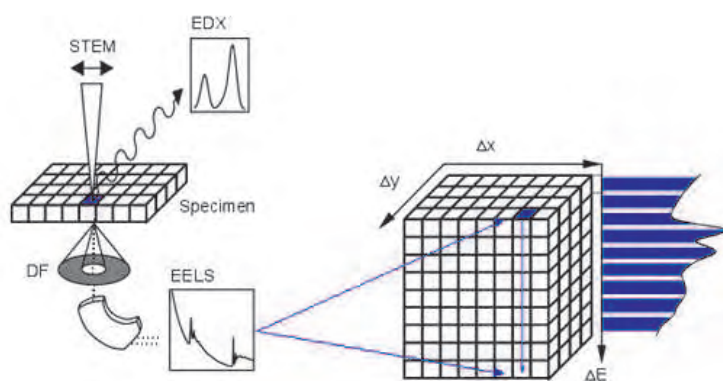


**Figure 5.7.:** A STEM *spectrum image* is acquired by stepping a focused electron probe from one pixel to the next. From Gatan, Inc. (2004).

not enough Z-contrast in the electron microscope to distinguish small Si-rich regions from the SiO<sub>2</sub> host as they were predicted above. Despite of recent advances using either HREM (Bonafos et al., 2004) or Fresnel imaging in under-focused bright field conditions (Ben Assayag et al., 2003; Bonafos et al., 2004), the conventional TEM cannot be used to image *all* Si precipitates contained in the oxide matrix. Specifically, this technique is unable to reveal the morphology of the multi-dot floating gate.

## PEELS-STEM

A much better image contrast can be gained with the help of Electron Energy Loss Spectroscopy (EELS) on electrons that have penetrated through the TEM specimen. Depending on the specimen material, those electrons can excite bulk Si or SiO<sub>2</sub> plasmons, giving rise to a characteristic energy loss of the transmitted electrons. The specific plasmon resonance energies of 17 eV and 24 eV for Si and SiO<sub>2</sub>, respectively, differ sufficiently to allow their discrimination.

In general, there are two ways of collecting and displaying EELS data in the electron microscope (Egerton, 1996; Jeanguillaume and Colliex, 1989). The first method is to select an energy-loss band in the spectrum and record the corresponding image. This is the energy filtered image, which can directly be obtained with a filtering microscope of Casting-Henry type (Casting and Henry, 1962; Reimer, 1995) or with a Scanning TEM (STEM) equipped with an EELS spectrometer. Iacona et al. (2004) and Puglisi et al. (2003) have used the energy filtered TEM (EFTEM) to image Si dots embedded in SiO<sub>2</sub> that have been synthesized by PECVD.

An alternative method of EELS analysis in the TEM consists of selecting an image area, e.g. with a fixed probe in STEM configuration, and recording the relevant spectrum. Stepping the electron probe across the sample as depicted in Figure 5.7 allows to acquire a 3D *spectrum image* consisting of full EELS spectra for each image pixel. With a parallel EELS (PEELS) detectors (Egerton, 1984; Shuman, 1981), the acquisition time is short enough (< 30 ms per pixel and spectrum) to minimize specimen drift and damage. Superior to EFTEM that utilizes only a cross section of the 3D spectrum image, PEEL-STEM gives way to more complex data evaluation methods (Jeanguillaume and Colliex, 1989).

## Samples

PEELS-STEM has been applied by Tencé et al. (2003) to distinguish Si and SiO<sub>2</sub> phases in three samples containing Si NCs (Müller et al., 2004a). Si<sup>+</sup> ions were implanted at 1 keV

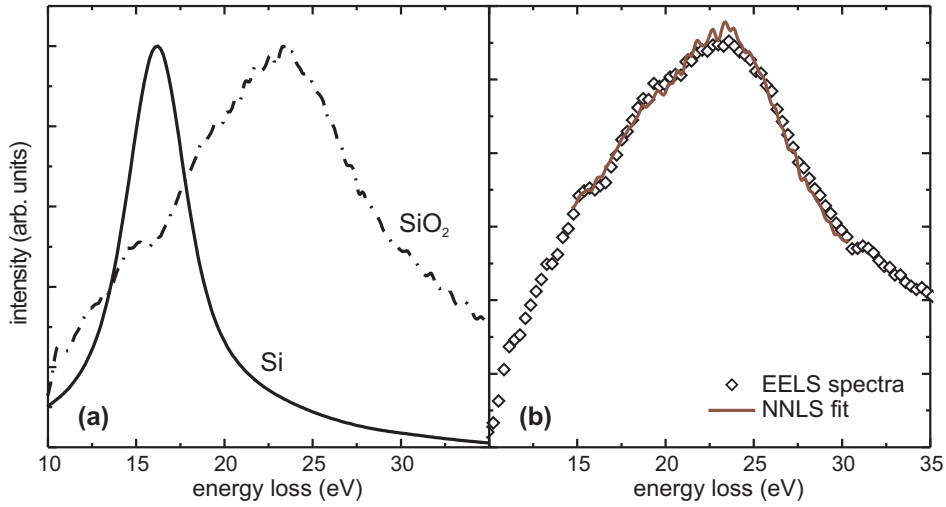


**Figure 5.8.:** (a) Electron energy loss (EELS) spectra for reference samples of Si and SiO<sub>2</sub>. (b) EELS spectra of a sample containing Si and SiO<sub>2</sub> phases and their fitting. The zero-loss peak has been omitted for both cases. By courtesy of Tencé et al. (2003).

energy into 10nm thick SiO<sub>2</sub> layers, which were thermally grown on (001) Si substrates. Using an AXCELIS GSD-ULTRA ultra-low-energy implanter, fluences of  $5 \times 10^{15} \text{ cm}^{-2}$ ,  $1 \times 10^{16} \text{ cm}^{-2}$ , and  $2 \times 10^{16} \text{ cm}^{-2}$  have been implanted at room temperature. Surface charging due to implantation was compensated by a Xe plasma electron flood gun. The implanted samples were cleaned using a piranha solution and furnace annealed for 30min in N<sub>2</sub> at 950°C.

From all samples, cross sectional and plane view TEM specimens were prepared by the standard procedure of grinding, dimpling and Ar<sup>+</sup> ion beam thinning. Electron energy loss spectroscopy (EELS) was performed on plane view samples using a Scanning TEM VG-HB 501 operating at 100kV that is equipped with a field emission cathode and a parallel Gatan 666 EELS spectrometer. Low-loss EELS spectra were recorded at each picture point, i.e. a EELS spectrum image was recorded for each sample. Reference EELS spectra were taken additionally for Si and thermally grown, amorphous SiO<sub>2</sub>, which are shown in Figure 5.8(a). Clear plasmon resonance peaks are observed at 17 eV and 24 eV for Si and SiO<sub>2</sub>, respectively. These reference spectra can be used to decompose the EELS spectra of samples containing Si NCs embedded in SiO<sub>2</sub>. An example of such an individual EELS spectrum (taken at one image STEM pixel) is shown in Figure 5.8(b). In good approximation, it can be considered as linear superposition of the reference spectra  $f_{\text{Si}}$  and  $f_{\text{SiO}_2}$  from Figure 5.8(a)

$$f_{\text{SiO}_x} = \alpha f_{\text{Si}} + \beta f_{\text{SiO}_2}. \quad (5.9)$$

The coefficients  $\alpha$  and  $\beta$  are to be determined by fitting the recorded EELS spectra. This has been done within a range of 15 - 30eV using a non-negative least square method (Lawson and Hanson, 1974). Exemplarily, a fitted spectra is shown in Figure 5.8(b) agreeing nicely with the recorded one. In this approach, potential size-effects like shifts of the plasmon resonance energy are not compensated nor surface plasmons have been taken into account. The fitting procedure is then carried out for all EELS spectra of a recorded spectrum image. A Si plasmon map can be build from these data, i.e. the gray level of an image

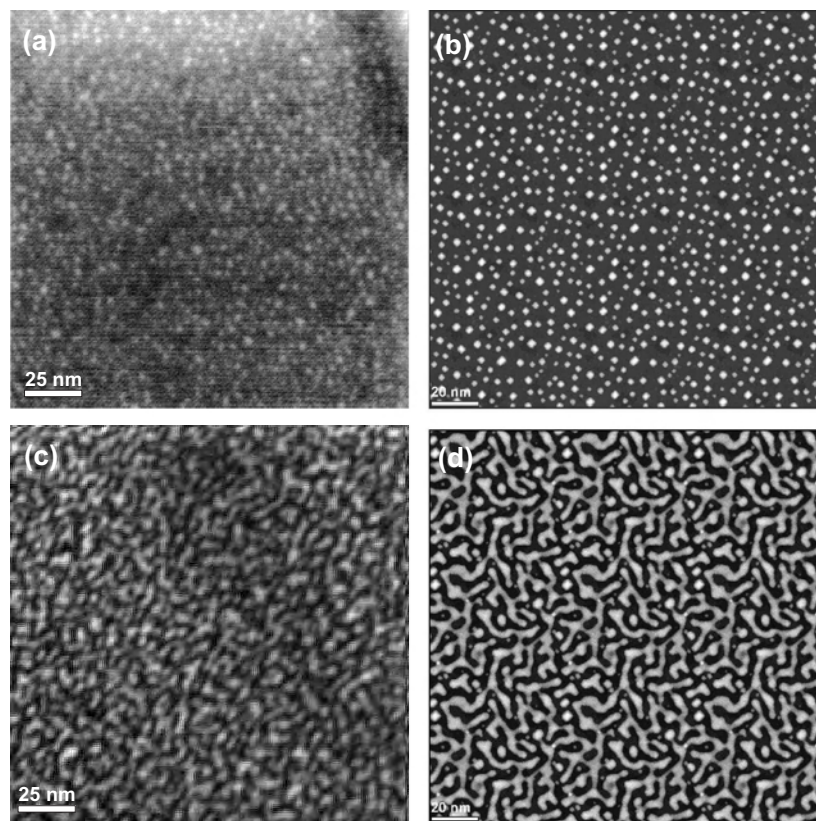


**Figure 5.9:** Morphology of phase separated Si in SiO<sub>2</sub>. PEELS-STEM images (a,c) are compared to corresponding KMC simulations (b,d). Nucleation of Si NCs is observed (a) for a Si fluence of  $1 \times 10^{16} \text{ cm}^{-2}$  and predicted with the same morphology for (b)  $3 \times 10^{15} \text{ cm}^{-2}$ . Spinodal patterns are imaged (c) for  $2 \times 10^{16} \text{ cm}^{-2}$  and simulated (d) for  $8 \times 10^{15} \text{ cm}^{-2}$ . White and black regions correspond to Si and SiO<sub>2</sub> phases, respectively.

pixel is determined by intensity ratio  $c$  according to (5.9) that measures the relative Si content. Quantitative Si concentrations, however, cannot be given by this technique, only the relative Si content is imaged. Such a plasmon map obtained by PEELS-STEM is shown in Figure 5.9(a) and (c).

### Plasmon maps and comparison to KMC simulation snapshots

KMC simulations of Si phase separation from SiO<sub>2</sub> have been performed for the corresponding implantation conditions. In order to compare the KMC simulation snapshot directly to the Si plasmon maps, subsequent image processing of the KMC data were necessary according to section 4.2.2. The images are shown in gray scale, where white corresponds to Si rich regions and black means that no Si excess is found in the SiO<sub>2</sub> matrix<sup>2</sup>. In plane view images, Si atoms of the underlying (001) Si substrate are not considered.

No Si precipitates were observed in the sample for the lowest Si<sup>+</sup> fluence of  $5 \times 10^{15} \text{ cm}^{-2}$  (TEM images not shown here). For the medium Si<sup>+</sup> fluence of  $1 \times 10^{16} \text{ cm}^{-2}$ , white spots in a dark background appear in the plane view Si plasmon map

<sup>2</sup>The gray scale is here reversed to its definition in section 4.2.2.



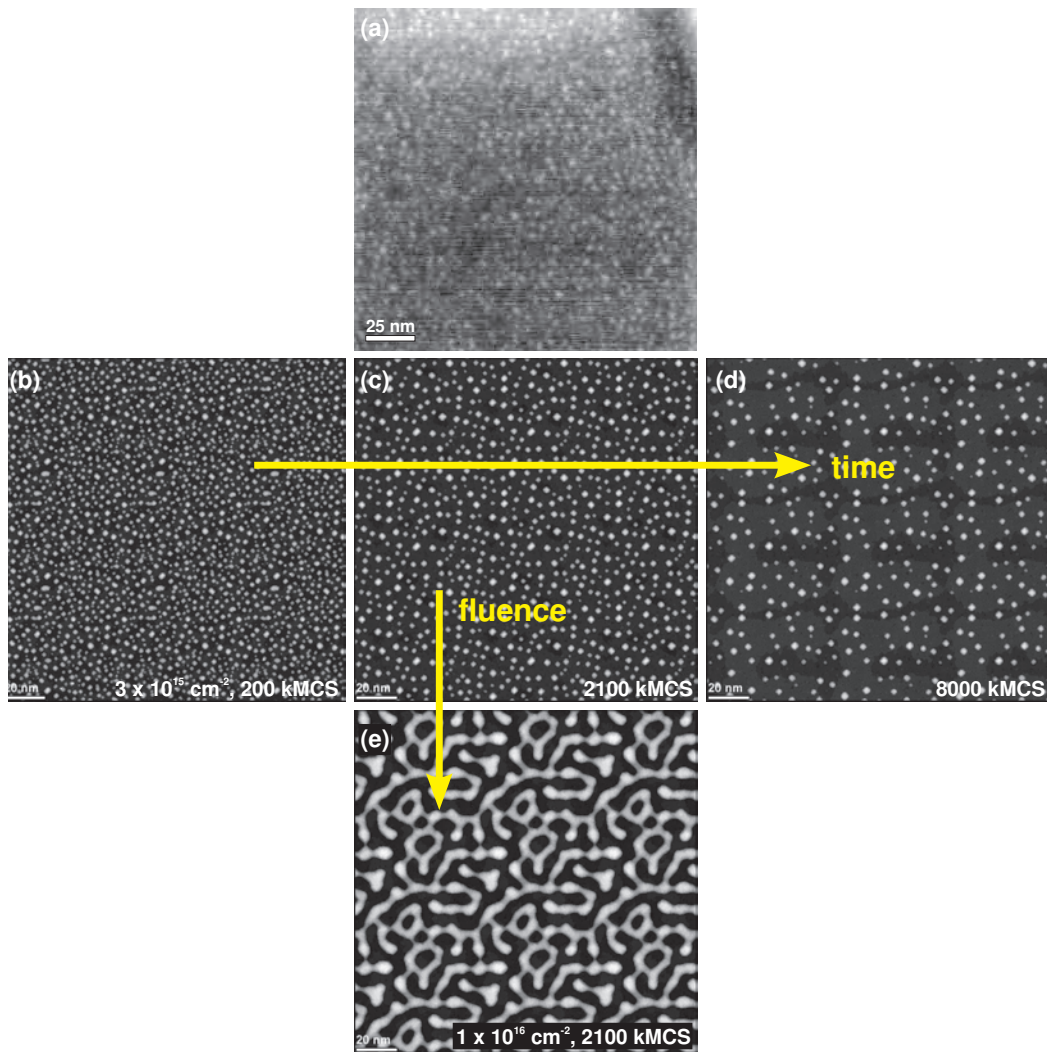


**Figure 5.10.:** A Si plasmon map (a) is compared to several KMC simulation snapshots (b,c,d,e).

shown in Figure 5.9(a) indicating spherical Si NCs embedded in the SiO<sub>2</sub> matrix. During thermal annealing, these NCs have formed by nucleation and growth in the Si enriched region of the implanted SiO<sub>2</sub> layer. The observed NCs are relatively small with an estimated mean diameter of 2.7 nm and have a high area density of  $3.3 \times 10^{12} \text{ cm}^{-2}$ . A similar precipitate morphology with the same mean NC size and density is found in the plane view KMC simulation snapshot of Figure 5.9(b), but for a significantly lower Si<sup>+</sup> fluence of  $3 \times 10^{15} \text{ cm}^{-2}$  and a KMC simulation (annealing) time of 2100 kMCS. The effect of a variation of the annealing time on the precipitate morphology can be seen in Figure 5.10. Most strikingly, the NC density does not deviate for shorter or longer annealing. It should be noted that even this “medium” experimental Si<sup>+</sup> fluence of  $1 \times 10^{16} \text{ cm}^{-2}$  leads in the KMC simulation to the formation of coalesced poly-Si layer buried in the SiO<sub>2</sub> (Müller et al., 2002). This discrepancy becomes evident by direct comparison of Figure 5.10(a) (PEELS-STEM) and Figure 5.10(e) (KMC simulation).

For the highest Si<sup>+</sup> fluence of  $2 \times 10^{16} \text{ Si}^+ \text{ cm}^{-2}$ , the morphology of the phase separated

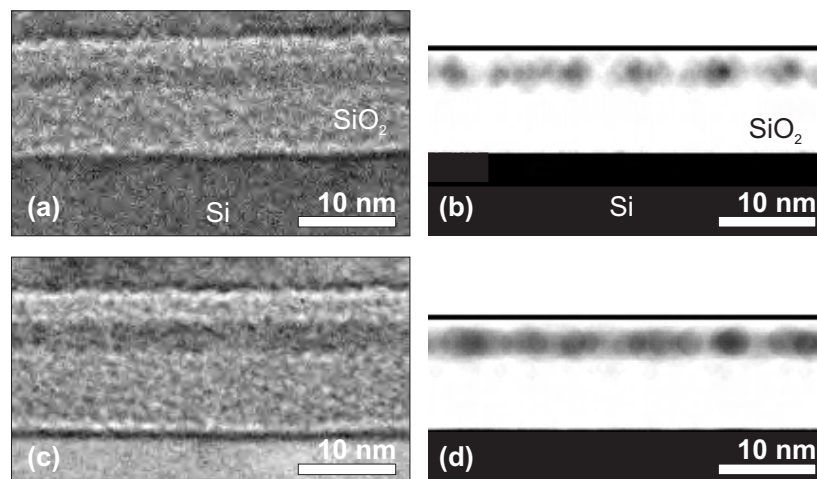


**Figure 5.11.:** Cross section view of the layer of phase separated Si in SiO<sub>2</sub>. Fresnel XTEM images for (a)  $1 \times 10^{16} \text{ cm}^{-2}$  and (c)  $2 \times 10^{16} \text{ cm}^{-2}$  are compared to cross sectional KMC simulation snapshots for (b)  $3 \times 10^{15} \text{ cm}^{-2}$  and (d)  $8 \times 10^{15} \text{ cm}^{-2}$ .

Si has changed completely as observed in Figure 5.9 (c). A thread-like network of white and black regions is found. This spinodal pattern clearly indicates that, at this fluence, phase separation took place by spinodal decomposition. Even more, percolation is observed. Si precipitates are no longer spatially isolated, but an interconnected network of phase separated Si has formed. An equivalent morphology with the same typical distances than in Figure 5.9 (c) between the spinodal fingers is found in the plane view KMC simulation snapshot of Figure 5.9(d). This results was obtained for  $8 \times 10^{15} \text{ Si}^+ \text{ cm}^{-2}$  and a simulation time of 300 kMCS. Strikingly, the morphology agrees remarkably well between both images, while simulation snapshots for other fluences or annealing times deviate considerably from the morphology seen in Figure 5.9 (c).

### XTEM investigations and comparison to KMC results

Samples were studied additionally in cross section by Bonafos et al. (2003) using a CM30 Phillips TEM equipped with a LaB<sub>6</sub> cathode operating at 300 kV. Fresnel imaging conditions were applied in order to achieve at least a weak contrast between Si and SiO<sub>2</sub> in XTEM images, i.e. images were taken at Out-of-Bragg alignment and under strongly underfocused bright field conditions. The responsible contrast mechanism has been detailed by Ben Assayag et al. (2003). Figure 5.11, (a) and (c) show the XTEM Fresnel images for fluences of  $1 \times 10^{16} \text{ Si}^+ \text{ cm}^{-2}$  and  $2 \times 10^{16} \text{ Si}^+ \text{ cm}^{-2}$ , respectively. Cross section KMC simulation snapshots are displayed on the r.h.s in Figure 5.11(b) and (d) for  $3 \times 10^{15} \text{ Si}^+ \text{ cm}^{-2}$  (2100 kMCS) and  $8 \times 10^{15} \text{ Si}^+ \text{ cm}^{-2}$  (300 kMCS), respectively. Thereby, the same type of image processing was applied to KMC cross section views than to plane views. However, substrate atoms are considered here too and the gray scale of the KMC images has been inverted. White and black regions correspond to SiO<sub>2</sub> and Si phases, respectively.

In all images, the phase separated Si forms a single, sharp layer seen as gray band in the SiO<sub>2</sub> that is well separated from the SiO<sub>2</sub>/Si interface. Due to the extremely shallow Si excess profile obtained by low-energy Si<sup>+</sup> implantation, phase separation is quasi con-

fined to two dimensions. For  $1 \times 10^{16} \text{ Si}^+ \text{ cm}^{-2}$ , Si precipitates align nicely in a thin layer, which is just a few nanometers thick, Figure 5.11(a). When the  $\text{Si}^+$  fluences is increased to  $2 \times 10^{16} \text{ Si}^+ \text{ cm}^{-2}$ , the precipitate layer remains comparatively well localized in depth, Figure 5.11(c), although the Si morphology observed in plane view has changed completely, Figure 5.9(c). The final  $\text{SiO}_2$  thickness including the Si NC layer is systematically smaller for the KMC simulations than for the corresponding Fresnel images. Nevertheless, the distance between the Si/ $\text{SiO}_2$  interface and the phase separated Si agrees nicely for experiment and simulation.

The Si fluences used in the KMC simulations chiefly underestimate the experimental values in order to obtain a similar morphology of phase separated Si. Apparently, not all Si, that has nominally been implanted into the  $\text{SiO}_2$ , is readily available for phase separation. The reason for this loss of free Si atoms is believed to be twofold. (i) Recent Time of Flight Secondary Ion Mass Spectroscopy measurements on low-energy, low-fluence  $^{30}\text{Si}^+$  implanted  $\text{SiO}_2$  samples indicate that only a fraction of about 0.5 – 0.7 of the nominal  $\text{Si}^+$  fluence has been implanted into the  $\text{SiO}_2$  (Perego et al., 2003). However, TRIDYN calculations predict that all implanted Si is expected to remain within the  $\text{SiO}_2$ , dynamic sputtering of previously implanted Si cannot explain the missing Si. Thus, the nominal fluences of  $1 \times 10^{16} \text{ Si}^+ \text{ cm}^{-2}$  and  $2 \times 10^{16} \text{ Si}^+ \text{ cm}^{-2}$  for the medium and high fluence sample, respectively, have certainly to be corrected to lower values although implantation has been carried out using a standard industrial implanter. (ii) It is known that (Si or Ge) NC formation in very thin  $\text{SiO}_2$  films is extremely sensitive to traces of oxidants being present either in the annealing ambient (Oswald et al., 2000) or being absorbed in the irradiation damaged glass network (Schmidt et al., 2002). A considerable amount of the implanted Si might become oxidized and therefore unavailable for NC formation during phase separation. Moreover, oxidation would give rise to a swelling of the overall  $\text{SiO}_2$  layer, a fact that is observed in Figure 5.11(a) and (c). This discussion will be continued in section 5.5.

Despite samples have been annealed under fixed experimental conditions, the KMC simulation snapshots of corresponding Si patterns refer to different simulation times. Two reasons might be responsible for this discrepancy in the evolution speed. At first, the oxidation of a substantial part of implanted Si might influence the kinetics, and secondly, the Si bulk diffusion in  $\text{SiO}_2$  might differ substantially from the Si diffusion at the Si/ $\text{SiO}_2$  interface, which was not taken into account in section 4.2.

### 5.2.3. Processing routes for self-aligned NC layer formation – Choosing the right precipitate morphology

In summary, three different regimes of phase separation have been predicted and were confirmed by PEELS-STEM studies, which are *nucleation and growth*, *spinodal decomposition* and *structural percolation*. These regimes result in rather different morphologies of the phase separated Si. A sharp border between the *nucleation and growth* regime and *spinodal decomposition* can certainly not be defined. A rather smooth transition is expected between both classical limits if the theory of phase separation is taken beyond the mean-field approximation as outlined in section 2.2.2. In the above described simulations, the transition between both regimes of phase separation can only be traced by the shape of the Si NCs (Figure 5.5). According to classical nucleation theory, stable nuclei obey a spherical shape, whereas spinodal decomposition leads to non-spherical structures due to the vanishing nu-

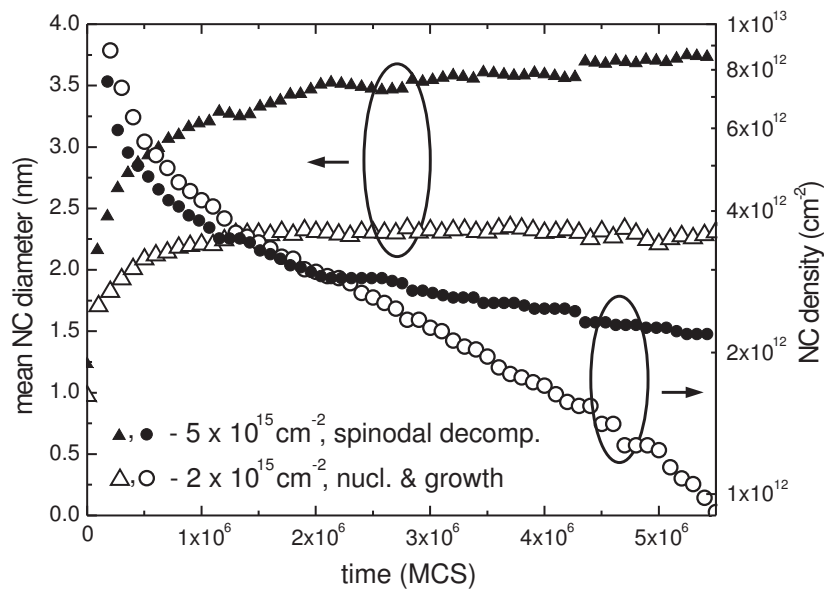


**Figure 5.12.:** Evolution of the mean NC size and density during annealing. Si<sup>+</sup> ions were implanted into 8 nm thick SiO<sub>2</sub> at an energy of 1 keV to a fluences of  $2 \times 10^{15} \text{ cm}^{-2}$  and  $5 \times 10^{15} \text{ cm}^{-2}$ .

cleation barrier. However, after long annealing, both regimes cannot be distinguished if one solely relies on the precipitate morphology. Spherical NCs result in both cases. Still memory relevant properties as NC size and density as well as the tunneling distance between the NC layer and the Si/SiO<sub>2</sub> interface differ between both regimes (see section 5.3). In contrast, the precipitate morphology observed in the *structural percolation* regime discerns clearly from the isolated precipitates formed in the other regimes.

From the comparison between the simulations and PEELS-STEM results, it follows that Si NCs are favorably to be synthesized in the *nucleation and growth* regime or at the onset of *spinodal decomposition*, where annealing still leads to spherical precipitates. Structural percolation has to be avoided, i.e. the Si fluences has not to be chosen too high in order to prevent the formation of interconnected poly-Si structures buried in the SiO<sub>2</sub>. If once formed, such Si network would act as a floating gate layer. Stored charge could spread over tens of nanometer and eventually find tunneling oxide defects through which the floating gate can be discharged. Experimentally, this is confirmed by studies of Kim et al. (2003), who related as fast charge loss to the existence lateral interconnected Ge precipitates. Retention was shown to improve substantially if the lateral percolation is avoided.

### 5.3. Prediction of the optimum NC size and density

Beyond the morphology of the phase separated Si other quantities are important parameters that influence the nonvolatile NC memory properties. These include precipitate size and density, size distribution and location of the NCs in the gate oxide with respect to the transistor channel (Si/SiO<sub>2</sub> interface) measured as outlined in section 4.2.2. KMC simulations are used here study the impact of changes in implantation and annealing conditions on these parameters.



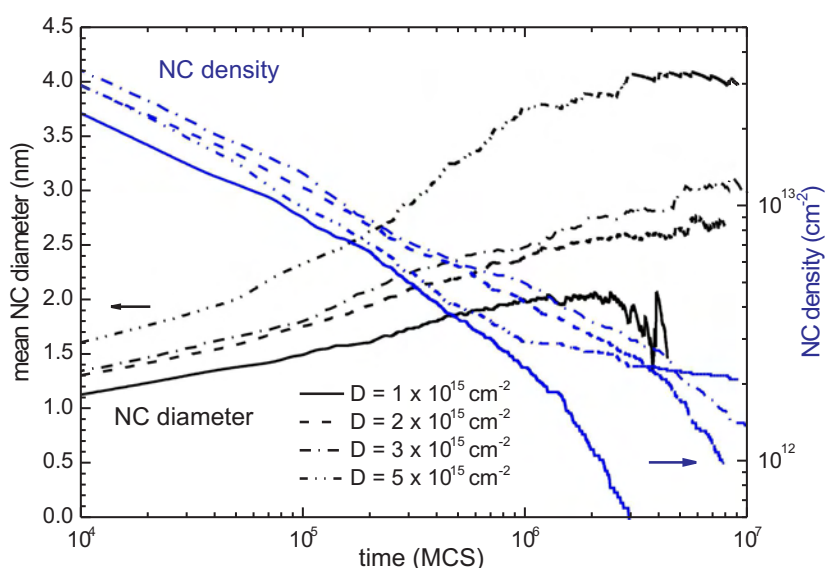


**Figure 5.13:** Evolution of the mean NC size and density during annealing.  $\text{Si}^+$  ions were implanted into 10 nm thick  $\text{SiO}_2$  at an energy of 1 keV. The ion fluence was varied from  $1 \times 10^{15} \text{ cm}^{-2}$  (nucleation regime) to  $5 \times 10^{15} \text{ cm}^{-2}$  (spinodal decomposition).

### 5.3.1. Regimes of phase separation

In Figure 5.12, this is shown for 1 keV  $\text{Si}^+$  implantation into 8 nm thick  $\text{SiO}_2$  at two ion fluences of  $2 \times 10^{15} \text{ cm}^{-2}$  and  $5 \times 10^{15} \text{ cm}^{-2}$ . These simulations were carried out at an inverse temperature of  $\varepsilon = 2$ , which have led to precipitate morphologies shown in Figure 5.5. The highest fluences of  $1 \times 10^{16} \text{ cm}^{-2}$  shown in Figure 5.5, has been omitted here due to percolation of the Si precipitates. NC size and density lose their common meaning there. Si NCs are observed initially at high areal densities, which decrease as coarsening proceeds. However, for  $2 \times 10^{15} \text{ cm}^{-2}$  the density decreases more rapidly and the mean NC size is less than for  $5 \times 10^{15} \text{ cm}^{-2}$ . More pronounced, the mean NC size saturates in Figure 5.12 for  $2 \times 10^{15} \text{ cm}^{-2}$  and the NC growth due to coarsening comes to rest, which is a result of the absorbing  $\text{SiO}_2/\text{Si}$  interface (see section 5.1). The competition between Si loss to the interface and OSTWALD ripening balances the mean NC diameter at this fluence (Müller et al., 2002). Long lasting annealing, however, results in the complete dissolution of the Si NCs seen as steep drop of the mean NC size in Figure 5.4.

Further KMC simulations have been performed for a slightly thicker oxide of 10 nm at otherwise constant conditions, which correspond directly to experimental conditions used in the NEON project. The predicted Si precipitate morphology was compared to PEELS-STEM images in Figure 5.9 of the previous section. At this oxide thickness, the influence of the absorbing  $\text{SiO}_2/\text{Si}$  interface is slightly less pronounced than for 8 nm as the interface is more distant. A balance resulting from the competition of Si loss to the interface and OSTWALD ripening has only been observed for the lowest ion fluence of  $1 \times 10^{15} \text{ cm}^{-2}$  as shown in Figure 5.13. A constant mean NC diameter is only found for a period of 2000 kMCS before the complete dissolution of the NCs occur. At the higher fluences ( $D \geq 2 \times 10^{15} \text{ cm}^{-2}$ ), the interface is too distant to have a strong influence on the time evolution of the mean NC size and density (Figure 5.13).

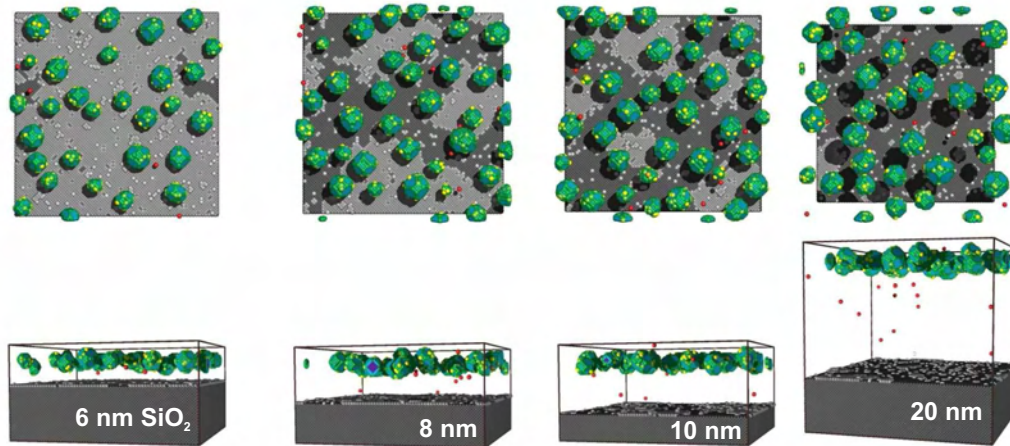


**Figure 5.14.:** KMC simulation snapshots (plane view in top row and cross section view at the bottom) of Si phase separation from thin SiO<sub>2</sub> layers of varying thickness implanted with Si at an annealing time of 1000 kMCS. The initial Si excess depth profile corresponds to 1 keV Si<sup>+</sup> implantation to a fluence of  $2 \times 10^{15} \text{ cm}^{-2}$  according to TRIDYN calculations of Figure 3.4. Ion beam mixing of the Si/SiO<sub>2</sub> interface for the thin oxides has not been considered.

Nevertheless, the KMC simulations for 10nm oxide thickness show the same trend than for 8 nm. The mean NC size and density increase if the ion fluences is increased at constant annealing time. Tough for the highest fluence of  $5 \times 10^{15} \text{ cm}^{-2}$  this is not the case. Rather, the NC density is lower (up to 1000 kMCS) than for  $3 \times 10^{15} \text{ cm}^{-2}$ . Simultaneously, the mean NC size has increased significantly, which indicates that a considerable amount of coalescence occurs during NC ripening. This is also supported by Figure 5.6 showing that the average precipitate shape deviates from the spherical form. Even more, the shape monitored by  $\delta$  in Figure 5.6 does not approach smoothly the value of an ideal sphere, but increases temporarily before it falls off again, which can only be attributed to coalescence. However during long thermal annealing (more than 5000 kMCS) the larger precipitates are more stable against dissolution in the presence of the nearby interface. So, The NC density decays more slowly for  $5 \times 10^{15} \text{ cm}^{-2}$  than for lower Si<sup>+</sup> fluences.

### 5.3.2. Impact of the oxide thicknesses

The impact of the distance of the absorbing SiO<sub>2</sub>/Si interface on the Si phase separation is studied in further simulations, the oxide thickness has been varied between 5 and 20 nm. Figure 5.15 displays KMC simulation snapshots of Si phase separation in 1 keV Si<sup>+</sup> implanted SiO<sub>2</sub> layers at an annealing time of 1000 kMCS. The simulations were carried out at  $\epsilon = 2$  for an ion fluence of  $2 \times 10^{15} \text{ cm}^{-2}$ , i.e. the initial Si excess profile was chosen according to the TRIDYN calculations of Figure 3.4. Mixing of the Si/SiO<sub>2</sub> interface by recoils has been neglected here to study solely the influence of the oxide thickness on the NC evolution.

It can clearly be seen in the top row of Figure 5.15 that more Si atoms (shown in light gray) have condensed onto the Si/SiO<sub>2</sub> interface in the case of the 6 nm thick SiO<sub>2</sub> than for the thicker oxides. The strong concentration gradient drives a flux of dissolved Si atoms towards the Si interface, where they become attached. Accordingly, this Si loss gives rise

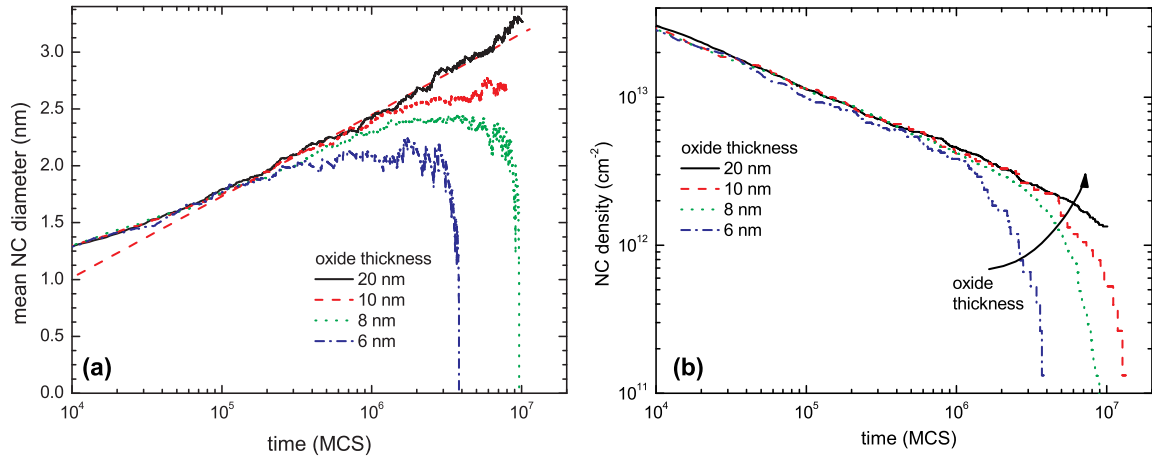
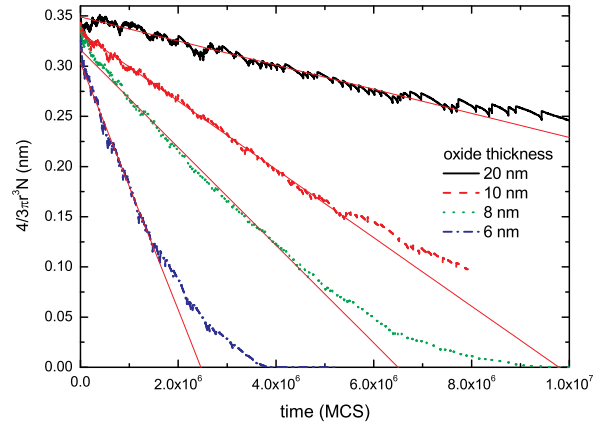


**Figure 5.15.:** KMC predictions for the time evolution of the NC size (a) and the NC density (b) for different oxide thicknesses. Simulations refer to 1 keV implantation to a fluence of  $2 \times 10^{15} \text{ cm}^{-2}$ .

**Figure 5.16.:** KMC prediction of the time evolution of the total precipitated Si volume per unit area estimated by  $4\pi/3\bar{r}^3N$ . Simulations were carried for different oxide thicknesses and refer to 1 keV implantation to a fluence of  $2 \times 10^{15} \text{ cm}^{-2}$ .



to smaller NCs at lower density in the thin oxide compared to thicker ones. However, this difference is not observed in early stages of annealing (up to 200 kMCS). Regardless of the oxide thickness, NCs grow initially nearly according to a *power law* seen as straight line in Figure 5.15(a). As similar behavior is found in Figure 5.15 (b) for the decay of the NC density. The NCs are screened initially from the strong sink of the absorbing interface, which can be qualitatively described by the *diffusional screening length*  $\lambda = (4/3\pi\bar{r}N_v)^{-2}$  introduced by Brailsford et al. (1976). Since NCs nucleate at very high density,  $\lambda$  is small at the beginning of annealing. Coarsening reduces the NC density and the screening length  $\lambda$  grows progressively until the NC are no longer screened from the diffusional interaction with the interface. This occurs first for the 6 nm thick oxide and can be seen in the time evolution of the mean NC size, Figure 5.15(a), as well as for NC density plotted in Figure 5.15(a). The NC size saturates for a period of further annealing before it drops rapidly to zero. Instead, the decrease of the NC density accelerates compared to the previous power law behavior. For the thicker oxides, the same qualitative behavior is observed setting in at later annealing times.

A linear volume loss has been predicted in section 5.1 for single NCs in the vicinity of an absorbing interface. Strikingly, this behavior holds true also for the total loss of precipitated

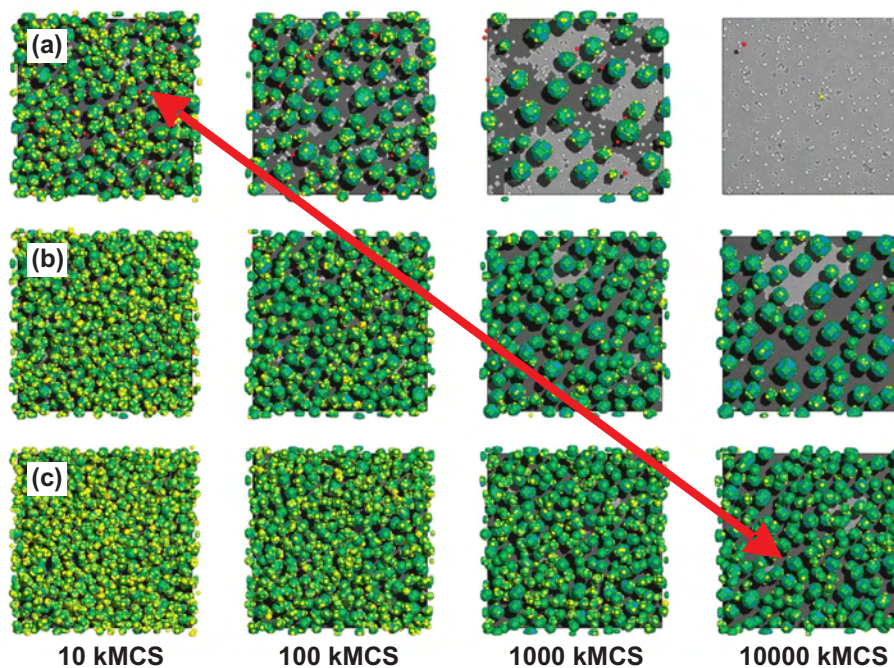


**Figure 5.17.:** KMC simulation snapshots (plane view) of Si phase separation in 8 nm thick SiO<sub>2</sub> for annealing temperatures of (a)  $\epsilon = 2.0$ , (b)  $\epsilon = 3.0$  and (c)  $\epsilon = 4.0$ . The simulations refer to 1 keV Si<sup>+</sup> implantation to a fluence of  $2 \times 10^{15} \text{ cm}^{-2}$  according to TRIDYN calculations of Figure 3.4. Similar precipitate morphologies are observed either for high temperatures ( $\epsilon = 2.0$ ) and short annealing times (10 kMCS) or low temperatures ( $\epsilon = 4.0$ ) and for long annealing (10000 kMCS).

Si per unit area that is approximately given by  $4\pi/3\bar{r}^3N$ . For different oxide thicknesses, this quantity is plotted in Figure 5.16 and clearly show the most rapid loss of Si for the lowest SiO<sub>2</sub> thickness of 6 nm. NCs in thicker oxides are progressively further apart from the interface and therefore loose Si at smaller rate due to the smaller concentration gradient.

### 5.3.3. Annealing temperature and time scale

Beyond annealing time and oxide thickness, the annealing temperature critically governs the NC evolution. Up to now KMC simulations were conducted for a single temperature only,  $\epsilon = 2$  according to equation (4.8). However, a direct link between  $\epsilon$  and experimental temperatures cannot be given due to the insufficient thermodynamic database (cp. section 4.2.1). Rather, KMC simulations are employed to study the reaction path of Si phase separation from SiO<sub>2</sub> instead of giving quantitative results for annealing times or temperatures.

Studies on diffusion controlled OSTWALD ripening deduced that a temperature change affects in first place just the speed of the NC evolution (Strobel, 1999). Qualitatively, the route of phase separation is not directly affected by a varied annealing temperature – a case that holds for low energy IBS as revealed by Figure 5.17. Shown are KMC simulation snapshots for 1 keV Si implantation into 8 nm thick SiO<sub>2</sub> to a fluence of  $2 \times 10^{15} \text{ cm}^{-2}$ , where the simulations were performed at three different temperatures ( $\epsilon = 2.0, 3.0$ , and  $4.0$ ). For the highest temperature ( $\epsilon = 2.0$ ), NCs nucleate and grow fast but dissolve then during



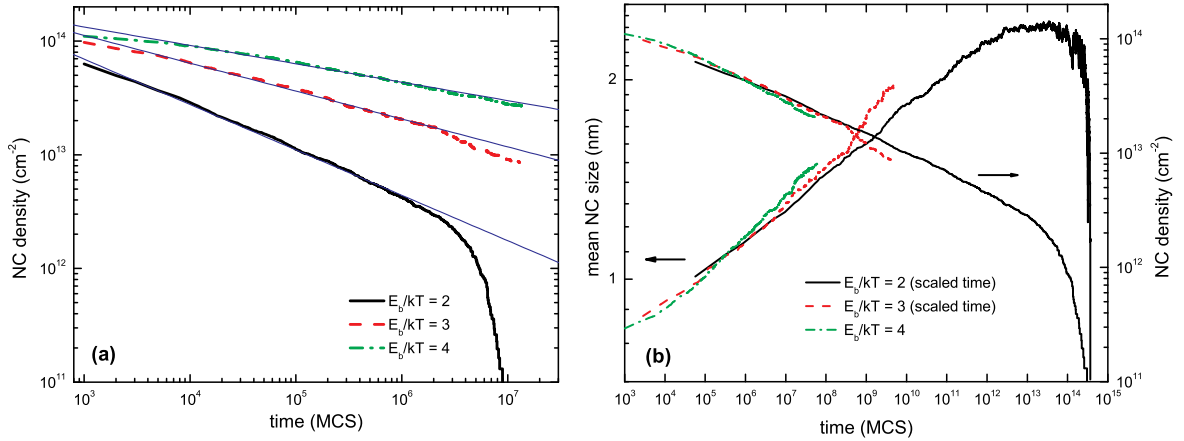


**Figure 5.18.:** (a) Time evolution of the NC density as predicted by KMC simulation of phase separation for 1 keV implantation to a fluence of  $2 \times 10^{15} \text{ cm}^{-2}$  into 8 nm thick SiO<sub>2</sub>. The simulation was carried out for three different temperatures. (b) Time evolution of the mean NC size and density for the same conditions. Only the annealing time has been scaled for simulations with  $\varepsilon = 2$  and  $\varepsilon = 3$  as described in the text. An universal curve for both NC size and density is obtained, which holds for all three annealing temperatures.

further annealing. A similar NC evolution is also found at lower temperature, however, at much lower speed. The last snapshot on the right of the bottom row of Figure 5.18 shows a NC morphology (NC size and density) that is similar to the snapshot shown on left of the top row.

Moreover, the NC densities displayed in Figure 5.18(a) follow a power law as long as the influence of the absorbing interface is not yet dominating, whose exponent depends on the annealing temperature

$$n_i(t) = a_i t^{b_i} \quad \text{for } \varepsilon_i = \{2, 3, 4\}. \quad (5.10)$$

The coefficients  $a_i$  and exponents  $b_i$  are obtained by fitting and obey a simple phenomenological scaling relation

$$\varepsilon_1 \rightarrow \varepsilon_2 \quad t_2 = \frac{a_1}{a_2} t_1^{(b_1/b_2)}, \quad (5.11)$$

which allows to scale the time such the curves for the two higher temperatures ( $\varepsilon = 2.0, 3.0$ ) to fit the time scale of the lowest temperature ( $\varepsilon = 4.0$ ). This is shown in Figure 5.18(b), where the necessary scaling parameters were determined according to (5.11). All three curves of the displayed NC density fall over each other and form one universal curve. Even more, the same scaling holds true for the time evolution of the mean NC size shown in Figure 5.18(b), despite the scaling parameters where determined based on the fitted NC densities only.

As a change in the annealing temperature leads only a different speed (time scale) of the NC evolution, it is justified to carry out KMC simulations only for a single temperature as long as only the route of phase separation is studied and quantitative results are not necessary. In the present work, KMC simulations were therefore performed at the highest temperature ( $\varepsilon = 2$ ), where phase separation proceeds with the highest speed. Additionally, this reduces the necessary computing time to study the NC evolution from nucleation up to the complete

dissolution<sup>3</sup>.

Nevertheless, it has to be noted that the present scaling analysis was carried out only for a Si excess concentration that leads to phase separation in the nucleation and growth regime. There, NCs are isolated from each other and can be characterized in good approximation by two parameters only, the mean cluster size and the cluster density. It might be different for phase separation by spinodal decomposition and might also affect percolation. Thus the scaling of the annealing time according to (5.11) might only hold in first approximation.

### 5.3.4. Characterization of the NC size distribution

IBS generally gives rise to a broad NC size distribution due to the competitive nature of OSTWALD ripening. However, the stationary LSW size distribution known for diffusion controlled OSTWALD ripening in diluted and homogeneous supersaturations (Lifshitz and Slyozov, 1961; Wagner, 1961) is certainly achieved due to high supersaturations, the inhomogeneity of the Si excess profile and the absorbing SiO<sub>2</sub>/Si interface.

Here, KMC simulations can give valuable insights into the nature of the NC size distribution and their evolution in the course of annealing. Using the cluster counting scheme described in section 4.2.2, the size distribution has been determined at different annealing stages for the implantation conditions of 1 keV Si implantation into 8 nm to a fluence of  $2 \times 10^{15} \text{ cm}^{-2}$ . The empirical distributions are plotted in Figure 5.19 together with the corresponding plane view snapshots. A right-skewed distribution is observed at the earliest annealing time of 100 kMCS with the mean at about 1.3 nm diameter. At that early stage, the size distribution can be approximated by a log-normal distribution

$$f(R) = \frac{1}{\sigma^* \sqrt{2\pi x}} \exp \left\{ -\frac{(\ln R - \mu^*)^2}{2\sigma^{*2}} \right\}, \quad (5.12)$$

drawn as solid line in Figure 5.19(a). The parameters<sup>4</sup>  $\mu^*$ ,  $\sigma^*$  were chosen to yield the same average cluster size and standard deviation than the empirical distribution of Figure 5.19. Longer annealing reduces first the skewness and then shifts the distribution modal to higher values such that it becomes left-skewed as a LSW distribution. However, the reduced NC density and therefore the lacking statistical reliability prevents a clear statement of the type of distribution at this stage.

Interestingly, the size distribution of precipitates formed already in the spinodal decomposition regime at an ion fluence of  $5 \times 10^{15} \text{ cm}^{-2}$  still shows a nice log-normal shape at early annealing times. The deviation of the empirical size distribution plotted in Figure 5.20(a) from a log-normal distribution is small and the probability plot of the log-sizes in Figure 5.20(b) shows nearly a straight line indicating that the cluster sizes are log-normal distributed. It must be noted that the NC diameter is not correctly captured by the detection algorithm as precipitates become elongated by spinodal decomposition. The cluster volume,

<sup>3</sup>With the applied Metropolis algorithm, the simulation of NC dissolution at the lowest temperature ( $\epsilon = 4$ ) is currently far beyond the computational abilities. Only continuous time Monte Carlo methods, that internally employ a scaled time, are capable to cover the complete process.

<sup>4</sup>The parameters  $\mu^*$  and  $\sigma^*$  are the mean and the standard deviation of the corresponding Gaussian distribution, respectively.

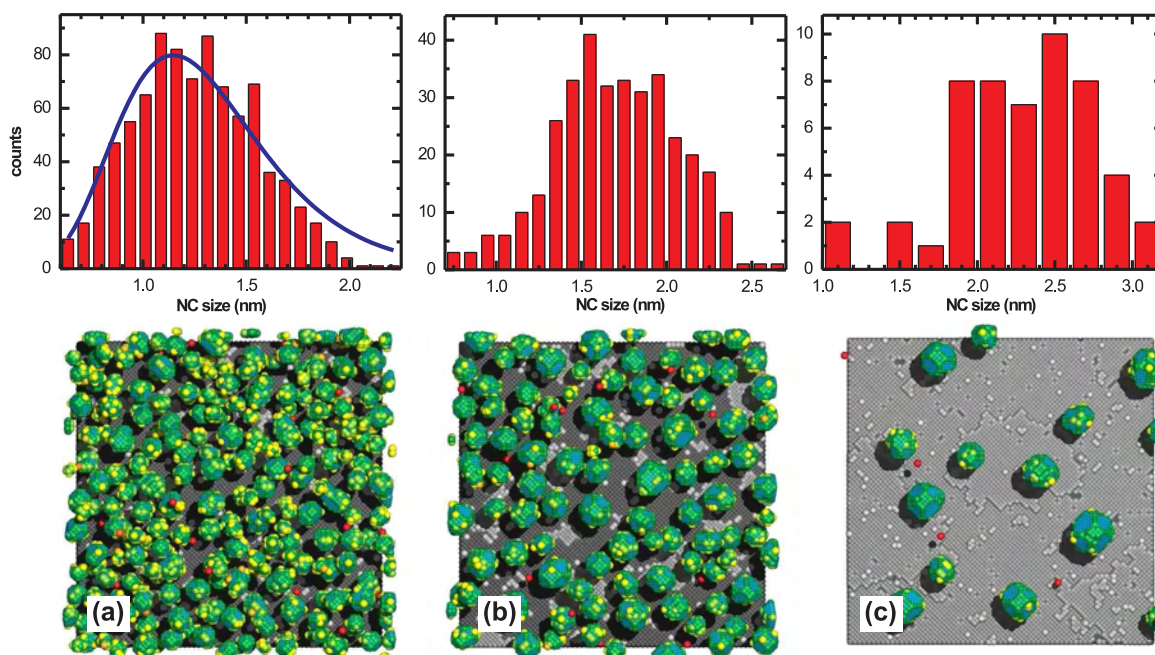


**Figure 5.19.:** NC size distribution (top) determined from KMC simulation snapshots (bottom) at (a) 10 kMCS, (b) 100 kMCS, and (c) 4000 kMCS. A log-normal distribution has been overlaid on (a) for comparison having the same mean and standard deviation. The simulation conditions correspond to 1 keV  $\text{Si}^+$  implantation to a fluence of  $2 \times 10^{15} \text{ cm}^{-2}$  into 8 nm thick  $\text{SiO}_2$ . Note that only a quarter of the simulation cell is shown in the plane view snapshots in the bottom row.

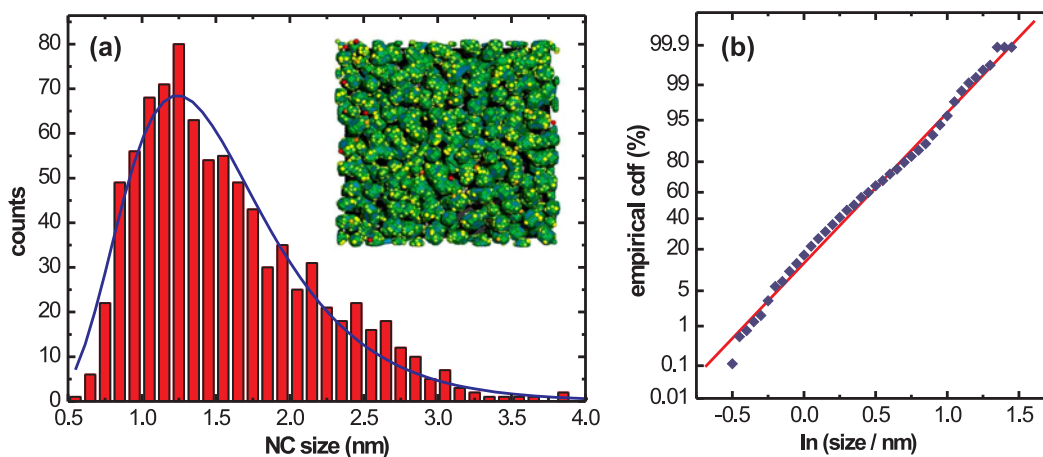


**Figure 5.20.:** (a) Predicted size distribution of Si precipitates formed by spinodal decomposition for an annealing time of 10 kMCS. The empirical distribution is close to a log-normal distributions shown as solid line. The simulation conditions correspond to 1 keV  $\text{Si}^+$  implantation to a fluence of  $5 \times 10^{15} \text{ cm}^{-2}$  into 8 nm thick  $\text{SiO}_2$ . (b) Probability plot of the empirical cumulative density function of the log cluster sizes. A straight line indicates a Gaussian distribution, hence, the NC sizes itself are log-normal distributed.

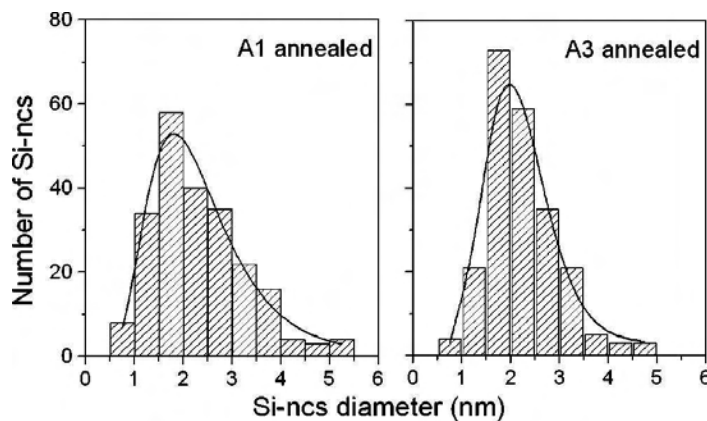


**Figure 5.21.:** Experimental NC size distribution measured by a combination of cross sectional high-resolution TEM and dark-field plane view TEM for 1 keV  $\text{Si}^+$  implantation to a fluence of  $5 \times 10^{15} \text{ cm}^{-2}$  into 9 nm thick  $\text{SiO}_2$ . A2 and A3 annealing is explained in the text. Taken from Normand et al. (2003).

however, is still correctly determined. Further, the log-normal distribution itself is invariant against such transformations, its shape is maintained upon the transition from cluster volumes to cluster diameters.

There is still a considerable debate in the literature about the microscopic origin of the log-normal size distribution, nevertheless some authors (Bergmann et al., 1998; Pande and Dantsker, 1991) attribute its occurrence to nucleation in the absence of cluster coarsening. Stretching this explanation further indicates that coarsening of Si NCs is here negligible up to 10 kMCS. In this respect, nucleation and spinodal decomposition behave quite similar. In both cases, a log-normal size distribution is observed initially despite of the different precipitate morphology.

Experiments of Normand et al. (2003) using low-energy ion beam synthesis of Si NCs have also revealed a size distribution that is close to the log-normal case. The empirical size distribution is shown in Figure 5.21 for 1 keV  $\text{Si}^+$  implantation to a fluence of  $2 \times 10^{16} \text{ cm}^{-2}$  into 9 nm thick  $\text{SiO}_2$ . The authors utilized different furnace anneal conditions: (a) 950 °C/30 min in inert  $\text{N}_2$  ambient and (b) 950 °C/30 min in  $\text{N}_2$  diluted oxygen (1.5%  $\text{O}_2$  per volume), referred as A1 and A3 in Figure 5.21. Consequently, NCs are on average smaller for annealing in oxidizing ambient (A3 annealing).

However, the experimental size distribution shown in Figure 5.21 has to be considered with some reluctance. PEELS-STEM studies (Müller et al., 2004a) revealed percolated spinodal Si patterns for these implantation condition (A1 annealed), hence the measured size distribution might reflect only the grain size distribution but not the distribution of the percolated Si precipitates.

### 5.3.5. Process options for an optimum NC size and density

In summary, low energy IBS can favorably be used to fabricate Si NCs in thin gate oxides for nonvolatile memory application. Average NC sizes of in the order of 1.5 to 3 nm can be achieved at areal densities of  $1 \dots 10 \times 10^{12} \text{ NCs cm}^{-2}$ . The necessary control over NC size and density is gained through:

- (i) the *ion fluence* implanted into the oxide and therefore the amount of the introduced Si excess. However, too high fluences alter the precipitate shape if the spinodal decomposition regime is reached (cp. section 5.2, Figure 5.5).



- (ii) The *annealing time* (and *temperature*) controls to which extent coarsening did proceed and therefore gives direct control over the NC size and density.

Still, the absorbing Si/SiO<sub>2</sub> interface influences the kinetics of NC growth and dissolution, which becomes especially pronounced for low Si excess concentrations. The power law behavior of cluster growth observed at early annealing times is detracted by the absorbing interface later on. The mean NC diameter stagnates after initial growth, then reaches a maximum before the NCs dissolve completely. This maximum NC diameter reached in the course of annealing is directly related to the distance of the NCs from the SiO<sub>2</sub>/Si interface. The closer the profile is located from the interface the faster the NCs dissolve and the smaller is the largest size of the NCs reached during annealing.

Nonetheless, it remains unclear whether the dissolution stage can actually be reached under the standard experimental conditions. There are strong indications that the NC coarsening has not proceeded far enough to reveal the late stage cluster dissolution. This is also supported by the log-normal shape of the empirical NC size distribution indicating nucleation in the absence of strong coarsening effects.

## 5.4. Process modeling of a self-aligned NCs formation

Process simulations clearly show that Si precipitates formed in the course of phase separation at low energy IBS *align* nicely in a thin layer parallel to the SiO<sub>2</sub>/Si interface – a fact that has been confirmed by XTEM investigations in Figure 5.11. The the predictions of Figure 5.5 and 5.14 reveal furthermore a thin zone between the NC layer and the SiO<sub>2</sub>/Si interface that is completely depleted of Si NCs (Müller et al., 2002)<sup>5</sup>. This NC free zone forms in a self-adjusting manner during the annealing and can act as tunneling barrier in a NC memory for charge injection by direct electron tunneling.

### 5.4.1. Prediction of a self-adjusted electron tunneling barrier

The SiO<sub>2</sub>/Si interface acts as a strong sink for diffusing Si atoms, and therefore leads to a NC-depleted zone parallel to the interface. This *denuded zone* will serve as tunneling oxide in the NC memory and isolates the NC from the transistor channel. At charge injection during the write pulse, electrons have to overcome the barrier by Fowler-Nordheim tunneling or could penetrate the barrier by quantum mechanical direct electron tunneling. In both cases, the width of the injection oxide critically determines the memory properties as writing speed required for charging of the NCs and charge retention. It is therefore of vital importance to control the tunneling distance at which NCs are separated from the SiO<sub>2</sub>/Si interface.

Different factors have been found to influence the width of the *denuded zone*:

- oxide thickness (Bonafos et al., 2004; NEON, 2003)
- ion energy (Bonafos et al., 2004; Carrada et al., 2003; NEON, 2002a)

---

<sup>5</sup>A fact that in general has been predicted for system undergoing OSTWALD ripening (Burghaus, 1998).

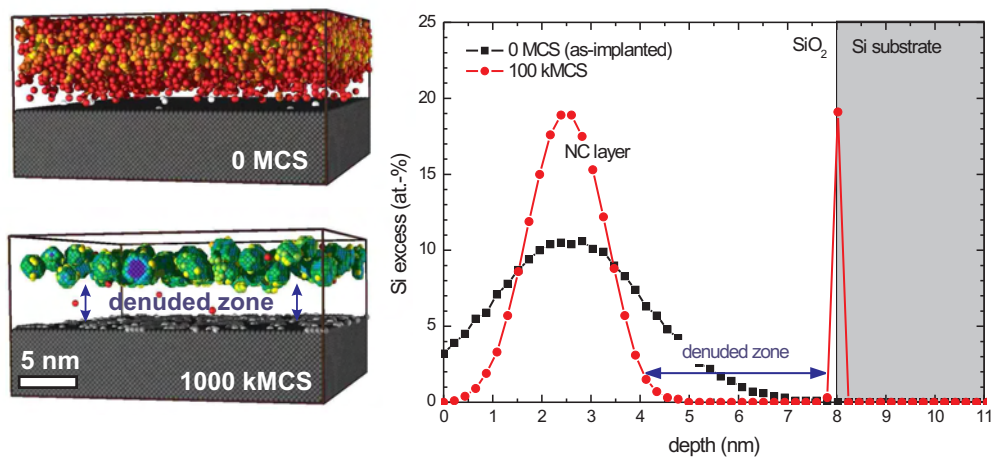


**Figure 5.22.:** Formation of a denuded zone free of NC at the SiO<sub>2</sub>/Si interface during phase separation as predicted by KMC simulations. On the left, two KMC simulation snapshots (cross section view) are shown for 1 keV Si<sup>+</sup> implantation into 8 nm thick SiO<sub>2</sub> to a fluence of  $2 \times 10^{15} \text{ cm}^{-2}$ . The first refers to the as-implanted case while the second was taken after 100 kMCS. On the right, the corresponding Si excess depth profiles are plotted.

- ion fluence (Carrada et al., 2003; Müller et al., 2002; NEON, 2002b)
- annealing temperature and time (Müller et al., 2002; NEON, 2002c)
- annealing ambient (NEON, 2002c; Normand et al., 2003)

The first two factors are certainly the most obvious one. In first order, NCs form during annealing around the projected range of the implanted Si<sup>+</sup> ions. Hence, ion energy and oxide thickness can directly be used to control the distance between Si NCs and the Si/SiO<sub>2</sub> interface. Still, it has to be noted that this control is not complete as additional effects come into play. The width of the denuded zone is not independent of the annealing time as it depends on the morphology of the multi-dot floating-gate formed by low energy IBS.

For this reason, KMC simulations were performed and evaluated to determine the distance between the Si NCs and the SiO<sub>2</sub>/Si interface. For this purpose, the depth profiles of the Si excess were recorded for different annealing times. An example is shown in Figure 5.22 for 1 keV Si<sup>+</sup> implantation into 8 nm thick SiO<sub>2</sub> to a fluence of  $2 \times 10^{15} \text{ cm}^{-2}$ . Si excess depth profiles are plotted for the as-implanted case and after 100 kMCS. Clearly, the Si excess profile became narrower and the peak concentration has increased due to Si precipitation<sup>6</sup>. Moreover, no Si excess is observed in 3...4 nm thick zone close to the SiO<sub>2</sub>/Si interface. Si atoms have either condensed onto the Si substrate or onto the formed Si NCs, which are further apart from the interface. The formed denuded zone can also be seen in the KMC simulation snapshots shown on the left of Figure 5.22.

In further KMC simulations, the width of the denuded zone is recorded at several intermediate annealing steps. It is measured as the distance from the SiO<sub>2</sub>/Si interface where the Si excess concentration first exceeds a threshold of 0.1 at.-%.

<sup>6</sup>This effect is sometimes called *up-hill diffusion* as it phenomenologically appears to be a time-reversed diffusional broadening of a thin marker layer.

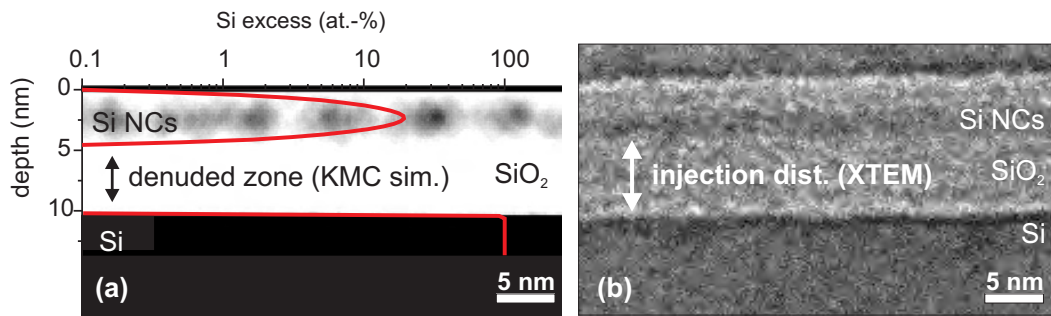


**Figure 5.23.:** Comparison of the denuded zone determined from a KMC simulation snapshot (a) with the injection distance measured on an XTEM image (b). The Si excess depth profile has been overlaid on the KMC simulation snapshot (a). The experimental conditions of (b) have been related to the simulation conditions of (a) through the equivalent morphology shown in plane view of Figure 5.9(a,b). The images refer to 1 keV Si<sup>+</sup> implantation into 10 nm thick SiO<sub>2</sub> at a fluences of (a)  $3 \times 10^{15} \text{ cm}^{-2}$  and (b)  $1 \times 10^{16} \text{ cm}^{-2}$ .

### 5.4.2. Comparison to XTEM results

How does the width of the denuded zone predicted by KMC simulations relate to experimentally determined values, e.g. by XTEM studies of Ben Assayag et al. (2003) and Carrada et al. (2003)? In general this is very difficult to answer due to the immanent uncertainties between experiment and simulation. However, the morphology of phase separated Si has been used for a comparison in section 5.2.2. With the help of PEELS-STEM investigations, experimental and simulation conditions were identified that yield equivalent morphologies as shown in Figure 5.9 and 5.11. With these results, the tunneling distance between Si NCs and the SiO<sub>2</sub>/Si interface can be assessed for 1 keV Si<sup>+</sup> implantation into SiO<sub>2</sub>.

For that aim, the cross-section views of Figure 5.11 are redisplayed in Figure 5.23 and 5.24, where in addition Si excess depth profiles have been overlaid onto the KMC simulation snapshots on the r.h.s of both figures. The KMC simulations and XTEM images agree remarkably well for both fluences, despite different tunneling distances were estimated. With a concentration threshold of 0.1 at.-% Si excess, a denuded zone of 5.4 nm width has been determined from Figure 5.23 (a). Carrada et al. (2003) give a much different value of about 7 nm for the XTEM image of Figure 5.23 (b). This difference becomes even more pronounced at the higher ion fluence for which the cross section views are displayed in Figure 5.24. Despite of the comparable cross section views, the width of the denuded zone was estimated to be 4.6 nm for the KMC simulation shown in Figure 5.24 (a). On the contrary, XTEM measurements give a value of more than 8 nm. Here the KMC simulation have accounted for the shoulder in the Si excess profile displayed in Figure 5.24 (a), while the XTEM investigation could not.

Accordingly, the apparent reason for the deviating tunneling distances between experiment and simulation are not in first place deviating conditions but a different definitions of the tunneling distance. The KMC simulation relies here on a thresholding procedure to a Si excess level of 0.1 at.-%. On the other hand, XTEM measurements merely estimate the layer-to-layer distance that can be seen in Figure 5.23 (b) and 5.24 (b).

From a more general point of view it is difficult to argue which definition of the tunneling distance is more relevant for the electrical properties of the NC memory. At high NC density, it is likely that charging of the Si NCs occurs by direct electron tunneling (or FN-tunneling)

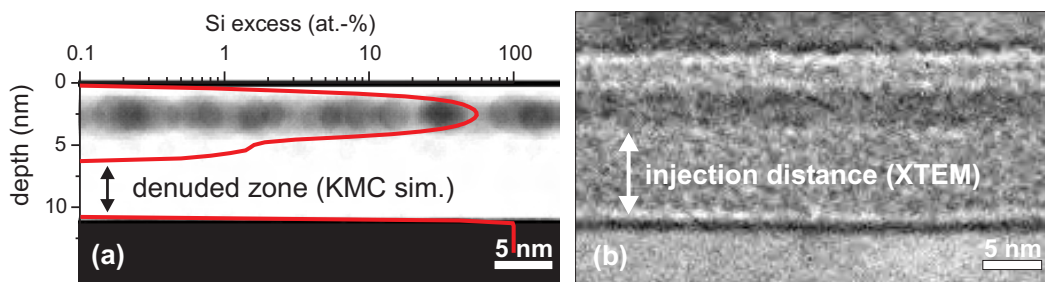


**Figure 5.24.:** Comparison of the denuded zone determined from a KMC simulation snapshot (a) with the injection distance measured on an XTEM image (b). The Si excess depth profile has been overlaid on the KMC simulation snapshot (a). The experimental conditions of (b) have been related to the simulation conditions of (a) through the equivalent morphology shown in plane view of Figure 5.9(c,d). The images refer to 1 keV Si<sup>+</sup> implantation into 10 nm thick SiO<sub>2</sub> at a fluences of (a)  $8 \times 10^{15} \text{ cm}^{-2}$  and (b)  $2 \times 10^{16} \text{ cm}^{-2}$ .

to the clusters being closest to the SiO<sub>2</sub>/Si interface as they exhibit the highest tunneling probability (Brown and Brewer, 1998, chapter 1.2). Charge can then spread from these NCs into the whole NC layer via a Pool-Frenkel mechanism. In that sense, the very first NCs will determine the width of the effective barrier between the transistor channel and the Si NCs, i.e. the denuded zone.

On the other hand, the density of these very close NCs is extremely small. So only a small current can flow through these NCs into the NC layer if the NC density is small, i.e. the distances between the clusters are large. Then the majority of the NCs are more likely to be charged by direct tunneling from the Si channel. In this case, the tunneling distance should be better defined as the onset of the majority of the NCs as it is done in XTEM measurement (Ben Assayag et al., 2003; Carrada et al., 2003).

Hence, defining an unique tunneling distance always involves some ambiguity due to the stochastic nature of the NCs position. Rather, the full distribution of the tunneling distances between individual NCs and the SiO<sub>2</sub>/Si interface has to be considered, which is directly available from KMC simulations. Nevertheless, the necessary comparison to experimental values proves rather difficult. Mapping Si plasmon with the help of energy filtered TEM or PEELS-STEM on cross-section samples might provide in future the necessary advance in spatial resolution at sufficient material contrast.

### 5.4.3. Evolution of the tunneling distance in different regimes of phase separation

The width of the denuded zone is not solely determined by geometrical factors as the projected range of the incident ions or the initial oxide thickness. It also depends on the regime of phase separation in which Si precipitates have formed and remains not constant throughout the annealing process. This is revealed by Figure 5.5 displaying consecutive process simulation snapshots for 1 keV Si<sup>+</sup> implantation into 8 nm thick SiO<sub>2</sub>. The width of the NC free zone between the SiO<sub>2</sub>/Si interface and the NC layer has been recorded at intermediate simulation times and is plotted in Figure 5.25 for different ion fluences. At the lowest fluence of  $2 \times 10^{15} \text{ cm}^{-2}$ , the width of the denuded zone increases quickly during

annealing as dissolved Si atoms condense onto the Si substrate and the Si NCs. NCs close to the interface dissolve and a steady denuded zone of 3 nm is formed, whose width does not change until the complete dissolution of the Si NCs. This is different for the  $\text{Si}^+$  fluences of  $5 \times 10^{15} \text{ cm}^{-2}$  and  $1 \times 10^{16} \text{ cm}^{-2}$ , where after a slow rise the width of the denuded zone decreases during longer annealing. A stable regime with a denuded zone of constant width for longer periods of annealing is not reached. The reason for this behavior is a change in the *precipitate morphology*.

Figure 5.25 illustrates this for the  $\text{Si}^+$  fluence of  $1 \times 10^{16} \text{ cm}^{-2}$ . Spinodal decomposition takes place at the first stage of annealing. However, at the tails of the Si excess depth profile, where the Si concentration is much less than at the peak maximum, NC nucleate and therefore only a thin denuded zone is observed initially. In the course of further annealing, these NCs dissolve and Si condenses either onto the percolated Si network located around the projected ion range or onto the  $\text{SiO}_2/\text{Si}$  interface. Accordingly, a growing denuded zone is observed that reaches its maximum at 2000 kMCS, Figure 5.25. Nevertheless, the percolated Si network does not contain sufficient material to form a stable continuous Si layer embedded in the  $\text{SiO}_2$ , Figure 5.5(c). Longer annealing leads to a fragmentation into large Si clusters that subsequently minimize their interfacial energy via surface diffusion. In this specific case, material conservation implies that these droplets almost span the full oxide thickness and a strong decrease of the denuded zone is observed. This behavior is confirmed experimentally by studies of Kim et al. (2003) on Ge NCs. The authors have shown that a thin layer of amorphous Ge deposited by pulsed laser deposition, decays during annealing into isolated Ge NCs, which lead to a pronounced reduction of the tunneling distance.

#### 5.4.4. Control of the NC layer location by the implantation energy

Changing the  $\text{Si}^+$  ion energy at constant  $\text{SiO}_2$  thickness is expected to give control over the tunneling distance at which NCs are separated from the transistor channel. However, experimental studies of Bonafos et al. (2004) have shown that by increasing the ion energy the tunneling distance can be reduced only down to a minimum value of 5 nm. Even more, no Si NCs were observed by XTEM for ion energies above 3 keV. Figure 5.27 shows the corresponding XTEM images for  $\text{Si}^+$  implantation into 10 nm thick  $\text{SiO}_2$  at energies from 1 keV to 5 keV to a fluence of  $1 \times 10^{16} \text{ cm}^{-2}$ . The dark gray layer visible in the  $\text{SiO}_2$  fades as the energy is increased from 1 to 3 keV and finally cannot be seen for 5 keV. In contrast, the  $\text{SiO}_2/\text{Si}$  interface becomes rough as visible in Figure 5.27(a) or even faceted (b).

Systematic TRIDYN calculations presented in Chapter 3.2 have revealed the influence of the ion beam induced mixing of the  $\text{SiO}_2/\text{Si}$  interface. The calculations shown in Figure 3.5 (a) point out that the initially sharp  $\text{SiO}_2/\text{Si}$  interface becomes broadened and takes an error-function shape for ion energies above 2 keV. Recoils that have penetrated through the interface have led to silicon and oxygen displacements into the adjacent material and caused a considerable intermixing of the  $\text{SiO}_2$  and the Si substrate.

Starting at 4 keV ion energy, the interface mixing becomes even the dominating factor and a Gaussian implantation peak can no longer be distinguished in the TRIDYN depth profiles of Si excess plotted in Figure 3.5(a). This directly relates to the experimental finding that for

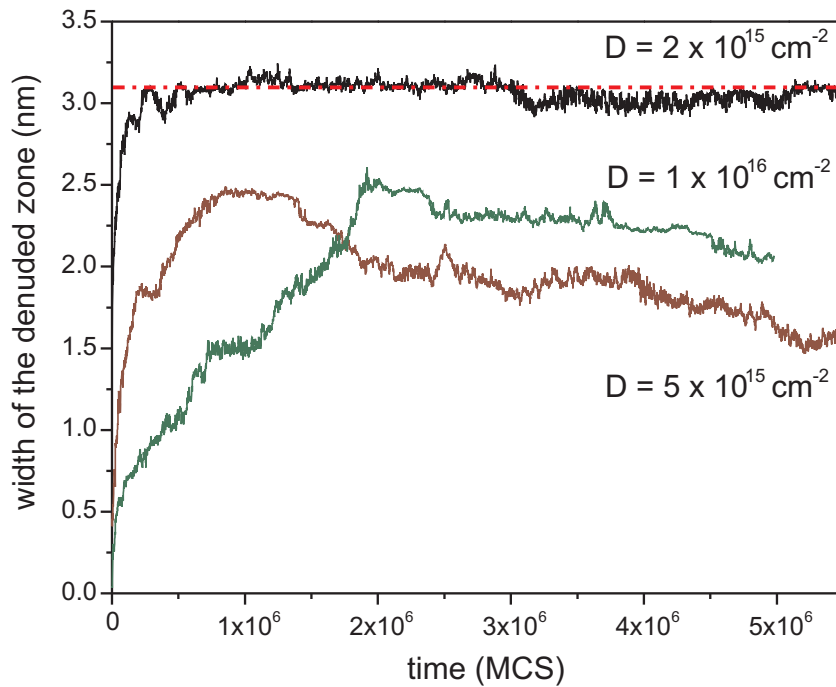


**Figure 5.25.:** Evolution of the width of the denuded zone as predicted by KMC simulation for 1 keV  $\text{Si}^+$  implantation into 8 nm thick  $\text{SiO}_2$ . The ion fluence was varied from  $2 \times 10^{15} \text{ cm}^{-2}$  to  $1 \times 10^{16} \text{ cm}^{-2}$ .

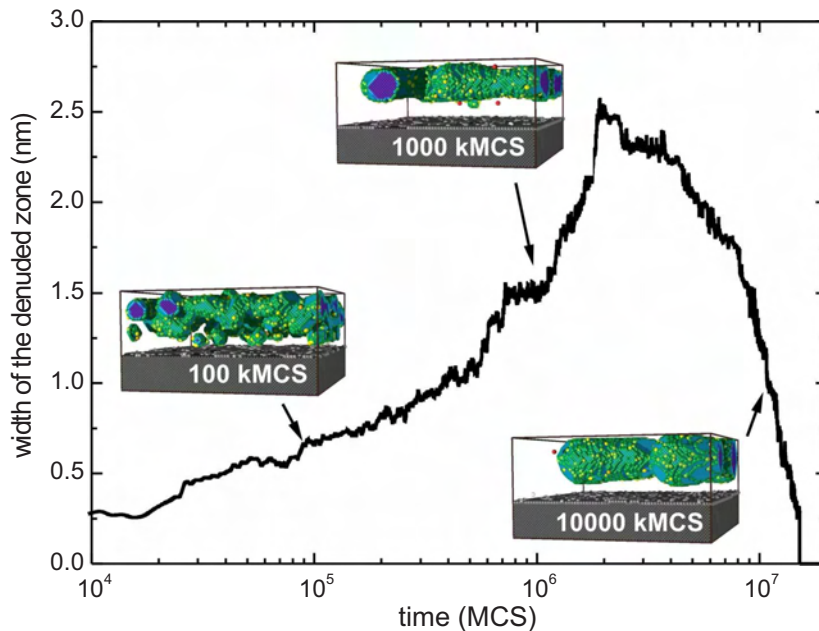


**Figure 5.26.:** Evolution of the denuded zone during annealing for 1 keV  $\text{Si}^+$  implantation into 8 nm thick  $\text{SiO}_2$  to a fluence of  $1 \times 10^{16} \text{ cm}^{-2}$ . The implanted Si excess forms large Si precipitates by spinodal decomposition that coalesce to an almost closed buried Si layer. During long annealing this layer fragments into large droplets that might even touch the  $\text{SiO}_2/\text{Si}$  interface.



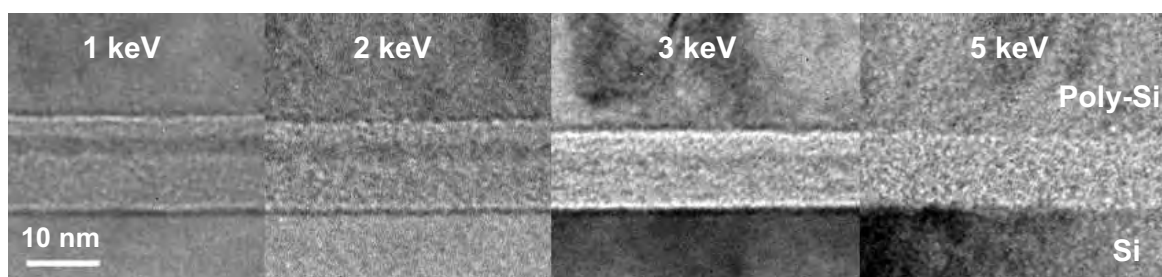


**Figure 5.27.:** Series of XTEM images taken under defocused bright field conditions for low energy IBS in 10 nm thick SiO<sub>2</sub> layers. The ion energy is progressively increased from 1 keV to 5 keV. From Bonafos et al. (2004).

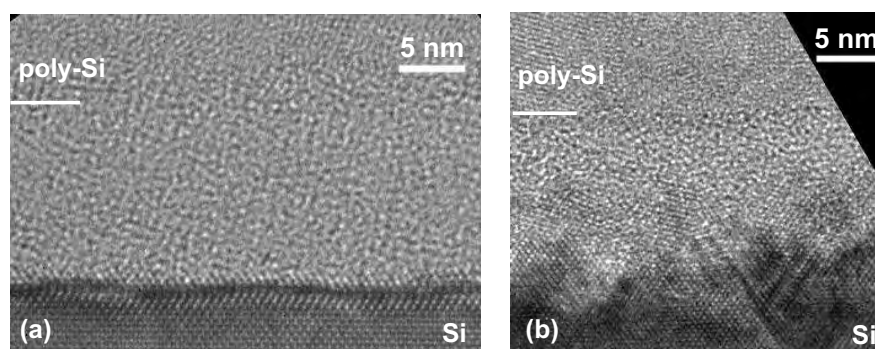


**Figure 5.28.:** HREM cross-sectional images of samples implanted at 5 keV to a fluence of (a)  $1 \times 10^{16} \text{ cm}^{-2}$  and (b)  $3.2 \times 10^{16} \text{ cm}^{-2}$ . Both have been annealed at 950 °C for 30 min in N<sub>2</sub>. The SiO<sub>2</sub>/Si interface is rough in both cases. A faceted interface as well as stacking faults and twins in the Si substrate are observed in (b). From Bonafos et al. (2004).

energies above 3 keV no Si NCs can be detected by XTEM, Figure 5.27. Phenomenologically, Si NCs are only observable by XTEM if a separate Gaussian peak is preserved in the Si excess profile (Bonafos et al., 2004). Despite of these results, all implantation conditions cause a significant Si excess in the SiO<sub>2</sub> layer that should precipitate during the annealing stage.

To clarify this discrepancy, KMC simulations of phase separation were performed which include the ion mixed SiO<sub>2</sub>/Si interface and study its impact on the NC formation. For this aim, the TRIDYN profiles of Figure 3.5 were approximated by a superposition of a Gaussian peak and an error-function as described in Chapter 3.2.3. These profiles were used as initial configuration for the further KMC simulation at  $\epsilon = 2$ . Snapshots of the KMC simulations are shown in cross section view in Figure 5.29, which utilizes a special false color scheme that shows both, Si precipitates in the SiO<sub>2</sub> (light blue to green) and SiO<sub>2</sub> precipitates in the Si substrate (violet). The corresponding depth profiles of Si excess are plotted in Figure 5.30.

Figure 5.29 (a) displays snapshot of the simulations that has already been shown in Figure 5.5 (c) for an ion energy of 1 keV. At this energy, phase separation leads to a layer of Si precipitates that is well localized in depth and separated by 2 to 3 nm from the SiO<sub>2</sub>/Si interface. A clear Gaussian profile of Si excess is found for this energy in Figure 5.30, which narrows during annealing.

If the ion energy is raised to 2 keV, the implantation profile broadens compared to 1 keV

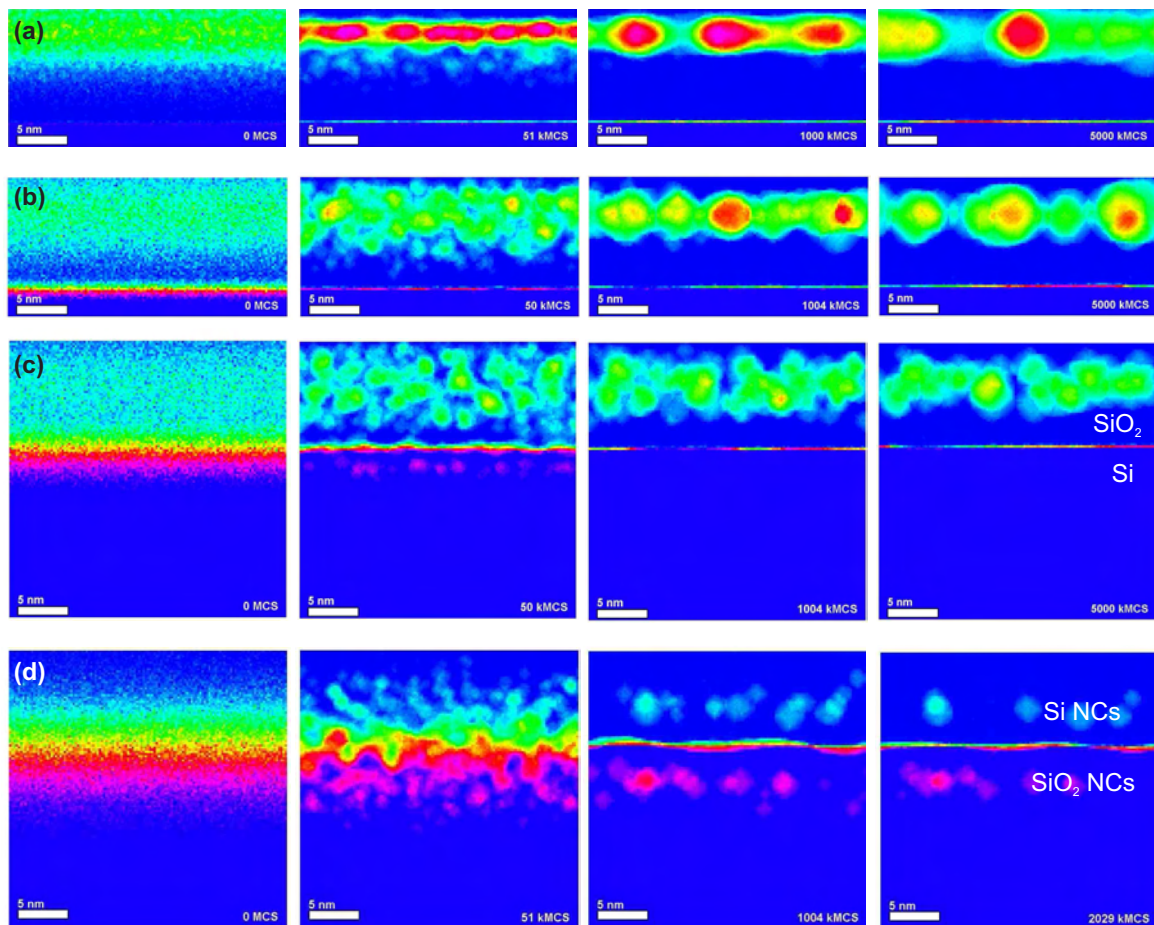


**Figure 5.29.:** KMC simulation snapshots (cross section view) in false-color cross-section view for  $\text{Si}^+$  implantation into 10 nm thick  $\text{SiO}_2$  to a fluence of  $1 \times 10^{16} \text{ cm}^{-2}$ . The  $\text{Si}^+$  ion energy is (a) 1 keV, (b) 2 keV, (c) 3 keV and (d) 5 keV. The size of the simulation cell has been  $27.8 \times 27.8 \times 13.9 \text{ nm}^3$  for (a,b) and  $27.8 \times 27.8 \times 27.8 \text{ nm}^3$  for (c,d).

and shift towards greater depth due to the increased ion range and range straggling. Additionally, interface mixing sets in and leads to a smoothing of the step-like Si profile at the  $\text{SiO}_2/\text{Si}$  interface. Upon phase separation, a rapid recovery of the mixed interface is observed as seen in Figure 5.29. The interface becomes again perfectly smooth. Additionally, Si precipitates are formed by spinodal decomposition in the  $\text{SiO}_2$  layer. These obey a broad initial depth distribution but narrow in the course of further annealing, Figure 5.30. A denuded zone free of NCs forms during this stage at the  $\text{SiO}_2/\text{Si}$  interface.

For 3 keV, the interface mixing becomes stronger and accordingly longer annealing is necessary for a complete recovery of the ion irradiated interface. Again, a broader distribution of the Si NCs emanates from the increased ion range straggling. The Si NCs span almost the full oxide and a denuded zone forms only during annealing as Si atoms condense onto the Si substrate, Figure 5.30. Note that these simulations also predict the formation of  $\text{SiO}_2$  precipitates in the Si substrate, which were also reported in experimental studies of Röntzsch (2003) for similar conditions of interface mixing.

At the highest energy of 5 keV, interface mixing dominates the Si excess profile, Fig-



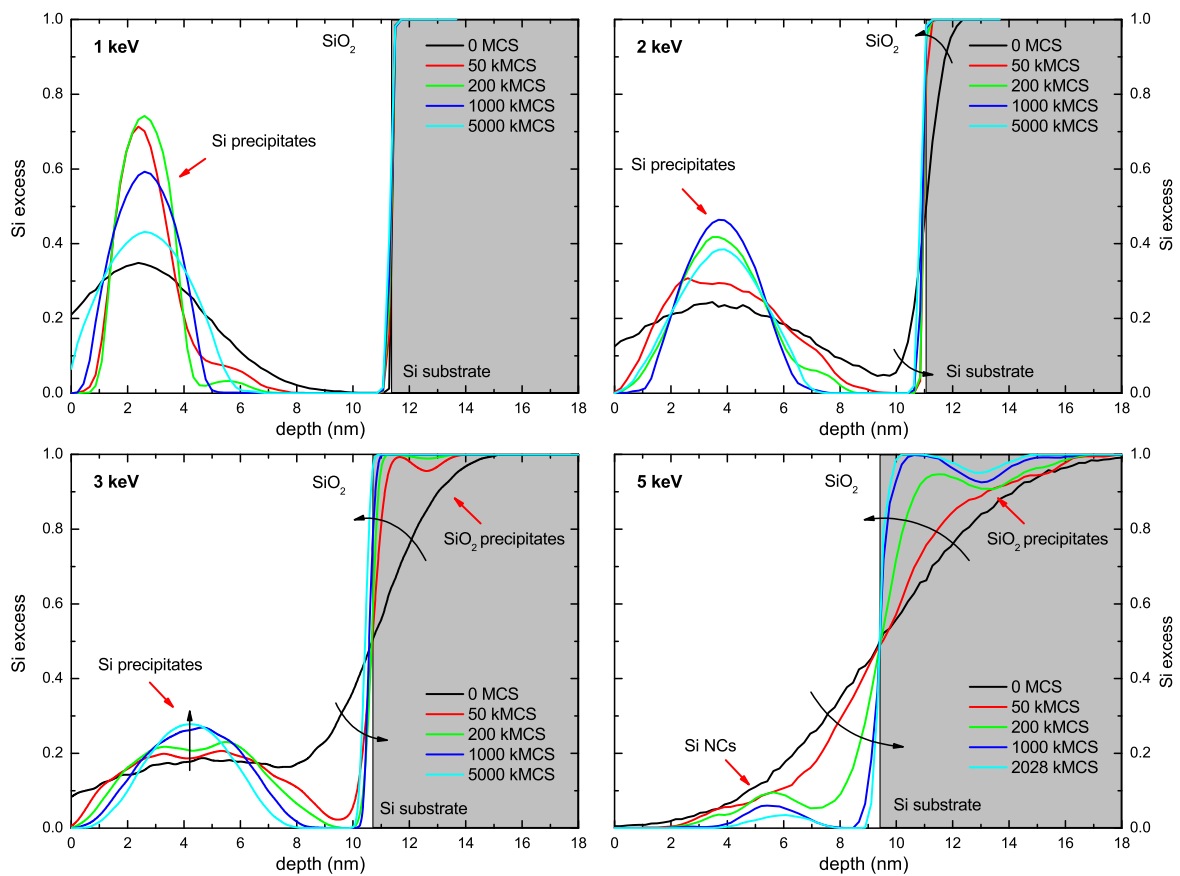


**Figure 5.30.:** Si excess depth profiles for the corresponding KMC simulation snapshots of Figure 5.29. The initial Si excess profiles were chosen according to TRIDYN calculations of Figure 3.5 (a) for a Si fluence of  $1 \times 10^{16} \text{ cm}^{-2}$ .

ure 3.5 (a), and it assumes a broad error-function like shape. Upon phase separation, the  $\text{SiO}_2/\text{Si}$  interface does recover only very slowly as apparent in Figure 5.29 (d). A layer of Si NCs in  $\text{SiO}_2$  as well as a layer of  $\text{SiO}_2$  inclusions in the Si substrate is left over, which both dissolve in the course of further annealing.

The time evolution of the width of the denuded zone is shown in Figure 5.31 for the conditions of Figure 5.29. The largest width of the denuded zone is found as it is expected for 1 keV  $\text{Si}^+$  implantation. Higher ion energies result in smaller tunneling distances since the Si ions have penetrated deeper into the oxide. Contrarily to the finding of Bonafos et al. (2004), Si NCs are predicted to form for all ion energies, either directly from the implanted Si (at low energies) or from the ion beam mixed Si excess (at larger ion energies).

A general remark has to be made concerning the low energy IBS involving ion beam mixing. It is important to recall that the Si substrate is amorphized upon implantation to a depth that increases with ion energy and fluence and typically ranges between 3 to 20 nm (Bonafos et al., 2004). Despite of the rapid solid phase epitaxial regrowth of the amorphized Si in the first milliseconds of the annealing, it is very likely that defects (e.g. dislocation loops) remain at the depth of the former amorphous/crystalline interface. These defects, which lay directly in the transistor channel may pose a threat to the electrical properties of

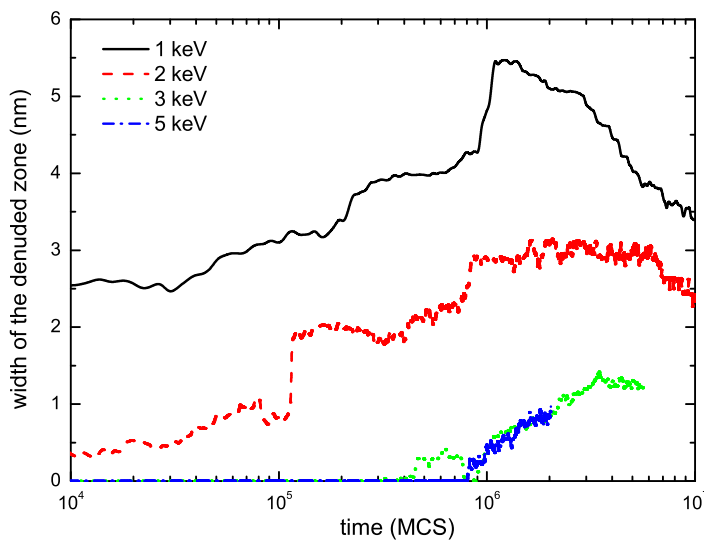


**Figure 5.31.:** Evolution of the width of the denuded zone as predicted by KMC simulation for  $\text{Si}^+$  implantation into 8 nm thick  $\text{SiO}_2$  at ion energies from 1 to 5 keV and a fluence of  $1 \times 10^{16} \text{ cm}^{-2}$ .

the NC memory cell transistor, e.g. reduce the carrier mobility, degrade the subthreshold slope or increase the sensitivity against punch-through of short-channel devices.

#### 5.4.5. Optimization of the initial oxide thickness

Another option to decrease the tunneling distance between the Si NCs and the  $\text{SiO}_2/\text{Si}$  interface is to decrease the initial oxide thickness at otherwise constant ion energy. In that case, the projected ion range and their range straggling of the implanted  $\text{Si}^+$  will remain constant. The layer of NCs is expected to form at a constant depth position during the annealing step having also a constant width. Changing the oxide thickness is expected to vary only the distance of that layer from the  $\text{SiO}_2/\text{Si}$  interface and therefore the injection distance between the Si NCs and the transistor channel.

Studies of Bonafos et al. (2004) confirmed this hypothesis and have shown that the tunneling distance can be controlled more efficiently than by the ion energy. Values as small as 2 nm can be achieved by this method. Figure 5.32 shows a sequence of XTEM images in underfocused bright field conditions for  $\text{SiO}_2$  thicknesses decreasing from 10 to 5 nm. Here, ion energy and fluence has been kept constant at 1 keV and  $10^{16} \text{ cm}^{-2}$ , respectively. An-

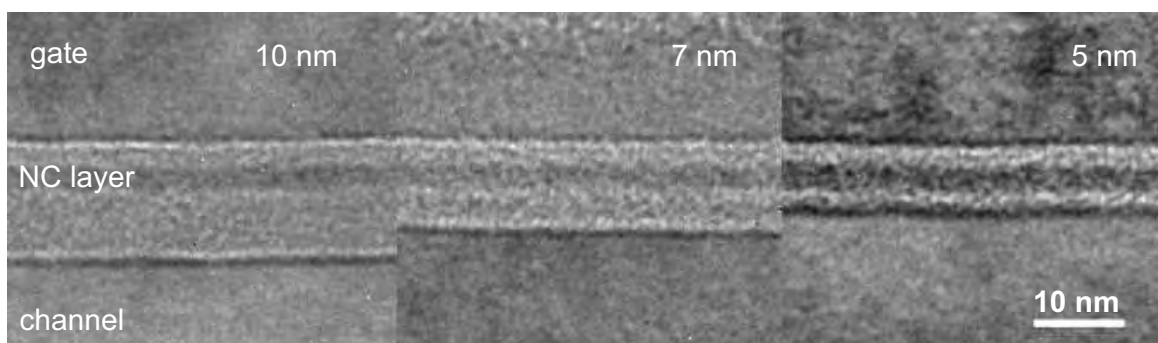


**Figure 5.32.:** Series of XTEM images taken under defocused bright field conditions for decreasing oxide thicknesses. From Bonafos et al. (2004).

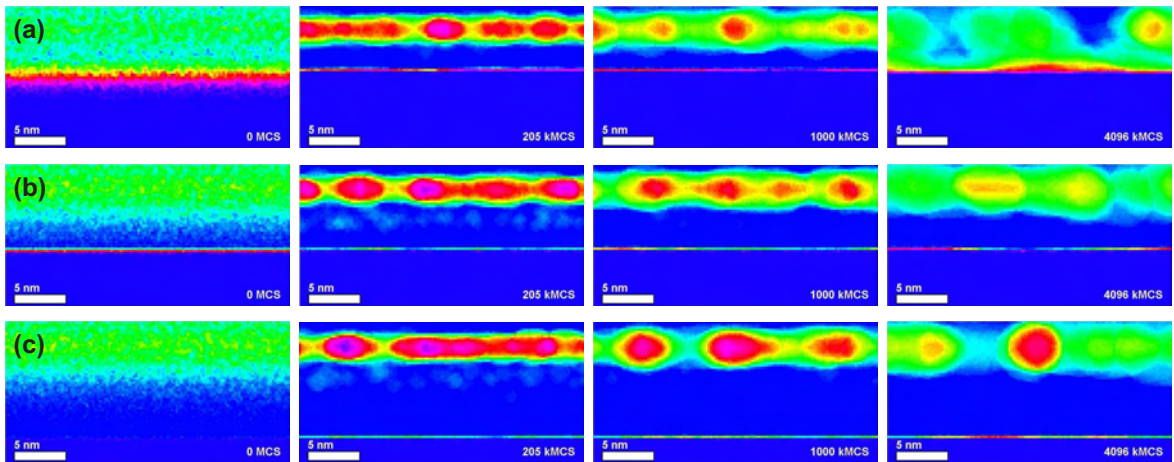


**Figure 5.33.:** KMC simulation snapshots (cross section views) in false-color cross-section view for 1 keV  $\text{Si}^+$  implantation into  $\text{SiO}_2$  to a fluence of  $10^{16} \text{ cm}^{-2}$ . The nominal oxide thickness has been varied from (a) 5 nm over (b) 7 nm to (c) 10 nm.

nealing was carried at  $950^\circ\text{C}$  for 30 min in  $\text{N}_2$ . The thickness of the control oxide (distance between the top of the NC layer and the  $\text{SiO}_2$  surface) as well as the width of the NC layer is almost constant for this case.

Rough  $\text{SiO}_2/\text{Si}$  interfaces are not observed in Figure 5.32, which is supported by TRIDYN calculations of Chapter 3.3.2. The TRIDYN depth profiles of Si excess of Figure 3.11 show a pronounced Gaussian implantation peak in the Si excess depth profile even for oxide thicknesses as small as 5 nm. The effect of ion beam mixing of the  $\text{SiO}_2/\text{Si}$  interface is weak due to the small ion energy and the therefore weak collision cascade in the oxide.

KMC simulations of phase separation have been performed for these oxide thickness using the TRIDYN profiles of Si excess as initial distribution. Figure 5.33 displays KMC cross section views at different annealing stages in false color representation. According to Figure 5.33, ion beam mixing is not dominating the NC evolution in this case. Rather, the initially intermixed  $\text{SiO}_2/\text{Si}$  interface reconfigures rapidly during the early annealing phase even for the lowest oxide thickness of 5 nm.

Up to an annealing time of 200 kMCS, the width of the NC layer is found to be indepen-

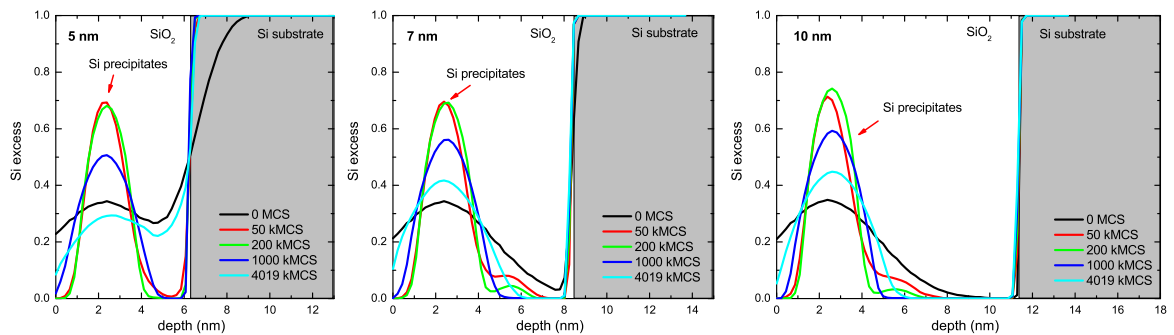


**Figure 5.34.:** Si excess depth profiles determined from KMC simulations of phase separation taken at different annealing stages. The oxide thickness was varied from 5 nm to 7 nm and was implanted at 1 keV energy to a fluence of  $1 \times 10^{15} \text{ cm}^{-2}$ .

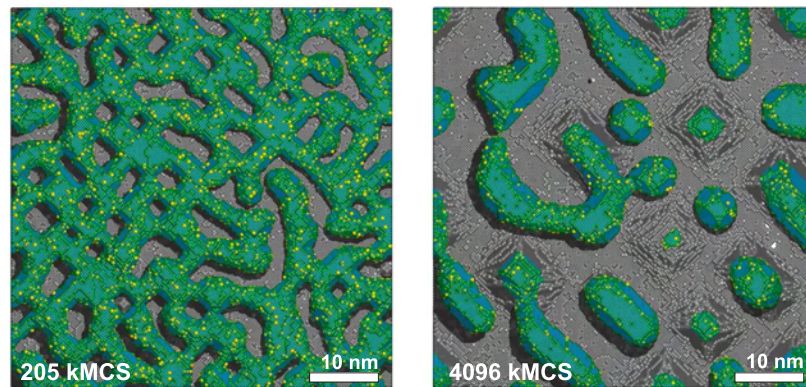


**Figure 5.35.:** KMC simulation snapshots (plane views) for 1 keV  $\text{Si}^+$  implantation into 5 nm thick  $\text{SiO}_2$  to a fluence of  $10^{16} \text{ cm}^{-2}$ . At longer annealing Si precipitates touch the Si substrate.

dent from the initial oxide thickness. Differences can only be observed at late stages. A few isolated Si NCs have formed in the tail of the concentration profile for thick oxides (7 and 10 nm) and can be seen as shoulder in Si excess profiles of Figure 5.34. These clusters dissolve during longer annealing. In the thinnest oxides, however, the formation of these NC is suppressed from the beginning due to the much stronger influence of the absorbing  $\text{SiO}_2/\text{Si}$  interface. Hence, a sharper NC depth distribution is achieved at early annealing times.

Additionally, long lasting annealing gives rise to the disintegration of the interconnected Si precipitates. Interface minimization drives precipitates towards a spherical shape and causes an increased width of the NC layer, a behavior that has been described above in section 5.4.3, Figure 5.26. Eventually Si precipitates touch the Si substrate for the 5 nm thick oxide. A plane view image of such an event is displayed in Figure 5.35 taken before and after the disintegration of the interconnected Si precipitates.

In summary, the KMC simulations underpin the possibility of controlling the tunnel distance by changing the initial oxide thickness, which appears more favorable than by changing the ion energy. Ion beam mixing of the  $\text{SiO}_2/\text{Si}$  interface is uncritical for this low energy, the location of the Si precipitates and the width of the NC layer is hardly affected by the oxide thickness. It has to be noted that too low oxide thicknesses brings Si precipitates too close to the  $\text{SiO}_2/\text{Si}$  interface or might even lead to a touching of the Si substrate. Quantitative results, however, cannot be given from the KMC simulations at this stage. Earlier comparisons with experimental results revealed that a fraction of the implanted Si is not available for phase separation, which certainly holds also here. The specific amount of implanted Si that is available for NC formation remains uncertain especially since corresponding PEELS-STEM studies on samples investigated by XTEM (Figure 5.32) are missing.

#### 5.4.6. Spatial fluctuations of tunneling distances

Advanced electron microscopy techniques (Ben Assayag et al., 2003) allow the precise measurement of the tunnel distance between the Si NCs (if formed at sufficiently high density) and the Si substrate. However, the statistical distribution of the tunnel distances between individual dots and the  $\text{SiO}_2/\text{Si}$  interface remains out of scope of today's experimental capa-



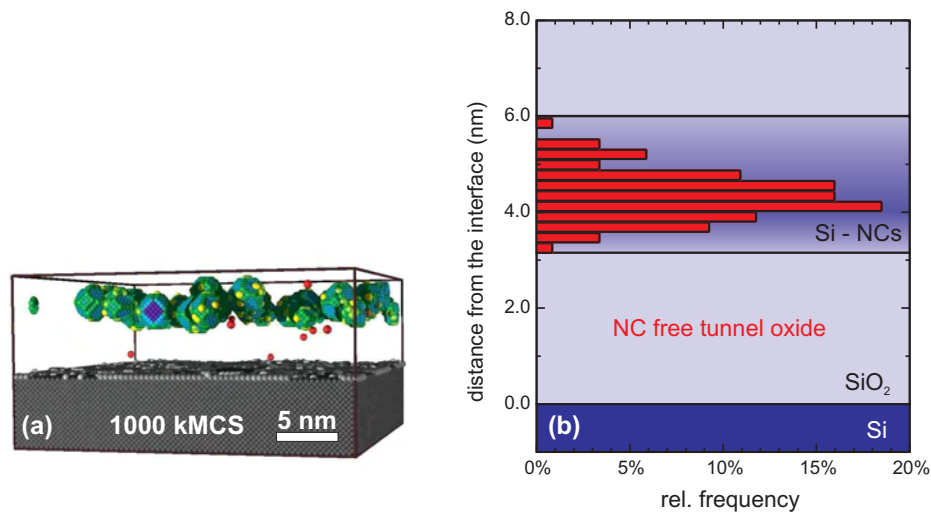


**Figure 5.36.:** (a) Cross section view and (b) statistical distribution of individual tunneling distances between the Si NCs and the SiO<sub>2</sub>/Si interface at 1000 kMCS. The KMC simulation was carried out for 1 keV Si implantation to a fluence of  $2 \times 10^{15} \text{ cm}^{-2}$  into 8 nm thick SiO<sub>2</sub>.

bilities. Here, KMC simulations could provide valuable insights.

Such a distribution of tunnel distances is shown in Figure 5.36 for an intermediated annealing (simulation) time of 1000 kMCS. The initial Si excess distribution was chosen according to the TRIDYN calculations of section 3.2 for 1 keV Si implantation to a fluence of  $2 \times 10^{15} \text{ cm}^{-2}$  into 8 nm thick SiO<sub>2</sub>. As it can be seen in Figure 5.36(a), the Si NCs arrange nicely in a thin layer in the SiO<sub>2</sub> just a few nanometers apart from the Si substrate. Their distance from the interface has been measured on the foremost clusters only from interface to interface. Figure 5.36(b) reveals a narrow distribution starting from 3 nm with the peak at about 4 nm distance from the interface. Hence, electrons will tunnel most likely to the first NCs at about 3 nm distance from the interface. A charging of the more distant NCs can then either be accomplished by direct electron (or Fowler-Nordheim) tunneling from the Si substrate or via a Pole-Frenkel mechanism which also involves neighboring NCs being closer to the interface. It is expected that distance of the foremost NCs thereby limits the tunneling probability and therefore the charging speed of the whole NC layer. Implicitly, a dense distribution of the Si NCs is then assumed. It has to be noted that the value of 3 nm distance for the foremost clusters is also in nice agreement with the previous estimate displayed in Figure 5.25, which was obtained from the Si excess depth profile in the KMC simulation.

## 5.5. Impact of the ambient on the NC formation

A nice qualitative agreement has been achieved between KMC predications and corresponding experiments. Quantitatively however, a strong discrepancy between both is observed. Much less Si is necessary in the KMC simulation than needed in the experiment to obtain Si NCs at similar morphology, size and area density. Additionally, the experiment identifies a *fluence threshold* for Si NC formation below which no NC formation is reported (Bonafos et al., 2004; Carrada et al., 2003). For 1 keV Si implantation into 10 nm thick SiO<sub>2</sub>, this

threshold ranges between  $5$  and  $7 \times 10^{15} \text{ cm}^{-2}$ . In contrast, KMC predictions on Si phase separation does not exhibit such a threshold. These findings are strong indications for an additional experimental factor influencing the NC growth at low energy IBS.

### 5.5.1. Humidity penetration into ion beam damaged oxide layers

High fluence implantation is known to damage the implanted host considerably. In particular under low energy ion implantation, the location of the maximum network damage is shifted closer to the  $\text{SiO}_2$  surface. A large number of broken bonds in the  $\text{SiO}_4$ -tetrahedra could then promote an inward diffusion of  $\text{H}_2\text{O}$  molecules from an adsorbed water layer or ambient humidity. Therefore, chemical reactions of the implanted Si atoms with H as well as with penetrated O atoms are likely to occur during any subsequent annealing.

A penetration of  $\text{H}_2\text{O}$  molecules into irradiation damaged  $\text{SiO}_2$  has been proven by Schmidt et al. (2002), who exposed thick  $\text{SiO}_2$  films irradiated by  $\text{Si}^+$ ,  $\text{Ge}^+$  or  $\text{Sn}^+$  ions to  $\text{N}_2$  atmosphere containing 40% humidity. The incorporated H of the water molecules was detected by nuclear reaction analysis with  $^{15}\text{N}^+$  ions using the nuclear reaction  $^{15}\text{N} + ^1\text{H} \rightarrow ^{12}\text{C} + ^4\text{He} + \gamma$  with a sharp resonance at 6.385 MeV. The measured H depth profiles reveal a water intake up to 40 nm if the  $\text{Ge}^+$  irradiation exceeded a threshold fluence of  $1 \times 10^{14} \text{ cm}^{-2}$ . Subsequent wet cleans were shown to increase the total intake further. From the measured H content,  $\text{H}_2\text{O}$  concentrations of 1 to 4 at.-% must be expected in the first 40 nm of the  $\text{SiO}_2$ . These results were qualitatively confirmed by ToF-SIMS studies of Perego et al. (2004a) on irradiated samples that contain  $\text{H}_2^{18}\text{O}$  absorbed from an artificial atmosphere with  $\text{H}_2^{18}\text{O}$  humidity. Further studies pointed out that humidity penetration can be prevented if the irradiated sample is heated to more than  $900^\circ\text{C}$  before it is exposed to air. The damaged  $\text{SiO}_2$  network reconfigures at this annealing step and a subsequent inward diffusion of  $\text{H}_2\text{O}$  is hindered.

Under normal conditions, however, a severe content of absorbed water must be expected within the first nanometers of the implanted sample. These high amounts of H and O are certainly sufficient to interfere with the phase separation process, i.e. implanted Si can become oxidized during following high temperature treatments.

### 5.5.2. Parasitic oxidation of NCs by penetrated humidity

Humidity penetration into the ion damaged  $\text{SiO}_2$  network leads to a considerable incorporation of excess O that is available later on for Si oxidation in the following annealing steps. Consequently, humidity penetration poses a serious threat to Si NC formation in thin gate oxides as large and especially uncontrollable amounts of implanted Si can become oxidized and are therefore not available for NC formation.

The parasitic oxidation of implanted Si explains in addition the discrepancy between simulation and experiment in the Si fluence that is necessary for Si NC formation (cp. section 5.2.2). TEM studies on low energy IBS at 1 keV energy and a  $\text{Si}^+$  fluence of  $5 \times 10^{15} \text{ cm}^{-2}$  did not reveal any Si NCs (Bonafos et al., 2004; Müller et al., 2004a). The implanted Si may have been oxidized completely during the thermal annealing. Simultaneously, the oxidation gives rise to a volume expansion of the  $\text{SiO}_2$  layer and therefore an increase in oxide thickness (Carrada et al., 2003). This fact can clearly be seen in the comparison between

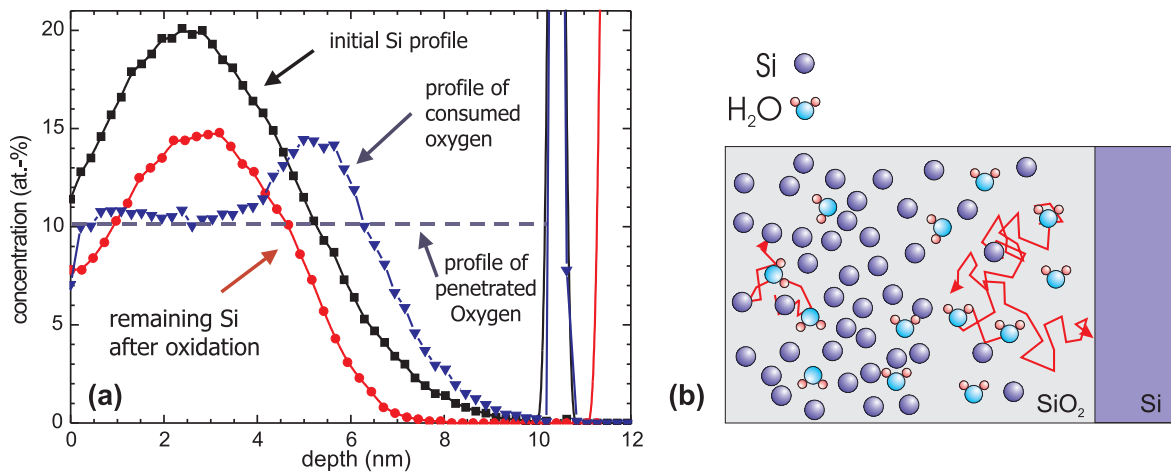


**Figure 5.37.:** KMC simulation of internal oxidation of implanted Si by penetrated humidity and, therefore, by incorporated oxygen (assumed as constant 10 at.-%). (a) For 1 keV Si<sup>+</sup> implantation to a fluence of  $5 \times 10^{15} \text{ cm}^{-2}$ , the initial profile of implanted Si (black squares) is reduced by oxidation (red circles), where the profile of consumed oxygen (blue triangles) indicates the location where the oxidation took place.

the XTEM images of Figure 5.11(a,c) and the corresponding KMC simulation snapshots of Figure 5.11(b,d), which only include the SiO<sub>2</sub> expansion due to the incorporated Si atoms (Müller et al., 2003). Here, the KMC simulations do not account for oxidation and the swelling caused by it. To do so, a multi-component KMC approach (Si + O) is needed in general, which is beyond the scope of the present work. However, the influence of the penetrated humidity on the NC depth and size distribution can be studied with the present KMC code if simplifying assumptions are taken<sup>7</sup>. For that aim, the kinetics of oxidation and precipitation of the net Si excess is divided into two steps. Oxidation is assumed to occur on a much faster time scale than the NCs growth, which relies on the fact that diffusion in SiO<sub>2</sub> is faster for O than Si, i.e. a large difference between the migration energies  $E_{A,O-diff} \ll E_{A,Si-diff}$  exists. Moreover, oxidation obeys almost no activation energy compared to nucleation ( $E_{A,oxidation} \sim 0 \ll E_{A,nucleation}$ ). With these assumptions, the KMC simulations are extended to include a *second mobile component* in the SiO<sub>2</sub> matrix, the oxidant O. Its initial profile is assumed to be constant with 10 at.-% in the 10 nm thick SiO<sub>2</sub>. This profile should give results being an upper limit of the effect of internal parasitic oxidation since experimental results remain beneath the 10 at.-% of O concentration. A further dependence on the Si<sup>+</sup> fluence at which the oxide has been irradiated is neglected.

In a first simulation step, this mobile excess O is allowed to diffuse through the SiO<sub>2</sub> matrix. Eventually it finds a Si excess atom, either being implanted or mixed from the Si substrate, which then will become oxidized, i.e. disappears from the simulation matrix. The depth positions of these oxidized Si atoms are recorded to quantify later on the target swelling associated with this parasitic Si oxidation. The process of O diffusion and annihilation is repeated as long as O atoms are still present in the SiO<sub>2</sub>.

A result of such a simulation of O and Si annihilation is displayed in Figure 5.37(a)

<sup>7</sup>Questions about the microscopic details of internal oxidation and its specific interference with the precipitation of Si excess remain open to further investigations.

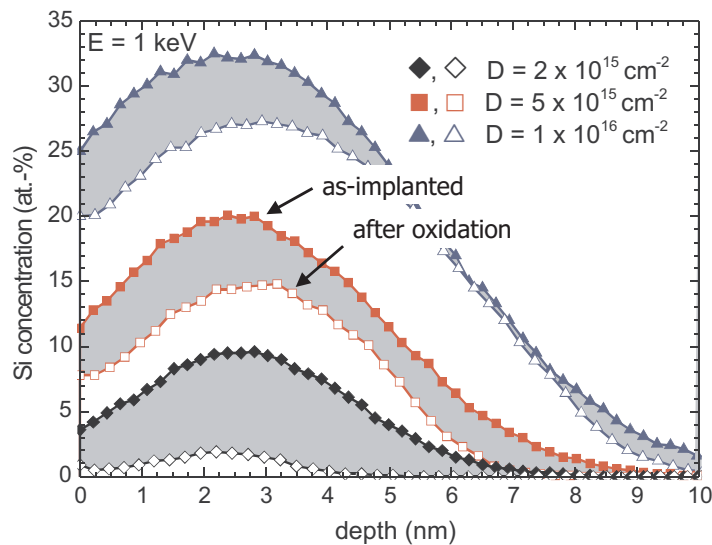


**Figure 5.38.:** Si depth profiles before and after internal oxidation are shown including the effect of target swelling due to oxidation, which shifts the profiles.

for 1 keV Si<sup>+</sup> implantation to a fluence of  $5 \times 10^{15} \text{ cm}^{-2}$ . The Si excess achieved by implantation is reduced by internal oxidation from 20 at.-% in the peak maximum to 15 at.-%. Surprisingly, oxidation occurs predominantly at the Si/SiO<sub>2</sub> interface and the deep tail of the Si excess profile, where the O concentration exceeds the Si excess. After an oxidation of the Si excess the remaining O atoms are free to diffuse either to the Si substrate or to regions of higher Si excess as depicted in Figure 5.37(b). This effect can clearly be seen by the peak in the depth profile of the location of the O-Si reactions in Figure 5.37(a). It broadens the zone which is completely depleted of Si excess. Simultaneously, target swelling occurs mainly in this depth region and gives rise to an increased injection distance after phase separation, an effect that has been observed experimentally by Carrada et al. (2003).

The Si excess profiles before and after parasitic oxidation are shown for varying fluence in Figure 5.38. About 5 at.-% of Si excess is lost in the peak maximum due to oxidation and

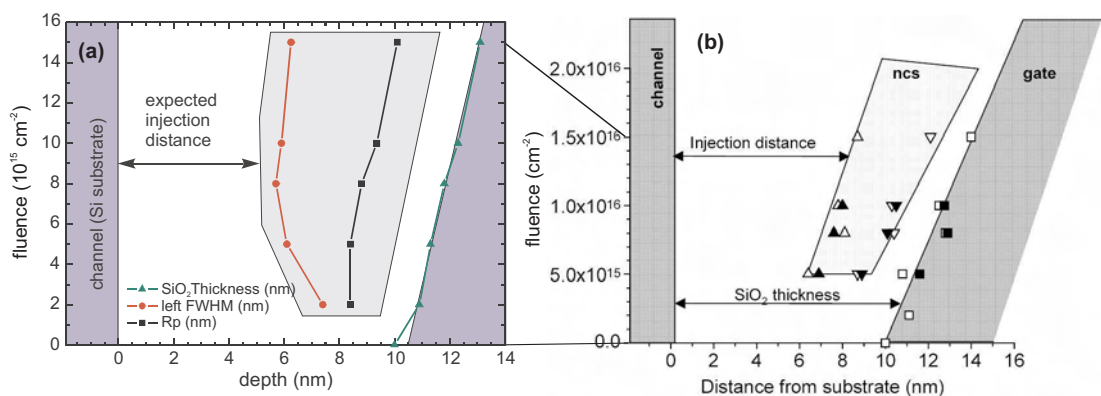


**Figure 5.39.:** Comparison between (a) simulation and (b) experiment (Carrada et al., 2003) of the effect of internal oxidation on the NC position with respect to the Si substrate. The initially 10 nm thick SiO<sub>2</sub> were implanted with Si<sup>+</sup> at 1 keV energy.



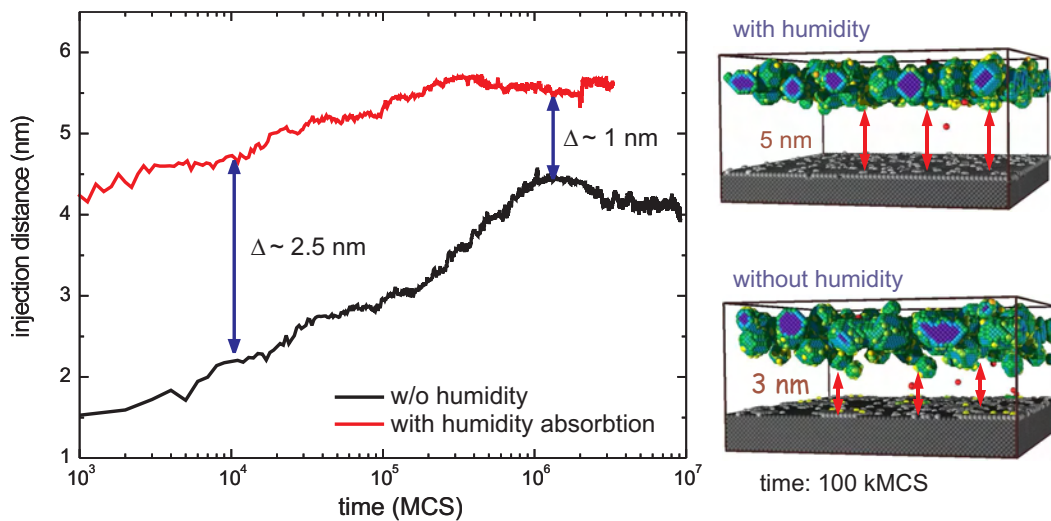


**Figure 5.40.:** Width of the injection oxide between the NC layer and the Si substrate taken from KMC simulations of phase separation in 1 keV  $\text{Si}^+$  implanted 10 nm thick  $\text{SiO}_2$  on Si. Simulations with or without taking into account the effect of internal oxidation by absorbed humidity are compared.

the profile becomes stretched by swelling. For the lowest fluences of  $2 \times 10^{15} \text{ cm}^{-2}$ , almost no Si excess survives the oxidation. Accordingly, an approximate threshold fluence for NC formation can be identified if internal oxidation is taken into account.

Based on the profiles of Figure 5.38, estimates of the NC positions can be given. The projected range is expected to define the mean depth of the NC layer. The width of the injection oxide might be approximated by the distance from Si substrate to the depth where half of the Si excess peak maximum is reached. These estimates are drawn in Figure 5.39 and compared to experimental values of Carrada et al. (2003). Qualitatively the same trend, the strong swelling of the  $\text{SiO}_2$  and the increase of the injection distance is observed although the exact amount of swelling is still underestimated.

In a second step, the Si depth profiles after internal oxidation (Figure 5.38) were used as input for KMC simulations of phase separation. For a fluence of  $5 \times 10^{15} \text{ cm}^{-2}$ , the time evolution of the injection distance is shown in Figure 5.40 together with cross section views for 100 kMCS. Internal oxidation has clearly lead to an injection distance that is, depending on the annealing time, 1 and 2.5 nm larger. The observed value of 5.5 nm agrees nicely with the 6 nm found in the experiment (Carrada et al., 2003). In addition, internal oxidation caused a sharper defined NC layer since the Si excess tails were annihilated by oxidation. The NC size and density is much less affected (in this fluence range) as shown in Figure 5.41. Taking the effect of humidity penetration into account, NCs are on average smaller as excess Si has been reduced due to oxidation. The NC density, however, is found to be slightly larger than without the influence of humidity penetration.

In summary, the effect of internal oxidation by absorbed humidity has been studied using KMC simulations. A threshold  $\text{Si}^+$  fluence of  $2 \times 10^{15} \text{ cm}^{-2}$  for NC formation has been identified, which is below the experimental value of  $5 \times 10^{15} \text{ cm}^{-2}$ . It has been shown that the disagreement between simulation and experiment can be caused by parasitic oxidation of implanted Si during annealing. One experimentally verified source of the parasitic oxidant

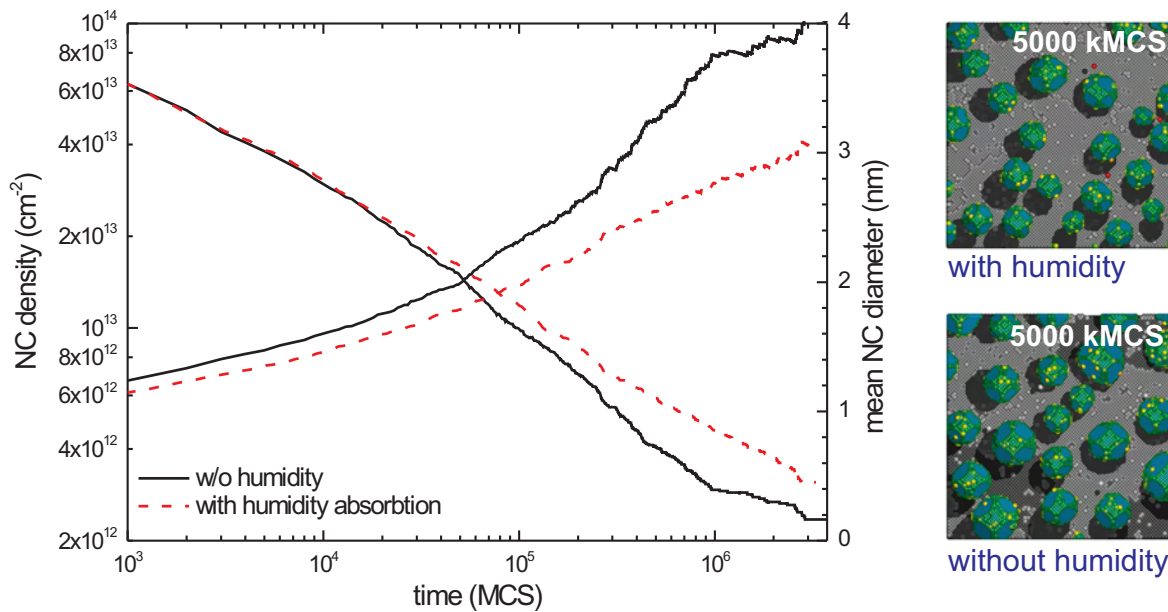


**Figure 5.41.:** Mean NC size and density evolution during annealing as predicted by KMC simulations of phase separation for 1 keV  $\text{Si}^+$  implantation into 10 nm thick  $\text{SiO}_2$  on Si. Simulations with or without taking into account the effect of internal oxidation by absorbed humidity are compared.

is air humidity penetration into as-implanted  $\text{SiO}_2$  prior to annealing. Traces of an oxidant in the annealing ambient might add to this parasitic oxidation.

## References

- G. Ben Assayag, C. Bonafos, M. Carrada, A. Claverie, P. Normand, and D. Tsoukalas. Transmission electron microscopy measurements of the injection distances in nanocrystal-based memories. *Applied Physics Letters*, 82(2):200–2002, 2003.
- R. B. Bergmann, F. G. Shi, and J. Krinke. Noncoarsening origin of logarithmic-normal size distributions during crystallization of amorphous thin films. *Physical Review Letters*, 80:1011–1013, 1998.
- C. Bonafos, H. Coffin, N. Cherkashin, G. Benassayag, S. Schamm, and G. Zanchi. Cross sectional electron microscopy studies on Si NC layers in thin silicon dioxide. private communication, 2003.
- C. Bonafos, M. Carrada, N. Cherkashin, H. Coffin, D. Chassaing, G. B. Assayag, A. Claverie, T. Müller, K. H. Heinig, M. Perego, M. Fanciulli, P. Normand, and D. Tsoukalas. Manipulation of two-dimensional arrays of Si nanocrystals embedded in thin  $\text{SiO}_2$  layers by low energy ion implantation. *Journal of Applied Physics*, 95(10):5696–5702, 2004.
- V. A. Borodin, K. H. Heinig, and S. Reiß. Self-organization kinetics in finite precipitate ensembles during coarsening. *Physical Review B*, 56(9):5332–5344, Sept. 1997.
- A. D. Brailsford, R. Bullough, and M. R. Hayns. Point defect sink strengths and void-swelling. *Journal of Nuclear materials*, 60:246–256, 1976.
- W. D. Brown and J. E. Brewer, editors. *Nonvolatile Semiconductor Technology - A comprehensive Guide to Understanding and Using NVSM Devices*. IEEE Press Series on Microelectronic Systems. IEEE Press, New York, 1998.

- R. Burghaus. Ostwald ripening in a semi-infinite system. *Physical Review E*, 57(3):3234–3236, Mar. 1998.
- M. Carrada, C. Bonafos, G. B. Assayag, D. Chassaing, P. Normand, D. Tsoukalas, V. Soncini, and A. Claverie. Effect of ion energy and dose on the positioning of 2D-arrays of Si nanocrystals ion beam synthesised in thin SiO<sub>2</sub> layers. *Materials Science and Engineering B*, 101:204–207, 2003.
- R. Casting and L. Henry. Filtrage magnétique des vitesses en Microscopie électronique. *Copl. Rend. (Paris)*, 255:76, 1962.
- R. F. Egerton. Parallel-recording systems for electron energy loss spectroscopy (EELS). *Journal of Electron Microscope Technology*, 1:37–52, 1984.
- R. F. Egerton. *Electron Energy Loss Spectroscopy in the Electron Microscope*. Plenum Press, New York, 2 edition, 1996.
- Gatan, Inc. EFTEM and STEM spectrum imaging, 2004. URL [http://www.gatan.com/analysis/eftem\\_stem.html](http://www.gatan.com/analysis/eftem_stem.html).
- S. Hayward, D. W. Heermann, and K. Binder. Dynamic percolation transition induced by phase separation: A Monte Carlo analysis. *Journal of Statistical Physics*, 49(5/6):1053–1081, 1987.
- D. W. Heermann and W. Klein. Percolation and droplets in a medium-range three-dimensional Ising model. *Physical Review B*, 27:1732–1735, 1983.
- F. Iacona, C. Bongiorno, C. Spinella, S. Boninelli, and F. Priolo. Formation and evolution of luminescent Si nanoclusters produced by thermal annealing of SiO<sub>x</sub> films. *Journal of Applied Physics*, 95(7):3723–3732, 2004.
- C. Jeanguillaume and C. Colliex. Spectrum-image: The next step in EELS digital acquisition and processing. *Ultramicroscopy*, 28:252, 1989.
- J. K. Kim, H. J. Cheong, Y. Kim, J.-Y. Yi, H. J. Bark, S. H. Bang, and J. H. Cho. Rapid-thermal-annealing effect on lateral charge loss in metal-oxide-semiconductor capacitors with Ge nanocrystals. *Applied Physics Letters*, 82(15):2527–2529, Apr. 2003.
- C. L. Lawson and R. J. Hanson. *Solving least square problems*. Prentice-Hall, Englewood cliffs, New-Jersey, 1974.
- I. M. Lifshitz and V. V. Slyozov. The kinetics of precipitation from supersaturated solid solutions. *J. Phys. Chem. Solids*, 19:35, 1961.
- T. Müller, K.-H. Heinig, and W. Möller. Size and location control of Si nanocrystals at ion beam synthesis in thin SiO<sub>2</sub> films. *Applied Physics Letters*, 81:3049–3051, 2002.
- T. Müller, K.-H. Heinig, and W. Möller. Nanocrystal formation in Si implanted thin SiO<sub>2</sub> layers under the influence of an absorbing interface. *Materials Science and Engineering B*, 101(1-3): 49–54, 2003.
- T. Müller, C. Bonafos, M. Tencé, K.-H. Heinig, H. Coffin, N. Cherkashin, G. Ben Assayag, S. Schamm, G. Zanchi, C. Colliex, W. Möller, and A. Claverie. Multi-dot floating-gates in MOS-FETs for nonvolatile memories - Their ion beam synthesis and morphology. *Materials Research Society Proceedings*, 792, 2004a.
- T. Müller, C. Bonafos, M. Tencé, K.-H. Heinig, H. Coffin, N. Cherkashin, G. Ben Assayag, S. Schamm, G. Zanchi, C. Colliex, W. Möller, and A. Claverie. Multi-dot floating-gates for non-volatile semiconductor memories - Their ion beam synthesis and morphology. *Applied Physics Letters*, 85(12):2373–2375, Sept. 2004b.

- NEON. Influence of ion implantation conditions on nanocrystal positioning within thin oxides. Deliverable D1, EU Growth Project NEON GRD1-2000-25619, Jan. 2002a. URL <http://www.cemes.fr/neon.html>.
- NEON. Report on model evaluation for process understanding of WP1 to WP3. Deliverable D11, EU Growth Project NEON GRD1-2000-25619, June 2002b. URL <http://www.cemes.fr/neon.html>.
- NEON. Report on the relative suitability of low energy and conventional i/i to fabricate memory devices. recommendations to industrial partners. Deliverable D17, EU Growth Project NEON GRD1-2000-25619, Athens, Greece, May 2003. URL <http://www.cemes.fr/neon.html>.
- NEON. Report on the influence of annealing conditions on nanocrystal size, density and positioning. Deliverable D2, EU Growth Project NEON GRD1-2000-25619, Feb. 2002c. URL <http://www.cemes.fr/neon.html>.
- NEON. Nanoparticles for electronics. Final technical report, EU Growth Project NEON GRD1-2000-25619, Toulouse, France, Mar. 2004. URL <http://www.cemes.fr/neon.html>.
- P. Normand, E. Kapetanakis, Dimitrakis, D. Tsoukalas, K. Beltsios, N. Cherkashin, C. Bonafos, G. Benassayag, H. Coffin, A. Claverie, V. Soncini, A. Agarwal, and M. Ameen. Effect of annealing environment on the memory properties of thin oxides with embedded Si nanocrystals obtained by low-energy ion-beam synthesis. *Applied Physics Letters*, 83:168–170, 2003.
- P. Normand, E. Kapetanakis, P. Dimitrakis, D. Skarlatos, K. Beltsios, D. Tsoukalas, C. Bonafos, G. B. Assayag, N. Cherkashin, A. Claverie, J. V. D. Berg, V. Soncini, A. Agarwal, M. Ameen, M. Perego, and M. Fanciulli. Nanocrystals manufacturing by ultra-low-energy ion-beam-synthesis for non-volatile memory applications. *Nuclear Instruments and Methods in Physics Research B*, 216:228–238, 2004.
- S. Oswald, B. Schmidt, and K.-H. Heinig. XPS investigation with factor analysis for the study of Ge clustering in SiO<sub>2</sub>. *Surface and Interface Analysis*, 29:249–254, 2000.
- C. S. Pande and E. Dantsker. On a stochastic theory of grain growth - III. *Acta Metallurgica et Materialia*, 39(6):1359–1365, 1991.
- M. Perego, S. Ferrari, S. Spiga, E. Bonera, M. Fanciulli, and V. Soncini. Time of flight secondary ion mass spectrometry study of silicon nanoclusters embedded in thin silicon oxide layers. *Applied Physics Letters*, 82(1):121–123, 2003.
- M. Perego, S. Ferrari, M. Fanciulli, B. Schmidt, and K.-H. Heinig. TOF-SIMS study of H<sub>2</sub><sup>18</sup>O penetration in irradiated SiO<sub>2</sub> films. NEON Internal Report, Mar. 2004a. URL <http://www.cemes.fr/neon.html>.
- M. Perego, S. Ferraria, M. Fanciullia, G. B. Assayag, C. Bonafos, M. Carrada, and Claverie. Characterization of silicon nanocrystals embedded in thin oxide layers by TOF-SIMS. *Applied Surface Science*, 231-232:813–816, 2004b.
- R. A. Puglisi, S. Lombardo, G. Ammendola, G. Nicotra, and C. Gerardi. Imaging of Si quantum dots as charge storage nodes. *Materials Science and Engineering C*, 23:1047–1051, 2003.
- L. Reimer. *Energy-Filtering Transmission Electron Microscopy*. Springer series in optical sciences. Springer, New York, 1995.

- S. Reiß and K.-H. Heinig. Ostwald ripening during ion beam synthesis - a computer simulation for inhomogeneous systems. *Nuclear Instruments and Methods in Physics Research B*, 84:229–233, 1994.
- L. Röntzsch. Self-organization of nanocluster  $\delta$ -layers at ion beam mixed Si-SiO<sub>2</sub> interfaces. Wissenschaftlich-Technische Berichte FZR-392, Forschungszentrum Rossendorf, Dresden, Germany, Nov. 2003. Diplomarbeit.
- B. Schmidt, D. Gambohle, and F. Herrmann. Impact of ambient atmosphere on as-implanted amorphous insulating layers. *Nuclear Instruments and Methods in Physics Research B*, 191:482–486, 2002.
- H. Shuman. Parallel recording of electron energy loss spectra. *Ultramicroscopy*, 6:163–168, 1981.
- D. Stauffer and A. Aharony. *Introduction to Percolation Theory*. Taylor & Francis, London, 2 edition, 1992.
- M. Strobel. Modeling and computer simulation of ion beam synthesis of nanostructures. Wissenschaftlich-Technische Berichte FZR-277, Forschungszentrum Rossendorf, Dresden, Germany, Nov. 1999. PhD thesis.
- M. Strobel, K.-H. Heinig, and W. Möller. Three-dimensional domain growth on the size scale of the capillary length: Effective growth exponent and comparative atomistic and mean-field simulations. *Physical Review B*, 64:245422, 2001.
- M. Tencé, S. Schramm, C. Bonafos, and C. Colliex. PEELS-STEM imaging of Si nanocrystals in thin SiO<sub>2</sub> layers. private communication, 2003.
- P. W. Voorhees and M. E. Glicksman. Solution to the multi-particle diffusion problem - I. theory. *Acta Metallurgica*, 32(11):2001–2011, 1984a.
- P. W. Voorhees and M. E. Glicksman. Solution to the multi-particle diffusion problem - II. computer simulations. *Acta Metallurgica*, 32(11):2013–2030, 1984b.
- C. Wagner. Theorie der Alterung von Niederschlägen durch Umlösen. *Z. Elektrochem.*, 65:581, 1961.
- R. Wagner, R. Kampmann, and P. W. Vorhees. Homogeneous second phase precipitation. In G. Kostorz, editor, *Phase Transformations in Materials*, chapter 5, pages 309–408. Wiley-VCH, Weinheim, 2001.



## Chapter 6.

# Results and Discussion: Electron Tunneling Percolation and Lateral Charge Isolation

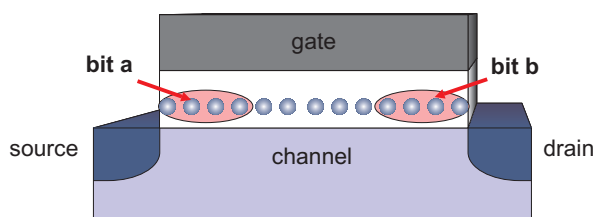
Truly separated Si NCs are essential to ensure good data retention and a fast operation of multi-dot floating gate memories. Only in the case that charge is stored in individual NCs being insulated from each other, possible defects in the thin tunneling oxide underneath the NCs cannot discharge a large fraction of the NC layer. If charge could spread over the NC layer it might easily be lost via oxide defects and therefore lead to a reduced data retention. To counteract this, the tunneling oxide thickness could be increased, but at the expense of the lost writing speed.

Even if no structural percolation exists, electrons might spread by quantum mechanical *direct electron tunneling* between very close, but not touching NCs, giving rise to a low  $e^-$ -hopping conductivity within the NC layer. This conductivity might be sufficient throughout long storage times to allow electrons to spread from cluster to cluster and find defects in the underlying tunnel oxide through which the NC layer could be discharged. Especially since oxide defects could be generated by repeated program and erase cycling, it is vital to minimize the resulting stress induced leakage current (SILC) by preventing any lateral charge migration.

Compagnoni et al. (2004) indeed have shown in their theoretical treatment on nanocrystal memory reliability that lateral tunneling is retention limiting for closely spaced NCs. The probability of lateral  $e^-$ -tunneling between NCs though drops exponentially with increasing NC separation and the NC memory becomes more immune against SILC.

Lateral charge isolation is further vital for two-bit memory architectures (Figure 6.1) that relies on source or drain side hot electron injection combined with forward and reverse sensing (Eitan et al., 2000). This type of memory originally been proposed for nitride trap layers can be also realized with Si NCs as charge storage sites. Hradsky et al. (2003) and Lombardo et al. (2004) have demonstrated two-bit operation of NC memories if the NC obey a sufficient spacing. At too low NC distance the lateral charge isolation might however be lost during long term storage with the consequence that both bits can no longer be distinguished and the data retention is lost.

**Figure 6.1.:** Storage of two physically separated bits near drain and source side of the memory transistor. Both bits are programmed by localized channel hot electron injection. Lateral charge migration has strictly to be avoided to ensure data retention.



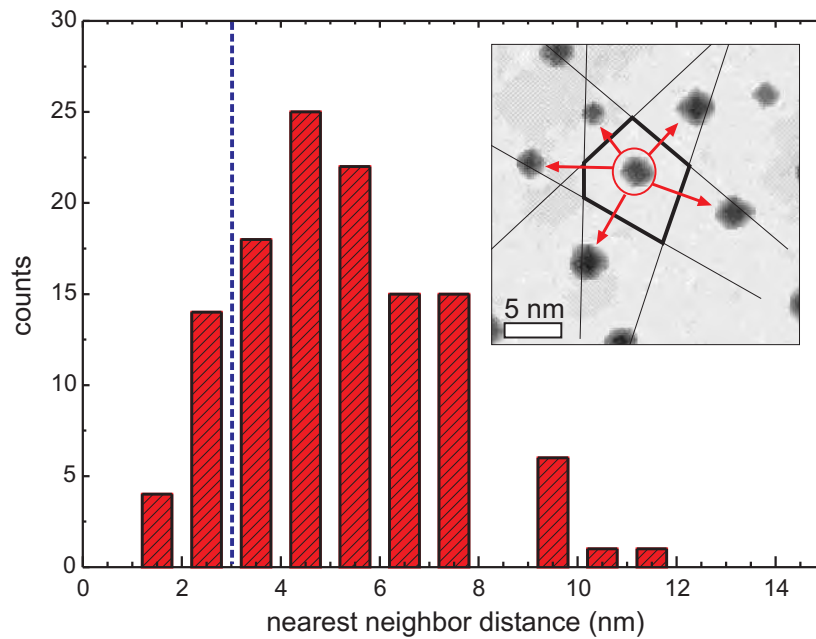


**Figure 6.2.:** Predicted nearest neighbor distribution of Si NCs for 1 keV  $\text{Si}^+$  implantation into 10 nm  $\text{SiO}_2$  to a fluence of  $2 \times 10^{15} \text{ cm}^{-2}$  and an annealing (simulation) time of  $t = 6000$  kMCS. The inset shows the Voronoi polygon being part of the tessellation used to determine the NN distances. The dashed blue line indicates a threshold of 3 nm below which NCs are considered to be coupled by electron tunneling.

## 6.1. Nearest Neighbor Distances and Their Distribution

Any lateral charge isolation is determined by the distances between neighboring Si NCs, which can be extracted from KMC simulation results. All atoms belonging to a NC were acquired according to the cluster counting algorithm described in Chapter 4.2.2 together with their centers of mass and diameters. Subsequently, all nearest neighbors (NN) of each NC were identified using Voronoi tessellations (Voronoi, 1908). The applied algorithm was modified to measure distances from surface to surface not between center of masses.

An empirical distribution of NN distances is displayed in Figure 6.2 for the example of a KMC simulation of 1 keV  $\text{Si}^+$  implantation into 10 nm  $\text{SiO}_2$  at  $2 \times 10^{15} \text{ cm}^{-2}$  and  $t = 6000$  kMCS. The inset in Figure 6.2 illustrates the applied Voronoi polygon construction for the NN search (only shown in 2D here). Figure 6.2 reveals that the Si NCs are not randomly distributed. NC distances below 2 nm are very unlikely due to the competitive coarsening by OSTWALD ripening. NCs are rather separated by an average distance of 4 to 6 nm. Deviations from the mean are however strong and NN distances up to 10 nm are recorded.

The time evolution of the NN distances is plotted in Figure 6.3(a) for the implantation conditions of Figure 6.2 (1 keV at  $2 \times 10^{15} \text{ cm}^{-2}$ ). Remarkably, a linear growth of the NN distance is observed at later stages of phase separation. Simultaneously, the width of the NN distribution increases indicated by the 10% and 90% quantile bands and the empirical



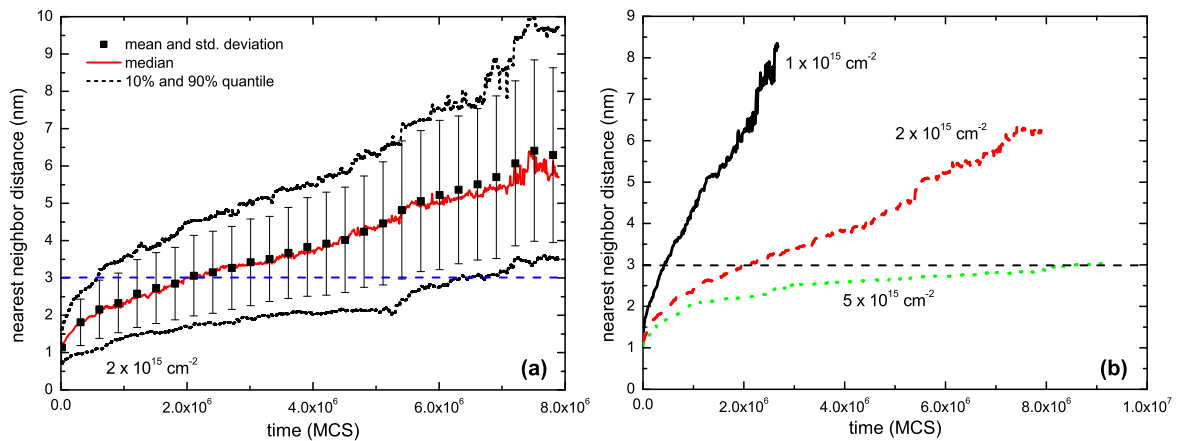


**Figure 6.3.:** Time evolution of the distance between neighboring NCs for (a) 1 keV  $\text{Si}^+$  implantation into 10 nm  $\text{SiO}_2$  to a fluence of  $2 \times 10^{15} \text{ cm}^{-2}$ . The mean and median values are plotted in (a) together with the empirical standard deviation as error bars. Additionally, 10% and 90% quantile bands were included to visualize the tails of the distribution. (b) The mean NN distance is plotted for  $1 \times 10^{15} \text{ cm}^{-2}$ ,  $2 \times 10^{15} \text{ cm}^{-2}$  and  $5 \times 10^{15} \text{ cm}^{-2}$ .

standard deviation drawn as error bars in Figure 6.3(a). The distribution of NN distances spreads e.g. at  $4 \times 10^6$  MCS from 2 to 5.5 nm, where the smaller distances might be sufficient to allow for electron tunneling while the larger ones are isolating enough.

In addition, the mean NN distances for different  $\text{Si}^+$  fluences is plotted in Figure 6.3(b), where the ion energy was kept constant at 1 keV. A linear growth of the NN distance with time is observed in all three cases, but at much different rates. The lowest fluence of  $1 \times 10^{15} \text{ cm}^{-2}$  has been shown above to result in small NCs by a nucleation mechanism (section 5.3). Their density was found to decrease rapidly during annealing due to the cluster coarsening as well as the loss of Si monomers to the Si interface. As a result, the NN distances between the NCs are large and grow fast in time. In the opposite case of a fluence of  $5 \times 10^{15} \text{ cm}^{-2}$ , the mean NN distance could not exceed a value of 3 nm even for  $1 \times 10^7$  MCS. However, NCs are not denser in the case of the higher ion fluence, rather their size is larger and reduces the remaining space in between.

## 6.2. Lateral Electron Tunneling – A Percolation Problem

Lateral conduction by quantum mechanical electron tunneling is assessed in following using a simple *threshold model*:

- NCs are considered to be *coupled* by direct electron tunneling if their distance is below a distance threshold  $d_{th}$ .
- NCs are assumed to be *isolated* from each other if they are further apart than  $d_{th}$ .

One reasonable choice of the tunneling threshold could be, e.g.  $d_{th} = 3$  nm, which is approximately the aimed distance between the Si NCs and the Si channel in the NEON project

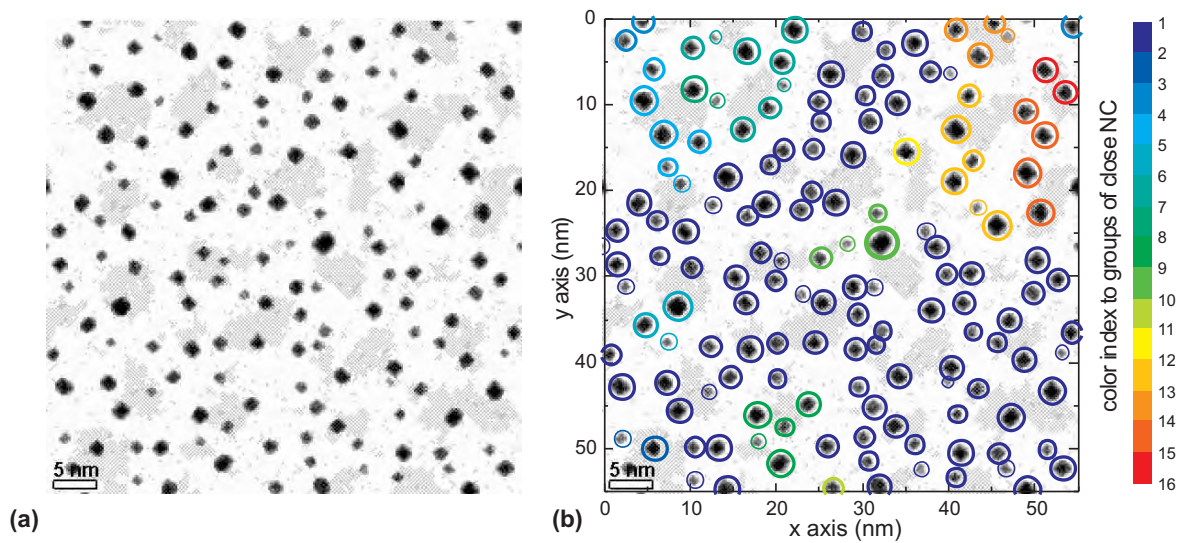


**Figure 6.4.:** (a) Plane view of the Si NC ensemble predicted by a KMC simulation for 1 keV  $\text{Si}^+$  implantation to a fluence of  $2 \times 10^{15} \text{ cm}^{-2}$  into 10 nm thick  $\text{SiO}_2$  and an annealing time of 300 kMCS. (b) Grouped clusters using a distance threshold of 3 nm.

(NEON, 2004). At a NN spacing of 3 nm,  $e^-$  are more likely to tunnel to the Si conduction band of the substrate rather than to spread among the NC layer by consecutive tunneling events.

### 6.2.1. Groups of percolated NCs

Following the above sketched threshold model, NCs can then be pooled into distinct groups of NCs. In this second<sup>1</sup> clustering procedure, all Si NCs are identified which are separated by NN distances being *less* than  $d_{th}$ . Hence, charge put onto a single NCs could spread by direct tunneling to all other NCs belonging to the same group without traveling across a NN distance that is larger than the defined threshold of  $d_{th}$ . In that sense, the NCs of the group are coupled by electron tunneling.

An example of this clustering procedure is shown in Figure 6.4. Si NCs are imaged in plane view in Figure 6.4(a) for a simulation of 1 keV  $\text{Si}^+$  implantation to a fluence of  $2 \times 10^{15} \text{ cm}^{-2}$  into 10 nm thick  $\text{SiO}_2$  at  $t = 300$  kMCS. In addition, Figure 6.4(b) shows the same snapshot but with color marks added. A color thereby indicates that all clusters belonging to this groups of closely space NCs can be reached without the need to cross a distance larger than  $d_{th} = 3$  nm. Several small groups with less than 5 NCs are found to be isolated from each other, but also a large group of close NCs (shown in blue in Figure 6.4(b)) is observed. This large group span the whole simulation cell, hence (tunneling) *percolation* has been reached. Charge brought to that group could spread by tunneling over the whole NC layer, while it would stay localized on other NC groups. A reliable and SILC-immune long term data storage cannot be expected in this case of tunneling percolation.

<sup>1</sup>In a first clustering algorithm all Si impurity atoms have been collected that form a topologically interconnected Si cluster, the Si nanocrystal.

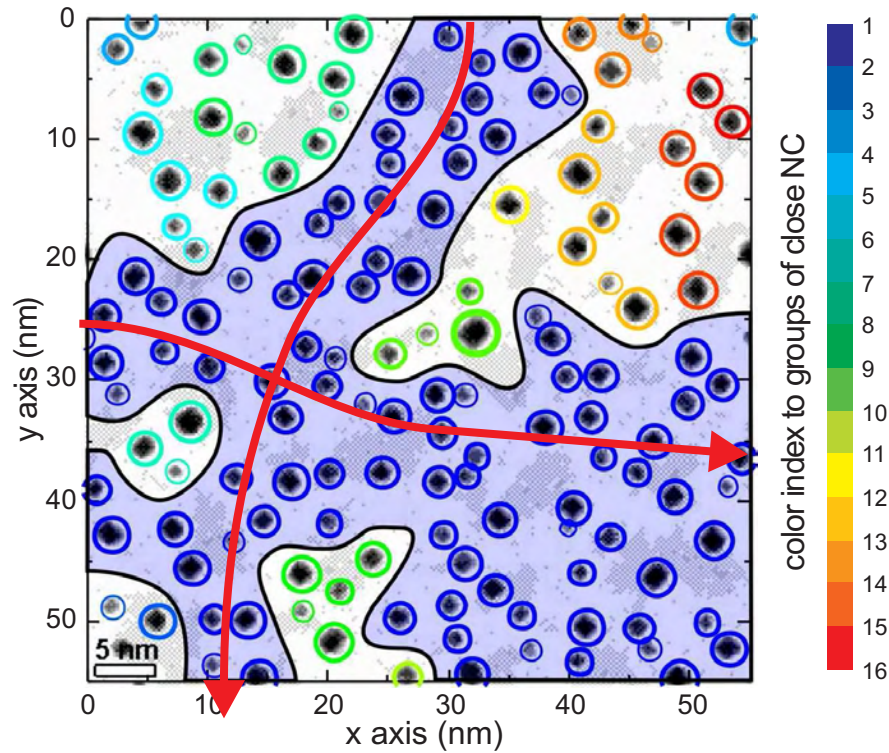


**Figure 6.5.:** Grouped NCs for a threshold distance of 3 nm. A large group of NCs (shaded in blue) spans the full simulation cell and tunneling percolation is reached. The KMC simulation was carried out for 1 keV  $\text{Si}^+$  implantation to  $2 \times 10^{15} \text{ cm}^{-2}$ . The plane view snapshot was taken at  $t = 300 \text{ kMCS}$ .

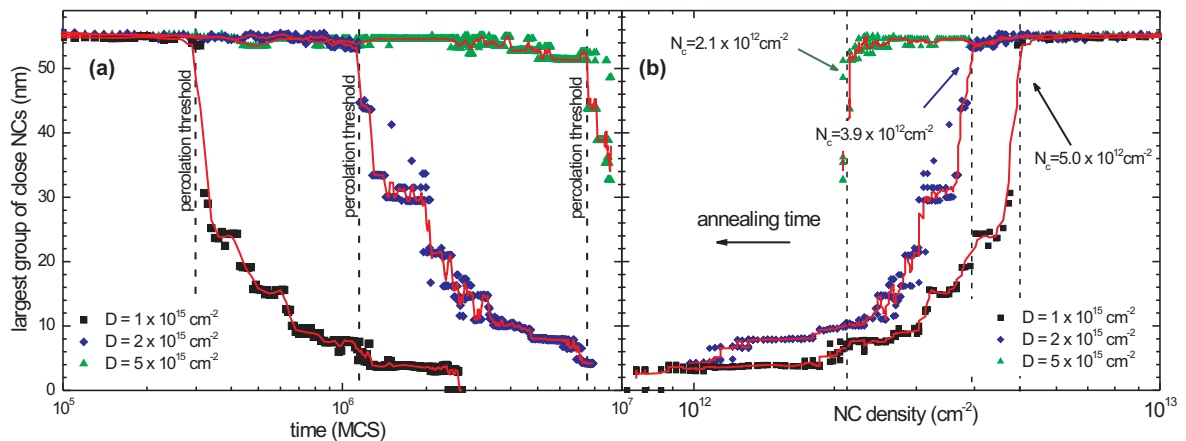


**Figure 6.6.:** Evolution of the size of the largest NC group in the simulation cell for a threshold distance of  $d_{\text{th}} = 3 \text{ nm}$  depending on (a) the annealing time or (b) the corresponding NC areal density. Electron tunneling percolation exists if the largest group of close NCs spans the whole simulation cell in at least one direction (55 nm size). The KMC simulation was performed for 1 keV  $\text{Si}^+$  implantation to  $2 \times 10^{15} \text{ cm}^{-2}$ .

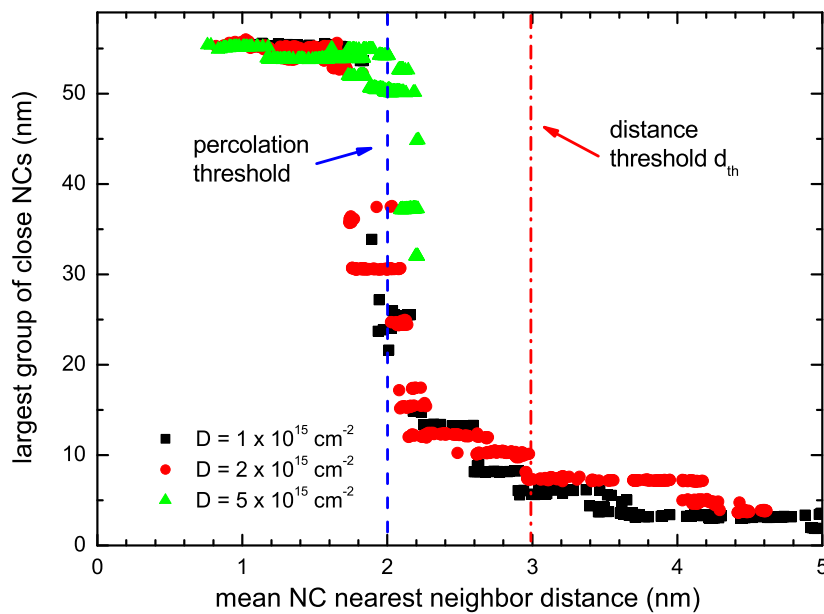


**Figure 6.7.:** Size of the largest NC group of close NCs vs. mean NC spacing predicted by KMC simulations for  $\text{Si}^+$  fluences of 1 to  $5 \times 10^{15} \text{ cm}^{-2}$ . All three curves fall nearly onto a single one. The percolation threshold is only for mean NC spacing that are smaller than 2 nm mean NC spacing although the distance threshold  $d_{th}$  has been set to 3 nm.

## 6.2.2. Predicted tunneling percolation threshold

To achieve a NC memory in which charge is stored localized and could not spread laterally it is necessary to prevent tunneling percolation. With the threshold model of the previous section, it has to be prevented that a single group of close NCs spans the full simulation cell, i.e. percolation is reached as in Figure 6.5.

The time evolution from a percolated system of close NCs to insulated, well-separated NCs is shown in Figure 6.6 for the example of 1 keV  $\text{Si}^+$  implantation into 10 nm thick  $\text{SiO}_2$  on Si to fluences ranging from 1 to  $5 \times 10^{15} \text{ cm}^{-2}$ . Percolation is accessed in these simulations through the size of the largest group of close NCs assuming a threshold distance of  $d_{th} = 3 \text{ nm}^2$ . As annealing proceeds, the ensemble of NCs crosses the percolation threshold due to progressive NC dissolution leading to a decreasing NC density (section 5.3, Figure 5.13). For the lowest  $\text{Si}^+$  fluence, NCs become isolated first, while higher fluences need longer annealing times to reach the percolation threshold as shown in Figure 6.6(a).

However for all  $\text{Si}^+$  fluences, according to Figure 6.6(b) the percolation threshold is reached for roughly the same critical NC density of  $N_{crit} = 2 \dots 5 \times 10^{15} \text{ cm}^{-2}$ . Deviations in the critical NC density  $N_{crit}$  arise here from the differing mean NC diameters (section 5.3, Figure 5.13). These can be lifted if the size of the large NC group is plotted versus the mean NC spacing as done in Figure 6.7. There, curves for all three ion fluences fall onto each other. However, the onset of percolation is found only for NCs as dense as 2 nm although a threshold distance  $d_{th} = 3 \text{ nm}$  has been used. This difference might originate in the large distribution of inter-cluster distances.

<sup>2</sup>The size is measured in the direction of the largest extension (either in x or y-direction).

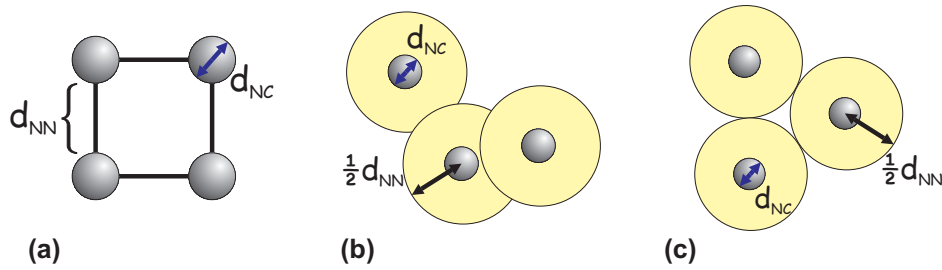


**Figure 6.8.:** Geometric 2D percolation models: (a) regular square lattice, (b) interpenetrating (soft core) particles, and (c) hard core particles.

### 6.2.3. Percolation thresholds in simple analytical models

In a rule of thumb, the critical NC density  $N_{crit}$  can be estimated using a regular quadratic lattice as displayed in Figure 6.8(a). The areal NC density is given by  $(d_{NN} + d_{NC})^{-2}$ , where  $d_{NN}$  denotes the nearest neighbor spacing of the NCs and  $d_{NC}$  their diameter. Any size distribution has been neglected here. With the help of the mean NC diameter  $\bar{d}_{NC}$  extracted from the KMC simulation the critical NC density (for a given threshold distance  $D_{th}$ ) can be estimated by

$$N_{crit} \cong \frac{1}{(d_{th} + \bar{d}_{NC})^2}. \quad (6.1)$$

Values obtained with (6.1) agree remarkably well with the critical density of the disordered NC layer, see Table 6.1. Figure 6.9 displays the NC density obtained from the KMC simulations versus the mean NC center-to-center distance. Apparently, the NC density agrees over almost one order of magnitude with the NC density estimated using (6.1) assuming a regular quadratic lattice.

More sophisticated estimates are based on continuum percolation theory for two dimensions<sup>3</sup>, which is more adequate for the quasi 2D layer of Si-NCs than full three dimensional

<sup>3</sup>Estimates from percolation theory were given for the percolation of two dimensional circles. The critical NC densities determined of the basis the KMC results are fully three dimensional, though. Only, the NCs

Fluence D (cm <sup>-2</sup> )		1 × 10 <sup>15</sup>	2 × 10 <sup>15</sup>	5 × 10 <sup>15</sup>
mean NC diameter d <sub>NC</sub> (nm)		1.66	2.35	3.85
critical densities N <sub>c</sub> (10 <sup>12</sup> cm <sup>-2</sup> )	continuum percolation of hard-core particles	3.4	2.6	1.6
	quadratic lattice	4.6	3.5	2.1
	<b>KMC simulations</b>	<b>5.0</b>	<b>3.9</b>	<b>2.1</b>
	continuum percolation of soft-core particles	6.7	5.1	3.1

**Table 6.1.:** Critical NC densities at which a percolation path with nearest neighbor spacings of less than  $d_{th} = 3$  nm is reached. Different estimates are compared to KMC simulation results.



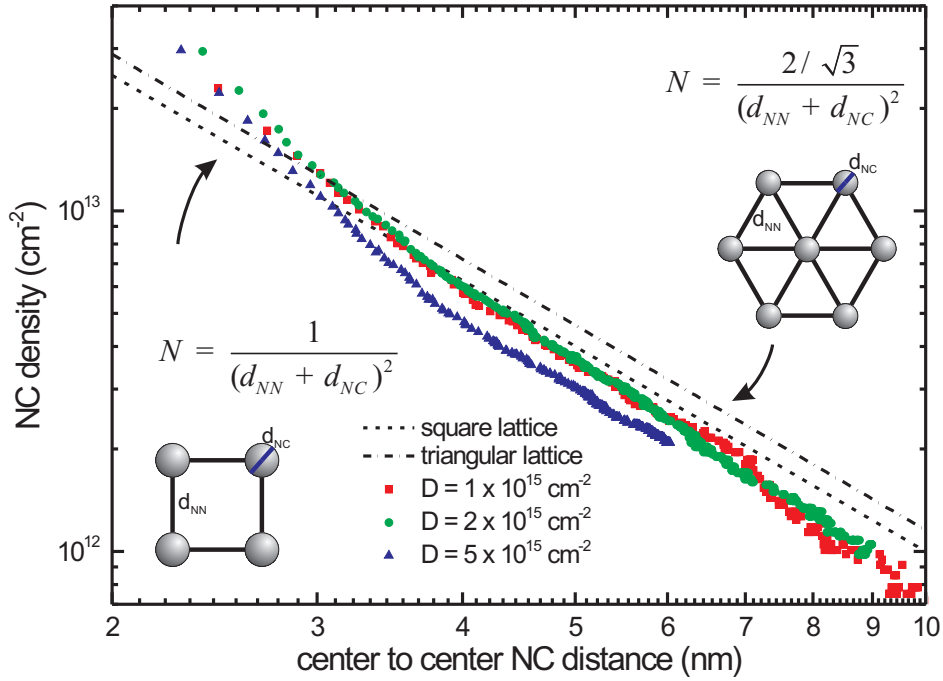


**Figure 6.9.:** NC density versus mean NC center-to-center distance predicted by KMC simulations of Si phase separation from SiO<sub>2</sub> for 1 keV Si<sup>+</sup> implantation into 10 nm thick SiO<sub>2</sub> and ion fluences ranging from 1 to 5 × 10<sup>15</sup> cm<sup>-2</sup>. Additionally, estimates based on regular square and hexagonal lattices are included.

percolation models. Scher and Zallen (1970) determined a critical area fraction of  $\phi = 0.44$  for the onset of percolation of randomly placed, non-overlapping circles of equal size (Figure 6.8(c)). The diameter of these circles can be identified here with the center-to-center distance ( $d_{NC} + d_{th}$ ) of neighboring NC having a critical spacing equal to  $d_{th}$ .

Nevertheless, the picture of non-overlapping circles is not very realistic in the case of a broad distribution of NC spacings as it is observed in Figure 6.2). A considerable fraction of NN distances is less than the threshold  $d_{th} = 3$  nm, which is not compatible with the hard-core circle assumption. Rather a certain degree of overlapping should be allowed, i.e. the occurrence of NN distances that are smaller than  $d_{th}$ . For such soft-core circles, Saeger and Pike (1974a) predicted a somewhat higher critical area fraction of  $\phi = 0.68$ . According to Xia and Thorpe (1988) the occupied area fraction  $\phi$  is related to the particle size and density by

$$\phi = 1 - e^{-NA}, \quad (6.2)$$

which leads to an expression for the critical NC density  $N_{crit}$

$$N_{crit} = -\frac{4 \ln(1 - \phi)}{\pi(d_{th} + d_{NC})}. \quad (6.3)$$

Critical NC densities have been calculated for both limiting cases using (6.3) and mean NC diameters extracted from the KMC simulations. These estimated are shown in Table 6.1 together with the critical densities determined directly from the KMC simulations.

obtained by low energy IBS are confined to a quasi two dimensional NC layer.

### 6.2.4. A relation to variable range hopping conduction

The dc conductivity of amorphous semiconductors, e.g. germanium, has been found to be consistent with the law

$$\sigma(T) \propto e^{\left\{-\left(\frac{T_0}{T}\right)^{1/4}\right\}}, \quad (6.4)$$

which has been predicted by Mott (1969) for the three-dimensional case. His idea is based on a charge transport model utilizing thermally activated hopping between localized and randomly distributed trapping sites. A situation, that should in principle be very similar to low-field conduction among Si NCs embedded in insulating SiO<sub>2</sub>. The conductivity between the individual nodes depends exponentially on their distance  $r_{ij}$

$$\sigma_{ij} = \sigma_0 \exp(-r_{ij}/a), \quad (6.5)$$

due to carrier wave function overlap with  $a$  being the radius of the localized wave function (Miller and Abrahams, 1960). The temperature  $T_0$  has been related by Mott (1969) to

$$k_B T_0 = \lambda \alpha^3 / \rho_0, \quad (6.6)$$

where  $\alpha$  is the coefficient of the exponential decay of the wave function of the localized states,  $\rho_0$  the density of states at the fermi level and  $\lambda$  a numerical constant. Later analysis, e.g. by Saeger and Pike (1974b) and Ambegaokar et al. (1971) revealed that the coefficient  $\lambda$  is closely related to a continuum percolation problem. This idea has been put forward by Ron and DiMaria (1984) for a theoretical description of the dc conduction of Si-rich SiO<sub>2</sub> for different temperature and field condition. Essentially, they derived a similar temperature behavior to (6.4) in the limit of low electric fields at low temperatures with

$$k_b T_0 = \frac{v_c}{4/3\pi N} \Delta E_g (2\alpha)^3, \quad (6.7)$$

where  $N$  is the volume NC density and  $\Delta E_g$  can be associated with the bandwidth of the ground state energies  $E_g$ . The factor  $(3v_v/4\pi N)^{-1/3}$  is the critical percolation length  $R_c$  (Saeger and Pike, 1974a). Volume conduction through an insulating matrix containing Si NCs according to (6.4) with (6.7) is exponentially affected by the NC density  $N^{-1}$  and the sample temperature  $T$ .

In low-energy ion beam synthesized NC layers, the conduction is however effectively confined to two dimensions. Applying Mott's result for two dimensions, one would obtain a different temperature behavior

$$\sigma(T) \propto e^{\left\{-\left(\frac{T_0}{T}\right)^{1/3}\right\}}. \quad (6.8)$$

Studies of Timp et al. (1986) on two-dimensional conduction of impurities in the inversion layer of a MOSFET have confirmed this temperature behavior, while other work indicate that Coulomb blockade present in the conduction through quantum dot arrays alters the temperature behavior distinctively at low temperatures. Yakimov et al. (2003) have shown that the conductivity of a 2D layer of Ge dots embedded in Si versus temperature  $T$  follows an

Efros-Shklovskii behavior  $\sigma \propto \exp\{-(T_0/T)^{1/2}\}$ . The Coulomb interaction between localized electrons creates there a 'soft' gap in the density of states near the Fermi level, the new temperature dependence of the hopping DC conductivity is the most important manifestation of the gap (Efros and Shklovskii, 1975). Unfortunately, experimental data on the temperature behavior of the conductivity of 2D layers containing Si NCs are currently missing.

Despite of the knowledge about the temperature behavior of low-field variable range hopping conduction, a fully quantum mechanical description of the electron dissipation in a SiO<sub>2</sub> layer was beyond the scope of the present work. In addition, the distinctive temperature dependence of the dc conductivity is only of minor interest for the NC memory data retention. Usually, temperature cannot be actively controlled in solid-state memories and therefore cannot be used to tune the NC layer conductivity<sup>4</sup>. The device temperature is rather tied to the desired operation scheme and power consumption. On the other hand, direct control over the layer conductivity can be gained by choosing the right mean NC size and spacing. Equation (6.1) gives here a simple, yet surprisingly accurate estimate of the critical NC density  $N_{crit}$  that has not to be exceeded in order to prevent percolation for a given threshold distance  $d_{th}$ .

## References

- V. Ambegaokar, B. I. Halperin, and J. S. Langer. Hopping conductivity in disordered systems. *Physical Review B*, 4(8):2612–2620, Oct. 1971.
- C. M. Compagnoni, D. Ielmini, A. S. Spinelli, A. L. Lacaita, C. Gerardi, and S. Lombardo. Statistical analysis of nanocrystal memory reliability. In *Proceedings of the 42nd Annual International Reliability Physics Symposium*, pages 509–514, Phoenix, 2004. IEEE 03CH37533.
- A. L. Efros and B. I. Shklovskii. Coulomb gap and low temperature conductivity of disordered systems. *Journal of Physics C: Solid State Physics*, 8(4):L49–L51, Feb. 1975.
- B. Eitan, P. Pavan, I. Bloom, E. Aloni, A. Frommer, and D. Finzi. NROM: a novel localized trapping, 2-bit nonvolatile memory cell. *IEEE Electron Device Letters*, 21:543–545, 2000.
- B. Hradsky, R. Rao, R. F. Steimle, M. Sadd, S. Straub, R. Muralidhar, and B. White. Local charge storage in silicon nanocrystal memories. IEEE Nonvolatile Semiconductor Memory Workshop, Monterey, CA, Feb. 2003.
- S. Lombardo, D. Corso, I. Crupi, C. Gerardi, G. Ammendola, M. Melanotte, B. De Salvo, and L. Perniola. Multi-bit storage through Si nanocrystals embedded in SiO<sub>2</sub>. *Microelectronic Engineering*, 72:411–414, 2004.
- A. Miller and E. Abrahams. Impurity conduction at low concentrations. *Physical Review*, 120(3):745–755, Nov. 1960.
- N. F. Mott. Conduction and switching in non-crystalline materials. *Contemporary Physics March*, 10(2):125–138, Mar. 1969.
- NEON. Nanoparticles for electronics. Final technical report, EU Growth Project NEON GRD1-2000-25619, Toulouse, France, Mar. 2004. URL <http://www.cemes.fr/neon.html>.

<sup>4</sup>It is of course of interest for device reliability as operation at somewhat elevated temperatures must be guaranteed.



- A. Ron and D. J. DiMaria. Theory of current-field relation in silicon-rich silicon dioxide. *Physical Review B*, 30(2):807–812, July 1984.
- C. H. Saeger and G. E. Pike. Percolation and conductivity: A computer study. I. *Physical Review B*, 10(4):1421–1434, Aug. 1974a.
- C. H. Saeger and G. E. Pike. Percolation and conductivity: A computer study. II. *Physical Review B*, 10(4):1435–1446, Aug. 1974b.
- H. Scher and R. Zallen. Critical density in percolation processes. *Journal of Chemical Physics*, 53: 3759–3761, 1970.
- G. Timp, A. B. Fowler, and A. Hartstein. Hopping conduction in a two-dimensional impurity band. *Physical Review B*, 34(12):8771–8785, Dec. 1986.
- G. Voronoi. Recherches sur les paralléloèdres Primitives. *Journal für die reine und angewandte Mathematik*, 134:198–287, 1908.
- W. Xia and M. F. Thorpe. Percolation properties of random ellipses. *Physical Review A*, 38(5): 2650–2656, Sept. 1988.
- A. I. Yakimov, A. V. Dvurechenskii, A. V. Nenashev, and A. I. Nikiforov. Evidence for two-dimensional correlated hopping in arrays of Ge/Si quantum dots. *Physical Review B*, 68:205310, 2003.



## Chapter 7.

# Resume: Prospects of Ion Beam Synthesized Si NCs for Future Nonvolatile Memories

The materials science of low energy IBS of Si NCs has been studied in this work by a combination of dynamic binary collision calculations and kinetic Monte Carlo simulations. In conjunction with experimental results they have lead to a deeper understanding of phase separation taking place in thin oxide. Furthermore, optimum condition of NC synthesis were identified in the course of these studies, which are specifically tailored for NC memories. However, their prospects of application in future nonvolatile memories depend on many other factors including also the performance of competing conventional and emerging memory concepts.

### 7.1. Process simulations of low energy IBS – A summary

Si NC formation by low energy IBS relies on self-organization phenomena during phase separation and therefore impose severe challenges on tailored experimental studies as well as on precise and conclusive materials analysis. There, process simulation provided a strong help and guidance in order to avoid tedious experiments on the one hand and on the other hand they were able to contributed considerably to a deeper fundamental understanding of phase separation in confined geometries. I.e. to elucidate the interplay of the NC formation process with the imposed starting and boundary condition. The specific starting condition achieved by high fluence Si implantation were studied using *dynamic binary collision calculations*, which have lead to a prediction of Si excess depth profiles in thin gate oxides of a remarkable quality. These simulations included naturally high fluence implantation effects as target erosion by sputtering, target swelling and ion beam mixing that are hardly assessable by experiments in the system of interest. However, these effects were shown to be of vital importance to be able to model the phase separation stage occurring in the second step of the IBS.

This modeling was accomplished with the help of a tailored *kinetic Monte Carlo* code that combined a detailed kinetic description of phases separation on the atomic level with the required degree of abstraction that was necessary to span the timescales involved. Large ensembles of Si NCs were simulated reaching the late stages of NC formation and dissolution at simulation sizes that allowed the direct comparison with experimental studies,

e.g. with electron energy loss resolved TEM investigations. These comparisons showed a nice degree of agreement, e.g. in terms of predicted and observed precipitate morphologies. However, they also pointed clearly onto the discrepancies between the experiment and the simulation that finally were attributed to an additional experimental influence that were overlooked in early experimental studies. Parasitic oxidation of implanted Si reduced the amount of implanted Si that is available for phase separation – a fact that was, of course, not occurring in the simulations. Moreover, the process simulations were generally applied to identify optimum processing regimes for a tailored Si NC formation for NC memories.

## 7.2. IBS of Si NCs for nanocrystal memories – Advantages and feasibility

As the optimum size of Si dots in NC memories lies below current lithographic capabilities, self-assembling techniques have been proven to be very attractive. IBS, in particular at low energies, demonstrated considerable potential because of its flexibility and manufacturing advantages.

**CMOS compatibility:** Inherently, IBS of Si NCs is fully compatible to today's aggressively scaled CMOS technology nodes. Ion implantation is widely applied and well controlled in each required energy range. The utilized thermal budget is not expected to hamper dopant profiles as the NC synthesis can be carried out before the more sensitive source/drain and channel implants.

**NC Morphology:** The morphology of the Si multi-dot floating gates fabricated by low-energy IBS sensitively depends on the synthesis conditions, i.e. the Si<sup>+</sup> fluence and energy. Low fluence Si<sup>+</sup> implantation with a peak concentration below 10 at.-% Si excess has been shown to result in dense but isolated Si NCs. Higher fluences instead cause structural percolation during the phase separation and lead to an interconnected Si network that mimics a floating gate structure. Such situations must be avoided.

**NC Location Control:** The distance between Si NCs and the transistor channel can be controlled on the nanometer scale, where especially adjusting the initial oxide thickness has proven to give the best control. Choosing higher ion energies rather than thinner gate oxides causes an undesired ion beam mixing of the SiO<sub>2</sub>/Si interface that in addition is likely to deteriorate the electrical channel quality by Si crystal defects. Here, dynamic binary collision simulations help to find the right balance.

**NC Size and Density:** Low energy IBS gives the opportunity to achieve quasi 2D NC layers parallel to the Si/SiO<sub>2</sub> interface (the transistor channel). These layers show an extremely high cluster densities while the average NC size is kept small, a situation that can hardly be achieved by other methods as CVD (Lombardo et al., 2004) or aerosol deposition (Ostraat et al., 2001). In addition, the NC density can be tuned by the annealing time as Si is lost during annealing to the nearby interface. The average NC size, on the other hand, is a strong function of the incorporated Si fluence. Within the nucleation regime, NCs in the range of 2 to 5 nm diameter are observed. Beyond

the evaluation of the average NC size and density, process simulations allowed here further to assess the electron tunneling percolation, a phenomenon that will limit data retention in a NC memory. An optimum NC density was estimated from the KMC results such that percolation is prevented but a high cluster density is retained. Electron tunneling is then sufficiently hindered and charge remains confined to individual clusters.

**Process control:** NC memories require reproducible memory characteristics at low statistical scatter arising from process variations. Despite of the easy CMOS integration and other technologically attractive options, many fabrications issues remain to be solved for low energy IBS of Si NCs. One important part, the influence of humidity of NC formation could have been identified with the help of KMC studies. Further topics as cleaning issues and energy contamination at low energy IBS are discussed by Normand et al. (2004).

Irradiation based concepts (Schmidt et al., 2004) could deliver in particular an alternative to low energy IBS that eliminates external influences on the NC formation at phase separation. Si excess is created close to SiO<sub>2</sub>/Si interfaces by ion beam mixing. For that purpose, the complete gate stack is irradiated by Si ions penetrating deeply into the Si substrate. As this techniques relies on ion beam mixing, NCs are only formed close to Si interfaces and their parameters cannot be varied over such a broad range than for low energy IBS. Large Si NCs with more than 3...4 nm distance from the SiO<sub>2</sub>/Si interface can hardly be formed by ion irradiation.

## 7.3. Can nanocrystal memories compete with other nonvolatile semiconductor memory concepts?

Si NCs have been successfully incorporated in nonvolatile memories as charge storage nodes, large memory arrays were demonstrated recently (De Salvo et al., 2003; Schmidt et al., 2004; Steimle et al., 2004). For a sustaining success however several criteria have to be met:

**Program/Erase Speed and Power Consumption:** Fast programming, i.e. at low voltages, can be achieved by different means. (i) Thin tunnel oxides allow for fast charge injection and erase by direct electron (or Fowler-Nordheim) tunneling but at the expense of degraded data retention due to the increased back tunneling rate such that a trade-off between speed and retention has to be found. However, injection is efficient in the sense that the supplied current is only used for charging or erase. Parasitic currents as, e.g. displacements currents, are negligible and the resulting power consumption of potential memory devices is expected to be attractively low. (ii) Alternatively to tunnel injection trough thin barriers, *channel hot electron injection* can be applied that allows to circumvent thicker barrier layers still at high injection speeds. Nonetheless, the power consumption under such operation will be worse as most of the accelerated electrons are not injected but collected at the drain side of the transistor.

**Data Retention:** Data retention critically depends on the tunnel barrier thickness and prevents a further scaling of the tunnel oxide in floating gate flash memories (Fazio, 2004). Here, NC memories promise an improved retention as charge is stored in discrete nodes, which allows for a further scaling of the tunnel oxide. Similar results are expected if other charge trapping materials are used. However, silicon nitride or oxynitride based memories demonstrated a data retention that is up to now superior to Si NC memories (Dimitrakis et al., 2004; Eitan et al., 2000; Libsch and White, 1998). This is partially attributed to the existence of deeper charge traps in these materials and to the injection oxide thickness that is often larger than in the reported Si NC memories. To allow a further reduction of the tunnel dielectric at maintained data retention, *crested barrier* composite films have been proposed as a replacement of the thermal SiO<sub>2</sub> giving the possibility to design barrier structures (Casperson et al., 2002; Likharev, 1998; Park et al., 2003; Wan et al., 2003). However, the materials in focus often exhibit charge traps themselves either at interfaces or in the bulk such that a successful application is yet to be demonstrated.

**Reliability:** The integrity of the tunnel dielectric is of vital importance but is often degraded during repeated write and erase cycling due to generated oxide defects. Especially hot carriers injection limits the device endurance of conventional flash memories to less than 10<sup>6</sup> cycles. This is not the case for NC memories that are charged by direct electron tunneling. An endurance of up to 10<sup>7</sup> cycles was demonstrated by Schmidt et al. (2004) for ion beam synthesized NCs. Interestingly, Compagnoni et al. (2003) reported that data retention is even improved at cycling due to the generation of deep traps at the Si NC/SiO<sub>2</sub> interface.

**Disturbs:** NC charging by direct electron tunneling can be utilized at low gate voltages but, in addition, increases the vulnerability of the memory to disturbs, i.e. the unwanted alteration of the charge state by electric fields. In order to drive a sufficiently large read current, gate and drain voltages are required that itself disturb the memory state by unintended charge injection. This imposes a severe limitation onto the allowed voltages or drives the memory cell design away from the ability to program at low voltages, e.g. by increasing the injection oxide thickness. However, a deterioration of the programming speed and cell reliability are then inevitable.

**Competitiveness and Scalability:** The ability to follow a clear shrink path together with an improved device characteristics will be the key to competition with established NVSM technologies. In the near future, conventional flash devices still appear to be ahead of any competition arising from emerging memory technologies. It is anticipated that scaling of the conventional flash memory will continue at comparable speed at least for this decade (Fazio, 2004). Underlining this assessment, Samsung (Byeon et al., 2005) and Toshiba/Sandisk (Hara et al., 2005) demonstrated recently an 8 Gb NAND multi-level memory using 63 nm and 70 nm ground rules in floating gate technology, respectively. Any emerging NVSM technology has to compete on this integration level in order to achieve a significant dissemination. Especially, NC memories are then forced to operate with only a few hundred clusters per memory transistor and need to deliver still a sufficiently tight statistical distribution of those

cells. At the same time, scaling reduces the size of conventional floating gates to dimensions that differ by less than factor 10 from the size of Si NCs. As this ratio worsens, the projected advantages of NC memories might start to vanish.

In summary, NC memories share the time-voltage dilemma with conventional flash memories, i.e. the write/erase voltages and therefore the programming speed cannot be tuned independently from data retention. However, device reliability is expected to be improved with NC memories compared to conventional floating gates. Unfortunately, this also holds for other charge trapping memories.

A further success of NCs in nonvolatile memories will ultimately depend on the achieved memory characteristics, the degree of process control of the Si NCs synthesis and their integration into the standard CMOS technology flow. The last issues has been studied in this work with the help Kinetic Monte Carlo simulations of phase separation. Ion beam synthesis has proven to yield Si NCs at small sizes and large densities in a reproducible manner, their formation can be tailored to achieve an optimum for multi-dot floating gate memories.

## References

- D.-S. Byeon, S.-S. Lee, Y.-H. Lim, J.-S. Park, W.-K. Han, P.-S. Kwak, D.-H. Kim, D.-H. Chae, S.-H. Moon, S.-J. Lee, H.-C. Cho, J.-W. Lee, M.-S. Kim, J.-S. Yang, Y.-W. Park, D.-W. Bae, J.-D. Choi, S.-H. Hur, and K.-D. Suh. An 8gb multi-level nand flash memory with 63nm sti cmos process technology. In *Proceedings of the IEEE International Solid-State Circuits Conference*, pages 46–47. IEEE, 2005.
- J. D. Casperson, L. D. Bell, and H. A. Atwater. Materials issues for layered tunnel barrier structures. *Journal of Applied Physics*, 92(1):261–266, 2002.
- C. M. Compagnoni, D. Ielmini, A. S. Spinelli, A. L. Lacaita, C. Previtali, and C. Gerardi. Study of data retention for nanocrystal flash memories. In *Proceedings of the 41st Annual International Reliability Physics Symposium*, pages 506–512, Dallas, Texas, 2003. IEEE 03CH37400.
- B. De Salvo, C. Gerardi, S. Lombardo, T. Baron, L. Perniola, D. Mariolle, P. Mur, A. Toffoli, M. Gely, M. N. Semeria, S. Deleonibus, G. Ammendola, V. Ancarani, M. Melanotte, R. Bez, L. Baldi, D. Corso, I. Crupi, R. A. Puglisi, G. Nicotra, E. Rimini, F. Mazen, G. Ghibaudo, G. Pananakakis, C. M. Compagnoni, D. Ielmini, A. S. Spinelli, A. L. Lacaita, Y. M. Wan, and K. van der Jeugd. How far will Silicon nanocrystals push the scaling limits of NVMs technologies? *IEEE International Electron Devices Meeting Technical Digest*, pages 597–600, 2003.
- P. Dimitrakis, E. Kapetanakis, D. Tsoukalas, D. Skarlatos, C. Bonafos, G. B. Assayag, A. Claverie, M. Perego, M. Fanciulli, V. Soncini, R. Sotgiu, A. Agarwal, M. Ameen, C. Sohl, and P. Normand. Silicon nanocrystal memory devices obtained by ultra-low-energy ion-beam synthesis. *Solid-State Electronics*, 48:1511–1517, 2004.
- B. Eitan, P. Pavan, I. Bloom, E. Aloni, A. Frommer, and D. Finzi. NROM: a novel localized trapping, 2-bit nonvolatile memory cell. *IEEE Electron Device Letters*, 21:543–545, 2000.
- A. Fazio. Flash memory scaling. *MRS Bulletin*, 29(11):841–817, Nov. 2004.
- T. Hara, K. Fukuda, K. Kanazawa, N. Shibata, K. Hosono, H. Maejima, M. Nakagawa, T. Abe, M. Kojima, M. Fujiu, Y. Takeuchi, K. Amemiya, M. Morooka, T. Kamei, H. Nasu, K. Kawano, C.-M. Wang, K. Sakurai, N. Tokiwa, H. Waki, T. Maruyama, S. Yoshikawa, M. Higashitani, T. D.



- Pham, and T. Watanabe. A 146mm<sup>2</sup> 8Gb NAND flash memory with 70 nm CMOS technology. In *Proceedings of the IEEE International Solid-State Circuits Conference*, pages 44–45. IEEE, 2005.
- F. R. Libsch and M. H. White. SONOS nonvolatile memory devices. In W. D. Brown and J. E. Brewer, editors, *Nonvolatile Semiconductor Technology - A comprehensive Guide to Understanding and Using NVSM Devices*, IEEE Press Series on Microelectronic Systems, chapter 5, pages 309–357. IEEE Press, New York, 1998.
- K. K. Likharev. Layered tunnel barriers for nonvolatile memory devices. *Applied Physics Letters*, 73(15):2137–2139, 1998.
- S. Lombardo, R. Puglisi, I. Crupi, D. Corso, G. Nicotra, L. Perniola, B. DeSalvo, and C. Gerardi. Distribution of the threshold voltage window in nanocrystal memories with Si dots formed by chemical vapor deposition: Effect of partial self-ordering. In *IEEE Nonvolatile Semiconductor Workshop*, pages 69–70, Aug. 2004.
- P. Normand, P. Dimitrakis, E. Kapetanakis, D. Skarlatos, K. Beltsios, D. Tsoukalas, C. Bonafos, H. Coffin, G. Benassayag, A. Claverie, V. Soncini, A. Agarwal, C. Sohl, and M. Ameen. Processing issues in silicon nanocrystal manufacturing by ultra-low-energy ion-beam-synthesis for non-volatile memory applications. *Microelectronic Engineering*, 73-74:730–735, 2004.
- M. L. Ostraat, J. W. D. Blauwe, M. L. Green, L. D. Bell, M. L. Brongersma, J. Casperson, R. C. Flanagan, , and H. A. Atwater. Synthesis and characterization of aerosol silicon nanocrystal nonvolatile floating-gate memory devices. *Applied Physics Letters*, 79(3):433–435, 2001.
- N.-M. Park, S.-H. Jeon, H.-D. Yang, H. Hwang., and S.-J. Park. Size-dependent charge storage in amorphous silicon quantum dots embedded in silicon nitride. *Applied Physics Letters*, 83(5): 1014–1016, Aug. 2003.
- B. Schmidt, K.-H. Heinig, L. Röntzsch, T. Müller, K.-H. Stegemann, and E. Votintsev. Ion irradiation through SiO<sub>2</sub>/Si-interfaces: Non-conventional fabrication of Si nanocrystals for memory applications. *Nuclear Instruments and Methods in Physics Research B*, 2004. accepted for publication.
- R. F. Steimle, R. Rao, C. Swift, K. Harber, S. Straub, R. Muralidhar, B. Hradsky, J. Yater, E. Prinz, W. Paulson, M. Sadd, C. Parikh, S. Anderson, T. Huynh, B. Acred, L. Grieve, M. Rossow, R. Mora, B. Darlington, K. Chang, and B. White Jr. Integration of silicon nanocrystals into a 6V 4Mb nonvolatile memory array. In *IEEE Nonvolatile Semiconductor Workshop*, pages 73–74, Aug. 2004.
- Q. Wan, N. L. Zhang, W. L. Liu, C. L. Lin, and T. H. Wang. Memory and negative photoconductivity effects of ge nanocrystals embedded in ZrO<sub>2</sub>/Al<sub>2</sub>O<sub>3</sub> gate dielectrics. *Applied Physics Letters*, 83(1):138–140, July 2003.

## Appendix A.

# Bit Encoding of the Kinetic Monte Carlo Lattice

KMC simulations with KAWASAKI type local exchange dynamics can be efficiently implemented on the basis of single bit manipulations (Heinig, 1994; Stauffer, 1991; Strobel et al., 2001). The implementation requires a mapping between of the  $f_{CC}$  coordinate space into the linear computer memory. For this purpose a simple cubic lattice with half of the  $f_{CC}$  lattice constant is constructed from which only half of the lattice – the  $f_{CC}$  sites – are used. The appropriate selection rule is:

A point  $(h, k, l)$  on the cubic lattice is a member of the  $f_{CC}$  lattice if  $h + k + l$  is even. (Newman and Barkema, 1999, chapter 13.1.3)

Using binary algebra the selection rule can be rewritten as

$$(x \text{ XOR } y \text{ XOR } z) \text{ AND } 1 = 1 \quad \forall f_{CC} \text{ lattice sites,} \quad (\text{A.1})$$

which will improve the computation speed (Heinig, 1994). Side lengths of the simulation cell are chosen to be powers of two times the  $f_{CC}$  lattice constant  $a$ , i.e.  $L_i = 2^{n_j} a$ ,  $j \in \{x, y, z\}$ , which is in particular has advantageous when using periodic boundary conditions. Coordinates  $x$  outside out of the simulation cell are projected back into the cell by

$$x' = (x \text{ AND } 2^{n_x} - 1). \quad (\text{A.2})$$

The important step is then the coordinate transformation that is necessary to map the 3D  $f_{CC}$  lattice into the linear computer memory (Figure 4.4). Previous KMC implementations have use different algorithms for the mapping between the cartesian coordinate space and the bit space. The *vector* and *cube* algorithms of (Heinig, 1994) and (Strobel, 1999) are examples. Both are described in detail in (Strobel, 1999, appendix A).

For the encoding of the  $f_{CC}$  simulation lattice a *cache-enhanced cube algorithm* has been developed, which improves the likelihood that neighboring lattice sites can be found in the same memory segment. Its predecessor, the *cube algorithm* of Strobel (1999) uses  $4 \times 4 \times 4$  bit cubes, which are now here extended to arbitrary sizes. A piece of the simulations lattice can be kept in the cache of the computer memory such that time consuming memory accesses can be minimized. Its very likely that all checks whether a neighboring site is occupied or not uses the same subset (cube) of the simulation lattice that already has been stored in the computer cache. Typical cube sizes used in this work are  $2^{b_x} \times 2^{b_{yz}} \times 2^{b_{yz}}$  lattice sites, where e.g.  $b_x = 5$  and  $b_{yz} = 4$  giving a cube size of 1024 Byte. In x-direction the cube size is limited to  $2^{b_x} = 2^5 = 32$  by the 32 bit computer architecture.



Here, the number indexing the cube and the index to the word within the cube has also been linked together to a single index  $m$ , which has the advantage that simple linear arrays with 32 bit words as elements (Integer) can be used. A single lattice site is then set to 1, i.e. the site is occupied using the following instruction:

```
BitField(n) = IBSET(BitField(n), xi)
```

Contrary, it can be emptied by:

```
BitField(n) = IBCLR(BitField(n), xi)
```

Despite of the increased complexity of this algorithm if compared with the original cube algorithm, the number of required bit manipulations remained the same (15 in both cases).

## References

- K.-H. Heinig. Efficient cellular automaton algorithm based on low-level bit manipulations. (unpublished), 1994.
- M. E. J. Newman and G. T. Barkema. *Monte Carlo Methods in Statistical Physics*. Oxford University Press, Oxford New York, 1999.
- D. Stauffer. Computer simulation of cellular automata. *Journal of Physics A*, 24:909–927, 1991.
- M. Strobel. Modeling and computer simulation of ion beam synthesis of nanostructures. Wissenschaftlich-Technische Berichte FZR-277, Forschungszentrum Rossendorf, Dresden, Germany, Nov. 1999. PhD thesis.
- M. Strobel, K.-H. Heinig, and W. Möller. Three-dimensional domain growth on the size scale of the capillary length: Effective growth exponent and comparative atomistic and mean-field simulations. *Physical Review B*, 64:245422, 2001.



# Acknowledgement

I'm deeply indebted to the INSTITUTE OF ION BEAM PHYSICS AND MATERIALS RESEARCH in the FORSCHUNGSZENTRUM ROSSENDORF and all its members. It has been a great pleasure to work in such a nice and inspiring environment. Sometimes, especially in the spring time, Rossendorf has been a scientist's ivory towers in its very best sense.

My thanks go in first place to Prof. Möller for the opportunity to work in the institute. He always had an open door for discussions and gave valuable advise where one was about to struggle.

Especially, I'd like to express my gratitude to Karl-Heinz Heinig, my direct supervisor in daily work and discussions. He always sought for further insights into self-organization phenomena and stimulated ones own creativity with his ideas, which he combined with a remarkable knowledge on current semiconductor developments and technology trends. Unforgotten are also our "coffee sessions" with him filled with discussions on daily topics but also spanning a surprisingly wide range from which I personally learned a lot. He especially encouraged and promoted me to present performed work in front of international audience at conferences, a part which I did not took for granted but enjoyed a lot.

Many thanks also go to the FWIP & FWIT team for the collegial and pleasant working atmosphere that I could enjoy. Warmly, I'll remember the small but regular breakfast rounds of our theory group (Matthias Posselt, Karl-Heinz Heinig and Hans Ulrich Jaeger) accompanied by more "experimentally oriented" people. The resulting mix of issues and discussions have always been diverting and inspiring. Here, I'd especially like to thank Bernd Schmidt from whom I've learned many things about semiconductor processing techniques and ion implantation in particular.

The work has been carried out within an European GROWTH project GRD1-2000-25619 and I kindly do acknowledge the financial support that have arisen from it. Above that the NEON project meant intense collaborations with people from several European countries and gave a vivid impression of an international scientific community. I especially want to thank

- Alain Claverie, Caroline Bonafos, and Gerard BenAssayag from CEMES, Toulouse for the intense and often controversy discussions on low energy IBS. As TEM and implantation experts they often were the natural opponent to simulation results, which in the end have lead to a sound picture of low energy IBS of Si NCs
- Michele Perego, Sabina Spiga, Marco Fanciulli from MDM-INFN, Milano, Italy,
- Panaotis Dimitrakis, Pascal Normand and Dimitiris Tsoukalas from IMEL Demokritos, Athens, Greece,
- Karl-Heinz Stegemann from ZMD AG, Dresden,

- and Arne N. Larsen from the Aarhus Univ., Danmark, with all I enjoyed numerous discussions.

Special thanks have to go to C. Colliex and M. Tence from LPS, Univ. Paris-Sud, Orsay, for the PEELS-STEM investigations on samples prepared in the CEMES in Toulouse. These valuable studies finally allowed a direct comparison of the morphology of phase separated Si with the performed KMC predictions.

Further I'd like to thank the numerous people that supported me in the one or the other way, that encouraged me or just lent me their ears in discussions. I wish to thank

- A. Mücklich for his support and help with the often tenacious TEM,
- Jan Schmidt, Volkhard Beyer, Lars Röntzsch and Stefan Hellwig for all the refreshing scientific and non-scientific discussions we had,
- J. Kreher and the friendly people from the IT department for their help with computer and network problems.

Among the many people to whom I am indebted for assistance and encouragement, I would like above all to thank my family. Without their continues support throughout the years, such a work would have never been possible. And maybe the most thanks above all belong to my girlfriend Steffi, who has supported me throughout tough times and always gave me the feeling that there's still life beyond work. Her steady interest in the things I was doing and her encouragement helped more than she might have thought. When she was around, I always had the best ideas.

# Ehrenwörtliche Erklärung

Hiermit versichere ich, dass ich die vorliegende Arbeit ohne unzulässige Hilfe Dritter und ohne Benutzung anderer als der angegebenen Hilfsmittel angefertigt habe; die aus fremden Quellen direkt oder indirekt übernommenen Gedanken sind als solche kenntlich gemacht. Die Arbeit wurde bisher weder im Inland noch im Ausland in gleicher oder ähnlicher Form einer anderen Prüfungsbehörde vorgelegt. Die vorliegende Arbeit wurde am Institut für Ionenstrahlphysik und Materialforschung im Forschungszentrum Rossendorf unter der Betreuung von Prof. W. Möller angefertigt. Die Prüfungsordnung der Fakultät Naturwissenschaften der TU Dresden erkenne ich an.

Dresden, den